



HAL
open science

Reduced Order Models, Forward and Inverse Problems in Cardiac Electrophysiology

Elisa Schenone

► **To cite this version:**

Elisa Schenone. Reduced Order Models, Forward and Inverse Problems in Cardiac Electrophysiology. General Mathematics [math.GM]. Université Pierre et Marie Curie - Paris VI, 2014. English. NNT : 2014PA066447 . tel-01092945

HAL Id: tel-01092945

<https://theses.hal.science/tel-01092945>

Submitted on 9 Dec 2014

HAL is a multi-disciplinary open access archive for the deposit and dissemination of scientific research documents, whether they are published or not. The documents may come from teaching and research institutions in France or abroad, or from public or private research centers.

L'archive ouverte pluridisciplinaire **HAL**, est destinée au dépôt et à la diffusion de documents scientifiques de niveau recherche, publiés ou non, émanant des établissements d'enseignement et de recherche français ou étrangers, des laboratoires publics ou privés.

**REDUCED ORDER MODELS,
FORWARD AND INVERSE PROBLEMS
IN CARDIAC ELECTROPHYSIOLOGY**

THÈSE DE DOCTORAT

Présentée par

Elisa SCHENONE

pour obtenir le grade de

**DOCTEUR DE
L' UNIVERSITÉ PIERRE ET MARIE CURIE - Paris VI**

Spécialité : MATHÉMATIQUES APPLIQUÉES

Soutenue publiquement le 28 Novembre 2014 devant le jury composé de :

Muriel BOULAKIA	Directrice de thèse
Yves COUDIÈRE	Rapporteur
Hervé DELINGETTE	Examinateur
Simone DEPARIS	Rapporteur
Jean-Frédéric GERBEAU	Directeur de thèse
Angelo IOLLO	Examinateur
Yvon MADAY	Président du jury
Damiano LOMBARDI	Invité

Après avis favorables des rapporteurs: Yves COUDIÈRE et Simone DEPARIS



Thèse préparée au sein de l'équipe-projet REO
Laboratoire Jacques-Louis Lions
Université Pierre et Marie Curie - Paris 6
et **Centre de Recherche Inria Paris-Rocquencourt**
Domaine de Voluceau, BP 105
78153 Le Chesnay CEDEX

REMERCIEMENTS

Mes premiers remerciements vont à mes directeurs de thèse Jean-Frédéric Gerbeau et Muriel Boulakia. Depuis ma timide arrivée à l'Inria, ils m'ont chaleureusement accueillie dans l'équipe. Ils m'ont transmis leur passion pour la recherche et ils ont su à la fois m'accompagner dans mon parcours et me laisser de l'autonomie. Merci pour vos conseils, votre enthousiasme, votre disponibilité et votre patience.

Je tiens à remercier mes rapporteurs Yves Coudière et Simone Deparis pour avoir accepté de lire ce manuscrit et pour leurs remarques constructives. Je remercie également Hervé Delingette, Angelo Iollo et Yvon Maday pour avoir accepté de faire partie de mon jury de thèse.

Merci à Michel Sorine, Qinghua Zhang et Claire Médigue de l'équipe SISYPHE de l'Inria Paris-Rocquencourt pour leur collaboration dans le développement du travail exposé dans le chapitre 5, grâce à leur algorithme de détection de fin d'onde T.

À la fin de ma première année j'ai eu la chance de participer à l'école d'été Cemracs'12. Cela m'a énormément apporté autant professionnellement que personnellement. Je tiens à remercier encore une fois tous les organisateurs et tous les amis que j'ai pu rencontrer. Merci en particulier à Christophe Prud'Homme, pour m'avoir permis de travailler sur le sujet des bases réduites appliquées au problème de la convection naturelle. Merci aussi à Stéphane pour avoir partagé cette expérience, ça a été un vrai plaisir de travailler avec toi.

Ensuite, un grand merci à tout le bâtiment 16. Merci aux "vieux" qui étaient là quand je suis arrivée et qui ont pu m'apprendre la vie à l'Inria, en particulier à mes premiers co-bureau Cristobal et Saverio. Et merci aux petits, auxquels j'espère avoir appris à mon tour quelque chose, en particulier à ma petite Chloé pour toutes les fois où j'ai frappé à ta porte. Merci aussi à Marina pour sa bonne humeur et son oeil bienveillant sur nous tous, et à Maryse pour son aide précieuse.

Merci à Damiano, pendant ces trois années tu as été pour moi à la fois un collègue, un directeur de thèse, un ami et un coach sportif; merci pour tes conseils, pour ton aide et tes explications, pour les moments de folie et rigolade, et pour toutes les discussions philosophiques sur les espaces complexes que nous sommes les seuls à pouvoir comprendre !

Un peu plus loin du bâtiment 16, merci à Annabelle, nous avons commencé et parcouru ensemble ces trois années non sans difficultés, mais ça a été un véritable plaisir de collaborer avec toi et je suis sûre que nous auront encore de belles aventures à partager.

Enfin, l'Inria n'est heureusement pas seulement le bâtiment 16, alors merci à la

Junior Seminar team, en particulier à Jonathan et Emanuele pour m'avoir accueillie dans l'équipe et fait découvrir les autres bâtiments.

Last but not least, pour "survivre" à la thèse ça a été indispensable d'être entourée d'amis, d'avoir eu le soutien de ma famille et la chance de trouver du réconfort le soirs en rentrant chez soi.

Alors, merci les filles : Elena, Giulia et Alyna, je ne pourrais pas imaginer ces quatre années sans nos diners, thés et apéros, les soirées italiennes, les séances de sport, ... Merci à mes parents, qui sont toujours si fiers de moi, même s'ils ne comprennent toujours pas ce que je fais et surtout pourquoi je le fais. Cependant, c'est grâce à eux si je suis là, ils ont compris ce que je voulais être "quand je serai grande" bien avant moi, et depuis ils ont jamais cessé de me soutenir dans tous mes choix. Et merci à Benoit, il n'y a pas besoin d'explications pour dire à quel point tu as été important.

REDUCED ORDER MODELS, FORWARD AND
INVERSE PROBLEMS IN CARDIAC ELECTROPHYSIOLOGY

Abstract: This PhD thesis is dedicated to the investigation of the forward and the inverse problems in cardiac electrophysiology. Since the equations that describe the electrical activity of the heart can be very demanding from a computational point of view, a particular attention is paid to the reduced order methods and to their application to the electrophysiology models.

First, we introduce the mathematical and numerical models of electrophysiology and we implement them to provide for simulations that are validated against various qualitative and quantitative criteria found in the medical literature. Since our model takes into account atria and ventricles, we are able to reproduce full cycle Electrocardiograms (ECG) in healthy configurations and also in several pathological cases.

Then, few reduced order methods are investigated for the resolution of the electrophysiology equations. The Proper Orthogonal Decomposition (POD) method is applied for the discretization of the electrophysiology equations in different configurations, as for instance the simulation of a myocardial infarction. Also, the method is used in order to solve some parameters identification problems such as the identification of an infarcted zone using the Electrocardiogram measures and the efficient simulation of restitution curves. To circumvent some limitations of the POD method, an innovative reduced order method based on the Approximated Lax Pairs (ALP) is investigated. This method is applied to the forward and inverse problems. Finally, a new reduced order algorithm is proposed, based on the ALP and the Discrete Empirical Interpolation methods. This new approach significantly improves the efficiency of the original ALP algorithm and allow us to consider more complex models used in electrophysiology.

Keywords: Mathematical modelling, Cardiac electrophysiology, Computational Electrocardiogram, Inverse problem, Reduced order method, Proper orthogonal decomposition, Approximated Lax pairs.

MODÈLES D'ORDRE RÉDUIT, PROBLÈMES
DIRECTS ET INVERSES EN ÉLECTROPHYSIOLOGIE CARDIAQUE

Resumé: Cette thèse de doctorat est consacrée à l'étude des problèmes direct et inverse en électrophysiologie cardiaque. Comme les équations qui décrivent l'activité électrique du cœur peuvent être très coûteuses en temps de calcul, une attention particulière est apportée aux méthodes d'ordre réduit et à leur applications aux modèles de l'électrophysiologie.

Dans un premier temps, nous introduisons les modèles mathématiques et numériques de l'électrophysiologie cardiaque. Ces modèles nous permettent de réaliser des simulations numériques que nous validons à l'aide de plusieurs critères qualitatifs et quantitatifs trouvés dans la littérature médicale. Comme notre modèle prend en compte les oreillettes et les ventricules, nous sommes capables de reproduire des cycles complets d'électrocardiogrammes (ECG) à la fois dans des conditions saines et dans des cas pathologiques.

Ensuite, plusieurs méthodes d'ordre réduit sont étudiées pour la résolution des équations de l'électrophysiologie. La méthode *Proper Orthogonal Decomposition* (POD) est appliquée pour la discrétisation des équations de l'électrophysiologie dans plusieurs configurations, comme par exemple la simulation d'un infarctus du myocarde. De plus, cette méthode est utilisée pour résoudre quelques problèmes d'identification de paramètres comme localiser un infarctus à partir de mesures d'un électrocardiogramme ou simuler une courbe de restitution. Pour contourner les limitations de la POD, une nouvelle méthode basée sur des couples de Lax approchés (Approximated Lax Pairs, ALP) est utilisée. Cette méthode est appliquée aux problèmes direct et inverse. Pour finir, un nouvel algorithme, basé sur les méthodes ALP et l'interpolation empirique discrète, est proposé. Cette nouvelle approche améliore significativement l'efficacité de l'algorithme original ALP et nous permet de considérer des modèles plus complexes utilisés en électrophysiologie cardiaque.

Mots-clés: Modélisation mathématique, Électrophysiologie cardiaque, Électrocardiogramme, Problèmes inverses, Méthodes d'ordre réduit, Proper Orthogonal Decomposition, Couples de Lax approchés.

Contents

Introduction	1
Thesis general context	1
Thesis outline	2
Published and pre-print articles	4
Introduction (Français)	5
Contexte général de la thèse	5
Plan de thèse	6
Articles publiés et pre-print	8
1 Cardiac electrophysiology: model, equations, inverse problems and approximations	9
1.1 Introduction	11
1.2 Heart physiology	11
1.3 Cardiac electrophysiology	18
1.4 Cardiac electrophysiology models	27
1.5 Inverse problems in cardiac electrophysiology	36
1.6 Reduced Order Methods: a brief overview	40
2 Numerical simulations of full electrocardiogram cycle	45
2.1 Introduction	47
2.2 Whole heart mesh	48
2.3 Modeling assumptions	50
2.4 Healthy and pathological numerical simulations	58
2.5 Electrodes vest	68
2.6 Chapter conclusions	70
2.A Mitchell and Schaeffer ionic model	72
2.B Minimal Ventricular ionic model	73
2.C Courtemanche, Ramirez and Nattel ionic model	75
3 Estimation of some FitzHugh-Nagumo model parameters	79
3.1 Introduction	81
3.2 State of the art and motivation	81
3.3 Regularity of the solution	83
3.4 Estimation of reaction parameter	88
3.5 Estimation of a parameter in the second equation	92
3.6 Chapter conclusions	96

4	Reduced-order modeling and parameters identification with POD	97
4.1	Introduction	99
4.2	Presentation of the model	99
4.3	Proper Orthogonal Decomposition method	101
4.4	Application of POD to forward problems	101
4.5	Application of POD to the parameters identification	106
4.6	Chapter conclusions	112
4.A	Genetic algorithm	114
5	Long-time simulations and Restitution Curves with POD	117
5.1	Introduction	119
5.2	Presentation of the models	119
5.3	Restitution Curve definition	120
5.4	Parameters identification in 0D case	125
5.5	Parameters identification with an ECG-based RC	126
5.6	Chapter conclusions	129
6	Reduced Order Model with Approximated Lax Pairs	131
6.1	Introduction	133
6.2	The ALP method	134
6.3	ALP in cardiac electrophysiology	140
6.4	Numerical experiments	146
6.5	Chapter conclusions	161
7	Inverse problems with ALP reduced-order method	163
7.1	Introduction	165
7.2	An overview on data assimilation	165
7.3	Application to Micro-Electrode Arrays measures	167
7.4	Application to epicardium potential reconstruction	172
7.5	Chapter conclusions	175
8	ROM with ALP and Discrete Empirical Interpolation Method	177
8.1	Introduction	179
8.2	The ALP-DEIM method	180
8.3	ALP-DEIM in cardiac electrophysiology	185
8.4	Numerical experiments	190
8.5	Perspectives	197
8.6	Chapter conclusions	200
	Conclusions	201
	Conclusions (Français)	203

A FELiScE	205
A.1 FELiScE general principles	207
A.2 Structure of the code	207
A.3 Electrophysiology equations implementation	211
A.4 Reduced-Order Models implementation	212
A.5 Author's contributions	215
B High performance computing for the reduced basis method	217
Bibliography	239

Introduction

Thesis general context

Cardiac electrophysiology is the science that studies the electrical activity of the heart. One of the most used exams providing an accurate recording of the heart's activity is the Electrocardiogram (ECG). This medical procedure represents a fast, noninvasive and inexpensive technique. The measure of the heart's electrical activity with an ECG allows a medical doctor to make a diagnosis. In the future, the mathematical modelling and the numerical simulation may also help to better exploit these signals and to improve the diagnosis and the prognosis.

Mathematical and numerical modelling allows us to represent the heart behavior. In particular, the idea is to reconstruct the cardiac electro-mechanical activity using some measures like the ECG. In this manuscript we will concentrate only on the electrical part and we will neglect the heart's mechanics.

In order to address the inverse problem of electrocardiology, *i.e.* reconstruct the electrical potential of the heart from an ECG, we choose to start from an accurate forward model that can describe this phenomenon. The equations which describe the cardiac electrical activity are called *bidomain* equations [Tun78]. It is a system of two partial differential equations which is coupled with a model describing the ionic exchanges between cardiac tissue cells. The resolution of these systems need some accurate numerical methods, such as the finite elements, which can be very expensive from a computational point of view. In the purpose of using these models for the resolution of the inverse problem and to make numerical tools useful for the clinicians, it is necessary to reduce as much as possible the computational time of the simulations. To decrease the computational time, we propose to use reduced order methods. These methods are used in several scientific computing fields. They are based on the idea of decreasing the number of degrees of freedom by adding some information hidden in the solution of the problem.

In the last decade, the cardiac electrophysiology modelling has been one of the main subjects of interest of REO team, in collaboration with the M Ξ DISIM team (previously MACS) of Inria-Saclay. Previous works developed in REO team provided accurate numerical simulations of cardiac electrophysiology equations, this was the context for instance of the PhD work of Nejib Zenzemi [Zem09]. A particular attention has been paid to the parameters identification problem. Also, the first applications of reduced-order methods with Proper Orthogonal Decomposition have been proposed.

The principal contributions of this work deal with the forward and inverse electrophysiology problems and with the application of reduced-order methods to both problems. The mathematical and numerical models used in [Zem09] have been improved in order to provide more realistic results, including simulations on the whole heart (atria and ventricles) and full cycle electrocardiograms computation in various pathological cases too. The results have been validated against various criteria found in the medical literature. Some reduced order models have been applied to the cardiac electrophysiology equations in several contexts and also used in the inverse problems of parameters identification and state estimation. In particular, the Proper Orthogonal Decomposition has been used and adapted for the simulation and the identification of a myocardial infarction. Also, some new approaches of the reduced-order models based on Approximated Lax Pairs have been applied to electrophysiology equations and used in a data assimilation technique to estimate the state of the system.

Thesis outline

In Chapter 1 the principal models used in this work are introduced. A description of the heart physiology and electrical activity is provided. We introduce the reader to the domain of electrophysiology and electrocardiograms with some historical notes on the subject. Then, the mathematical models used in cardiac electrophysiology are detailed. Finally, the state-of-art on cardiac electrophysiology inverse problems and on reduced-order methods is provided.

In Chapter 2 we detail the improvement accomplished in the numerical simulations of electrocardiograms. This work provides full cycle electrocardiograms thanks to the coupling of the ventricles geometry (volume domain) to the atria geometry (surface). In fact, a modelling effort has been made in order to couple these two structures since atria are a thin surface and need specific model equations. Also, the introduction of a more realistic and complete geometry allowed us to provide accurate simulations of several pathologies. This work is in collaboration with Annabelle Collin, PhD student in M Ξ DISIM team, and Jean-Frédéric Gerbeau and is part of a paper that has to be submitted.

Chapter 3 provides some theoretical results on the estimates of some parameters of the electrophysiology equations. These results are obtained in collaboration with Muriel Boulakia.

In Chapters 4 and 5 the Proper Orthogonal Decomposition (POD) method is applied to cardiac electrophysiology. In particular, in Chapter 4 the POD method is used for the simulation of electrocardiograms when some parameters of the model change and for the simulation of myocardial infarction. Also, the method is applied to the identification of four of the parameters of the model and to the identification of the infarcted region with a Genetic Algorithm. This work is in collaboration with Muriel Boulakia and Jean-Frédéric Gerbeau and it is part of a published paper.

In Chapter 5 we introduce the definition of the restitution curve and we use it for

the identification of some of the ionic parameters. Also, this definition is extended to the electrocardiogram measures and the identification of the parameters using some synthetic data reproduced with the POD method.

Chapters 6, 7 and 8 deal with a new reduced order method based on Approximated Lax Pairs (ALP), which has been introduced by Gerbeau and Lombardi in [GL14]. These works have been developed in collaboration with Damiano Lombardi, researcher in the REO team, and Jean-Frédéric Gerbeau.

The method is applied to electrophysiology equations in Chapter 6 in some particular challenging settings such as the heterogeneity of some parameters and source terms which are unknown.

In Chapter 7 we deal with some inverse problems. In particular the reduced-order method introduced in Chapter 6 is applied to a data assimilation technique in order to estimate the state in two configurations: the identification of a source term location using some synthetic Micro-Electrode Arrays measures, and the estimation of the epicardial potential using some electrodes vest measures on a simplified geometry.

In Chapter 8 a new reduced-order approach based on Approximated Lax Pairs and Discrete Empirical Interpolation Methods is introduced. The method is applied to the electrophysiology equations and the possible developments of this method are exposed.

Finally, the main conclusions are drawn.

Most of the chapters can be read independently, except for Chapters 7 and 8 whose comprehension is strictly linked to Chapter 6. However, we suggest a reading in the order proposed by the author.

Published and pre-print articles

- Muriel Boulakia, Elisa Schenone, Jean-Frédéric Gerbeau, *Reduced-order modeling for cardiac electrophysiology. Application to parameter identification*, Int. J. Num. Meth. Bioeng. Volume 28, Issue 6-7, Pages 727-744, 2012.
- Elisa Schenone, Stéphane Veys, Christophe Prud'Homme, *High Performance Computing for the Reduced Basis Method. Application to Natural Convection*, ESAIM: Proceedings 43(2013), Pages 255-273.
- Jean-Frédéric Gerbeau, Damiano Lombardi, Elisa Schenone, *Reduced Order Model in Cardiac Electrophysiology with Approximated Lax Pairs*, To appear in *Advances in Computational Mathematics*, Special Issue on MoRePas.
- Elisa Schenone, Annabelle Collin, Jean-Frédéric Gerbeau, *Numerical simulations of full electrocardiogram cycle*, Submitted.
- Muriel Boulakia, Elisa Schenone, *Theoretical study of the estimate of some FitzHugh-Nagumo model parameters*, To be submitted.
- Jean-Frédéric Gerbeau, Damiano Lombardi, Elisa Schenone, *Reduced Order Model in Cardiac Electrophysiology with Approximated Lax Pairs and Discrete Empirical Interpolation Method*, To be submitted.

Introduction (Français)

Contexte général de la thèse

L'électrophysiologie cardiaque est la science qui étudie l'activité électrique du cœur. L'un des examens les plus utilisés permettant d'avoir une mesure précise de l'activité électrique du cœur est l'électrocardiogramme (ECG). Cet outil médical représente une technique rapide, non invasive et peu coûteuse. La mesure de l'activité électrique du cœur par l'ECG permet aux médecins d'établir un diagnostic. Dans le futur, la modélisation mathématique et la simulation numérique permettront peut-être de mieux exploiter ces signaux, et d'améliorer le diagnostic et le pronostic.

La modélisation mathématique et numérique permet de fournir une représentation du comportement du cœur. En particulier, l'idée est de pouvoir reconstruire l'activité électro-mécanique cardiaque à partir de mesures de type électrocardiogramme. Dans ce manuscrit on se concentrera uniquement sur l'aspect électrique du cœur.

Pour pouvoir résoudre le problème inverse de l'électrocardiologie, c'est à dire reconstruire le potentiel électrique du cœur à partir d'un ECG, nous choisissons de nous baser sur un modèle direct précis qui décrit ce phénomène. Les équations qui décrivent l'activité électrique cardiaque sont appelées les équations *bidomaine* [Tun78]. Il s'agit d'un système de deux équations aux dérivées partielles couplé à des modèles décrivant les échanges ioniques entre les cellules du tissu cardiaque qui peuvent être constituées de plusieurs équations différentielles. La résolution de ces systèmes nécessite des modèles numériques précis, ce qui implique que les simulations qui en découlent peuvent être très coûteuses en temps avec des méthodes de résolution telle que la méthode des éléments finis. Dans le but d'utiliser ces modèles pour la résolution du problème inverse et de rendre ces outils numériques utilisables par les cliniciens, il est nécessaire que les simulations soient le plus rapide possible. Pour diminuer les temps de calculs, on propose d'utiliser des méthodes d'ordre réduit. Le principe de ces méthodes, utilisées dans plusieurs domaines de calcul scientifique, est de diminuer le nombre de degrés de liberté tout en ajoutant des informations apportées par la solution du problème.

Durant la dernière décennie, l'électrophysiologie cardiaque a été l'un des principaux sujets d'intérêt de l'équipe REO, en collaboration avec l'équipe M Ξ DISIM (anciennement MACS) de l'Inria-Saclay. Les travaux précédents de l'équipe REO ont fourni des simulations numériques précises des équations de l'électrophysiologie cardiaque, comme par exemple dans la thèse de doctorat de Nejib Zemzemi [Zem09]. Une attention particulière a été apportée au problème d'identification de paramètres.

Les premières applications de modèles d'ordre réduit avec la Proper Orthogonal Decomposition furent de plus proposées.

Les contributions principales de cette thèse portent sur les problèmes direct et inverse de l'électrophysiologie cardiaque, et à l'application de modèles d'ordre réduit à ces problèmes. Les modèles mathématiques et numériques utilisés dans [Zem09] ont été améliorés pour fournir des résultats plus réalistes, comprenant des simulations sur un cœur entier (oreillettes et ventricules) et le calcul d'un électrocardiogramme pour un cycle cardiaque complet sur des cas sains mais aussi pour différentes pathologies. Les résultats ont été validés à l'aide de divers critères issus de la littérature médicale. Des modèles d'ordre réduit ont été appliqués aux équations de l'électrophysiologie cardiaque et utilisés aussi dans le problème inverse d'identification de paramètres et d'estimation d'état. En particulier, la *Proper Orthogonal Decomposition* a été utilisée et adaptée pour la simulation et l'identification d'un infarctus du myocarde. De plus, de nouvelles techniques de réduction de modèle basées sur des couples de Lax approchés ont été appliquées aux équations de l'électrophysiologie et utilisées dans une technique d'assimilation de données pour estimer l'état du système.

Plan de thèse

Dans le chapitre 1, les principaux modèles utilisés dans ce travail sont introduits. Une description de la physiologie du cœur et de son activité électrique sont fournis. Nous introduisons l'électrophysiologie et les électrocardiogrammes avec des notes historiques sur le sujet. Ensuite, les modèles mathématiques utilisés en électrophysiologie cardiaque sont détaillés. Finalement, un état de l'art sur les problèmes inverses de l'électrophysiologie cardiaque et sur les méthodes d'ordre réduit est présenté.

Dans le chapitre 2, nous détaillons les améliorations apportées par la simulation numérique des électrocardiogrammes. Ce travail reproduit numériquement un cycle complet de l'électrocardiogramme grâce au couplage de la géométrie des ventricules (domaine volumique) et de la géométrie des oreillettes (domaine surfacique). Un effort de modélisation a été effectué pour coupler ces deux structures puisque les oreillettes sont une surface fine et ont besoin d'un modèle adapté. De plus, l'introduction d'une géométrie plus réaliste et complète nous a permis de fournir des simulations plus précises de plusieurs pathologies. Ce travail a été fait en collaboration avec Annabelle Collin, doctorante dans l'équipe M Ξ DISIM, et Jean-Frédéric Gerbeau et fait partie d'un article qui doit être soumis.

Le chapitre 3 présente des résultats théoriques sur l'estimation de quelques paramètres des équations de l'électrophysiologie. Ces résultats ont été obtenu en collaboration avec Muriel Boulakia.

Dans les chapitres 4 et 5, la méthode de la *Proper Orthogonal Decomposition* (POD) est appliquée à l'électrophysiologie cardiaque. En particulier, dans le chapitre 4, la méthode de la POD est utilisée pour la simulation des électrocardiogrammes quand certains paramètres du modèle varient et pour la simulation d'un infarctus du myocarde. De plus, cette méthode est combinée à une méth-

ode d'algorithme génétiques afin d'identifier quatre des paramètres du modèle et à identifier un l'infarctus. Ces travaux ont été effectués en collaboration avec Muriel Boulakia et Jean-Frédéric Gerbeau et font partie d'un article publié.

Dans le chapitre 5, nous introduisons la notion de courbes de restitution et nous l'utilisons pour l'identification de certains paramètres ioniques. De plus, cette définition est élargie aux mesures de l'électrocardiogramme et à l'identification de paramètres en utilisant des données synthétiques obtenues avec la méthode de la POD.

Les chapitres 6, 7 et 8 concernent une nouvelle méthode d'ordre réduit basée sur des couples de Lax approchées (ALP – Approximated Lax Pairs), qui a été introduite par Gerbeau et Lombardi [GL14]. Ces travaux ont été développés en collaboration avec Damiano Lombardi, chercheur dans l'équipe REO, et Jean-Frédéric Gerbeau.

La méthode est appliquée aux équations de l'électrophysiologie dans le chapitre 6 dans des configurations particulièrement complexes comme des hétérogénéités de paramètres et de termes source "inconnues". Ce chapitre décrit les résultats d'un papier, en phase de révision, en collaboration avec Damiano Lombardi et Jean-Frédéric Gerbeau

Dans le chapitre 7, nous nous intéressons à plusieurs problèmes inverses. En particulier, la méthode présentée au chapitre précédent est appliquée à une technique d'assimilation de données pour estimer l'état dans deux configurations différentes: l'identification de la localisation d'un terme source en utilisant des mesures synthétiques de Micro-Electrode Arrays, et l'estimation du potentiel de l'épicarde en utilisant des mesures de type veste d'électrodes sur une géométrie simplifiée.

Dans le chapitre 8, une nouvelle méthode d'ordre réduit basée sur les couples de Lax approchés et sur la méthode d'interpolation empirique discrète (DEIM – Discrete Empirical Interpolation Method) est introduite. La méthode est appliquée aux équations de l'électrophysiologie et les possibles développements de la méthode sont exposés.

Enfin, les conclusions principales de la thèse sont exposées.

La plupart des chapitres peuvent être lus indépendamment les uns des autres, à l'exception des chapitres 8 et 7 dont la compréhension est liée au chapitre 6. Cependant, nous suggérons une lecture dans l'ordre proposé par l'auteur.

Articles publiés et pre-print

- Muriel Boulakia, Elisa Schenone, Jean-Frédéric Gerbeau, *Reduced-order modeling for cardiac electrophysiology. Application to parameter identification*, Int. J. Num. Meth. Bioeng. Volume 28, Issue 6-7, Pages 727-744, 2012.
- Elisa Schenone, Stéphane Veys, Christophe Prud'Homme, *High Performance Computing for the Reduced Basis Method. Application to Natural Convection*, ESAIM: Proceedings 43(2013), Pages 255-273.
- Jean-Frédéric Gerbeau, Damiano Lombardi, Elisa Schenone, *Reduced Order Model in Cardiac Electrophysiology with Approximated Lax Pairs*, À paraître dans *Advances in Computational Mathematics*, Special Issue on MoRePas.
- Elisa Schenone, Annabelle Collin, Jean-Frédéric Gerbeau, *Numerical simulations of full electrocardiogram cycle*, Soumis.
- Muriel Boulakia, Elisa Schenone, *Theoretical study of the estimate of some FitzHugh-Nagumo model parameters*, À soumettre.
- Jean-Frédéric Gerbeau, Damiano Lombardi, Elisa Schenone, *Reduced Order Model in Cardiac Electrophysiology with Approximated Lax Pairs and Discrete Empirical Interpolation Method*, À soumettre.

Cardiac electrophysiology: model, equations, inverse problems and approximations

In this chapter we present the models used in this thesis. The main aim of this work is to present some techniques on reduced models for the so-called forward and inverse problems of cardiac electrophysiology. All the elements needed to the understanding of the next chapters are given: a brief description of the heart physiology and the cardiac electrical activity; the definition of the Electrocardiogram with some historical notes on its origins; the mathematical models used to represent the cardiac electrical potential and the electrical potential on the body skin, which is necessary to build the Electrocardiogram. Then, some specific mathematical notions are illustrated. First, the inverse problems in cardiography are presented. Second, we give a description of the Reduced Order Models largely used in this thesis.

Contents

1.1	Introduction	11
1.2	Heart physiology	11
1.2.1	Heart geometry and location	11
1.2.2	Blood and electrical cardiac cycles	12
1.2.3	Electrical cycle at microscopic scale	17
1.3	Cardiac electrophysiology	18
1.3.1	From Descartes “animal spirits”...	18
1.3.2	...through modern Electrocardiography ...	22
1.3.3	...to numerical simulations of electrocardiograms	25
1.4	Cardiac electrophysiology models	27
1.4.1	The bidomain and the monodomain equations	28
1.4.2	Ionic models	30
1.4.3	The body diffusion problem and heart-torso coupling conditions	31
1.4.4	Other approximations	33
1.4.5	Numerical approximation	34
1.5	Inverse problems in cardiac electrophysiology	36
1.5.1	The “classical” inverse problem of electrocardiography	36
1.5.2	Transmembrane potential reconstruction problem	39
1.5.3	Parameters identification inverse problem	39
1.6	Reduced Order Methods: a brief overview	40
1.6.1	Reduced Basis	40
1.6.2	Proper Orthogonal Decomposition	41
1.6.3	Reduce Order Method based on Approximated Lax Pairs	44

1.1 Introduction

To better understand the works presented hereafter, we present here the main useful fields. First, we introduce the cardiac electrophysiology from a medical point of view. In particular, in Section 1.2, we give some basic skills on the heart physiology with a detailed description of its electrical activity. Using these notions, in Section 1.3 we present an overview on the cardiac electrophysiology, giving some historical notes on the origin of the Electrocardiogram and a detailed description of it.

Second, we illustrate the main mathematical instruments useful in the next chapters. In Section 1.4 the equations used in cardiac electrophysiology are described: the bidomain equations [Tun78] to model the heart potential, the ionic models useful to approximate the ionic exchanges in the cardiac tissue, and the equations used to model the potential in the rest of the body (torso). In Section 1.5, we focus on the inverse problems in electrophysiology, with a particular attention to the “classical” inverse problem of reconstruction of the electrical potential on the heart surface using some skin potential measures. Finally, in Section 1.6 we give a description of Reduced-Order Methods, in particular we briefly describe the standard technique of the reduced basis [MR02], we better analyze the Proper Orthogonal Decomposition method [KV01, RP04] largely used in the next chapters, and we introduce the Approximated Lax Paris methods [GL14], which will be detailed in Chapters 6 and 8.

1.2 Heart physiology

The cardiovascular system consists of the blood, the heart and the blood vessels. In this section we give a brief description of the main actor of the cardiovascular system: the heart. We first present from a medical point of view the heart geometry, location and functions. Then, we concentrate on the blood and electrical cycles. Finally, we describe the electrical cycle at a microscopical scale, giving a description of the main ionic exchanges that give rise to the cardiac electrical activity.

1.2.1 Heart geometry and location

The heart is a hollow muscle whose role is to pump the blood to the body’s blood vessels. Blood must be constantly pumped to reach body cells and organs, most of human organs cannot survive more than a few minutes without supply of oxygenated blood. In order to accomplish this, the heart beats more than 100,000 times every day.

The heart is located in the chest between the lungs, behind the sternum and above the diaphragm and about two-thirds of the mass of the heart lies on the left of the body’s midline (see Figure 1.1). It is a relatively small organ: about 12cm long, 9cm wide at its broadest point, and 6cm thick, with an average mass of 300 g in adult males [TD08]. The shape of the heart is similar to a cone lying on its side. The base of the heart is its posterior surface and the apex is the tip of the lower chamber (see Figure 1.3 top-left).

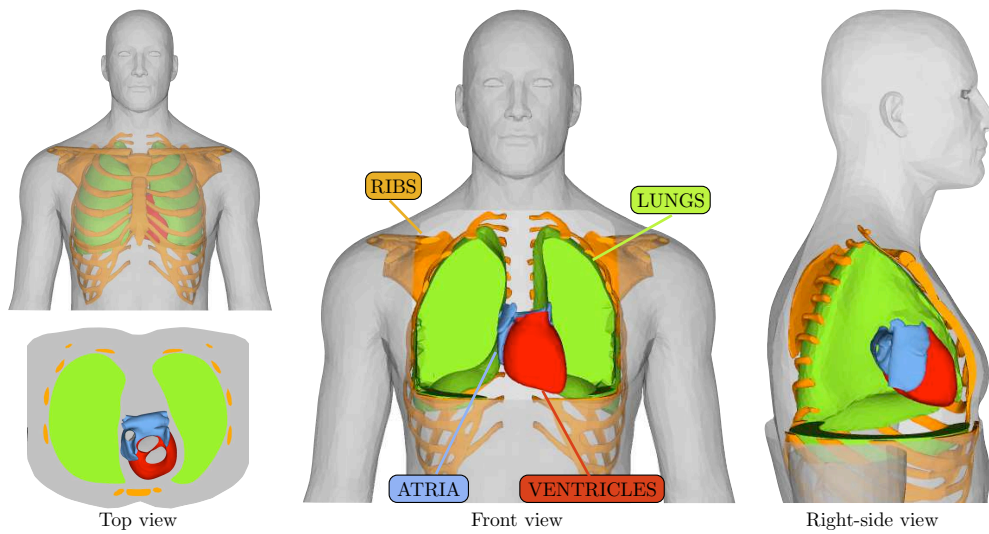


Figure 1.1: Heart location in the thoracic cavity.

It is divided into four chambers: two atria and two ventricles (see Figure 1.2). The two superior ones are the atria that receive blood from the veins, the inferior ones are the ventricles that pump blood into the aorta and arteries. In particular, the right atrium forms the right border of the heart and receives blood from *superior vena cava*, *inferior vena cava* and *coronary sinus*, and it pumps it into the left ventricle through *tricuspid valve*. The left atrium receives blood from the lungs through four *pulmonary veins* and pumps it into the left ventricle through the *bicuspid (mitral) valve*. Also, blood is pumped from the right ventricle into the pulmonary trunk, which divides into right and left *pulmonary arteries*, through the *pulmonary valve*, and from the left ventricle into the ascending aorta through the *aortic valve*. Atria and the right ventricle are about 2-3mm and 4-5mm in average thickness respectively, while the left ventricle is the thickest chamber with an average thickness of 1-15mm [TD08]. The ventricles are thicker than atria since they pump blood under higher pressure over greater distance. In particular, the right and left ventricles act as two separate pumps, the right one pumps blood only to the lungs while the left one pumps blood at higher pressure in the rest of the body, that is why its walls are the thickest. At every heart beat, each chamber contracts in order to push a volume of blood into ventricles or arteries.

1.2.2 Blood and electrical cardiac cycles

The contractions of atria and ventricles are jointed to the electrical activity of the heart. The electrical activity is autorhythmic, *i.e.* it is independent from the blood supply and continues even if the heart is removed from the body, for instance for a transplantation. The source of the cardiac electrical activity is a network of

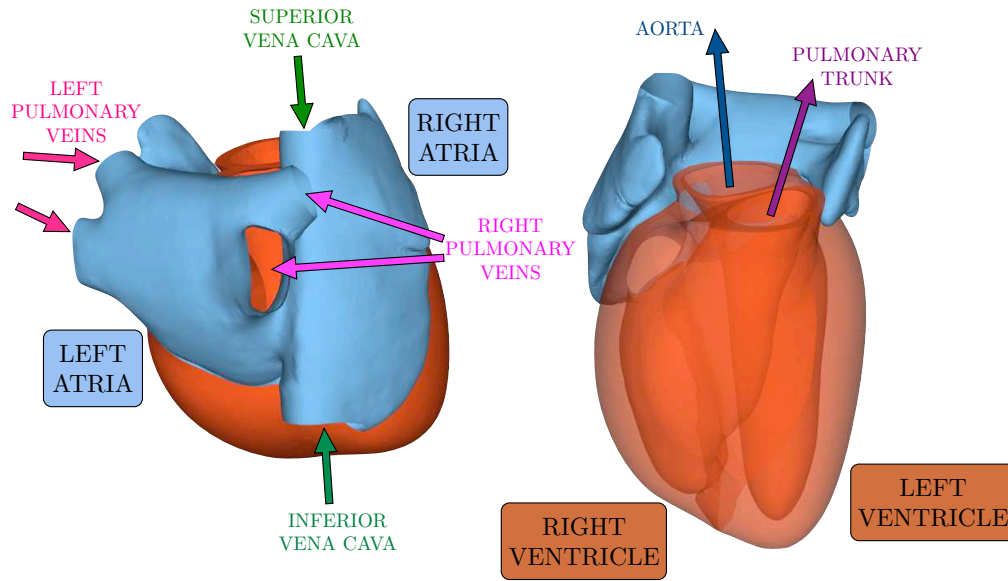


Figure 1.2: Heart geometry with vessels.

muscle fibers, the so-called conduction system, that generates action potentials that trigger heart contractions. The conduction system defines the electrical pathway which the cardiac action potential propagate through and that allows the chambers to contract successively.

The cardiac cycle is summarized into five phases, schematized in Figures 1.4 and 1.5:

1. The cardiac excitation starts from the sinoatrial (SA) node, in the right atria (see Figure 1.3 top-right). The cells placed in the SA node act as a pacemaker: their resting potential is not stable, so they spontaneously depolarize to threshold. When the threshold is reached, the action potential is triggered and propagates throughout atria. Since atria are depolarized, they contract. Then, tricuspid and mitral valves open and let blood through into ventricles.
2. After propagating in the atria, the action potential reaches the atrioventricular (AV) node, located in the cardiac septum, between atria and ventricles (see Figure 1.3 bottom-left). The action potential propagates through the bundle of His, which is the unique electrical connection between atria and ventricles since a fibrous skeleton preventing conduction is present elsewhere. Through the bundle of His, the action potential enters the ventricles, propagates through the septum and reaches the apex of the heart. After the injection of the blood in the ventricles, tricuspid and mitral valves close.
3. The Purkinjie fibers conduct the action potential from the apex of the heart to the rest of the myocardium. Consequently, the ventricles contract, aortic and

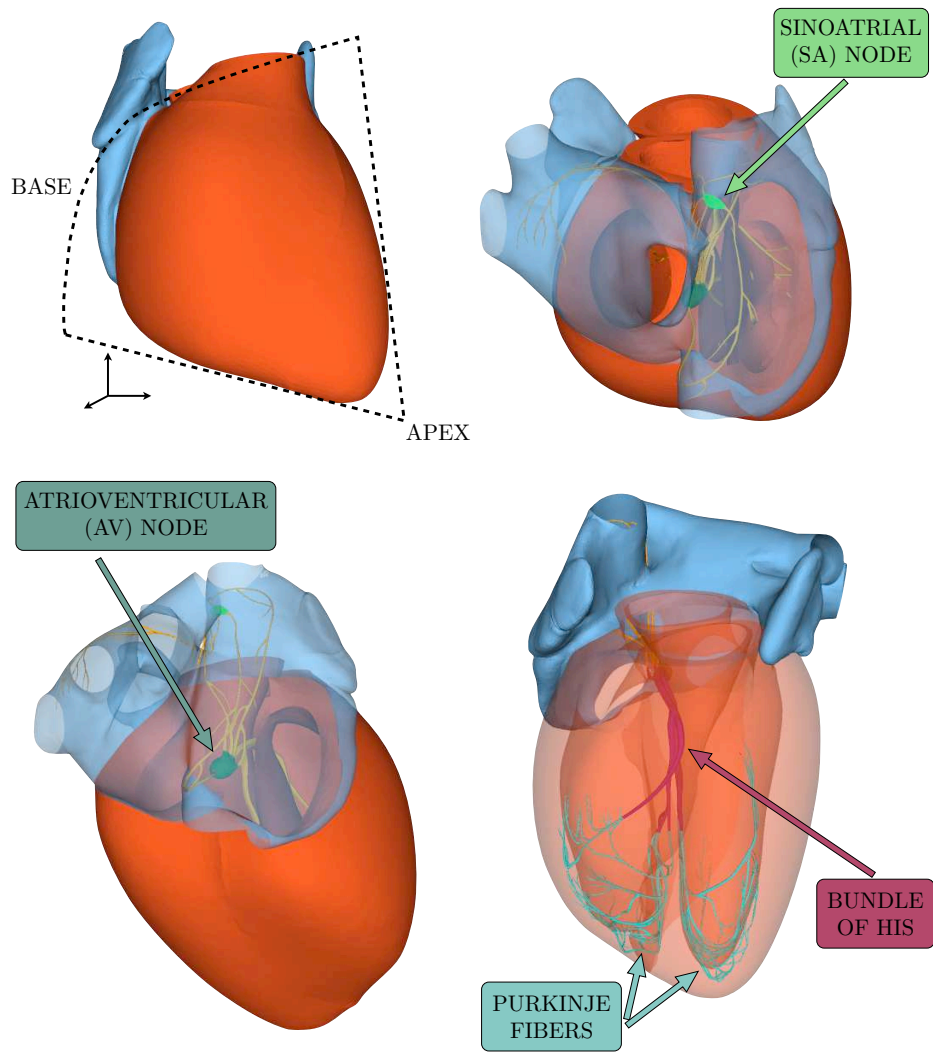


Figure 1.3: Heart geometry with conduction system.

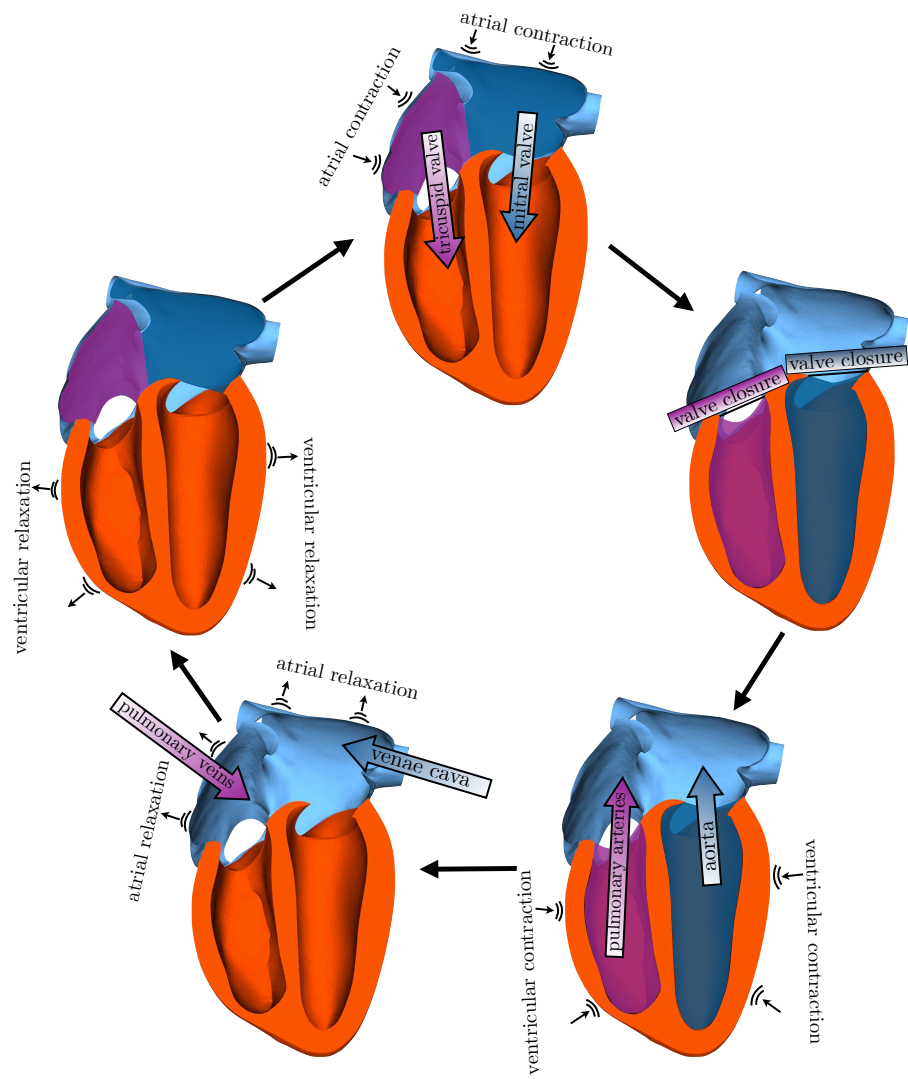


Figure 1.4: Blood perfusion in a cardiac cycle: oxygenated blood in blue and deoxygenated blood in purple.

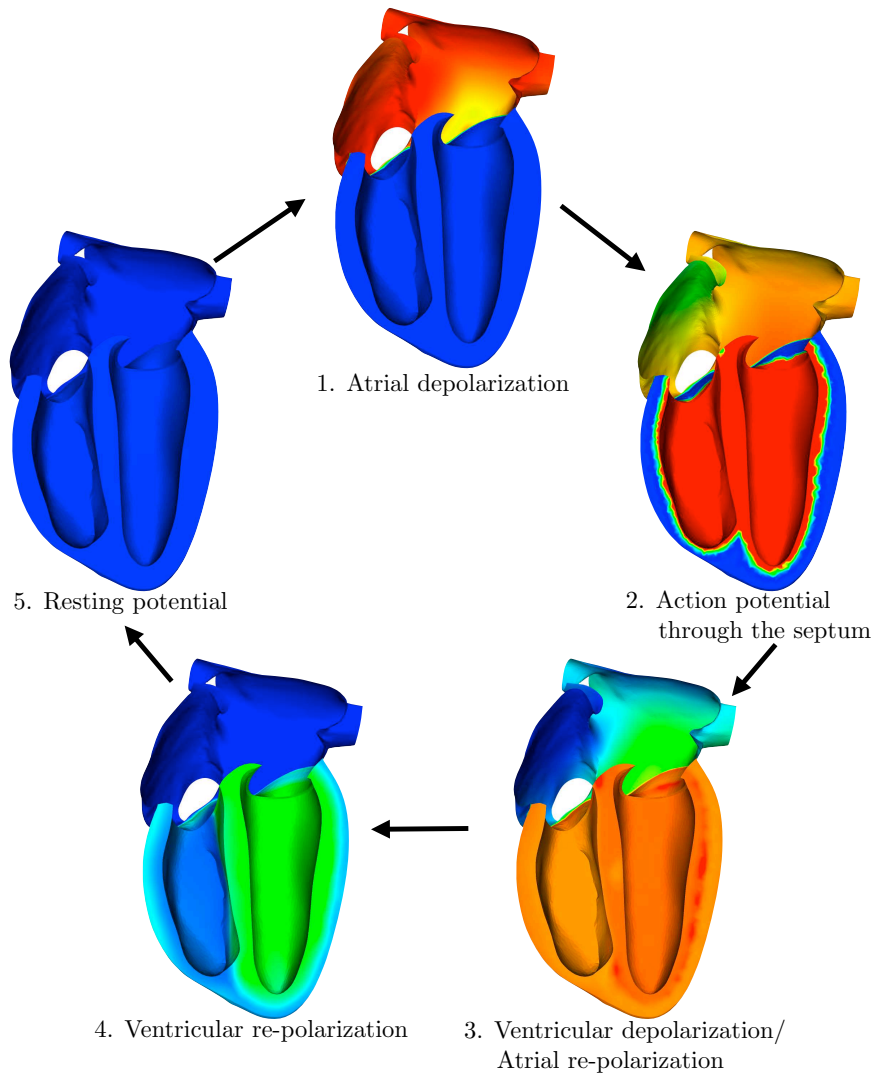


Figure 1.5: Electrical cardiac cycle: from resting potential (blue) to action potential (red) and viceversa.

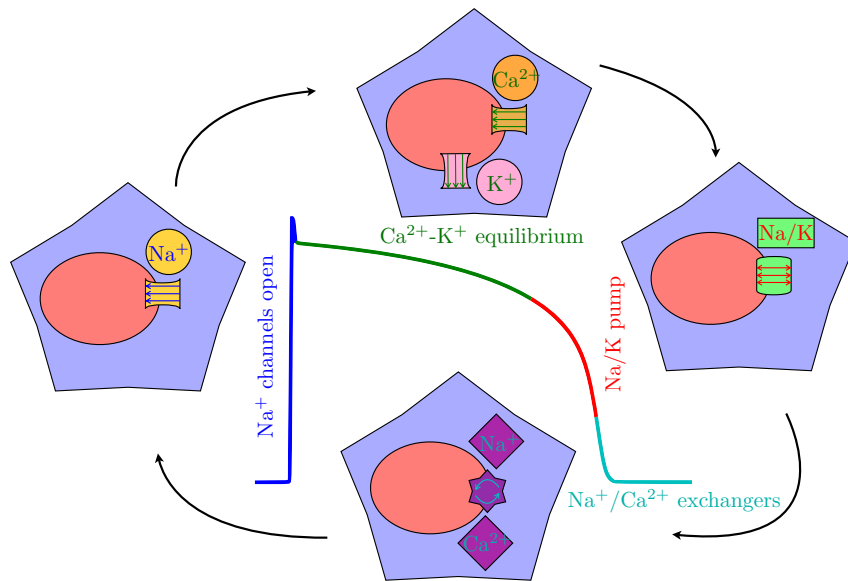


Figure 1.6: Cell electrical cycle and action potential.

pulmonary valves open and the blood is injected into aorta and pulmonary arteries. Also, during this phase, atria are re-polarized and lead to atria relaxation.

4. At the end of ventricles contraction, their repolarization takes place. At the same time, atrial relaxation let the blood inject through venæ cava and pulmonary veins.
5. Finally, the whole heart is at resting potential. Ventricular muscle relaxes too, and let the blood flow in through tricuspid and mitral valves.

1.2.3 Electrical cycle at microscopic scale

At the microscopic scale, each cell follows an electrical cycle (see Figure 1.6). In order to describe the cell state, the so-called membrane potential is measured, which is the difference between the extra- and the intra-cellular potentials.

- First, the cell has a stable resting membrane potential. When the action potential reaches the cell, its sodium ion channels, also called voltage-gated fast Na⁺ channels, open. The opening of these channels let the Na⁺ flow into the cell and produces a rapid depolarization and contraction.
- Second, a *plateau* phase is observed, the cell remains depolarized and contracted. The partial opening of voltage-gated slow Ca²⁺ channels let calcium get into the cell while several voltage-gated K⁺ channels also open and let potassium ions leave the cell. Therefore, the *plateau* is given by the equilibrium between inflowing Ca²⁺ and outflowing K⁺ ions.

- Then, the action of Na/K pump induces the decreasing of the K^+ ions concentration into the cell. The repolarization starts, the cell potential decreases and it relaxes again.
- Finally, potassium channels close and Na^+/Ca^{2+} exchangers let sodium flow back into the cell and calcium flow out, bringing back the cell to its resting potential.

1.3 Cardiac electrophysiology

We introduce the reader to cardiac electrophysiology by presenting some historical notes on the discovery of electrical activity of the heart at each heart beat. Then, a detailed description of the standard 12 lead Electrocardiogram introduced by Einthoven is given. Finally, an overview on the numerical approximation advances is given.

1.3.1 From Descartes “animal spirits”...

Since the 16th century, physicists, medical doctors and philosophers have been interested in the causes of living movements. The first work stating that the blood and the nervous system are the causes of the body movements is due to René Descartes, French Philosopher (1596–1650) best known for the philosophical statement “Cogito ergo sum”. The post-mortem treatise Passions of the Soul (*Les passions de l’âme*) is published in 1662. Descartes defines the “animal spirits” as produced in the blood and responsible for the body movements. These spirits function in a capacity similar to modern medicine’s nervous system. The treatise was published after his death since he abandoned the work because of persecution of other radical thinkers such as Galileo Galilei. [Wik14b]

After Descartes work, many experiments have been conducted on the subject. Between 1664 and 1668 several studies on living muscles induced to give up the idea of an “animal spirit” and suggest the modern definition of nervous system. The mechanist theory of the french philosopher was first disproved by a Dutchman, Jan Swammerdam, who conducted studies on a frog. He observed that after removing the heart from a living frog, the frog was still capable of swimming, while it could not anymore after the ablation of the brain. It was during its dissection that the muscled twitched after the stimulation of several nerves. Few years later his first experiment on frogs, Swammerdam refines his theory on nerve conduction observing the movement of a muscle suspended in a glass tube caused by the irritation of the nerves with a silver wire. The movement of the muscle was probably due to the induction of a small electrical charge. [GJ96]

In the latest 1700s, two italians gave the main contribution to modern electrophysiology. In 1786, the italian anatomist Luigi Galvani showed that a direct contact with an electrical generator leads to a muscle contraction. Later, he proved that an electrical stimulation of a frog’s heart leads to cardiac muscular contraction. Only

In 1774, the electricity was used for the first time for a medical purpose. The Humane Society, later called Royal Humane Society, was founded in London to promulgate the idea of attempting to resuscitate the deads.

Few months after the foundation of the Human Society, the first case of “resuscitation” using electrical shock was published. A 3-year-old child named Catherine Sophie Greenhill had been pronounced dead after she fell from the first storey window. A society member, an apothecary named Squires, occurred to the scene within twenty minutes and, after the “consent of the parents”, he proceeded to give the child several shocks with a portable electrostatic generator to various parts of the body without any apparent success. After several minutes, upon transmitting a few shocks through the thorax, he perceived a small pulsation. This treatment caused her to regain pulse and respiration, and she recovered fully, after a time in coma.

The resuscitation of little Catherine Greenhill was probably the first successful cardiac defibrillation of a human being. In 1788, the Human Society member Charles Kite awarded a silver medal for advocating the resuscitation of victims in cardiac arrest and developing his own electrostatic revivifying machine. [Har90]

few years later, in 1792, Alessandro Volta, Italian Scientist and inventor, showed that the electrical current is generated by the combination of two dissimilar metals, disproving the theory of “animal electricity” from Galvani. Of course, both of them were right, saying that the electrical current comes on one side from the animal tissue and on the other one from the metals. [GJ96]

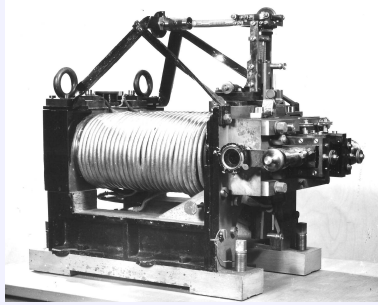
Two other italians, Leopoldo Nobili, Professor of Physics at Florence, and Carlo Matteucci, Professor of Physics at the University of Pisa and student of Nobili, pursued the research on the field. Nobili, who was working to support the theory of animal electricity, felt demonstrated it: in 1827, he detected the current flow in the body of a frog from muscles to spinal cord. The main improvements are due to Matteucci who, in 1838, showed that an electric current accompanies each heart beat. He tried to demonstrate the conduction in nerves but his instruments were not sensitive enough. [GJ96]

The first description of “action potential” accompanying each muscular contraction was given by Emil Du Bois-Reymond, a German physiologist, in 1834. He was capable of detecting the small voltage potential of resting muscles and the decreasing of this potential with muscle contractions. Du Bois-Reymond divided the signal that he detected into different parts which he called “disturbance curves”: “o” was the stable equilibrium point, and p , q , r and s were the other points of the deflection. [GJ96]

In the early 1870s, two British physiologists, John Burdon Sanderson and Frederick Page, recorded for the first time the heart’s electrical current. In 1878, they reported that each heart beat is accompanied by an electrical variation consisting of two phases, this was the first description of ventricular depolarization and repolarization. The first phase, later called QRS, was characterized by a disturbance of short duration “*in which the apex becomes positive*”, while the second one “*in which the apex tends to negativity*” was much longer. [Fye94]

The “galvanometer” is the first instrument which measures and record electricity. The term “galvanometer”, in common use by 1836, was derived from the Italian researcher Luigi Galvani. The first instruments, called “tangent” galvanometer, relied on the Earth’s magnetic field and had to be oriented before use.

Later, “astatic” galvanometer becomes independent of the Earth’s magnetic field and operates in any orientation. In 1858, William Thompson (Lord Kelvin), Professor of Natural Philosophy at Glasgow University, invented the “mirror galvanometer” that was



able to detect very rapid current changes. In 1867, Thompson improved his instrument including the recording of the detected currents onto paper.

Edward Weston extensively improved the design. By 1888, Weston had patented and brought out a commercial “portable” form of the instrument, transportable from place to place.

This is essentially what an ECG is, a sensitive galvanometer. [Wik14a]

String galvanometer. Source: [Alp].

In the same years, at the St. Mary’s Hospital Medical School in London, August D. Waller made several experiments leading him in 1887 to the first recorded human electrocardiogram. He connected electrodes to the front and the back of a man’s chest showing that each heart beat was “*accompanied by an electrical variation*”, and he proved that the electrical activity preceded the heart contraction. Also, he made the first step towards the modern bipolar leads, affirming that it was not necessary to apply the electrodes to the subject’s chest: “*if the two hands or one hand and one foot be plugged into two dishes of salt solution connected with the two sides of the electrometer, the column of mercury will be seen to move at each beat of the heart, though less than when the electrodes are strapped to the chest*”. [Fye94]

Willem Einthoven saw Waller demonstration on his dog Jimmy at the First International Congress of Physiologists in Basel in 1889. As Einthoven, many physiologists assisted to Waller’s demonstration and pursued the experiments. In 1891, two british physiologists of University College of London, William Bayliss and Edward Starling, showed a triphasic variation accompanying (or preceding) each heart beat, later called P, QRS and T, while Waller identified only two. In 1895, Einthoven published his first paper on the subject where he claimed the presence of five distinguished deflections during each heart beat, including drawings of these deflections that he called P, Q, R, S and T. Einthoven, knowing the limitations of the instruments used, improved the string galvanometer in order to record high frequency. His studies on the electrical devices used to measure the cardiac electrical activity owned Einthoven to win the Nobel Prize in Medicine in 1924.

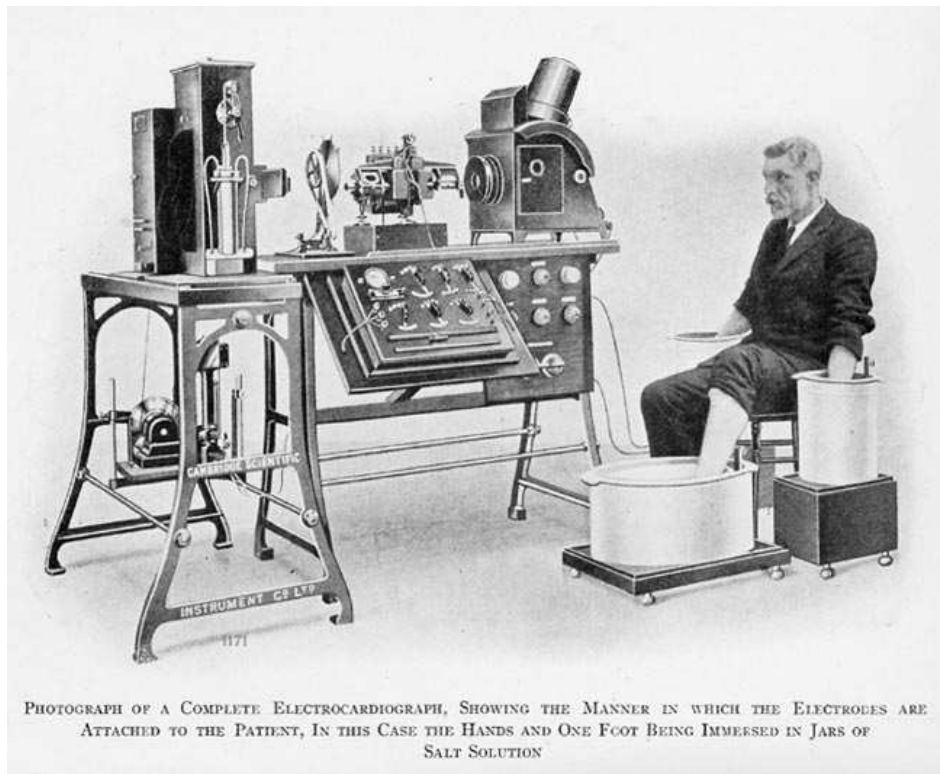
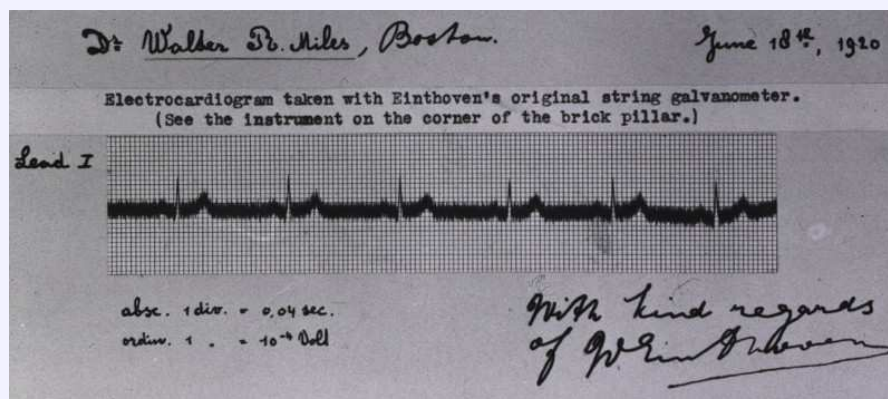


Figure 1.7: An early commercial ECG machine, built in 1911 by the Cambridge Scientific Instrument Company. Source: [Wik14c].

The five deflections introduced by Einthoven were labelled PQRST following the convention introduced by Descartes using letters of the second half of the alphabet. Since N and O have other meanings in mathematics, P was the first available letter, and Q, R, S, T and eventually U were simply the next.



An ECG strip recorded by Einthoven's original string galvanometer. Source: [Alp].

1.3.2 . . . through modern Electrocardiography . . .

Since Einthoven first measures, many advances in electrocardiography have been made. The instrumentation has evolved from a cumbersome laboratory apparatus to compact electronic systems. Also, the modern Electrocardiogram includes 12 standard leads (I, II, III, aVR, aVL, aVF, V1, V2, V3, V4, V5, V6) given by 9 electrodes placed on the skin (see Figure 1.8 left). The leads are of two types: bipolar and unipolar. Bipolar leads are the tracing of the voltage difference between two electrodes and have a positive and a negative pole, while in unipolar leads the negative pole is given by a composite pole made up of signals from multiple electrodes.

The 12 leads are divided into three groups. The so-called limb-leads I, II and III are bipolar leads whose electrodes are placed on the right arm (R), on the left arm (L) and on the left foot (F). These electrodes form the so-called Einthoven triangle, an inverted equilateral triangle, formed by the two shoulders and the pubis, with the heart at the center that produces zero potential when voltages are summed up (see Figure 1.8 top-right). Lead I is given by the voltage between left arm and right arm electrodes (see Figure 1.8 bottom-right), lead II by the voltage between the left foot and the right arm, and lead III between the left foot and the left arm:

$$I = v(L) - v(R), \quad II = v(F) - v(R), \quad III = v(F) - v(L). \quad (1.1)$$

Next, aVR, aVL and aVF are called augmented limb leads. They are derived from the same electrodes as limb leads, but they are unipolar leads since their negative pole is given by the Wilson central terminal, or Wilson lead, defined by

$$V_W = \frac{1}{3}(v(R) + v(L) + v(F)). \quad (1.2)$$

Lead augmented vector right (aVR) has the positive electrode on the right arm (R) and its negative electrode is a combination of the left arm (L) electrode and the left foot (F) electrode, which “augments” the signal strength of the positive electrode on the right arm:

$$aVR = v(R) - \frac{1}{2}(v(L) + v(F)) = \frac{3}{2}(v(R) - V_W). \quad (1.3)$$

In the same way, augmented vector left lead (aVL) has its positive pole on the left arm:

$$aVL = v(L) - \frac{1}{2}(v(R) + v(F)) = \frac{3}{2}(v(L) - V_W) \quad (1.4)$$

and augmented vector foot (aVF) has its positive pole electrode on the left foot:

$$aVF = v(F) - \frac{1}{2}(v(R) + v(L)) = \frac{3}{2}(v(F) - V_W). \quad (1.5)$$

Leads aVR, aVL, aVF need to be amplified of a factor $3/2$ because the signal is too small to be useful since their negative pole is given by the Wilson lead.

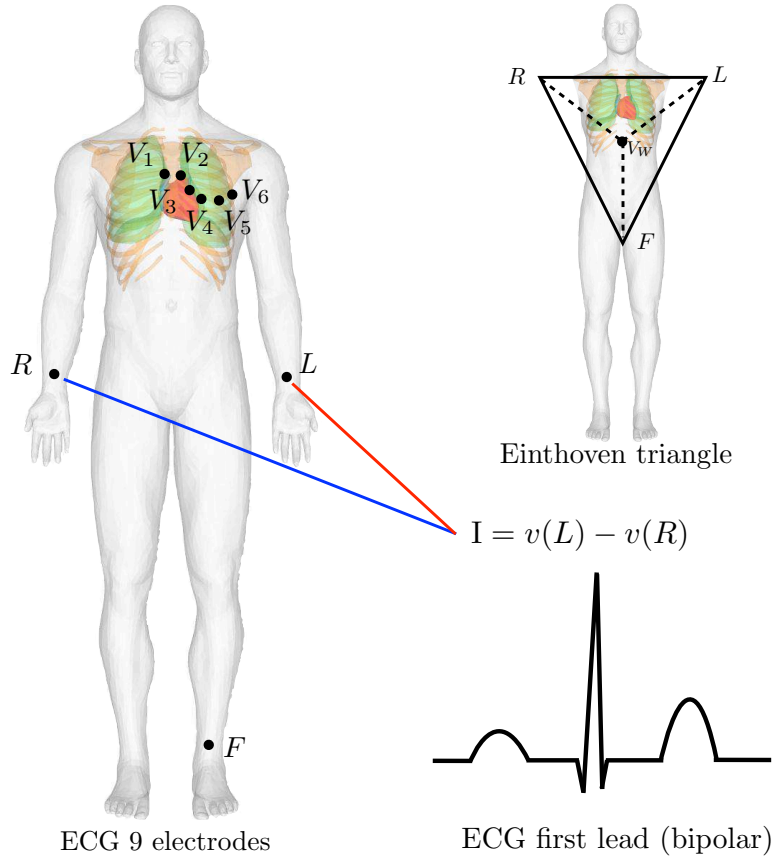


Figure 1.8: Standard 12-lead ECG electrodes position, Einthoven triangle and first lead definition.

Finally, leads V_1, \dots, V_6 , called precordial leads, are unipolar leads whose positive pole is placed on the chest and negative one is the Wilson lead. On the opposite of augmented limb leads, precordial leads do not need any augmentation. Then they are defined by

$$\begin{aligned}
 V_1 &= v(V_1) - V_W, & V_4 &= v(V_4) - V_W, \\
 V_2 &= v(V_2) - V_W, & V_5 &= v(V_5) - V_W, \\
 V_3 &= v(V_3) - V_W, & V_6 &= v(V_6) - V_W.
 \end{aligned} \tag{1.6}$$

The typical ECG of a heart beat consist in six deflections, called P, Q, R, S, T and U wave. The last one is usually invisible since it is hidden by the T wave. The P wave represents atrial depolarization, the QRS complex occurs during ventricular depolarization and hides atrial repolarization, and the T wave during ventricular repolarization, see Figure 1.10. In a normal healthy heart, the baseline is equivalent to the isoelectric line and represents the periods in the cardiac cycle when there are no currents. In the same way, the interval between the P wave and the QRS complex, and between the QRS and the T wave, respectively called PQ and ST segments, are

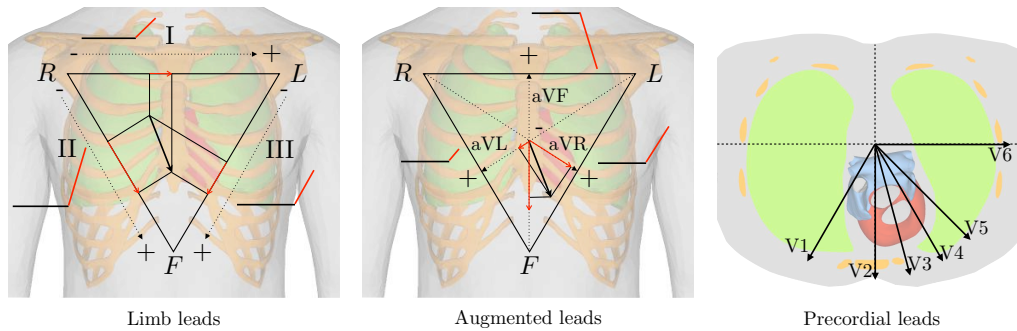


Figure 1.9: Representation of the 12 ECG leads on the frontal plane (left and middle) and on the horizontal plane (right).

isoelectric too.

At each time instant, the depolarization (resp. repolarization) front is defined as the limit between the depolarized cardiac region and the resting one (resp. between the repolarized cardiac region and the depolarized one). Along the depolarization fronts, several elementary dipoles, independently indicated by a vector, form the so-called activation front that can also be represented by a vector. If all the cardiac vectors of a cardiac cycle are jointed together, the Vectocardiogram (VCG) is obtained. The VCG is represented by three loops, the first represents the atrial depolarization, the second which is much bigger represents the ventricular depolarization (see Figure 1.11) and the third one the ventricular repolarization.

The limb leads and the augmented leads are the representation of the depolarization (or repolarization) on the frontal plane, see Figure 1.1. In particular, the limb leads are the projection of the cardiac vector on the edges of the Einthoven Triangle as show in Figure 1.9 left, while the augmented limb leads are the (augmented) projection on the bissectrices of the translated Einthoven triangle (Figure 1.9 middle). On the opposite, the precordial leads V_1, \dots, V_6 are the representation of the cardiac vector on the horizontal plan with different angles as shown in Figure 1.9 right.

Let us better analyze the ventricular depolarization and the QRS complex generation in the first lead. In Figure 1.11 the lead I is built using the cardiac vector represented on the left of Figure 1.11. The cardiac vector is projected onto the Einthoven triangle: the top edge of the triangle represents the lead I, with its positive pole on the right (left arm, L) and its negative pole on the left (right arm, R), the left between F and R represents the lead II and the right edge $F-L$ the lead III. First, the septum is depolarized from left to right leading to a small negative depolarization vector on the first lead axes, which corresponds to the small negative Q wave (first line of Figure 1.11). Second, the depolarization front spreads through the septum in the direction of the apex of the heart, generating a depolarization vector of higher amplitude to the apex which leads to the generation of the R wave (second line of Figure 1.11). Then, the depolarization front reaches the epicardium from the apex to the base of the heart, generating a low intensity dipole which

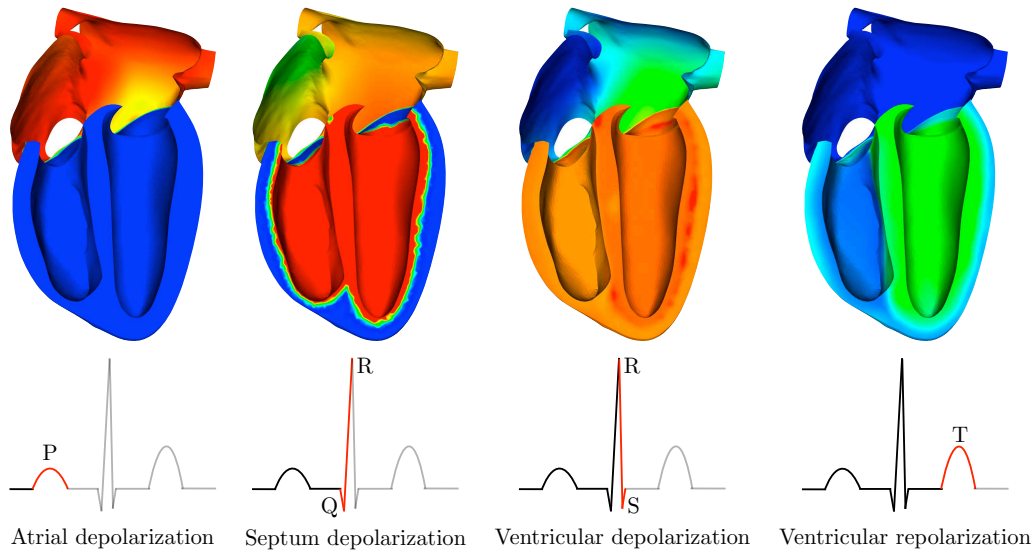


Figure 1.10: First lead waves generation.

corresponds to the S wave (third line of Figure 1.11). Finally, all the ventricular tissue is depolarized, leading to the isoelectric ST segment.

1.3.3 ... to numerical simulations of electrocardiograms

The first attempts at simulating ECGs based on partial differential equations were proposed only in the late 1980s. The first models, which appeared between the 1970s and 1980s, were not based on the membrane equations. In 1978, the first numerical simulation of ECG was proposed by Miller and Geselowitz [MIG78a, MIG78b], the heart wavefront was approximated by the mean direction of a sheet of current dipoles and the surface potentials were calculated using this discrete set of current dipoles. These models were called *cellular automata*: only action potential could be approximated, its duration was preassigned and there were no interaction between the depolarization and the subsequent repolarization sequences. As shown in Figure 1.12, results were very promising, but a lot of modelling work still had to be done.

Many advances have been made in the next years: a PDEs-based model that approximated the intra- and extra-cellular potentials, the so-called *bidomain equations*, was proposed by Tung in his PhD dissertation [Tun78], see Section 1.4; cardiac anisotropy caused by fibers orientation was introduced [CFCV⁺82, WOH⁺95]; torso inhomogeneities were investigated [VOH89]; and accurate numerical approximations were proposed. Since the implementation and the computational costs in order to obtain accurate simulations with membrane and intra- and extra-cellular conductive medium were unfeasible for the date, see [BP84], few years occurred before the first simulation based on a PDEs model was provided. In the early 1990s, Colli Franzone *et al.* [CFGR90, CFG93] used a reaction-diffusion model based on realistic ionic currents and a bidomain model for electronic interactions to provide very accurate,

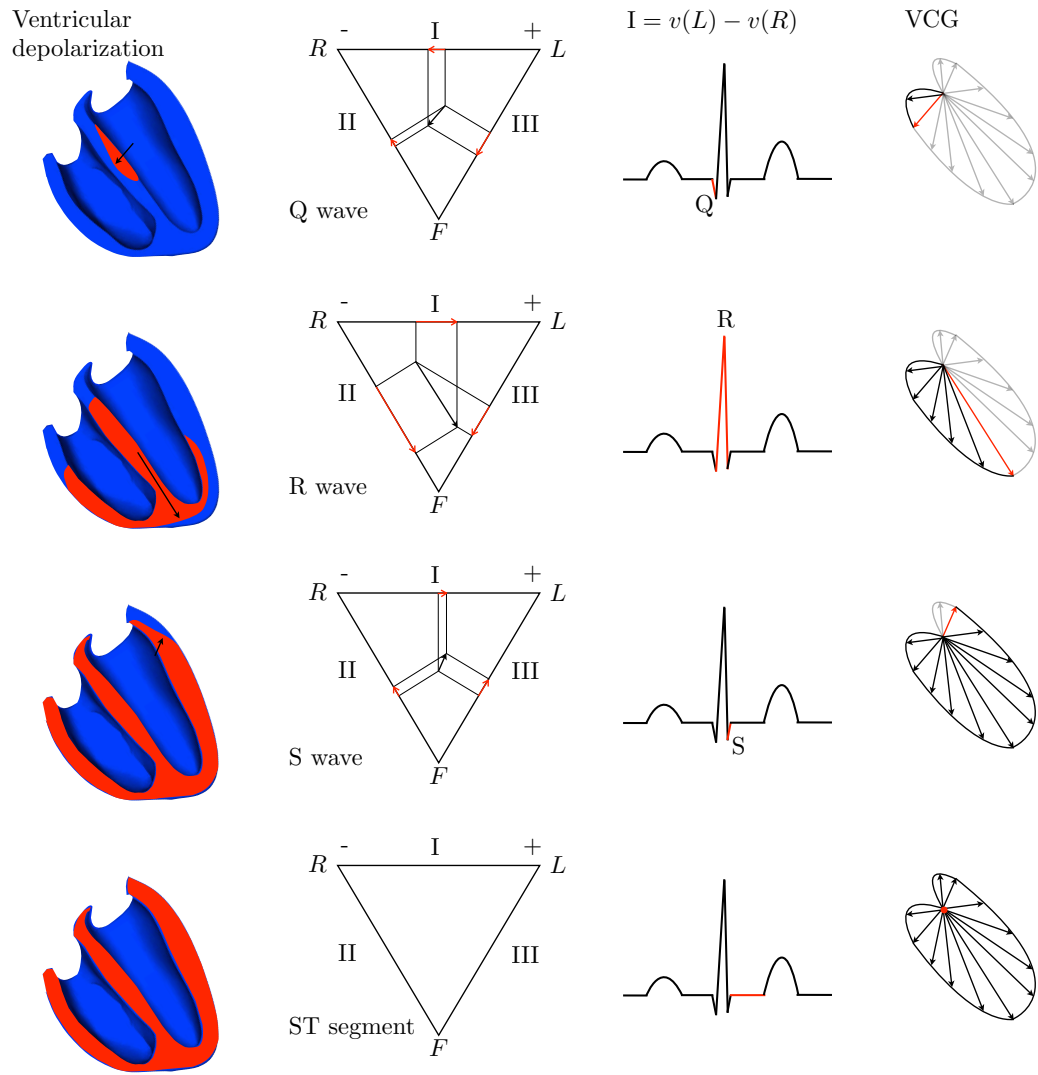


Figure 1.11: Ventricular depolarization, first lead QRS complex generation and associated Vectocardiogram (VCG).

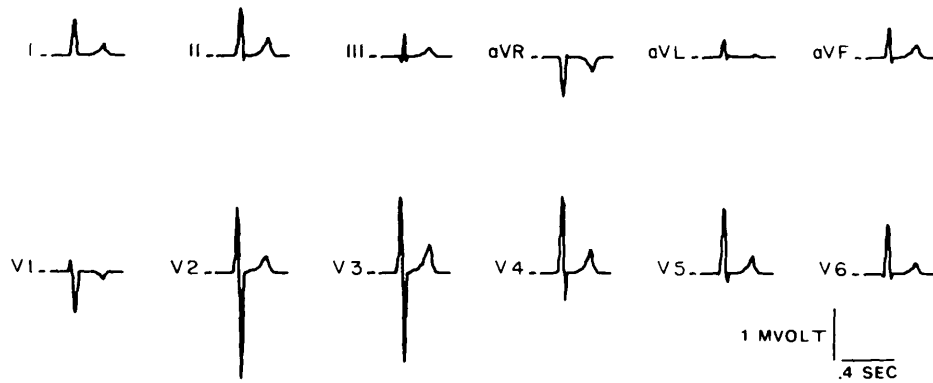
FIGURE 18 *The simulated standard 12-lead ECG.*

Figure 1.12: First simulation of 12-lead ECG with a multiple dipoles approximation. Source: [MIG78a].

but expensive, simulations on a 3D small block of myocardial tissue including rotating anisotropy. It is only in 1998 that Huiskamp used the anisotropic monodomain electronic interaction, coupled with Drouhard-Roberge–Beeler-Reuter membrane equations [DR86], in order to perform a simulation of a complete myocardial action potential cycle in a realistic ventricles 3D model, including fibers rotation [Hui98].

In the last decade, many attempts to improve ECGs numerical simulations have been made. We can cite for instance [PDG03, TDP⁺04, PDV09, BCF⁺10, MDFG12]. The increasing accuracy of heart geometries, ionic models including physiological models, cardiac tissue models, etc. leads to realistic simulations of ECGs including healthy and pathological cases. In these works, the heart is approximated by a realistic geometry of the ventricles, then only the QRS complex and the T wave are simulated. More recently, many papers [HC00, KST⁺11, CGH⁺13] considered atria electrophysiology simulations but without providing ECGs. We will show in Chapter 2 how to model a complete (atria and ventricles) heart which leads to a full cycle ECG including P, QRS and T waves.

1.4 Cardiac electrophysiology models

In this section, we introduce mathematical models largely used in cardiac electrophysiology. In particular, we present the so-called bidomain equations [Tun78], which are the most used model for the cardiac electrical potential. Bidomain equations are coupled with some ionic models, hereafter we present the two that are the most used in the next chapters: the Fitzugh-Nagumo model [Fit61, NAY62], and the Mitchell and Schaeffer one [MS03]. In order to obtain an Electrocardiogram, a body potential model (called in what follows torso model) is presented and coupled to the bidomain equations. Finally, some specific approximation and the numerical schemes used in this thesis are presented.

1.4.1 The bidomain and the monodomain equations

As explained in Section 1.2, the heart tissue is composed of two parts: the cardiac muscle cells, whose domain is called the *intra-cellular* domain, and the rest of the media, which is called the *extra-cellular* domain. We denote by Ω_H the heart domain, and Ω_i and Ω_e respectively the intra- and the extra-cellular domains such that $\overline{\Omega_H} = \overline{\Omega_i} \cup \overline{\Omega_e}$ and $\Omega_i \cap \Omega_e = \emptyset$. The membrane junction between the intra- and the extra-cellular domains is denoted by $\Gamma_m = \overline{\Omega_i} \cap \overline{\Omega_e}$.

The bidomain equations, introduced by Tung [Tun78] are based on the Ohm's law and the conservation of the charge. Let us call \mathbf{j}_i and \mathbf{j}_e respectively the electric currents in the intra- and extra-cellular domains. Applying the Ohm's law, their expression is given by

$$\begin{aligned}\mathbf{j}_i &= \boldsymbol{\sigma}_i \nabla u_i, \\ \mathbf{j}_e &= \boldsymbol{\sigma}_e \nabla u_e,\end{aligned}\tag{1.7}$$

where $\boldsymbol{\sigma}_{i,e}$ and $u_{i,e}$ are respectively the conductivity tensors (their expressions are given below, see Section 1.4.4) and the electrical potential in the intra- (resp. extra-) cellular domain.

The electric currents \mathbf{j}_i , \mathbf{j}_e can be separated into two components: the surface charge $\mu_{i,e}$ changes due to the membrane capacitor behavior, and the total ionic current $I_{\text{ion}}^{\text{tot}}$ that measures the current exchanges from Ω_i to Ω_e . Then, we obtain

$$\begin{aligned}\frac{\partial \mu_i}{\partial t} + I_{\text{ion}}^{\text{tot}} &= \mathbf{j}_i \cdot \mathbf{n}, \\ \frac{\partial \mu_e}{\partial t} - I_{\text{ion}}^{\text{tot}} &= -\mathbf{j}_e \cdot \mathbf{n},\end{aligned}\tag{1.8}$$

where \mathbf{n} is the unit normal pointing from Ω_i to Ω_e .

To obtain the bidomain equations, an assumption is in order: the surface charge is supposed to be linearly proportional to the transmembrane potential $V_m = u_i - u_e$:

$$\mu_i = C_m V_m\tag{1.9}$$

where C_m is the capacitance per unit area of membrane. Then, equations (1.8) and (1.9) lead to the first equation of the bidomain model at the microscopic scale

$$C_m \frac{\partial V_m}{\partial t} + I_{\text{ion}}^{\text{tot}} = \mathbf{j}_i \cdot \mathbf{n}.\tag{1.10}$$

Also, the conservation law is applied on the membrane Γ_m to the electric currents, which leads to the second equation of the bidomain model at microscopic scale

$$\mathbf{j}_i \cdot \mathbf{n} = -\mathbf{j}_e \cdot \mathbf{n},\tag{1.11}$$

Using the definition of transmembrane potential and equations (1.7), the bidomain

equations (1.10), (1.11) can be written in terms of V_m and u_e at microscopic scale:

$$\begin{cases} C_m \frac{\partial V_m}{\partial t} + I_{\text{ion}}^{\text{tot}} - \boldsymbol{\sigma}_i \nabla V_m \cdot \mathbf{n} - \boldsymbol{\sigma}_i \nabla u_e \cdot \mathbf{n} = 0, & \text{on } \Omega_i, \\ -(\boldsymbol{\sigma}_i + \boldsymbol{\sigma}_e) \nabla u_e \cdot \mathbf{n} - \boldsymbol{\sigma}_i \nabla V_m \cdot \mathbf{n} = 0, & \text{on } \Gamma_m. \end{cases} \quad (1.12)$$

Equations (1.12) represent a discrete description of the model on the intra- and extra-cellular domains Ω_i , Ω_e . An homogenization is necessary to write the continuous material equations at the macroscopical scale. We do not detail the homogenization step and refer to the original work of Tung [Tun78], and to more recent works as for instance [HP10] and [Col14]. This homogenization leads to the classical formulation of the bidomain equations on the whole heart domain Ω_H (keeping the same notation as for the microscopic scale for the sake of simplicity)

$$\begin{cases} A_m \left(C_m \frac{\partial V_m}{\partial t} + I_{\text{ion}} \right) - \nabla \cdot (\boldsymbol{\sigma}_i \nabla V_m) - \nabla \cdot (\boldsymbol{\sigma}_i \nabla u_e) = A_m I_{\text{app}}, \\ -\nabla \cdot ((\boldsymbol{\sigma}_i + \boldsymbol{\sigma}_e) \nabla u_e) - \nabla \cdot (\boldsymbol{\sigma}_i \nabla V_m) = 0, \end{cases} \quad (1.13)$$

where A_m is the ratio of membrane area per unit volume, and the total ionic current has been separated into the ionic exchanges current I_{ion} and the applied exterior stimulus I_{app} .

Concerning the boundary conditions, we first assume that the intra-cellular current \mathbf{j}_i does not spread outside the heart domain, that reads

$$\boldsymbol{\sigma}_i \nabla u_i \cdot \mathbf{n} = 0, \quad \text{on } \partial\Omega_H, \quad (1.14)$$

or in terms of transmembrane potential and extra-cellular potential

$$\boldsymbol{\sigma}_i \nabla u_e \cdot \mathbf{n} + \boldsymbol{\sigma}_i \nabla V_m \cdot \mathbf{n} = 0, \quad \text{on } \partial\Omega_H, \quad (1.15)$$

where \mathbf{n} is the outer normal of $\partial\Omega_H$. Second, in all the works presented in this manuscript, the heart is considered isolated from the surrounding domain, called in what follows “torso”. Then, the second boundary condition for equations (1.13) reads

$$\boldsymbol{\sigma}_e \nabla u_e \cdot \mathbf{n} = 0, \quad \text{on } \partial\Omega_H. \quad (1.16)$$

A discussion on the possibility of a strong coupling between heart and torso, and on the related boundary conditions, is given in Section 1.4.3.

A simplified model, called *monodomain model* rises from the bidomain one. The monodomain model only considers the transmembrane potential. This model is used for instance in Chapters 3 and 6 for its simplicity, but it is unusable when we are interested in calculating the ECG. The monodomain model reads

$$\begin{cases} A_m \left(C_m \frac{\partial V_m}{\partial t} + I_{\text{ion}} \right) - \nabla \cdot (\boldsymbol{\sigma}_i \nabla V_m) = A_m I_{\text{app}}, & \text{in } \Omega_H \times (0, T) \\ \boldsymbol{\sigma}_i \nabla V_m \cdot \mathbf{n} = 0, & \text{on } \partial\Omega_H \times (0, T). \end{cases} \quad (1.17)$$

The model is obtained directly from equations (1.13) by assuming that the intra- and the extra-cellular conductivity tensors have the same anisotropic ratio $\sigma_i = \lambda\sigma_e$. More details about the conductivity tensors anisotropy and their approximation are given in Section 1.4.4.

1.4.2 Ionic models

In this section, we describe the term I_{ion} of equations (1.13), *i.e.* the so-called ionic current. We also present two ionic models which are the most used in this work: the FitzHugh-Nagumo ionic model [Fit61, NAY62] (see Chapter 3 and 6) and the Mitchell and Schaeffer ionic model [MS03] (see Chapters 4, 5, 8 and part of Chapter 2).

The ionic current represents the transmembrane exchanges through ionic channels, exchangers and pumps, as shown in Figure 1.6. This term gives rise to an action potential which propagates in the cardiac tissue, as explained in Section 1.2. In general, it depends on the transmembrane potential and on some gate variables $\mathbf{w} = (w_1, \dots, w_n)$ that takes into account the opening and closing of ionic channels and some concentrations. Most of the ionic models read

$$\begin{cases} I_{\text{ion}} = I_{\text{ion}}(V_m, \mathbf{w}), \\ \frac{\partial \mathbf{w}}{\partial t} + \mathbf{g}(V_m, \mathbf{w}) = 0, \end{cases} \quad (1.18)$$

where the second equation takes into account the time variation of the gate variables \mathbf{w} and depends on the ionic model.

The first ionic model that has been presented is the Hodgkin-Huxley model [HH52] in 1952. It is a physiological model, first formulated for neurons and then adapted for electrophysiology by Noble [Nob62]. The ionic current is divided into three terms (sodium, potassium and leakage currents), and it contains three ODEs for three ionic variables. Many models have been derived from the Noble model with higher number of currents and variables and an increasing complexity. We cite for instance the Luo-Rudy model [LR94], adapted for the ventricular action potential, and the Courtemanche-Ramirez-Nattel mode [CRN98] for the atria (see Section 2.C) used in Chapter 2.

On the opposite to the physiological models, which are more precise but can rise to high computational costs due to the number of equations, there are phenomenological models. Phenomenological models are easier and contain in general less ODEs and variables, but they are often precise enough to obtain good numerical results. The first phenomenological model which has been derived is the FitzHugh-Nagumo model [Fit61, NAY62]. This model has only one gate variable w and reads

$$\begin{cases} I_{\text{ion}}(v_m, w) = kv_m(v_m - a)(1 - v_m) - w, \\ \frac{\partial w}{\partial t} = \gamma v_m - \beta w, \end{cases} \quad (1.19)$$

where v_m is the adimensionalized transmembrane potential, $v_m = (V_m - V_{\text{min}})/(V_{\text{max}} -$

V_{\min}), where V_{\min} and V_{\max} are the minimal and maximal values of V_m , typically $V_{\min} = -80\text{mV}$, $V_{\max} = 20\text{mV}$, and k , a , β and γ are positive constants linked to the steepness of the depolarization and repolarization fronts, and to the length of each phase of the cycle. An estimation on the parameters k and γ of the FitzHugh-Nagumo model is given in Chapter 3, and the model is used in Chapter 6 taking advantage of the fact that it is polynomial.

The model which is the most used in this work is the Mitchell and Schaeffer ionic model [MS03]. This model is very similar to the FitzHugh-Nagumo one. Among its advantages, the role of each parameter is described in a more explicit way and the depolarization and repolarization fronts are less steep. On the opposite side, it is a non-polynomial model. The Mitchell and Schaeffer model reads

$$\begin{cases} I_{\text{ion}}(v_m, w) = w \frac{v_m^2 (v_m - 1)}{\tau_{\text{in}}} - \frac{v_m}{\tau_{\text{out}}}, \\ \frac{\partial w}{\partial t} = \begin{cases} \frac{1-w}{\tau_{\text{open}}}, & v_m < v_{\text{gate}} \\ \frac{-w}{\tau_{\text{close}}}, & v_m > v_{\text{gate}} \end{cases} \end{cases} \quad (1.20)$$

where v_{gate} is the so-called change-over voltage, and τ_{in} , τ_{out} , τ_{open} , τ_{close} are the ionic parameters. In particular, τ_{in} and τ_{out} are related to the steepness of the action potential respectively during the depolarization and repolarization phases, and τ_{open} , τ_{close} to the length of the *plateaux*, as shown in Figure 1.13. The Mitchell and Schaeffer model is largely used in the works presented in the next chapters, in particular an analysis of some properties of the model is given in Chapter 5.

1.4.3 The body diffusion problem and heart-torso coupling conditions

In order to compute the ECG, *i.e.* to measure the potential on the skin, an efficient simulation of the electrical potential diffusion in the torso is in order. Let us denote by Ω_T the body domain (excluding the heart, see Figure 1.8 left) and u_T the electric potential in this domain. The torso domain is considered as a passive conductor so a simple Poisson problem has to be solved:

$$\nabla \cdot (\sigma_T \nabla u_T) = 0, \text{ in } \Omega_T, \quad (1.21)$$

where σ_T is the conductivity coefficient. For more details on this problem and its derivation, see for instance [Sac04], [PBC05] or [SLN⁺06]. The media is considered

τ_{in}	τ_{out}	τ_{open}	τ_{close}	v_{gate}
1.0	10.0	30.0	50.0	0.13

Table 1.1: Ionic parameters for Mitchell and Schaeffer model (1.20).

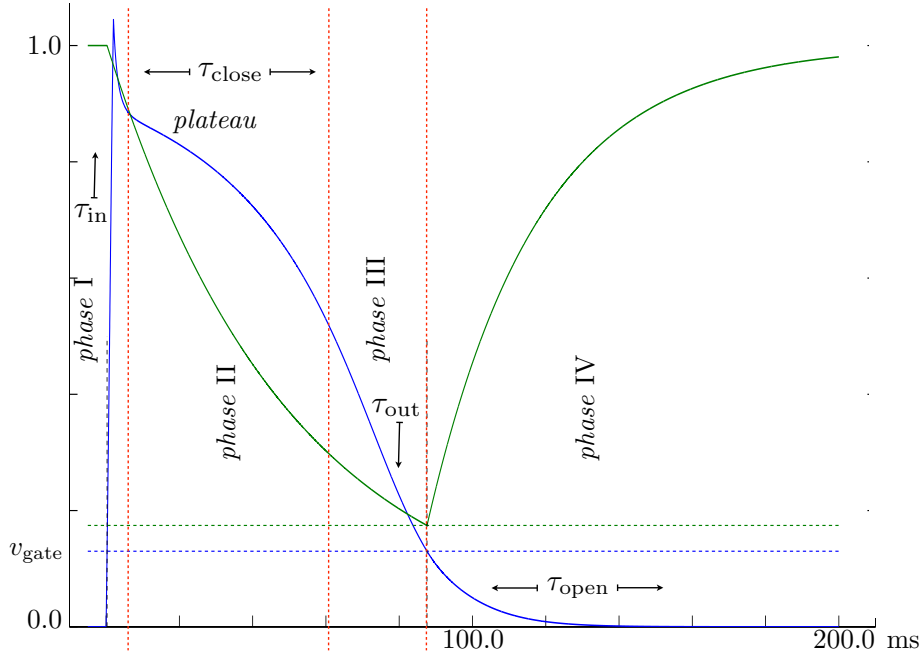


Figure 1.13: Potential v_m (blue) and gate variable w (green) for one electrical cycle with Mitchell and Schaeffer ionic model (1.20). Parameters are taken as in Table 1.1.

isotropic and in this work we take into account only three tissues:

$$\sigma_T = \begin{cases} \sigma_T^l, & \text{in the lungs} \\ \sigma_T^r, & \text{in the ribs} \\ \sigma_T^t, & \text{elsewhere.} \end{cases} \quad (1.22)$$

Dealing with the coupling conditions between the heart and the torso, many choices can be made. The natural one is to consider the continuity of the potential and of the current between the two domains. Then, the complete model reads

$$\left\{ \begin{array}{ll} A_m \left(C_m \frac{\partial V_m}{\partial t} + I_{\text{ion}} \right) - \nabla \cdot (\sigma_i \nabla V_m) - \nabla \cdot (\sigma_i \nabla u_e) = A_m I_{\text{app}}, & \text{in } \Omega_H \\ -\nabla \cdot ((\sigma_i + \sigma_e) \nabla u_e) - \nabla \cdot (\sigma_i \nabla V_m) = 0, & \text{in } \Omega_H \\ \nabla \cdot (\sigma_T \nabla u_T) = 0, & \text{in } \Omega_T, \\ u_T = u_e, & \text{on } \Sigma, \\ -\sigma_T \nabla u_T \cdot \mathbf{n}_H = \sigma_e \nabla u_e \cdot \mathbf{n}_H, & \text{on } \Sigma, \\ \sigma_T \nabla u_T \cdot \mathbf{n}_T = 0, & \text{on } \Omega_T^{\text{ext}}, \end{array} \right. \quad (1.23)$$

where $\Sigma := \overline{\Omega}_H \cap \overline{\Omega}_T$, $\Omega_T^{\text{ext}} := \partial\Omega_T \setminus \Sigma$ and $\mathbf{n}_{H,T}$ are respectively the outer normal from Ω_H to Ω_T and from Ω_T to the external domain.

This problem is of very high computational cost, thus an approximation is needed. A possibility is to consider that the heart is isolated, see equations (1.15), (1.16).

This simplification is studied for instance in [BCF⁺10] and it is shown that it does not impact the shape of the ECG but only the amplitude. Then, only the continuity of the potential is imposed when the torso potential is solved:

$$\begin{cases} \nabla \cdot (\sigma_T \nabla u_T) = 0, & \text{in } \Omega_T, \\ u_T = u_e, & \text{on } \Sigma, \\ \sigma_T \nabla u_T \cdot \mathbf{n}_T = 0, & \text{on } \Omega_T^{\text{ext}}. \end{cases} \quad (1.24)$$

In this case, the operator that links the boundary condition u_e to the solution of (1.24) is linear. So, when solving the discrete problem, in order to compute the ECG, the so-called transfer matrix can be applied. This technique is used to compute the ECG in all the works presented in this thesis, except when specified. For more details about the computation of the transfer matrix see [BCF⁺10].

Finally, it exists a third possibility which is based on the resistor-capacitor behavior of the pericardium. This condition has been introduced in [BCF⁺10] and it is used in Chapter 2 when modeling the full (atria and ventricles) heart domain. In particular the boundary condition reads

$$R_p(\sigma_T \nabla u_T) \cdot \mathbf{n}_H = R_p C_p \frac{\partial(u_T - u_e)}{\partial t} + (u_T - u_e) \quad (1.25)$$

where C_p and R_p are respectively the capacitance and the resistance coefficients of the pericardium. More details about this condition can be found in Section 2.3.4 or in [BCF⁺10].

1.4.4 Other approximations

Concerning the cardiac tissue, the cells properties change compared to their position into the muscle. In particular, in order to obtain the ECG T-wave described in the previous section, which corresponds to the ventricular repolarization, the duration of the *plateau* has to be different in epicardial, mid-myocardial and endocardial cells of the ventricles. The depolarization front spreads through the ventricular muscle from the endocardium to the mid-myocardium, and finally reaches the epicardium, while the repolarization goes in the opposite direction from the external tissue to the interior one. A representation of the action potential of cells belonging to the three layers is given in Figure 1.14. In order to obtain different action potential curves, the τ_{close} parameter takes different values: in the left ventricle three layers are considered ($\tau_{\text{close}}^{\text{epi}}$, $\tau_{\text{close}}^{\text{Mcell}}$, $\tau_{\text{close}}^{\text{endo}}$), while the right ventricle it is considered homogeneous ($\tau_{\text{close}}^{\text{RV}}$). The values are given in Table 1.2. More details about the separation into the three layers can be found in [BCF⁺10].

A_m	C_m	τ_{in}	τ_{out}	τ_{open}	$\tau_{\text{close}}^{\text{endo}}$	$\tau_{\text{close}}^{\text{Mcell}}$	$\tau_{\text{close}}^{\text{epi}}$	$\tau_{\text{close}}^{\text{RV}}$	v_{min}	v_{max}	v_{gate}
200	10^{-3}	16	360	100	120	130	140	90	-80	20	-67

Table 1.2: Ionic parameters for heart model.

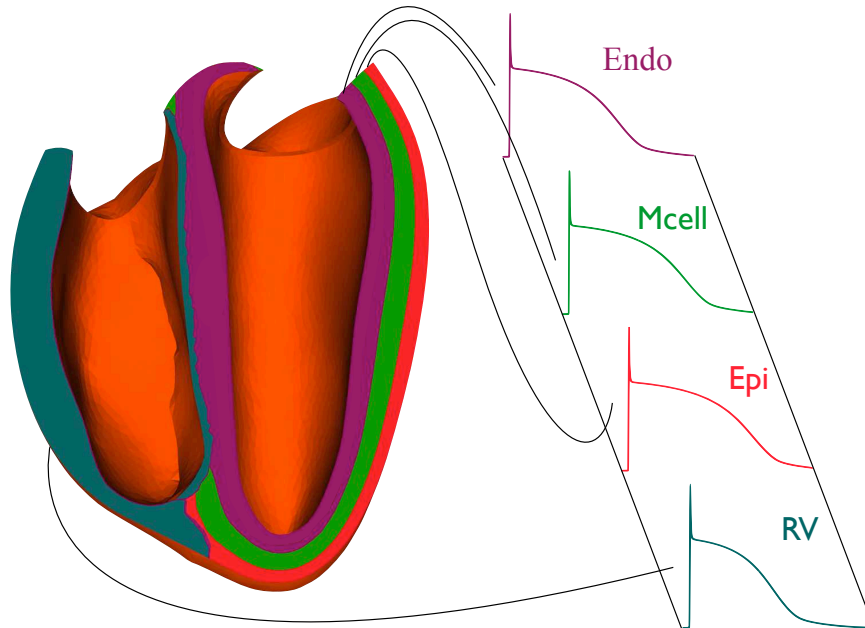


Figure 1.14: Synthetic layers of endocardial, mid-myocardial and epicardial cells in the left ventricle and action potentials obtained with the Mitchell and Schaeffer ionic model (1.20). Parameters are taken as in Table 1.2.

The last approximation that is in order deals with cardiac fibers. The heart muscle is characterized by a fiber architecture that enforces the electrical signal to propagate faster along these directions. In order to take into account the anisotropy in the intra- and extra-cellular media, the conductivity tensors read

$$\sigma_{i,e} = \sigma_{i,e}^t \mathbf{I} + (\sigma_{i,e}^l - \sigma_{i,e}^t) \vec{a} \otimes \vec{a}, \quad (1.26)$$

where \mathbf{I} denotes the identity matrix, $\sigma_{i,e}^t$ indicate the intra- and extra-cellular conductivity coefficients in the fiber direction and $\sigma_{i,e}^l$ across the fibers, and \vec{a} is a unit vector parallel to the local fiber direction. The fibers orientation is illustrated in Figure 1.15. For more information, we cite for instance [BCF⁺10].

1.4.5 Numerical approximation

All the simulations presented in this work are computed using the finite element library FELISCE¹. The equations are discretized in space with a Finite Element Method (FEM) and in time with a Backward Differentiation Formula (BDF) of order 2, except for the Reduced-Order Models whose discretization is detailed when necessary, while the ionic model is solved using an explicit method of order 2 as shown below.

¹<http://felisce.gforge.inria.fr> – A brief description of the library, the implementation of the electrophysiology into the code and the author contributions is given in Appendix A.

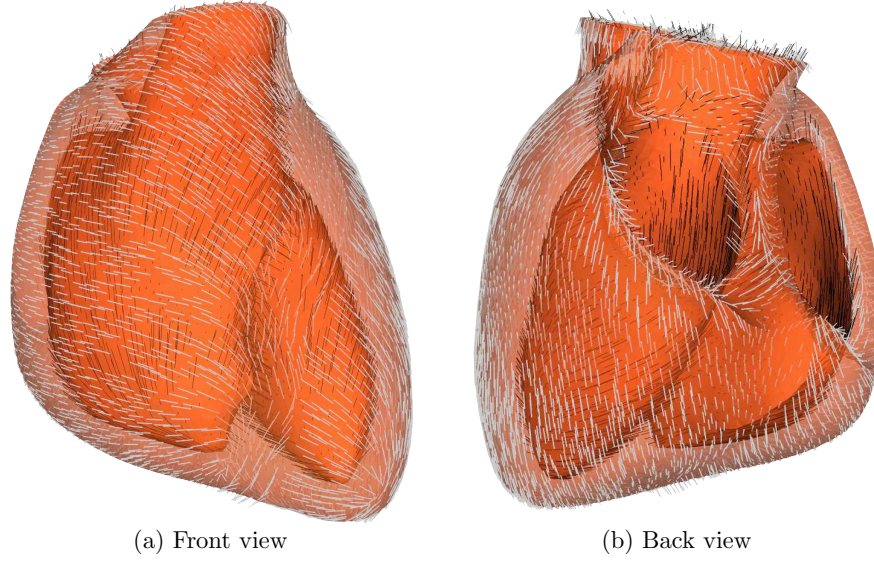


Figure 1.15: Fibers architecture

The weak form of equations (1.13), (1.15), (1.16) reads for all $t > 0$ find $V_m(\cdot, t) \in H^1(\Omega_H)$, $u_e(\cdot, t) \in H^1(\Omega_H)/\mathbb{R}$, $w(\cdot, t) \in L^\infty(\Omega_H)$, such that

$$\left\{ \begin{array}{l} A_m \int_{\Omega_H} \left(C_m \frac{\partial V_m}{\partial t} + I_{\text{ion}} \right) \varphi + \int_{\Omega_H} \left(\sigma_i \nabla V_m + \sigma_e \nabla u_e \right) \cdot \nabla \varphi = A_m \int_{\Omega_H} I_{\text{app}} \varphi, \\ \int_{\Omega_H} \left((\sigma_i + \sigma_e) \nabla u_e + \sigma_i \nabla V_m \right) \cdot \nabla \psi = 0, \\ I_{\text{ion}} = I_{\text{ion}}(V_m, w), \quad \frac{\partial w}{\partial t} + g(V_m, w) = 0, \text{ in } \Omega_H, \end{array} \right. \quad (1.27)$$

for all $\varphi \in H^1(\Omega_H)$, $\psi \in H_0^1(\Omega_H)$, where $H^1(\Omega)/\mathbb{R} := \{v : v \in H^1(\Omega), \int_\Omega v = 0\}$.

From (1.27), the semi-discretization formulation can be obtained, in the finite dimensional spaces of continuous piecewise affine functions $V_h \subset H^1(\Omega_H)$, $U_h \subset H^1(\Omega_H)/\mathbb{R}$, $W_h \subset L^\infty(\Omega_H)$.

For all $T > 0$, let $N \in \mathbb{N}^*$ be a given integer and consider a uniform partition of the time interval $[0, T]$, $t^n = n\delta t$, for all $n \geq 0$ with $t^0 = 0$, $t^N = T$. Let us denote by (V_m^n, u_e^n, w^n) the approximation of the solution (V_m, u_e, w) at time t^n in the finite dimensional space $V_h \times U_h \times W_h$. Then, using the discretization method described above, the solution at each time-step $n \geq 0$ is computed as follows

1. compute the second order extrapolation: $\tilde{V}_m = 2V_m^n - V_m^{n-1}$;
2. solve the ionic model for w^{n+1} : $\delta t^{-1} \left(\frac{3}{2} w^{n+1} - 2w^n + \frac{1}{2} w^{n-1} \right) + g(\tilde{V}_m, w^{n+1}) = 0$ (nodal-wise);
3. evaluate the ionic current: $I_{\text{ion}} = I_{\text{ion}}(\tilde{V}_m, w^{n+1})$;

4. find (V_m^{n+1}, u_e^{n+1}) , with $\int_{\Omega_H} u_e^{n+1} = 0$, solution of the system

$$\begin{aligned} A_m \int_{\Omega_H} \left(C_m \delta t^{-1} \left(\frac{3}{2} V_m^{n+1} - 2V_m^n + \frac{1}{2} V_m^{n-1} \right) + I_{\text{ion}} \right) \varphi_h + \int_{\Omega_H} \sigma_i \nabla V_m^{n+1} \cdot \nabla \varphi_h + \\ \int_{\Omega_H} \sigma_i \nabla u_e^{n+1} \cdot \nabla \varphi_h = A_m \int_{\Omega_H} I_{\text{app}}(t^{n+1}) \varphi_h, \\ \int_{\Omega_H} \left((\sigma_i + \sigma_e) \nabla u_e^{n+1} + \sigma_i \nabla V_m^{n+1} \right) \cdot \nabla \psi_h = 0, \end{aligned} \quad (1.28)$$

for all $\varphi_h \in V_h$, $\psi_h \in U_h$.

1.5 Inverse problems in cardiac electrophysiology

One of the goal of this work is to make some attempts in cardiac electrophysiology inverse problems. The aim of the inverse problems is to reconstruct the electrical activity of the heart assuming that we have access to some measurements of the electrical potential u_T on part of the torso skin. This problem has been investigated in the last four decades and many strategies have been proposed.

The first approach that has been proposed was to estimate equivalent electrical dipoles [MKI⁺77, GRS84]. Later, the problem of recovering the heart surface potential, or the epicardial potential, was addressed. We will call this problem the “classical” inverse problem [BRS77, BTR00, WKJ11], was introduced. Finally, a new approach consists in estimating the transmembrane potential by solving an inverse problem on the whole (heart and torso) domain.

In this section, we give an overview on the classical inverse problem, which is known to be ill-posed, and on some regularization techniques. Second, we briefly present the transmembrane potential estimation problem. Finally, we introduce the problem of identification of some parameters useful to reconstruct the heart electrical activity which will be largely used in the next chapters.

1.5.1 The “classical” inverse problem of electrocardiography

The most widely used formulation of the electrocardiology inverse problem is related to the so-called forward problems (1.13), (1.15), (1.16), and (1.24). It can be formalized as: let d be a given function in $H^{1/2}(\partial\Omega_T^{\text{ext}})$,

$$\text{find } g \in H^{1/2}(\partial\Omega_H) \text{ s.t. } R(g) = d, \quad (1.29)$$

where R is a linear mapping such that

$$R : H^{1/2}(\partial\Omega_H) \rightarrow H^{1/2}(\partial\Omega_T^{\text{ext}}), \quad R(g) = u_T(g)|_{\partial\Omega_T^{\text{ext}}},$$

corresponding to a measure of the potential on the body surface. The measure can be given on a part of the body surface. For instance, d can be the standard 12 lead ECG, as shown in Chapter 4, or only the first ECG lead, see Chapter 5, or it can be

issued from an electrodes vest [PBC05, SLN⁺06], see Chapters 2 and 6.

In order to solve problem (1.29), a least squares method can be applied. Then, the related minimization problem reads:

$$\min_{g \in V} \|R(g) - d\|_{L^2(\partial\Omega_T)}^2, \quad (1.30)$$

where $V = H^{1/2}(\partial\Omega_H)$.

The inverse problem (1.29) is known to be an ill-posed problem, *i.e.* R^{-1} is unbounded and small errors on the observation d may lead to larger errors on the solution g . Many techniques have been proposed to approximate this problem by a well-posed one. Let us briefly describe some standard approaches to the regularization of the inverse problem in its discrete formulation.

A first approach to the reconstruction of the heart surface potentials has been proposed by Barr, Ramsey and Spach [BRS77]. The potential u_T related to a body surface point $x \in \partial\Omega_T^{\text{ext}}$ depends linearly on the heart surface potential u_e . This relation can be expressed on the discretized unknowns by the fact that

$$\varphi_T = A\varphi_H, \quad (1.31)$$

where φ_T is the torso surface potential discretized on a finite number N of points of $\partial\Omega_T$, φ_H is the heart surface potential on a finite number M of points of $\partial\Omega_H$, and A is an $N \times M$ transfer matrix, whose coefficients only depend on the geometry of the epicardial and the body surfaces. The matrix A is in general not squared, and $A^T A$ is poorly conditioned. Then, the solution of a regularized problem associated to problem (1.31) will be written in a general form as

$$\varphi_H = A_\lambda^\dagger(\varphi_T) \quad (1.32)$$

where A_λ^\dagger is the regularized inverse. The regularized inverse can be calculated using different techniques, the most widely used are the Tikhonov regularization [MRR88], the use of temporal information [OR92, GH98], or the Truncated Singular Value Decomposition or truncated Total Least Square [FGHO97, PBC05].

1.5.1.1 Tikhonov regularization

The Tikhonov regularization modifies the minimization function by adding a smooth term, as small as possible. The approximated objective function of the minimization problem for each time t is defined by

$$J_{\lambda_t} = \|A\varphi_H - \varphi_T\|^2 + \lambda_t^2 \|T\varphi_H\|^2 \quad (1.33)$$

where $T \in \mathbb{R}^{N \times N}$ is a constraint matrix, and λ_t is the constraint parameters that depends on the time t . Then $A_{\lambda_t}^\dagger$ reads

$$A_{\lambda_t}^\dagger = (A^T A + \lambda_t^2 T^T T)^{-1} A^T. \quad (1.34)$$

The Tikhonov regularization order depends on the constraint matrix T . A zeroth-order regularization is obtained applying $T = I$, where I is an identity matrix; a first-order regularization can be computed imposing $T = G$, where G represents a discrete approximation to the surface gradient operator; and a second-order regularization corresponds to $T = L$, where L is a discrete approximation to the surface Laplacian operator. A zeroth-order regularization can be viewed as a constraint on the amplitude of the solution, a first-order one on the surface gradient and a second-order one on the surface curvature.

Many studies on the Tikhonov regularization have been conducted, *e.g.* [MRR88], and they showed that zeroth-order Tikhonov regularization performs as well as the higher order ones. Better results can be obtained with large values of λ_t in the case of second or third order regularization.

1.5.1.2 Truncated Singular Value Decomposition (TSVD)

The Truncated Singular Value Decomposition (TSVD) regularization method [FGHO97, PBC05] aims to find a λ_t -rank approximation A_{λ_t} of the transfer matrix A using the truncated SVD of A :

$$A_{\lambda_t} = U_{\lambda_t} \Sigma_{\lambda_t} V_{\lambda_t} \quad (1.35)$$

where Σ_{λ_t} is the diagonal matrix of the first λ_t eigenvalues of A and $U_{\lambda_t}, V_{\lambda_t}$ contain the first λ_t left and right eigenvectors of A , respectively. Then, $A_{\lambda_t}^\dagger$ reads

$$A_{\lambda_t}^\dagger = V_{\lambda_t}^T \Sigma_{\lambda_t}^{-1} U_{\lambda_t}^T. \quad (1.36)$$

The efficiency of the TSVD method has been studied [PBC05] and its performance is often indistinguishable from the zeroth-order Tikhonov regularization one.

1.5.1.3 Time dependant regularization

None of the studied regularization techniques for the electrocardiography inverse problem takes into account the time dependency of the solution. As a matter of fact, the discretized minimization problem (1.30) has to be solved at each time step $\tau = 0, \dots, M$. An approach that takes into account this time dependency [OR92, GH98] suggests to add a regularization term that imposes a continuity on the solution:

$$\min_{g^\tau \in V} \|R(g^\tau) - d^\tau\|_{L^2(\partial\Omega_T)}^2 + \varepsilon \|g^\tau - g^{\tau-1}\|_V^2. \quad (1.37)$$

With this technique, small oscillations of the solution can appear. Moreover, the choice of the initial state of the solution strongly influences the solution of the inverse problem.

1.5.2 Transmembrane potential reconstruction problem

More recently, another approach has been proposed [MSM⁺04], which is the estimation of the transmembrane potential using the second equation of the bidomain model (1.13)

$$-\nabla \cdot ((\boldsymbol{\sigma}_i + \boldsymbol{\sigma}_e) \cdot \nabla u_e) - \nabla \cdot (\boldsymbol{\sigma}_i \cdot \nabla V_m) = 0, \text{ in } \Omega_H. \quad (1.38)$$

In practice, the torso diffusion equations are solved on the whole body (heart and torso) domain, for a continuous variable $u = u_e \mathbf{1}_{\Omega_H} + u_T \mathbf{1}_{\Omega_T}$, where $\mathbf{1}_\Omega$ is the indicator function on Ω . Then, the coupled system reads

$$-\nabla \cdot (\boldsymbol{\sigma} \cdot \nabla u) = f(x,t), \text{ in } \bar{\Omega}_H \cup \bar{\Omega}_T, \quad (1.39)$$

where $\boldsymbol{\sigma} = (\boldsymbol{\sigma}_i + \boldsymbol{\sigma}_e) \mathbf{1}_{\Omega_H} + \boldsymbol{\sigma}_T \mathbf{1}_{\Omega_T}$, and f is zero in Ω_T while it can be viewed as a source term in Ω_H . Then, solving the inverse problem is equivalent to getting the source term of (1.39).

The ‘‘classical’’ inverse problem and this new approach were compared in [MSM⁺04]. The authors conclusion is that the new formulation is more promising since it is based on a stronger biophysical *a priori*. Still, the transmembrane potential approach is ill-posed and must be regularized, too. Many attempts have been made on the subject, *e.g.* [LLH06] where four variants of L^2 -Tikhonov regularization are compared, and [NCL07] where a H^1 -Tikhonov regularization is used. Also, in [NCL07] the identification of the myocardial infarction location is solved using a combined technique within the estimation of the transmembrane potential and a level set technique. This approach is then generalized in [WKMJ13] to more general objective functions and constraints in order to identify ischemic regions, investigating two different regularizations: the Tikhonov regularization and the Total Variation regularization.

1.5.3 Parameters identification inverse problem

The inverse problems of electrocardiology that we presented above often require good regularization techniques in order to be solved. In particular, we point out that none of them takes advantage of the fact that the heart equations are known. An alternative way to solve the inverse problem is the following one: if we suppose that the heart model is good enough, then we can imagine that the only source of error when a simulation is run with the model itself is due to the parameters. This leads to the parameters identification inverse problem: we use some ECG or electrodes vest type measures in order to estimate the parameters of the bidomain equations or of the ionic model. Of course, the forward problem needs to be as accurate as possible. In this thesis we present some attempts made in parameters estimation using different techniques: a minimization problem is solved in Chapter 4 with genetic algorithms, the so-called restitution curve rising from long-time simulations ECG is used in Chapter 5, while a data assimilation technique is applied in Chapter 6.

1.6 Reduced Order Methods: a brief overview

The forward and inverse problem in electrophysiology are known to be very challenging from a computational cost point of view. In order to reduce this computational cost, various Reduced-Order Methods (ROM) have been applied in this work. Let us first give a brief overview on the ROM and in particular on two of the main techniques in ROM.

For the sake of convenience, let us consider a generic parabolic problem on a bounded domain $\Omega \subset \mathbb{R}^d$ for all $t > 0$

$$\frac{\partial u}{\partial t} - \nabla \cdot (D \nabla u) = f(u, t), \quad (1.40)$$

with some proper boundary and initial conditions. Let us write the problem in its variational form:

for any $t > 0$, find $u(t) \in V \subseteq H^1(\Omega)$ such that

$$\frac{d}{dt}(u(t), v) + a(u(t), v; D) = (f(u(t), t), v), \quad (1.41)$$

for all $v \in V$, where $a(u, v; D) = (D \nabla u, \nabla v)$ and (\cdot, \cdot) indicates the L^2 inner product. In order to describe the ROM, let us introduce a finite element discretization of this problem, by considering a discrete subset $V_{\mathcal{N}} \subset V$, of dimension \mathcal{N} . The Galerkin approximation of the problem reads: for any $t > 0$, find $u_{\mathcal{N}}(t) \in V_{\mathcal{N}} \subseteq H^1(\Omega)$ such that

$$\frac{d}{dt}(u_{\mathcal{N}}(t), v_{\mathcal{N}})_{\mathcal{N}} + a_{\mathcal{N}}(u_{\mathcal{N}}(t), v_{\mathcal{N}}; D) = (f(u_{\mathcal{N}}(t), t), v_{\mathcal{N}})_{\mathcal{N}}, \quad (1.42)$$

for all $v_{\mathcal{N}} \in V_{\mathcal{N}}$, where $(\cdot, \cdot)_{\mathcal{N}}$ indicates the inner product in the finite space $V_{\mathcal{N}}$.

ROM aims to decrease the computational costs of the spatial discretization by approximating the Galerkin problem in a subspace of $V_{\mathcal{N}}$, $V_N \subset V_{\mathcal{N}}$, of dimension $N \ll \mathcal{N}$. Many techniques for the choice of the space V_N exist, we briefly present two different approaches: the Reduced-Basis approach [MR02], used in Appendix B, and the Proper Orthogonal Decomposition (POD) [KV01, RP04], used in Chapters 4 and 5. Also, an introduction to a new approach based on Lax Pairs Approximation (ALP) [GL14], used in Chapters 6 and 8, is given.

1.6.1 Reduced Basis

The Reduced Basis method was first introduced in [NP80] for non-linear deflections in composite materials in aerospace fields. In [MR02] the method was mathematically reformulated, allowing the resolution of steady elliptic problems affine in parameters. The method is mainly divided into an *offline* and an *online* phases that let take advantage of (possibly expensive) preliminary computations to decrease the resolution time. Later, many works to improve the offline phase, *e.g.* [MPR02, RHP07, RNP09, DR09, HKB13], gave also some *a priori* error estimators.

To briefly resume the methods, let us consider the problem (1.40) in a steady case:

$$\nabla \cdot (D\nabla u) + f(u) = 0. \quad (1.43)$$

If we suppose that the conductivity term D is constant (real, positive), then problem (1.43) can be written in its variational form as:

find $u \in V \subseteq H^1(\Omega)$ such that

$$Da(u,v) + (f(u), v) = 0, \quad (1.44)$$

for all $v \in V$, where $a(u,v) = (\nabla u, \nabla v)$.

The offline step consists in computing a reduced basis of size $N \ll \mathcal{N}$ which is the space generated by a set \mathcal{S} of finite element solutions of the problem for different values of D :

$$\mathcal{S} = (u_{\mathcal{N}}(D_1), \dots, u_{\mathcal{N}}(D_N)). \quad (1.45)$$

where (D_1, \dots, D_N) are a given set of parameters.

For all $D \in \mathbb{R}_+$, the approximated solution $u_{\mathcal{N}}(D)$ can be written in the reduced form as

$$\hat{u}(D) = \sum_{i=1}^N \alpha_i u_{\mathcal{N}}(D_i), \quad (1.46)$$

and the Galerkin approximation of the reduced problem reads: find $\hat{u}(D) = (\alpha_1, \dots, \alpha_N)$ such that

$$DK_N \hat{u}(D) + F_N = 0, \quad (1.47)$$

where the matrix K_N and the vector F_N elements can be computed in the offline phase:

$$[K_N]_{i,j} = (\nabla u_{\mathcal{N}}(D_i), \nabla u_{\mathcal{N}}(D_j)), \quad [F_N]_i = f(u_{\mathcal{N}}(D_i)). \quad (1.48)$$

Then, the online step is very quickly solved since the matrix K_N is of small size. We remark that here we presented a scholar case in the purpose of giving an idea of the method, of course it is applicable in more complicated cases where, for example, the conductivity parameter D is constant in each subdomain of a given partition of Ω .

1.6.2 Proper Orthogonal Decomposition

The Proper Orthogonal Decomposition (POD) method was introduced in the 1960s by Lumley [Lum67] for the analysis of turbulent flows, discovering that the principal components corresponded to some coherent spatial structures that occurred cyclical in time. Later, with the introduction of the Galerkin approximation for the Navier-Stokes equations, the idea to approximate the solution in the space generated by a finite number of principal components arises. Also, more recently, several developments of this technique have been proposed, *e.g.* [KGAB11, CF11, WABI12]. Let us briefly recall the procedure to build a POD basis which will be used later in Chapters 4, 5 and 6.

We consider the Galerkin approximation in a finite space $V_N = \text{span}\{\varphi_1, \dots, \varphi_N\}$

of the solution of (1.40): for all $x \in \Omega$ and $t \in [0, T]$ it reads

$$u(x, t) \simeq \sum_{k=1}^N a_k(t) \varphi_k(x), \quad (1.49)$$

where N is the dimension of V_N . In general, the basis functions φ_k are given a priori, for example they can be elements of the finite element basis, Legendre polynomials or Chebyshev polynomials, and the coefficients $a_k = a_k(t)$ depend on the choice of the basis. In this case, the basis functions are determined independently of the solution to compute. If we suppose that the basis is orthonormal, *i.e.*

$$\int_{\Omega} \varphi_i(x) \varphi_j(x) dx = \delta_{ij}, \quad \forall i, j = 1, \dots, N \quad (1.50)$$

where δ_{ij} is the Kronecker function, then the coefficients a_k of (1.49) can be written as

$$a_k(t) = \int_{\Omega} u(x, t) \varphi_k(x) dx, \quad (1.51)$$

and then

$$u(x, t) \simeq \sum_{k=1}^N \langle u(\cdot, t), \varphi_k \rangle \varphi_k(x), \quad (1.52)$$

where $\langle \cdot, \cdot \rangle$ is the $L^2(\Omega)$ inner product.

Contrary to the FE basis, the POD basis is obtained from the data of the solution $u(x, t_i)$ at M time instants t_1, \dots, t_M . The POD basis is obtained as the solution of the following problem: find the orthonormal functions $\{\varphi_k\}_{k=1}^N$, $N \ll \mathcal{N}$, where \mathcal{N} is for instance the dimension of a finite element discretization, which minimize

$$\sum_{i=1}^M \left\| u(x, t_i) - \sum_{k=1}^N \langle u(\cdot, t_i), \varphi_k \rangle \varphi_k(x) \right\|_{L^2(\Omega)}^2. \quad (1.53)$$

In practice, we consider M realizations of $u(\cdot, t_i)$, $1 \leq i \leq M$, which are given at \mathcal{N} different points $x_1, \dots, x_{\mathcal{N}}$, *e.g.* the vertices of a finite element evaluation. Then, the set of data $\mathcal{U} = \{\mathbf{u}(t_1), \dots, \mathbf{u}(t_M)\}$ is arranged in a matrix called Snapshot Data Matrix $A = [\mathbf{u}(t_1) \dots \mathbf{u}(t_M)]$, $A \in \mathbb{R}^{\mathcal{N} \times M}$, where $\mathbf{u}(t_i) = [u(x_1, t_i), \dots, u(x_{\mathcal{N}}, t_i)]^T \in \mathbb{R}^{\mathcal{N}}$. Then the solution of the minimization problem (1.53) will be expressed thanks to the truncated Singular Value Decomposition (SVD) of length N of A .

Let us explain in details how the minimization problem (1.53) is solved. We recall that the SVD of A is the factorization

$$A = U \Sigma V^\dagger \quad (1.54)$$

where $U \in \mathbb{R}^{\mathcal{N} \times \mathcal{N}}$ and $V \in \mathbb{R}^{M \times M}$ are (non unique) orthogonal matrices and $\Sigma \in \mathbb{R}^{\mathcal{N} \times M}$ is the diagonal matrix of singular values ordered by decreasing order,

and V^\dagger denotes the transpose of V .

Let us consider the finite element solution such that for each time t_i , $i = 1, \dots, M$,

$$u(x, t) \simeq \sum_{k=1}^{\mathcal{N}} u_k(t_i) \psi_k(x), \quad (1.55)$$

where $V_{\mathcal{N}} = \{\psi_1, \dots, \psi_{\mathcal{N}}\}$ is the finite element space, and let us define the finite element mass matrix $\mathcal{M} \in \mathbb{R}^{\mathcal{N} \times \mathcal{N}}$, $\mathcal{M}_{ij} = \langle \psi_i, \psi_j \rangle$, the associated inner product $(u, v) = u^T \mathcal{M} v$ and the \mathcal{M} -norm $\|u\|_{\mathcal{M}}^2 = u^T \mathcal{M} u$, for any $u, v \in \mathbb{R}^{\mathcal{N}}$. Assume that the POD basis functions $\{\varphi_k\}_{k=1}^N$ are in the linear space spanned by the finite element functions $\{\psi_k\}_{k=1}^{\mathcal{N}}$

$$\varphi_k(x) = \sum_{j=1}^{\mathcal{N}} \hat{\varphi}_{k,j} \psi_j(x). \quad (1.56)$$

Then, the minimization problem (1.53) writes as

$$\min_{\varphi_1, \dots, \varphi_N} \sum_{i=1}^M \|\mathbf{u}(t_i) - \sum_{k=1}^N (\mathbf{u}(t_i), \varphi_k) \varphi_k\|_{\mathcal{M}}^2. \quad (1.57)$$

The minimization problem (1.57) can be written in a matrix representation as a minimization problem in the Frobenius norm²

$$\min_{Z \in \mathbb{R}^{\mathcal{N} \times N} \text{ s.t. } Z^T Z = I_N} \|\hat{A} - Z Z^T \hat{A}\|_F^2 \quad (1.58)$$

where I_N is the N dimensional identity matrix, $\hat{A} \in \mathbb{R}^{\mathcal{N} \times M}$ is defined by $\hat{A} = (\mathcal{M}^{1/2})^T A$, and $Z \in \mathbb{R}^{\mathcal{N} \times N}$ is $Z = (\mathcal{M}^{1/2})^T \Phi$, with $\Phi = [\hat{\varphi}_1 \dots \hat{\varphi}_N] \in \mathbb{R}^{\mathcal{N} \times N}$. Thus, we are looking for a N dimensional basis Φ such that $Z Z^T \hat{A}$ is the best approximation of \hat{A} compared with all subspaces of dimension N . Then, thanks to Eckart-Young theorem³, the solution is given by the truncated SVD of \hat{A} of length N

$$\hat{A}_N = U_N \Sigma_N V_N^T \quad (1.59)$$

where $\Sigma_N = \text{diag}(\sigma_1, \dots, \sigma_N)$ is the diagonal matrix of the N first singular values of \hat{A} , U_N corresponds to the first N columns of U and V_N to the first N rows of V .

Finally, we find that Φ solves

$$(\mathcal{M}^{1/2})^T \Phi = U_N. \quad (1.60)$$

The coefficients of the POD basis functions are defined by the solution of (1.60).

²The Frobenius norm is defined by $\|B\|_F = \sqrt{\sum_{i=1}^n \sigma_i^2(B)}$, where $n = \text{rank}(B)$, and σ_i are the singular values of any matrix B .

³[EY36] $\min_{X: \text{rank}(X) \leq k} \|A - X\|_F = \|A - A_k\|_F$ where A_k is the truncated SVD of A .

1.6.3 Reduce Order Method based on Approximated Lax Pairs

A new technique has been recently proposed in [GL14], called ALP method since it is based on Approximated Lax Pairs. The main difference with the methods presented above relies on the fact that the space where the solution is approximated evolves in time. The initial basis is built using an approximated Lax pair [Lax68], and then this basis evolves according to the dynamics of the specific problem. This approach is particularly useful to solve with front propagations such as cardiac electrophysiology equations. It is therefore applied to monodomain and bidomain equations in Chapter 6. We invite to consult the dedicated chapter for a complete description of the method. Finally, a new formulation of the ALP model that uses the Discrete Empirical Interpolation (DEIM) [CS10b] method is detailed and applied to bidomain equations in Chapter 8.

Numerical simulations of full electrocardiogram cycle

This chapter is dedicated to the simulation of full cycles of the electrical activity of the heart and the corresponding body surface potential. The model is based on a realistic torso and heart anatomy, including ventricles and atria. One of the specificities of our approach is to model the atria as a surface, which is the kind of data typically provided by medical imaging for thin volumes. The bidomain equations are considered in their usual formulation in the ventricles, and in a surface formulation on the atria. Two ionic models are used: the Courtemanche-Ramirez-Nattel model on the atria, and the “Minimal model for human Ventricular action potentials” (MV) by Bueno-Orovio, Cherry and Fenton in the ventricles. The heart is weakly coupled to the torso by a Robin boundary condition based on a resistor-capacitor transmission condition. Various ECGs are simulated in healthy and pathological conditions (left and right bundle branch blocks, Bachmann’s bundle block, atrioventricular block, Wolff-Parkinson-White syndrome). To assess the numerical ECGs, we use several qualitative and quantitative criteria found in the medical literature. Our simulation tool can also be used to generate the signals measured by a vest of electrodes. We illustrate this capability at the end of the chapter.

The results presented in this chapter lead to the manuscript
Elisa Schenone, Annabelle Collin, Jean-Frédéric Gerbeau. **Numerical simulations of full electrocardiogram cycle**, Submitted.

Contents

2.1	Introduction	47
2.2	Whole heart mesh	48
2.3	Modeling assumptions	50
2.3.1	Bidomain model	50
2.3.2	Surface bidomain model	52
2.3.3	Simulations on the whole heart	53
2.3.4	Coupling with the body	56
2.3.5	Electrocardiogram computation	58
2.4	Healthy and pathological numerical simulations	58
2.4.1	Healthy electrocardiograms	59
2.4.2	Pathologic electrocardiograms	60
2.4.3	Comparison with the Mitchell-Schaeffer model	66
2.5	Electrodes vest	68
2.6	Chapter conclusions	70
2.A	Mitchell and Schaeffer ionic model	72
2.B	Minimal Ventricular ionic model	73
2.C	Courtemanche, Ramirez and Nattel ionic model	75

2.1 Introduction

An electrocardiogram (ECG) is a recording of the electrical activity of the heart [MP95, War75]. The standard 12-lead ECG is obtained from 9 electrodes located on the body surface, as detailed in Section 1.3. This non-invasive and inexpensive procedure is probably the most used clinical tool for the detection of cardiac pathologies. The motivation for the modeling and the simulation of ECGs is twofold. First, the ECG is a simple output of the complex simulation of the cardiac electrical activity: while the latter is difficult to validate without invasive measurements, the former is easy to assess by a medical expert. Second, the simulation of ECGs can be viewed as a step toward the inverse problem of electrocardiography (see e.g. [NCL07, WKMJ13, LLH06, JXS⁺08]) as shown in next chapters. Indeed, the inverse problem can be reformulated as a problem of identifying the parameters of the model used to simulate ECGs, see for instance Chapter 4. From this perspective, the design of a model based on biophysical principles and able to produce ECGs in healthy and pathological condition is an important endeavor. This is the main purpose of this study.

Many attempts at simulating ECGs can be found in the literature [Hui98, LBG⁺03, KSW⁺07]. A brief overview is given in Section 1.3. The simulation of 12-lead ECG based on partial differential equations (PDE) appeared during the last decade [PDG03, TDP⁺04, PDV09, BCF⁺10, MDFG12]. More recently, a focus on the T-wave was proposed in [HK14]. Because of the difficulty in imaging and modeling the atria, all these studies only consider the ventricles. As a consequence, they cannot produce the P-wave of the ECG. On the contrary, papers considering atria, as [HC00, KST⁺11], usually do not include ventricles and do not provide ECGs. Recently, a full cycle electrocardiogram was proposed in [SMLD13], but for an idealized geometry. To our knowledge, the present work is the first one to propose a full cycle ECG – including the P, QRS and T waves – based on a real anatomy of the heart and on the simulation of a PDE biophysical model.

Another limitation of the existing works on ECG simulation is their lack of precise evaluation of the results. This question is indeed delicate since a “healthy ECG” is not a unique object, and there is no obvious metric to measure the discrepancy between this somehow fuzzy notion and the result of a simulation. In this paper, we gather many criteria, found in the medical literature, that can be used to assess both qualitatively and quantitatively the numerical ECGs. We show that our healthy ECG fulfills almost all the qualitative and quantitative properties of real ECGs, which is a significant progress with respect to the state of art. Pathological cases are also investigated in order to show the capability of our model to predict the features used by medical doctors to detect a disease.

Here is a brief description of our approach. A standard 3D bidomain model is used for the ventricles [Tun78, Sac04] and a recent asymptotic surface-based bidomain model is used for the atria [CCG12, CGH⁺13]. Two different ionic models are considered: the physiological model proposed by Courtemanche, Ramirez and Nattel in [CRN98] on the atria, and the “Minimal model for human Ventricular action

Left Ventricle	Volume (ml)	Mass (g)	Mitral (cm)	Aortic (cm)
<i>Measures</i>	53.7	111.3	2.9	2.3
<i>Reference</i>	46 ± 11	112 ± 27	2.5 ± 0.4	2.3 ± 0.2
Left Atrium	Major axis (cm)	Area (cm ²)	Volume (ml)	Pulm. Veins (cm)
<i>Measures</i>	4.65	15.9	47	1.14 – 1.45
<i>Reference</i>	3.4 ± 0.6	17.5 ± 2.5	58 ± 34	1.3 ± 0.2

Table 2.1: Comparisons of the model dimensions with typical end-systolic values found in the literature [CM07, HPF⁺05, OSTW82, ERBL⁺10, ZBMHO94, CWS⁺95, JHR⁺08].

potentials” (MV) model proposed by Bueno-Orovio, Cherry and Fenton in [BOCF08] in the ventricles. The coupling conditions between the heart and the body are based on the resistor-capacitor coupling condition presented in [BCF⁺10].

The outline of this chapter is as follows. In Section 2.2, the geometry of the heart used for the simulation is described. It is based on a surface region for the atria and a volume region for the ventricles. Its main characteristics are compared with those of a normal human heart. Section 2.3 deals with the biophysical modeling of the atria and the ventricles and the coupling condition with the rest of the body. Section 2.4 concerns the simulations of the standard 12-lead ECG. A healthy case is given and validated against numerous criteria used to assess real electrocardiograms. Some pathological cases are also studied: left and right bundle branch blocks, Bachmann’s bundle block, atrioventricular block, and the Wolff-Parkinson-White syndrome which is a pathology caused by the presence of an abnormal accessory electrical conduction pathway between the atria and the ventricles. In the last part of this section, we investigate the impact of the ionic models on the ECGs by using in the ventricle and in the atria the phenomenological Mitchell-Schaeffer model [MS03]. In Section 2.5, we show that our simulator can also produce signals that are richer than the standard ECG. As an illustration, we analyse the potential measured by a “virtual electrode vest” made of 1216 electrodes. In particular, the correlation between the signals of different electrodes is studied. We also give an analysis of the dependence of the electrode measures with respect to their positions on the body.

2.2 Whole heart mesh

To obtain full cycle ECGs, the first step is to build a whole heart realistic mesh. The ventricles can be easily obtained from medical imaging and meshed in 3D. On the contrary, the atria have a very thin wall which makes them difficult to image in 3D. In addition, generating a 3D mesh on these very thin volumes would dramatically, and uselessly, increase the computational cost. For these reasons, we choose to model the geometry of the atria as a surface. We therefore obtain an hybrid mesh, made of tetrahedra in the ventricles and of triangles in the atria.

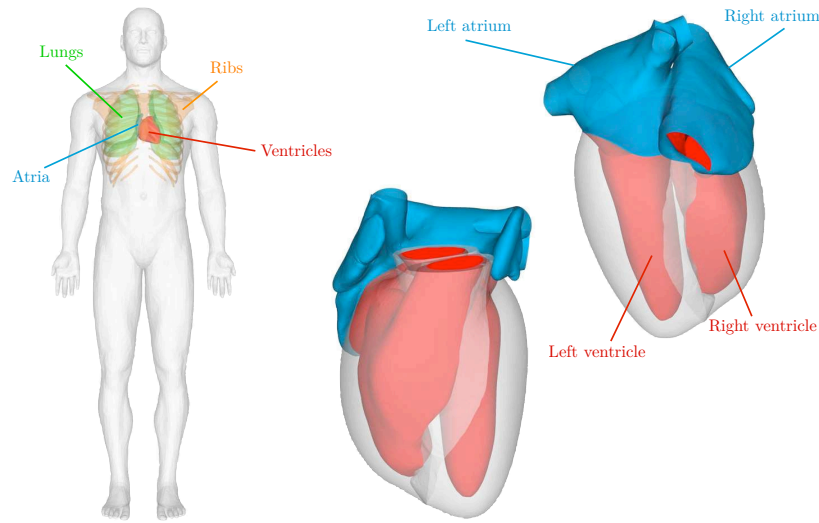


Figure 2.1: Whole heart mesh (right) and body mesh (left).

The heart model is obtained from an anatomical data set called *Zygote*¹. The **3-matic** software is used to obtain a surface mesh satisfying the standard quality criteria of a finite element mesh, and **Yams** [Fre01] to refine the surface mesh. Then, the volume of the two ventricles is meshed using **Gmsh** [GR09]. We can see in Figure 2.1 different views of the whole mesh, which contains about 230,600 tetrahedra, 73,500 triangles and 67,300 vertices. A simplified mesh of the body (Fig. 2.1), including the lungs and the ribs, is also built from the *Zygote* data set and the aforementioned software. The body mesh contains 408,171 tetrahedra, 89,222 triangles and 85,196 vertices.

The mechanical deformation of the heart is not taken into account in this work (see for instance [AANQ11, RBAP⁺13]). The dimensions of the fixed domain correspond to the end of the systole (small ventricles, large atria). Table 2.1 shows a comparison of a few dimensions of the geometrical model with standard end-systolic values. The following quantities are compared: left ventricle volume and mass, mitral and aortic valves diameters, left atrium major axis, area, volume and four pulmonary veins diameters. We observe a good agreement with the values found in the literature [CM07, HPF⁺05, OSTW82]. We also have a good agreement for the diameters of mitral [ERBL⁺10] and aortic [ZBMHO94] valves, the surface of the left atrium [CWS⁺95, JHR⁺08].

Cardiac tissue has a fiber architecture. The electrical conductivity is higher along the fibers than in the transverse direction. This implies that the fiber orientation is very important in the study of the electrical activity of the heart. To identify and to prescribe the fibers at the endocardium and at the epicardium of the atria, we use [HASQ02, HSQ09, KST⁺11]. As we can see in Figure 2.2 (top), the fibers orientation may vary extremely quickly across the thickness. The colors represent

¹www.3dscience.com

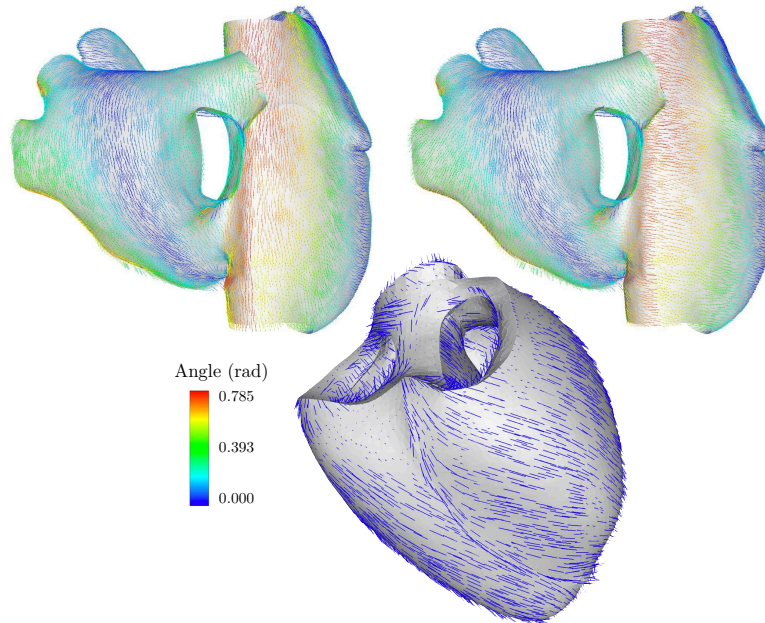


Figure 2.2: Fibers directions at the atrial endocardium (top-left) and atrial epicardium (top-right), and in ventricles (bottom).

the angle θ defined as half of the angular difference between the endocardium and the epicardium. We use [NH00, Str79] to prescribe the fibers in the ventricles, see Figure 2.2 (bottom).

Figure 2.3 represents a schematic view of the heart conduction system in a healthy heart: the sinus and atrioventricular nodes, the Bachmann's bundle and the Purkinje fibers. In this work, the atrio-ventricular node and the Purkinje fibers are not explicitly modeled (see below).

2.3 Modeling assumptions

In this section, we present the electrophysiology equations and the ionic models used in the ventricles and the atria. We also present the coupling conditions between the atria and the ventricles and between the heart and the body.

2.3.1 Bidomain model

In order to describe the electrical potential in the heart we used the standard nonlinear reaction-diffusion bidomain equations (see for instance [Sac04, SLC⁺06]). As previously described in Section 1.4, in terms of extracellular potential u_e and transmembrane potential $V_m = u_i - u_e$, with u_i the intracellular potential, the

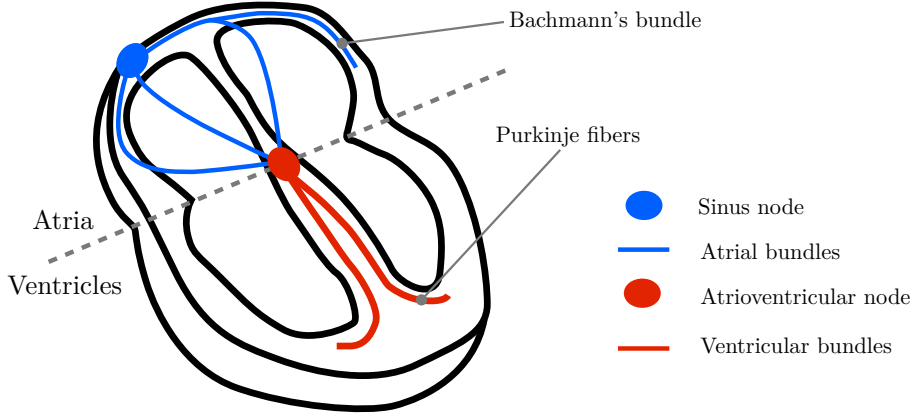


Figure 2.3: Heart conduction system.

bidomain model reads

$$\begin{cases} A_m(C_m \frac{\partial V_m}{\partial t} + I_{\text{ion}}(V_m, w_1, \dots, w_n)) - \text{div}(\bar{\sigma}_i \cdot \bar{\nabla} V_m) - \text{div}(\bar{\sigma}_i \cdot \bar{\nabla} u_e) = A_m I_{\text{app}} \\ -\text{div}((\bar{\sigma}_i + \bar{\sigma}_e) \cdot \bar{\nabla} u_e) - \text{div}(\bar{\sigma}_i \cdot \bar{\nabla} V_m) = 0 \end{cases} \quad (2.1)$$

in $\mathcal{B} \times (0, T)$, where \mathcal{B} denotes the 3D domain of interest, A_m is a positive constant denoting the ratio of membrane area per unit volume, C_m the membrane capacitance per unit surface, I_{ion} the ionic current which depends on n ionic variables w_1, \dots, w_n and I_{app} a given applied stimulus current.

We make the standard assumption that the extracellular current does not flow through the epicardium, so that the first boundary condition is

$$(\bar{\sigma}_e \cdot \bar{\nabla} u_e) \cdot \bar{n} = 0, \quad \text{in } \partial\mathcal{B} \times (0, T). \quad (2.2)$$

The second boundary condition comes from the fact that, by definition, the intracellular current does not propagate outside the heart [Tum78]

$$(\bar{\sigma}_i \cdot \bar{\nabla} u_e) \cdot \bar{n} = -(\bar{\sigma}_i \cdot \bar{\nabla} V_m) \cdot \bar{n}, \quad \text{in } \partial\mathcal{B} \times (0, T). \quad (2.3)$$

In order to define the I_{ion} term, equations (2.1) must be coupled with a ionic model, i.e. a system of nonlinear ordinary differential equations (ODEs). For the ventricular domain, we apply the ‘‘Minimal model for human Ventricular action potentials’’ (MV) introduced in [BOCF08]. MV is a phenomenological model associated with three ionic currents, three gate variables, and governed by 28 parameters. Its expression and parameters are briefly reported in Appendix 2.B.

As previously explained, the fiber architecture of the cardiac muscle is considered. In order to include the anisotropy between the orthogonal and the tangent direction

of the fibers, the conductivity tensors $\bar{\sigma}_i$ and $\bar{\sigma}_e$ are defined by

$$\bar{\sigma}_{i,e} = \sigma_{i,e}^{v,t} \bar{I} + (\sigma_{i,e}^{v,l} - \sigma_{i,e}^{v,t}) \bar{\tau} \otimes \bar{\tau},$$

where \bar{I} denotes the 3D identity matrix, the vector $\bar{\tau}$ is of unit length and parallel to the local fiber direction, and $\sigma_{i,e}^{v,l}$ and $\sigma_{i,e}^{v,t}$ are respectively the conductivity coefficients in the intra- and extra-cellular ventricular medium measured along and across the fiber direction.

The bidomain model can be rewritten in weak form as follows. For all $t > 0$, find $V_m(\cdot, t) \in H^1(\mathcal{B})$, $u_e(\cdot, t) \in H^1(\mathcal{B})$ and $w_1(\cdot, t), \dots, w_n(\cdot, t) \in L^\infty(\mathcal{B})$ with $\int_{\mathcal{B}} u_e = 0$, such that

$$\begin{cases} A_m \int_{\mathcal{B}} \left(C_m \frac{\partial V_m}{\partial t} + I_{\text{ion}}(V_m, w_1, \dots, w_n) \right) \phi + \int_{\mathcal{B}} \left(\bar{\sigma}_i \cdot (\nabla V_m + \nabla u_e) \right) \cdot \nabla \phi \\ \qquad \qquad \qquad \qquad \qquad \qquad \qquad \qquad = A_m \int_{\mathcal{B}} I_{\text{app}} \phi \\ \int_{\mathcal{B}} \left((\bar{\sigma}_i + \bar{\sigma}_e) \cdot \nabla u_e \right) \cdot \nabla \psi + \int_{\mathcal{B}} \left(\bar{\sigma}_i \cdot \nabla V_m \right) \cdot \nabla \psi = 0 \end{cases} \quad (2.4)$$

for all $\phi, \psi \in H^1(\mathcal{B})$ such that $\int_{\mathcal{B}} \psi = 0$. Under some regularity assumptions, we have existence and uniqueness of a solution of the bidomain model, see *e.g.* [BCP09]. The hypothesis $\int_{\mathcal{B}} u_e = 0$ is necessary in order to have uniqueness and we show in Section 2.3.3 how to adapt this condition when atria and ventricles are coupled.

2.3.2 Surface bidomain model

As explained in Section 2.2, it is more convenient to work with a surface mesh for the atria. The electrophysiology model set on this surface is the one proposed and analyzed in [CCG12], derived from the volume bidomain model, and defined over the midsurface of the thin region. This surface-based model was obtained from a rigorous asymptotic analysis and was specifically designed for thin cardiac structures. It takes into account the strong anisotropy variations across the thickness and it is extremely attractive in term of computation time compared to its 3D counterpart. We denote by \mathcal{S} the midsurface of the wall and we denote by $H^1(\mathcal{S})$ the associated space. The surface-based bidomain model can be rewritten in weak form as follows: for all $t > 0$, find $V_m(\cdot, t) \in H^1(\mathcal{S})$, $u_e(\cdot, t) \in H^1(\mathcal{S})$ and $w_1(\cdot, t), \dots, w_n(\cdot, t) \in L^\infty(\mathcal{S})$ with $\int_{\mathcal{S}} u_e = 0$, such that

$$\begin{cases} A_m \int_{\mathcal{S}} \left(C_m \frac{\partial V_m}{\partial t} + I_{\text{ion}}(V_m, w_1, \dots, w_n) \right) \phi + \int_{\mathcal{S}} \left(\underline{\sigma}_i \cdot (\nabla V_m + \nabla u_e) \right) \cdot \nabla \phi \\ \qquad \qquad \qquad \qquad \qquad \qquad \qquad \qquad = A_m \int_{\mathcal{S}} I_{\text{app}} \phi \\ \int_{\mathcal{S}} \left((\underline{\sigma}_i + \underline{\sigma}_e) \cdot \nabla u_e \right) \cdot \nabla \psi + \int_{\mathcal{S}} \left(\underline{\sigma}_i \cdot \nabla V_m \right) \cdot \nabla \psi = 0 \end{cases} \quad (2.5)$$

for all $\phi, \psi \in H^1(\mathcal{S})$ such that $\int_{\mathcal{S}} \psi = 0$. We denote by $\sigma_{i,e}^{a,l}$ and $\sigma_{i,e}^{a,t}$ the conductivity coefficients in the intra- and extra-cellular atrial medium measured along and across the fiber direction. We define the intra- and extra-cellular diffusion tensors $\underline{\sigma}_i$ and $\underline{\sigma}_e$ by

$$\underline{\sigma}_{i,e} = \sigma_{i,e}^{a,t} \underline{I} + (\sigma_{i,e}^{a,l} - \sigma_{i,e}^{a,t}) [I_0(\theta) \underline{\tau}_0 \otimes \underline{\tau}_0 + J_0(\theta) \underline{\tau}_0^\perp \otimes \underline{\tau}_0^\perp], \quad (2.6)$$

where \underline{I} denotes the identity tensor in the tangential plane, $\underline{\tau}_0$ is a unit vector parallel to the local fiber direction on the atria midsurface, and $\underline{\tau}_0^\perp$ such that $(\underline{\tau}_0, \underline{\tau}_0^\perp)$ gives an orthonormal basis of the tangential plane. We use the fibers direction at the endocardium and at the epicardium to define the fibers direction $\underline{\tau}_0$ on the atria midsurface and the angle variation θ between the endocardium and the epicardium. The effect of angular variations appears in the model with the coefficients $I_0(\theta) = \frac{1}{2} + \frac{1}{4\theta} \sin(2\theta)$ and $J_0(\theta) = 1 - I_0(\theta)$. Note that $J_0(\theta) = 0$ (and $I_0(\theta) = 1$) if and only if $\theta = 0$, which corresponds to a constant direction in the thickness and then $\underline{\sigma}_{i,e} = \sigma_{i,e}^{a,t} \underline{I} + (\sigma_{i,e}^{a,l} - \sigma_{i,e}^{a,t}) \underline{\tau}_0 \otimes \underline{\tau}_0$. By contrast, important angular variations make I_0 decrease and J_0 increase in (2.6) and the diffusion becomes more isotropic. In [CGH⁺13] this model was compared to several 3D models proposed in the literature [DGSJ12, HC00, MLW⁺09].

The physiological model introduced by Courtemanche, Ramirez and Nattel in [CRN98] – a classic atrial model – is considered (12 ionic currents and 20 other variables). The two atria are connected only by two regions, the Bachmann bundle and the *Fossa Ovalis*. A brief description of the model and its parameters are reported in Appendix 2.C, we refer to [CGH⁺13] for more details.

2.3.3 Simulations on the whole heart

Coupled model

From a mathematical point of view, volume and surface models are incompatible. It would be erroneous to solve them separately because the uniqueness criterion for the first model is not consistent with the second one. As seen in Sections 2.3.1 and 2.3.2, the unique solution $u_e(\cdot, t) \in H^1(\mathcal{B})$ of (2.4) is s.t. $\int_{\mathcal{B}} u_e = 0$ and the unique solution $u_e(\cdot, t) \in H^1(\mathcal{S})$ of (2.5) is s.t. $\int_{\mathcal{S}} u_e = 0$. This is why we consider a whole domain $\mathcal{B} \cup \mathcal{S}$ and a new global criterion. The resulting coupled problem is well-posed at the discrete level, but its mathematical analysis remains to be done. Let $\Omega_h = \mathcal{B}_h \cup \mathcal{S}_h$, where \mathcal{B}_h is the mesh of the ventricles and \mathcal{S}_h is the mesh of the atria, and let \mathcal{L}_h be the line such that $\mathcal{B}_h \cap \mathcal{S}_h = \mathcal{L}_h$. We denote by $\gamma_{\tilde{\Omega}} u$ the restriction of a function u to a subdomain $\tilde{\Omega}$. The finite dimensional approximation spaces \mathcal{V}_h and \mathcal{V}_h^0 are then defined by: $v_h \in \mathcal{V}_h$ if and only if v_h is continuous in Ω_h , $\gamma_{\mathcal{B}_h} v_h \in H^1(\mathcal{B}_h)$, $\gamma_{\mathcal{S}_h} v_h \in H^1(\mathcal{S}_h)$, and $u_h \in \mathcal{V}_h^0$ if and only if $u_h \in \mathcal{V}_h$ and $\int_{\mathcal{B}_h} u_h = 0$. Using (2.4), (2.5), the full model reads: find $(V_{m,h}, u_{e,h}) \in \mathcal{V}_h \times \mathcal{V}_h^0$ such

$\sigma_e^{a,t}$	$\sigma_e^{a,l}$	$\sigma_i^{a,t}$	$\sigma_i^{a,l}$	$\sigma_e^{s,t}$
$9.0 \cdot 10^{-4}$	$2.5 \cdot 10^{-3}$	$2.5 \cdot 10^{-4}$	$2.5 \cdot 10^{-3}$	$7.5 \cdot 10^{-7}$

Table 2.2: Atria conductivity parameters (S.cm⁻¹).

$\sigma_e^{v,t}$	$\sigma_e^{v,l}$	$\sigma_i^{v,t}$	$\sigma_i^{v,l}$
$6.0 \cdot 10^{-4}$	$2.0 \cdot 10^{-3}$	$2.0 \cdot 10^{-4}$	$2.0 \cdot 10^{-3}$

Table 2.3: Ventricles conductivity parameters (S.cm⁻¹).

that $\forall \phi \in \mathcal{V}_h$, $\psi \in \mathcal{V}_h^0$,

$$\left\{ \begin{array}{l} A_m \int_{\mathcal{L}_h} \left(C_m \frac{\partial V_{m,h}}{\partial t} + I_{\text{ion}}(V_{m,h}, \dots) \right) \phi + \int_{\mathcal{S}_h} \left(\underline{\sigma}_i \cdot (\nabla V_{m,h} + \nabla u_{e,h}) \right) \cdot \nabla \phi \\ \quad + \int_{\mathcal{B}_h} \left[\bar{\sigma}_i \cdot (\bar{\nabla} V_{m,h} + \bar{\nabla} u_{e,h}) \right] \cdot \bar{\nabla} \phi = A_m \int_{\mathcal{L}_h} I_{\text{app}} \phi \\ \int_{\mathcal{S}_h} \left((\underline{\sigma}_i + \underline{\sigma}_e) \cdot \nabla u_{e,h} + \underline{\sigma}_i \cdot \nabla V_{m,h} \right) \cdot \nabla \psi \\ \quad + \int_{\mathcal{B}_h} \left((\bar{\sigma}_i + \bar{\sigma}_e) \cdot \bar{\nabla} u_{e,h} + \bar{\sigma}_i \cdot \bar{\nabla} V_{m,h} \right) \cdot \bar{\nabla} \psi = 0. \end{array} \right. \quad (2.7)$$

Connection surface

As previously mentioned, the atrioventricular node is the only pathway for the electrical signal between the atria and the ventricles. From a physiological point of view, a fibrous skeleton separates atria boundaries from ventricles epicardium. This layer isolates the atrial cells from the ventricular ones [MTT11, MdBV⁺96]. We propose to model this fibrous skeleton with a thin layer of the atrial surface, represented on the left of Figure 2.4. The idea is that in this area there is only a low conduction of the extracellular potential. In this region, denoted by $\mathcal{S}_c \subset \mathcal{S}$, the intracellular conductivity is set to zero and the extracellular conductivity denoted by $\sigma_e^{s,t}$ is very low (see Table 2.2). Finally, the surface and volume bidomain equations (2.7) are solved simultaneously on this ‘‘hybrid’’ domain with

$$\begin{aligned} \bar{\sigma}_{i,e} &= \sigma_{i,e}^{v,t} \bar{I} + (\sigma_{i,e}^{v,l} - \sigma_{i,e}^{v,t}) \bar{\tau} \otimes \bar{\tau}, \\ \underline{\sigma}_{i,e} &= \sigma_{i,e}^{a,t} \underline{I} + (\sigma_{i,e}^{a,l} - \sigma_{i,e}^{a,t}) [I_0(\theta) \underline{\tau}_0 \otimes \underline{\tau}_0 + J_0(\theta) \underline{\tau}_0^\perp \otimes \underline{\tau}_0^\perp], \text{ in } \mathcal{S} \setminus \bar{\mathcal{S}}_c, \\ \underline{\sigma}_i &= \underline{0}, \text{ and } \underline{\sigma}_e = \sigma_e^{s,t} \underline{I}, \text{ in } \mathcal{S}_c. \end{aligned}$$

Parameters and applied currents

The values of the membrane parameters are $A_m = 200.0 \text{ cm}^{-1}$ and $C_m = 10^{-3} \text{ mF.cm}^{-2}$ for the whole heart. The conductivity takes different values depending on the region in the ventricles and atria (Tables 2.3, 2.2).

In the atria, the regions of fast conduction are the Bachmann bundle (BB), see Figure 2.3, the *Crista Terminalis* (CT) and the pectinate muscles (PM). By contrast,

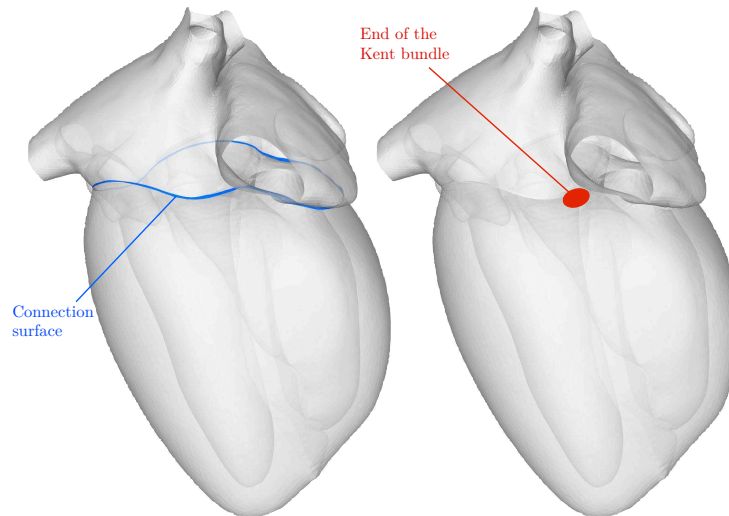


Figure 2.4: Surface connection between the atria and the ventricles (left) and Kent bundle (right).

regular tissue	PM	CT	BB	FO
7.8	11.7	31.2	46.8	3.9

Table 2.4: Maximal conductance g_{Na} in the different atrial areas (nS.pF⁻¹).

the *Fossa Ovalis* (FO) is a region of slow conduction. In order to model the different propagation velocities, we modify the values of g_{Na} , the maximal conductance of the Na^{2+} current I_{Na} . Table 2.4 gives the parameters used for g_{Na} . Furthermore, the action potential duration is forced to be shorter, *i.e.* the parameter g_{Ks} is five times bigger than in [CRN98].

In the ventricles, we modify the duration of the plateau too. In the MV model, we change the values of τ_{so1} parameter in order to reduce the action potential duration for epicardial, endocardial and midmyocardial cells. This heterogeneity is considered in the left ventricle, for the positivity of T wave [YA98]. In the right ventricle, the cells are considered homogeneous and their parameters are taken as in the left ventricle epicardium, except for τ_{so1} (Table 2.5).

Activation is initiated at the sinus node with a stimulus of 2ms which triggers a depolarization wavefront in the atria (Figure 2.3). For the sake of simplicity, the atrioventricular node, which is the only electrical connection between the atria and the ventricles, is not modeled with a sophisticated physiological model. Instead,

	EPI	ENDO	M	RV
[BOCF08]	30.0181	40.0	91.0	/
Heart	25.0	40.0	61.0	26.0

Table 2.5: Changed ionic parameter τ_{so1} of MV compared to [BOCF08].

the excitation is triggered in the ventricle after a parameterized delay (in healthy condition, we choose to start it at 190ms). Similarly, the fast conduction in the Purkinje fibers (Figure 2.3) is modeled with a predefined stimulus pattern: a time-dependent thin subendocardial layer is activated by an external current on both right and left ventricle. A description of a ventricular external stimulus is given in [BCF⁺10] for more details.

Simulation results

The various simulations of this work are performed with the finite element library FELiScE², developed at Inria by the REO and MÆDISIM teams. The numerical methods used to solve problem (2.7) are presented in [BCF⁺10]. Figure 2.5 shows a full cardiac cycle. The corresponding first lead electrocardiogram is also represented. The electrical signal starts at the sinus node where the atrial depolarization (AD) begins. By 50ms the wave quickly spreads along the *Crista Terminalis* as a consequence of the high conductivity in this part. Importantly, because of the rapid conduction in the Bachmann bundle, the wave spreads to the left atrial appendage and activates a substantial part of the left atrial wall. The depolarization of the right and left atria terminates at 100ms and 110ms, respectively. The ventricular depolarization begins at 190ms. During this period, the atrial repolarization (AR) occurs. As we can see in the figure, at 200ms the endocardium of the ventricles rapidly depolarizes. Then, the wave propagates across the ventricles. The repolarization ends at 430ms in the right ventricle and at 470ms in the left ventricle.

2.3.4 Coupling with the body

The last step in order to obtain an electrocardiogram is to couple the heart model with a diffusion problem in the rest of the body

$$-\operatorname{div}(\sigma_T \bar{\nabla} u_T) = 0, \text{ in } \Omega_T, \quad (2.8)$$

where the electrical conductivity σ_T takes different scalar values in the ribs and the lungs (see [BP03] and Table 2.6).

On the body surface $\partial\Omega_T^{\text{ext}}$, an homogeneous Neumann boundary condition is imposed $\sigma_T \bar{\nabla} u_T \cdot \bar{n} = 0$. To define the transmission conditions at the heart-body interface $\partial\Omega_H$, we assume that the extracellular current does not flow through the pericardium (isolated heart assumption)

$$\bar{\sigma}_e \cdot \bar{\nabla} u_e \cdot \bar{n} = 0 \quad (2.9)$$

and we consider the resistor-capacitor conditions presented in [BCF⁺10]

$$R_p(\sigma_T \bar{\nabla} u_T) \cdot \bar{n} = R_p C_p \frac{\partial(u_e - u_T)}{\partial t} + (u_e - u_T) \quad (2.10)$$

²<http://felisce.gforge.inria.fr> – A brief description of the library, the implementation of the electrophysiology into the code and the author contributions is given in Appendix A.

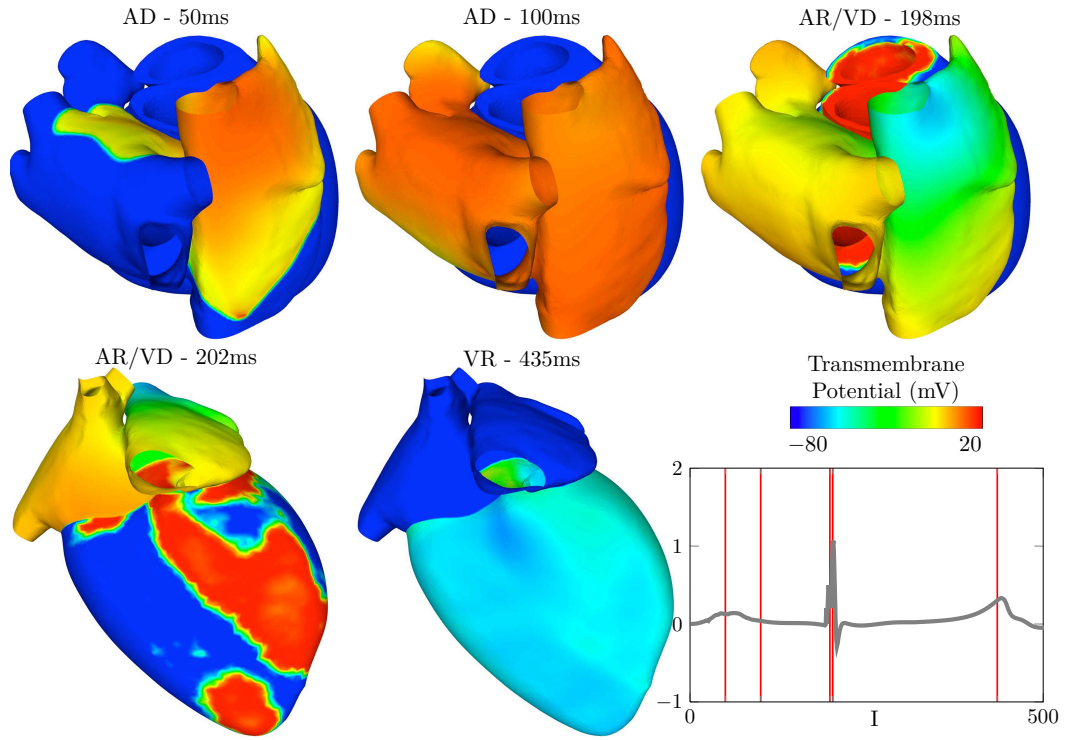


Figure 2.5: Simulations of heart depolarization in a healthy case with the corresponding electrocardiogram first lead.

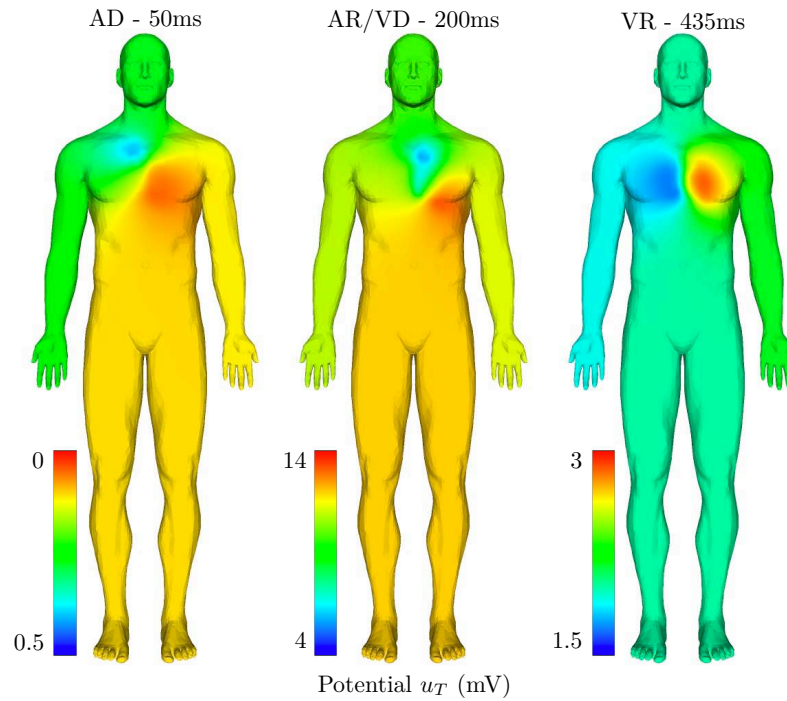


Figure 2.6: Simulations body potential of heart depolarization in a healthy case (Figure 2.5), with coupling condition (2.10).

σ_T^{body}	σ_T^{bones}	σ_T^{lungs}
$3.0 \cdot 10^{-2}$	$1.2 \cdot 10^{-2}$	$2.0 \cdot 10^{-3}$

Table 2.6: Body conductivity parameters ($\text{S}\cdot\text{cm}^{-1}$).

where C_p and R_p stand for the capacitance and resistance of the pericardium, respectively.

Condition (2.9) is an approximation that has been shown not to affect too much the shape of the ECG in [BCF⁺10]. It allows us to solve the heart-body system as a one-way coupled problem, which dramatically reduced its computational cost.

Condition (2.10) allows us to model the fact that the transmission of potential through the pericardium is not perfect, and can be different for the ventricles and the atria. We take $R_p = 10^2 \Omega\cdot\text{cm}^2$ on the surface in contact with the ventricles and $R_p = 10^5 \Omega\cdot\text{cm}^2$ on the surface in contact with the atria. We neglect the capacitor effect by taking $C_p = 0 \text{ mF}\cdot\text{cm}^2$ in (2.10). The transmission between the heart and the body is therefore modeled as a Robin boundary condition

$$R_p(\sigma_T \bar{\nabla} u_T) \cdot \bar{n} + u_T = u_e, \text{ on } \partial\Omega_H. \quad (2.11)$$

Figure 2.6 shows the body surface potential corresponding to the simulation shown in Figure 2.5.

2.3.5 Electrocardiogram computation

A standard electrocardiogram is based on the body surface potential recorded by 9 electrodes ($\Gamma_{ECG} = \{R, L, F, V_1, \dots, V_6\}$, see Figure 2.7). These measures are combined to define 12 differences of potential, known as the 12 leads of the standard ECG

$$\begin{aligned} \text{I} &= u_T(L) - u_T(R) & aVR &= 1.5(u_T(R) - u_w) \\ \text{II} &= u_T(F) - u_T(R) & aVL &= 1.5(u_T(L) - u_w) \\ \text{III} &= u_T(F) - u_T(L) & aVF &= 1.5(u_T(F) - u_w) \\ V1 &= u_T(V_1) - u_w & V4 &= u_T(V_4) - u_w \\ V2 &= u_T(V_2) - u_w & V5 &= u_T(V_5) - u_w \\ V3 &= u_T(V_3) - u_w & V6 &= u_T(V_6) - u_w \end{aligned}$$

where $u_w = \frac{1}{3}(u_T(L) + u_T(R) + u_T(F))$ is the Wilson potential. A more detailed description of the ECG is given in Section 1.3 or for instance [MP95].

2.4 Healthy and pathological numerical simulations of electrocardiograms

In this Section, we present the ECGs provided by the aforementioned model in healthy and pathological conditions. The healthy ECG is obtained by carefully choosing the parameters of the model in order to match most of the qualitative and

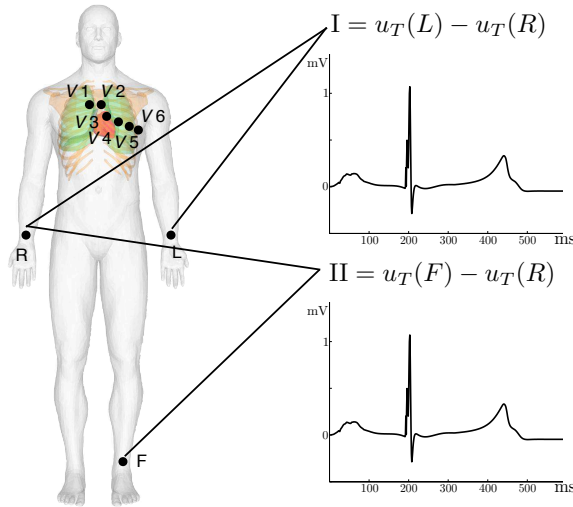


Figure 2.7: Standard 9 electrodes locations and first and second ECG leads.

quantitative features of a physiological ECG. To obtain the pathological ECGs, the approach is different: starting from the nominal values corresponding to a healthy ECGs, we modify the parameters in order to model the *physical characteristics* of the pathology. Then we observe the effects of these modifications on the numerical ECG, and we compare its features with the ones described in the literature. It is important to emphasize that, for the pathological cases, the parameters are not intentionally fixed to match a given ECG. Thus, if the ECGs obtained after modeling the diseases match the main features observed on real patients, it gives confidence in the prediction capabilities of the model.

2.4.1 Healthy electrocardiograms

Figure 2.9 shows the simulated electrocardiogram in healthy conditions, corresponding to the simulation of Figure 2.5. An electrocardiogram is typically described by distinguishing five events during the heartbeat, called P, Q, R, S and T “waves” (we will keep this standard terminology even though these events have nothing to do with waves). The P wave corresponds to the atrial depolarization, the QRS complex corresponds to the ventricular depolarization, the T wave corresponds to the ventricular repolarization. The typical durations of each wave, or each interval, are given in Table 2.7.

Table 2.7 also presents the durations of the simulated healthy ECG of Figure 2.9. These durations are obtained in the numerical ECG from the landmarks defined according to the following rules: the P wave (resp. QRS complex) starts if 1% of the atria (resp. ventricles) is activated (*i.e.* if the transmembrane potential V_m is greater than a threshold voltage V_{gate}); the P wave (resp. QRS complex) ends when 99% of the atria (resp. ventricles) are activated; the T wave starts when 20% of the ventricles are repolarized (*i.e.* $V_m \leq 0$); the T wave ends when 99% of the ventricles

	P wave	PR interval	Q wave	QR interval	S wave	QRS interval	QT interval
Typical ECG	< 0.12	0.12 to 0.21	< 0.04	< 0.03 V1-V2 < 0.05 V5-V6	< 0.04	< 0.10	0.35 to 0.45
Healthy Simul.	0.08	0.19	0.015	0.015 V1-V2 0.02 V5-V6	0.01	0.04	0.29

Table 2.7: Durations of the simulated healthy ECG of Figure 2.9 compared with typical durations [War75] (seconds).

are fully repolarized ($V_m \leq 0$). If the minimal value of v_m is $V_{\min} = -80\text{mV}$ and its maximal value $V_{\max} = 20\text{mV}$, we define $V_{\text{gate}} = -67\text{mV}$, which corresponds to a threshold voltage $\theta_w = 0.13$ in the MV model.

Table 2.8 gives the main features of each wave in a normal electrocardiogram. Note that the simulated ECG verifies almost all the expected criteria. We only observe a discrepancy in the aVL lead, but this lead is not the most important one for the ECG interpretation.

To qualitatively assess the waves amplitude and orientation, the schematic presented in Figure 2.10 is very convenient. It is adapted from [War75] and shows the normal variations of wave amplitude measured in adults. A visual comparison of Figures 2.9 and 2.10 shows that, for almost every lead, each wave of our numerical ECG is in the range of the normal values. Note that in Figure 2.10, the length of each wave was arbitrarily chosen as its maximal normal duration. This is the reason why the full PQRST duration is so long in this schematic.

Here is another qualitative assessment. The R wave is known to have an important property in the precordial leads: it uniformly progresses from a RS complex in V1-V2 to a QRS complex in V5-V6 via a RS complex in V3-V4. The top of Figure 2.8, which represents this R variation, is extracted from [War75]. The bottom of the same Figure shows the results of our simulation. Again, the qualitative agreement is very satisfactory.

A last qualitative comment is in order: we note that the P wave presents some oscillations in all the leads of the numerical ECG. The explanation of these oscillations is the brutal changes of the fibers' direction in the atria. It is also possible that the surface representation of the atria accentuate these oscillations.

2.4.2 Pathologic electrocardiograms

In this Section, we modify the protocol of the simulation that provided the healthy ECG (Figure 2.9) in order to simulate different cardiac pathologies. Then we verify if the numerical ECGs present the main features that allow a medical doctor to detect the pathology. The different pathologies are schematically represented in Figure 2.11, along with the most important leads in each case.

Wave/Interval	Description	Simulated ECG
P wave	$\leq 0.25\text{mV}$	\checkmark 0.2mV
	positive I, II, V3 to V6	\checkmark
	negative aVR	\checkmark
Q wave	limb leads $\leq 25\%$ of R	\checkmark
	precordial leads $\leq 15\%$ of R	\checkmark
	always negative	\checkmark except for aVL
R wave	limb leads $\leq 2\text{mV}$	\checkmark
	precordial leads $\leq 3\text{mV}$	\checkmark
	always positive, negative in aVR	\checkmark
	R wave progression, see Figure 2.8	\checkmark
S wave	always negative	\checkmark
	small I, II, V5, V6	\checkmark
	important V1 to V3	\checkmark
ST interval	-0.05mV to 0.1mV	\checkmark
	isoelectric	\checkmark
	displacement of 0.02mV in V1, V3	\checkmark
T wave	positive I, II, V3 to V6	\checkmark
	negative aVR (follow the QRS)	\checkmark

Table 2.8: Criteria for a typical electrocardiogram [War75] compared with simulated ECG of Figure 2.9.

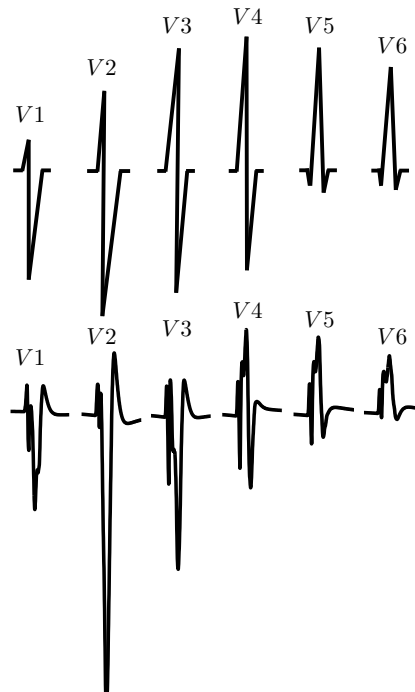


Figure 2.8: R wave progression in the precordial leads: schematic view from [War75] in the top, and simulated ECG in the bottom.

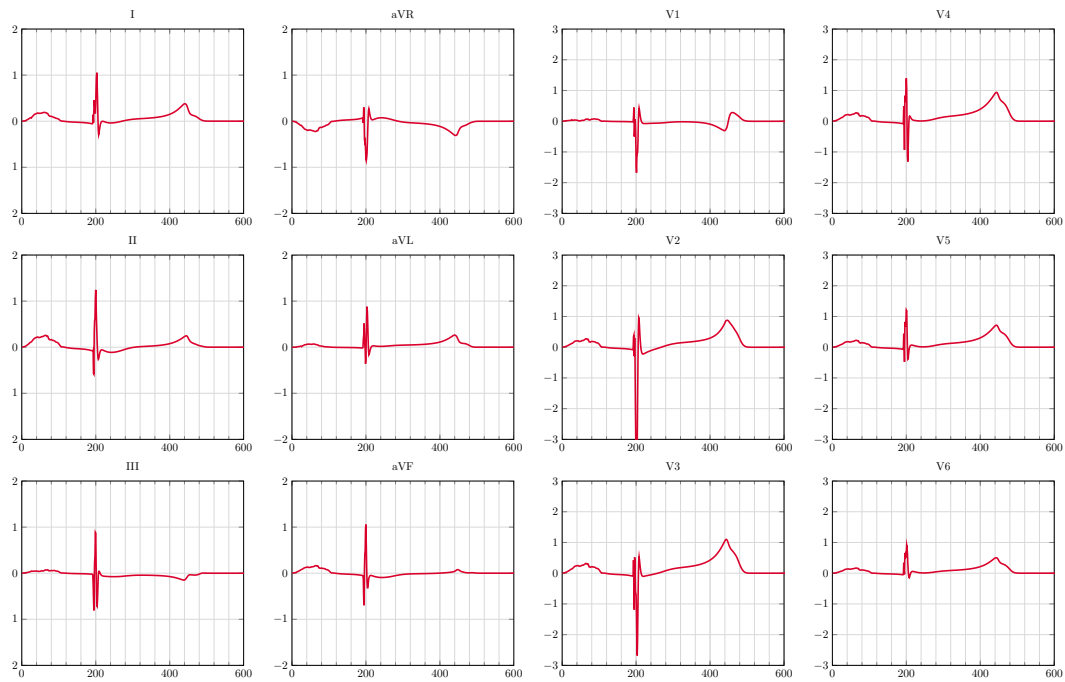


Figure 2.9: Healthy electrocardiogram corresponding to simulation of Figure 2.9 (voltages (mV) versus time (ms)).

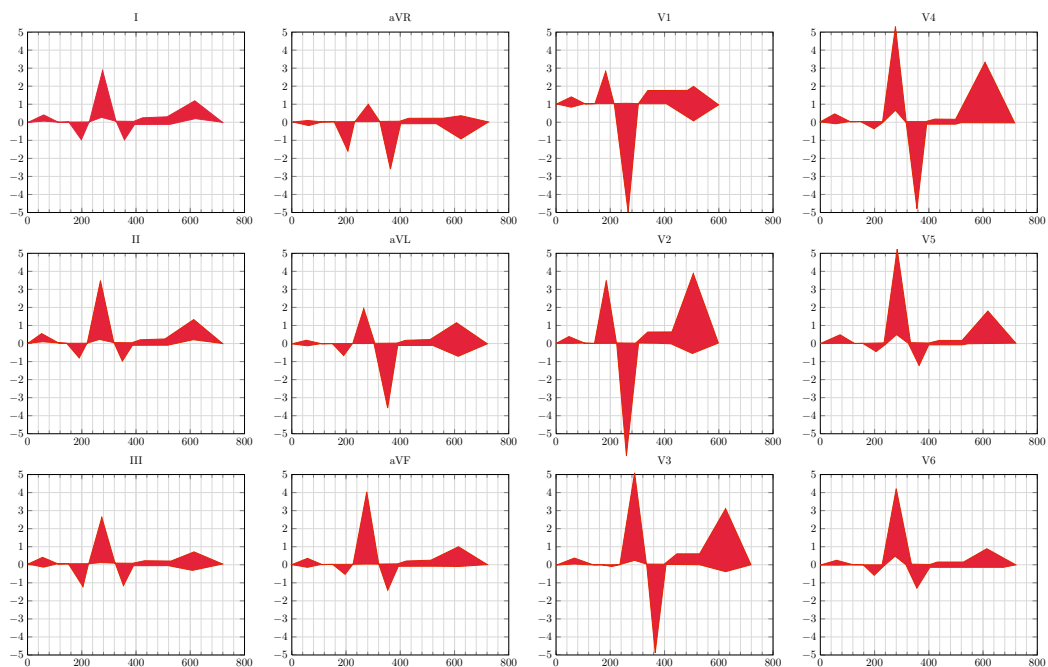


Figure 2.10: Typical variations of amplitude measurements in adults healthy ECG [War75].

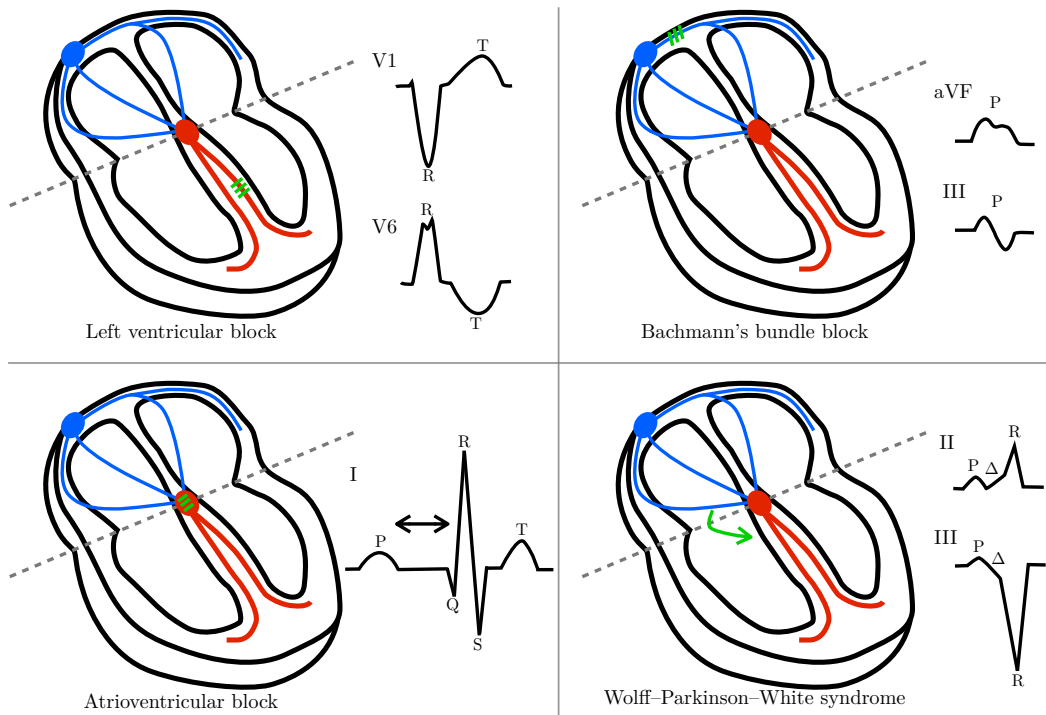


Figure 2.11: Different pathologies.

2.4.2.1 Left and right ventricular block

We start with a left or a right bundle branch block. In a healthy case, the right and the left ventricles are activated simultaneously. Now, in order to simulate a left (or a right) bundle branch block, the initial activation is blocked in the left (resp. right) ventricle. In the top-left of Figure 2.11, we can see a left ventricular block. In order to obtain a left (resp. right) bundle branch block, the depolarization of the left (resp. right) Purkinje fibers is delayed as indicated in [BCF⁺10]. Results are reported in Figure 2.12 for the left and right bundle branch blocks. We recognize the main characteristics reported in the medical literature: larger QRS, lead V1 without Q-wave [MP95], leads V1 and V6 similar to those presented in Figure 2.11 (top left). The QRS-complex exceeds 0.12 seconds in both cases. Furthermore, it can be seen in Figure 2.12 that the duration between the beginning of the QRS complex and its last positive wave in V1 (resp. V6) exceeds 0.04 seconds which is a known sign of right (resp. left) bundle branch block [MP95].

2.4.2.2 Bachmann's bundle block

In the heart conduction system, the Bachmann's bundle connects the left atrium with the right atrium and is the preferential path for the electrical activation of the left atrium. A Bachmann's bundle block is represented at the top-right of Figure 2.11. It is characterized by the presence of P-wave duration that equals or exceeds 0.12 seconds and presents usually a bimodal morphology, especially in leads I, II, aVF

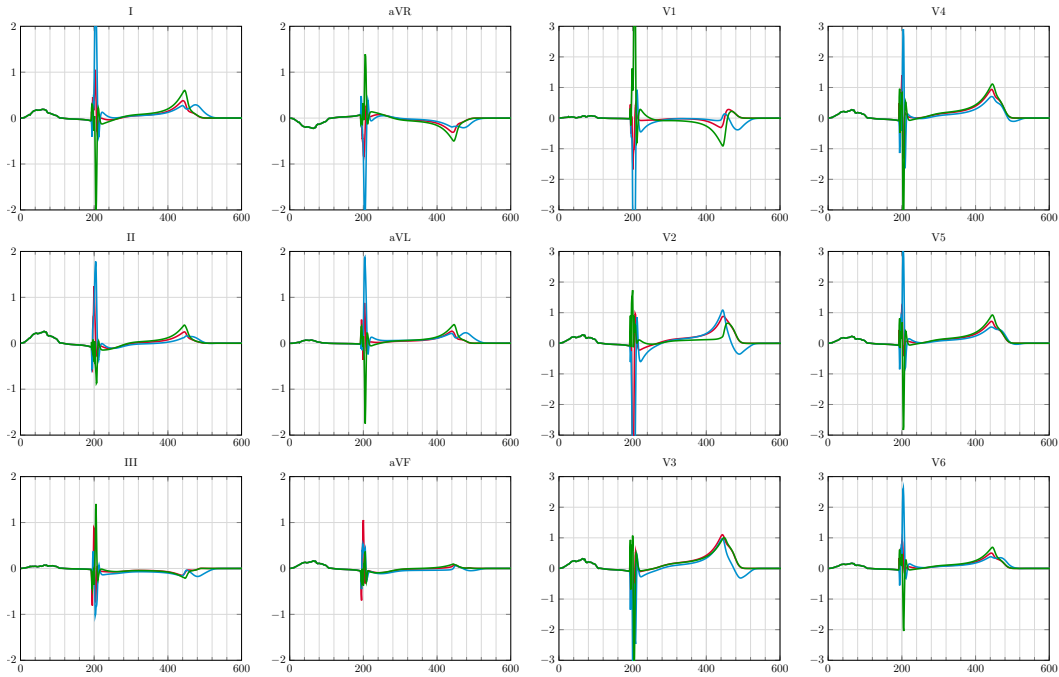


Figure 2.12: Left and Right Bundle Branch Block, see Section 2.4.2.1 – Healthy case in red, LBBB in blue and RBBB in green (voltages (mV) versus time (ms)).

and the lead III becomes biphasic, as we can see in Figure 2.11. This is a very specific sign of left atrial enlargement [Net69, MP95]. We simulate it by decreasing the maximal conductance $g_{Na} = 7.8$ in the Bachmann's bundle. The results are given in Figure 2.13. The more important the block, the more negative the P wave on lead III. A negative P wave in the third lead corresponds to the retrograde depolarization of the left atrium. The morphology of the simulated P wave is in very good agreement with the criteria given in [BdLGVn+99, BdLPC+12] for various degrees of Bachmann's bundle blocks.

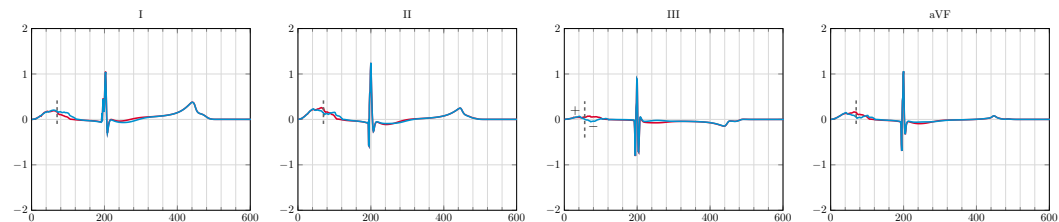


Figure 2.13: A Bachmann's Bundle Block, see Section 2.4.2.2 – Healthy case in red, BBB in blue (voltages (mV) versus time (ms)).

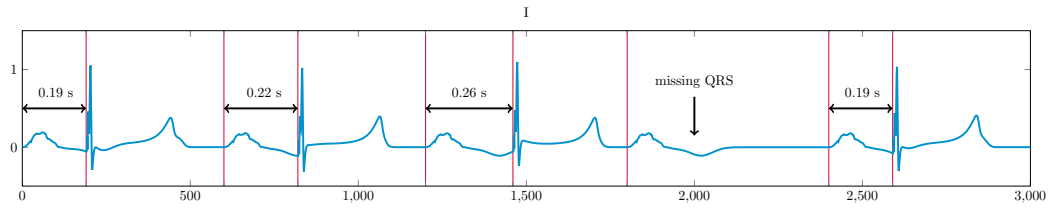


Figure 2.14: Wenckebach atrioventricular block (voltages (mV) versus time (ms)), see Section 2.4.2.3.

2.4.2.3 Atrioventricular block

An atrioventricular block (or AV block) is a damage of the conduction between atria and ventricles. Under normal conduction, the atrioventricular node is activated by the atrial wave and it delays the activation by approximately 0.12 seconds. This delay is extremely important since it allows the atria to eject all their blood into the ventricles before the ventricular contraction. The bottom-left of Figure 2.11 represents an atrioventricular block. There are different degrees and types of atrioventricular blocks [MP95]. We consider here a Wenckebach atrioventricular block. To obtain it, we progressively increase the ventricular activation time: the delay between atrial and ventricular stimulus is 190 ms in the first beat, 220 ms in the second one, 260 ms in the third one, and at the fourth beat the ventricles are not stimulated at all. The Wenckebach block is characterized by a progressive prolongation of the PR interval on consecutive beats followed by a blocked P wave. After the missing QRS complex, the PR interval resets and the cycle repeats. Figure 2.14 correctly represents these features.

2.4.2.4 Wolff-Parkinson-White syndrome

The Wolff-Parkinson-White syndrome is one of the numerous pathologies of the conduction system of the heart. It corresponds to a pre-excitation syndrome and is caused by the presence of an abnormal electrical conduction pathway between the atria and the ventricles, named the Kent bundle. Electrical signals travel down this abnormal pathway and may stimulate the ventricles prematurely. In the bottom-right of Figure 2.11, we can see a schematic of the Wolff-Parkinson-White syndrome. We model the abnormal pathway by stimulating a ventricle area near of the atria represented at the right of Figure 2.4. The Wolff-Parkinson-White syndrome is commonly diagnosed with the electrocardiogram [RBKM99]. It is characterized by a delta wave, a slurring of the initial segment of the QRS complex, due to the arrival of the impulses at ventricles via the abnormal route, which is associated with a short PR interval. Another feature is a QRS complex widening with a total duration greater than 0.12 seconds. We can indeed observe these characteristics, in particular the delta wave in Figure 2.15.

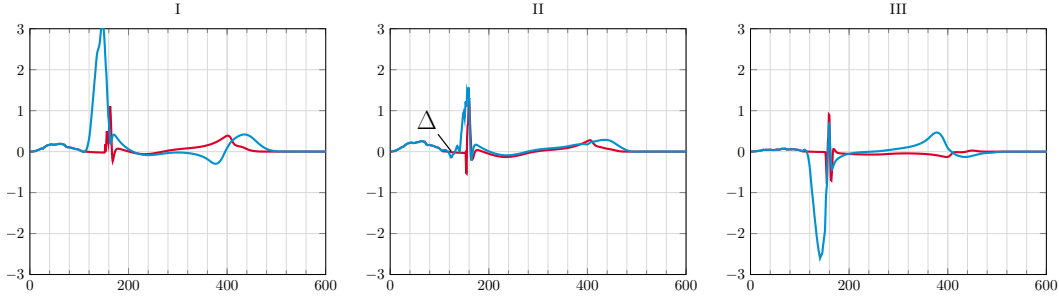


Figure 2.15: Wolff-Parkinson-White syndrome, see Section 2.4.2.4 – Healthy case in red and WPW in blue (voltages (mV) versus time (ms)).

τ_{in}	τ_{out}	τ_{open}	τ_{close}^{endo}	τ_{close}^{Mcell}	τ_{close}^{epi}	τ_{close}^{RV}	V_{min}	V_{max}	V_{gate}
4.0	90.0	300.0	120.0	100.0	80.0	90.0	-80.0	20.	-67.0

Table 2.9: Mitchell and Schaeffer parameters and constants (different values of τ_{close} are given because of an heterogeneous tissue is considered, see [BCF⁺10]).

2.4.3 Comparison with the Mitchell-Schaeffer model

In this section we are interested in the impact of the ionic model on the ECG simulation. The membrane current are now described with the Mitchell-Schaeffer model [MS03] which is a one-current phenomenological ionic model, offering interesting properties with a very limited number of parameters. Equations are reported in Appendix 2.A.

The Mitchell-Schaeffer model is applied with the same conductivity parameters (except for some atrial areas, see below) and the same initial stimulus as described above. Table 2.9 gives the value of the Mitchell-Schaeffer parameters, with the scaling used in [BCF⁺10]. In order to correctly reproduce the T wave, we take into account three layers of cells in the left ventricles and an homogeneous tissue in the right ventricle as described in Section 2.3.3. The τ_{close} parameter varies according to the type of cell (Table 2.9). On the atria surface, the repolarization “propagates” in the same direction as the depolarization. We therefore take a constant value for τ_{close} , equals to 100 ms. As previously explained, we changed the values of the maximal

	regular tissue	PM	CT	BB	FO
$\sigma_i^{a,t}$	$2.5 \cdot 10^{-4}$	$4.5 \cdot 10^{-4}$	$7.5 \cdot 10^{-4}$	$1.19 \cdot 10^{-3}$	$2.5 \cdot 10^{-4}$
$\sigma_e^{a,t}$	$9.0 \cdot 10^{-4}$	$1.35 \cdot 10^{-3}$	$2.7 \cdot 10^{-3}$	$4.3 \cdot 10^{-3}$	$9.0 \cdot 10^{-4}$
$\sigma_i^{a,l}$	$2.5 \cdot 10^{-3}$	$4.5 \cdot 10^{-3}$	$1.09 \cdot 10^{-2}$	$1.86 \cdot 10^{-2}$	$2.27 \cdot 10^{-3}$
$\sigma_e^{a,l}$	$2.5 \cdot 10^{-3}$	$4.5 \cdot 10^{-3}$	$1.09 \cdot 10^{-2}$	$1.86 \cdot 10^{-2}$	$2.27 \cdot 10^{-3}$

Table 2.10: Atrial conductivity parameters (all in $S.cm^{-1}$) for the Mitchell-Schaeffer model.

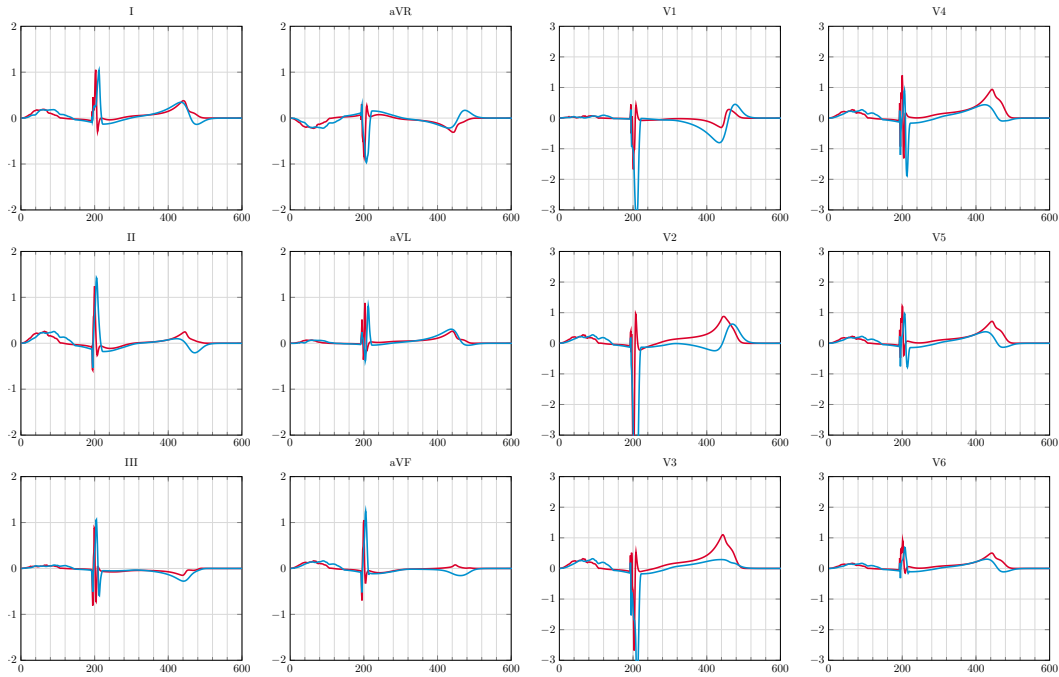


Figure 2.16: ECGs obtained with different ionic models – Courtemanche/MV ionic model in red and Mitchell and Schaeffer model in blue (voltages (mV) versus time (ms)).

conductance g_{Na} in the different atrial areas in the Courtemanche-Ramirez-Nattel model in order to take into account these bundles. The Mitchell-Schaeffer model does not allow the same flexibility then we decide to directly modify the value of conductivity parameters. The atrial conductivities are modified as reported in Table 2.10 in order to represent the different slow and fast bundles.

Figure 2.16 shows the ECGs obtained with the Mitchell and Schaeffer (MS) model and the combined Courtemanche/MV model. We can see that the results are reasonably close. With the MS model some oscillations in the P wave and the QRS complex are fixed, but the R wave progression in precordial leads is less precise and the T wave of V2 and V3 is not satisfactory. It is interesting to note that the results of the simulations are robust with respect to the choice of the ionic model: the Courtemanche/MV model in general gives better results, but it can be replaced by the MS model in order to reduce the computational costs and the model complexity without affecting too much the ECG. This remark is especially important if the ECG simulator has to be used for inverse problems as presented for instance in Chapters 4 and 5: in that case, a model with a reduced number of parameters may be more attractive.

2.5 Electrodes vest

In the previous sections, we focused on the 12-lead ECG because it is widely used in practice, and it can be easily assessed with the medical literature. But our simulator can of course provide more sophisticated measurements, like those obtained with electrode vests.

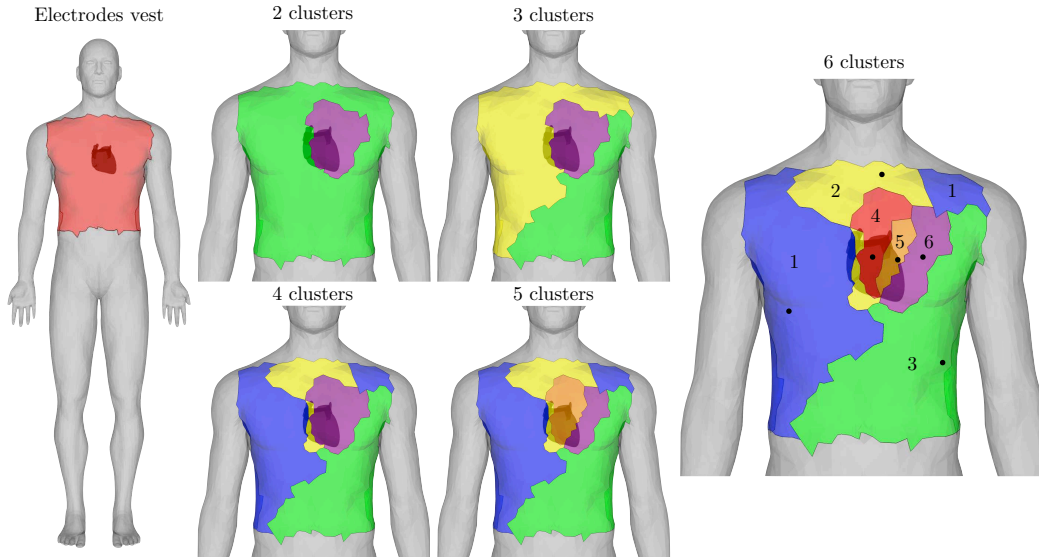


Figure 2.17: Human body mesh, “electrode vest”(left) and clustering results (right). From left-top to right-bottom clustering agglomeration, from 2 to 6 clusters.

Many studies have been carried out on this topic: on the forward problem and the analysis of the number of electrodes, see for instance [HG97, HUvO99]); on the inverse problem of reconstruction of the potential on the heart surface, see for instance [PBC05, SLN⁺06]. Our objective here is less ambitious: we just show an example of a statistical analysis that can be done with the measures provided by our ECG simulator.

To do so, we simulate a virtual “electrode vest” which contains $N_{ECG} = 1,216$ electrodes. Figure 2.17 (left) shows the measures points which are all the nodes of the mesh in the red region of the torso. The heart geometry used in this study contains $N_{\partial\Omega_H} = 28,510$ boundary vertices. We compute the body surface potential as described in Section 2.3.

We are interested in analyzing the electrode signals with respect to their positions on the body. In order to divide the signals into different groups, an agglomerative hierarchical clustering analysis is applied to the 1,216 measures. Clustering is a statistical technique used to classify data based on *similarities*, or *distances*, between them. In particular, in agglomerative hierarchical clustering method, at the beginning each individual (data) represents a group itself. Then, these groups are merged together according to their decreasing distance. The procedure is schematized in

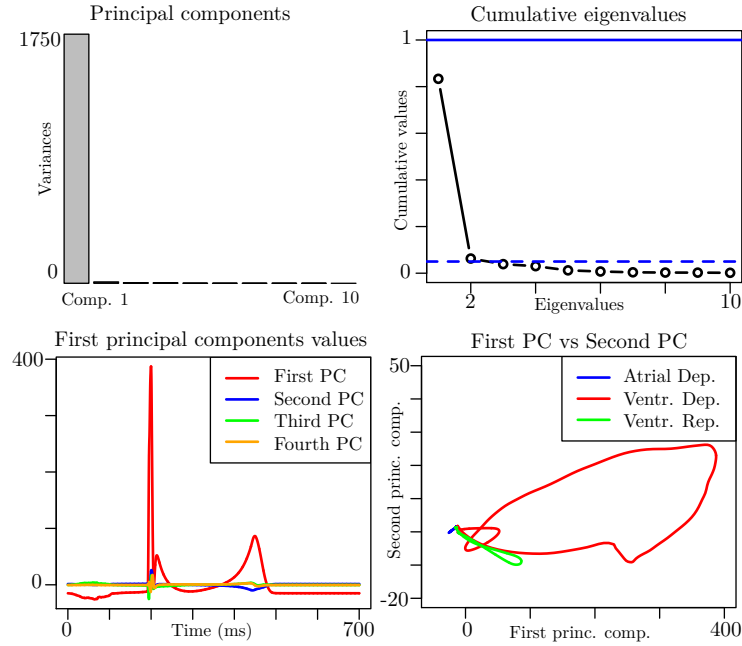


Figure 2.18: Principal components analysis on electrode vest signals.

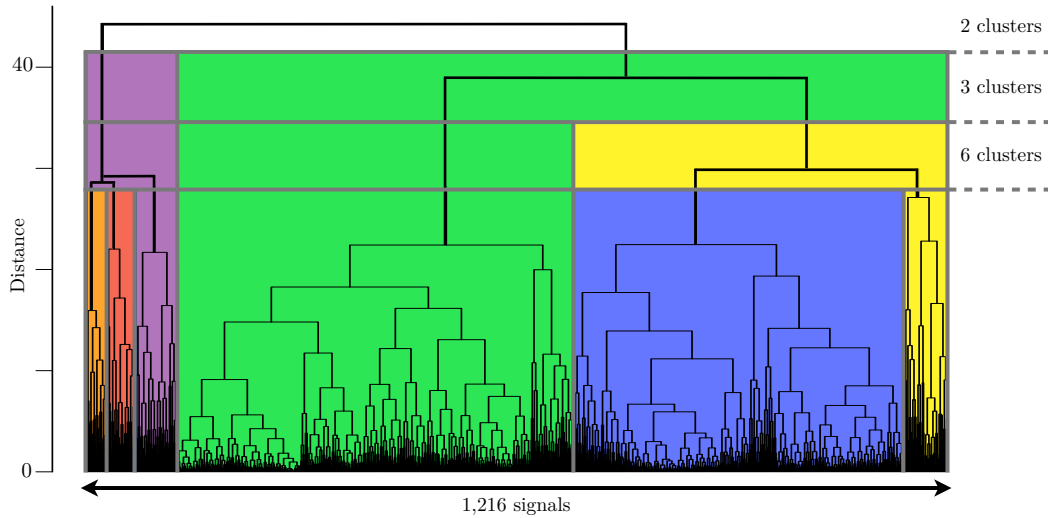


Figure 2.19: Clustering agglomeration of electrodes measures potential using euclidean distance and complete linkage. Colors represent the clusters of points as shown in Figure 2.17.

Figure 2.19: the bottom of the clustering tree represents the 1,216 signals, the top represents a unique group. In order to measure the similarity between data, an Euclidean distance is used

$$\text{dist}(V_i, V_j) = \sqrt{\sum_n (V_i(t^n) - V_j(t^n))^2} \tag{2.12}$$

where V_i , $i = 1, \dots, 1216$, represents an electrode signal. Last, we need to define a *linkage* method, *i.e.* the criteria used to merge groups. Here we use a *complete* linkage, *i.e.* the distance between two groups is defined as the maximal distance between the data of the first group and the data of the second one

$$\text{dist}(C_i, C_j) = \max_{k,h} (\text{dist}(\{V_k \in C_i\}, \{V_h \in C_j\})) \quad (2.13)$$

where C_i represents the i -th cluster. For further details on the clustering analysis we refer for instance to [JW07].

In Figure 2.17 we show the agglomeration procedure from 2 to 6 clusters. First, the division into two clusters indicates a separation between the heart region (purple area of Figure 2.17) and the rest of the vest (green region). Second, a division into 2 parts underlies the atria-ventricular axes (separation of green and yellow zones). Then, we can see from the clustering agglomeration plot of Figure 2.19, that the separations into 4, 5 and 6 groups (blue, orange and red areas) are made at very closed distances. The last subdivision we consider is made of 6 groups. In Figure 2.20 we plot the signals belonging to the 6 clusters and their center values. The center values of each cluster are computed as the point minimizing the distance between itself and the other points of the cluster

$$m_i = \arg \min_j \left(\sum_k \text{dist}(V_j, V_k) \right), \quad \forall i. \quad (2.14)$$

Then, we re-apply the principal components decomposition on the 6 centers of the cluster, the points indicated in Figure 2.17 (right). Comparing results of Figure 2.21 with Figure 2.18 we observe that the first principal component is again much larger than the other ones, and the same curves represent the first, second and third principal components.

The two approaches – the principal components decomposition and the hierarchical clustering analysis – suggest that it is not necessary to have a very high number of skin electrodes to describe the body surface potential. It seems that a limited number of correctly positioned electrodes would be enough to represent most of the features of the signal. A deeper analysis of the number and the locations of the electrode goes beyond the scope of this study. The purpose here was just to illustrate that our simulator could be used to generate more general signals than the standard 12-lead ECGs.

2.6 Chapter conclusions

We have presented a comprehensive model for the simulation of full cycle ECGs. The main ingredients are: volume bidomain equations in the ventricles with the MV ionic model, surface bidomain equations in the atria with the Courtemanche ionic model, a one-way coupling between the heart and the torso through a resistor transmission condition.

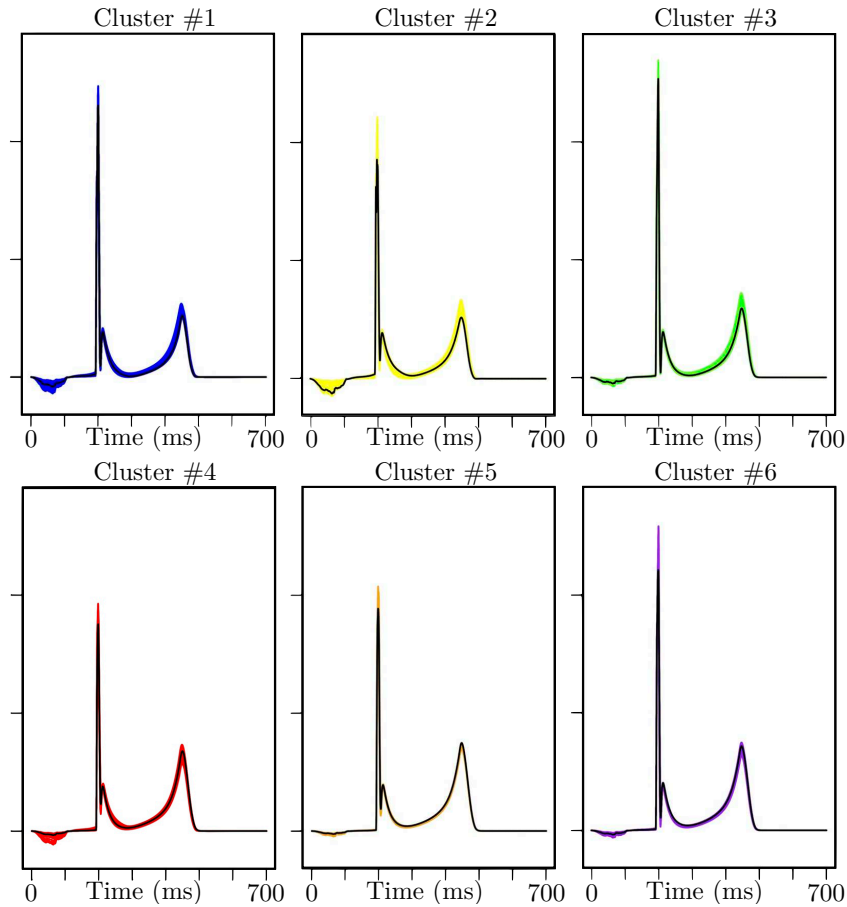


Figure 2.20: Signals in different clusters as shown in Figure 2.17(right). Black lines indicate the “mean” point (points of Figure 2.17(right)).

This modeling effort has provided a healthy ECG whose quality can be assessed with several qualitative and quantitative criteria reported in the medical literature. Four pathological cases have been investigated: left and right bundle branch blocks, Bachmann’s bundle block, AV block and Wolff-Parkinson-White syndrome. In the healthy case, we have shown that similar results could be obtained with the one-current phenomenological ionic model proposed by Mitchell and Schaeffer.

This work can be improved in different directions. More physiological model of the atrio-ventricular node and the Purkinje fibers could be included. A strong coupling with the torso could be done to assess the impact of the isolated heart assumption. The electromechanical simulations presented in [CFG⁺09] could be extended to include the atria and performed with the present electrical model of the heart.

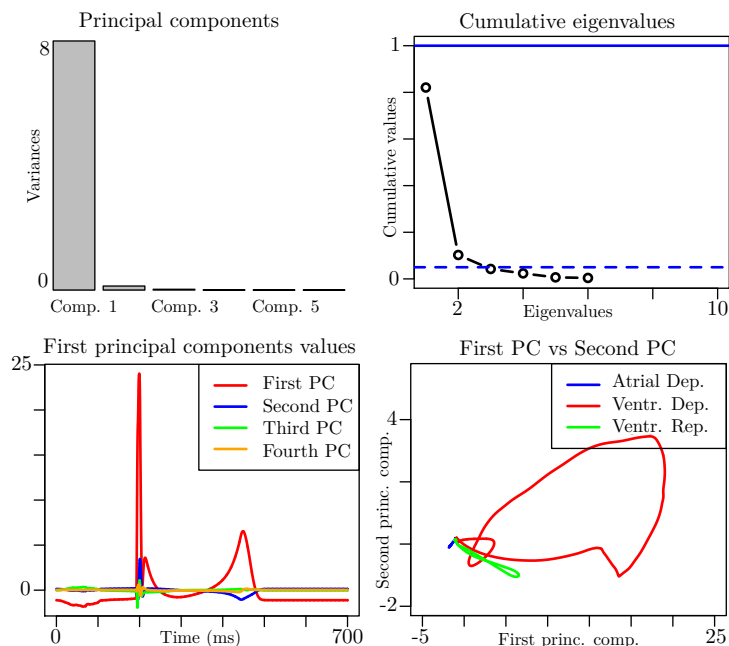


Figure 2.21: Principal components analysis on 6 electrodes signals.

2.A Mitchell and Schaeffer ionic model [MS03]

We report here the Mitchell and Schaeffer ionic model [MS03] used in Section 2.4.3. A detailed description of this phenomenological one-current model is given in Section 1.4.2. Some equations properties linked to the study of restitution curves are illustrated in Chapter 5. Also, it is used in many parts of this thesis work, for instance in Chapter 4 in order to simulate a myocardial infarction and to the related parameters investigation.

The Mitchell and Schaeffer equations read

$$I_{\text{ion}}(v, w) = w \frac{v^2(1-v)}{\tau_{\text{in}}} - \frac{v}{\tau_{\text{out}}}$$

$$\frac{dw}{dt} = \begin{cases} \frac{1-w}{\tau_{\text{close}}}, & v \leq v_{\text{gate}} \\ -\frac{w}{\tau_{\text{open}}}, & v > v_{\text{gate}} \end{cases} \quad (2.15)$$

Concerning this Chapter, the parameters used are given in Table 2.9.

2.B Minimal model for human Ventricular action potentials (MV) [BOCF08]

Dealing with the ventricular part of the mesh, in this Chapter we used the *Minimal model for human Ventricular action potentials* (MV) [BOCF08]. The MV model is a phenomenological model, more accurate than the Mitchell and Schaeffer one, and it has been adapted to the ventricular tissue including midmyocardial, epicardial and endocardial cells. It is associated with three ionic currents, J_{fi} , J_{so} and J_{si} , and three gate variables, v , w , s , and governed by 28 parameters.

The ionic current I_{ion} is given by the sum of the currents

$$I_{\text{ion}} = J_{\text{fi}} + J_{\text{so}} + J_{\text{si}}. \quad (2.16)$$

The currents are defined by

$$\begin{aligned} J_{\text{fi}} &= -H(u - \theta_v)(u - \theta_v)(u_u - u) \frac{v}{\tau_{\text{fi}}}, \\ J_{\text{so}} &= (1 - H(u - \theta_w)) \frac{u - u_o}{\tau_o} + \frac{H(u - \theta_w)}{\tau_{\text{so}}}, \\ J_{\text{si}} &= -H(u - \theta_w) \frac{ws}{\tau_{\text{si}}}, \end{aligned} \quad (2.17)$$

where u is the transmembrane potential, $H(x)$ is the standard Heaviside function and the gate variables are solution of the equation system

$$\begin{aligned} \partial_t v &= (1 - H(u - \theta_v)) \frac{v_\infty - v}{\tau_v^-} - H(u - \theta_v) \frac{v}{\tau_v^+}, \\ \partial_t w &= (1 - H(u - \theta_w)) \frac{w_\infty - w}{\tau_w^-} - H(u - \theta_w) \frac{w}{\tau_w^+}, \\ \partial_t s &= \frac{(1 + \tanh(k_s(u - u_s))) / 2 - s}{\tau_s}. \end{aligned} \quad (2.18)$$

Several parameters depends on the voltage variable u and are defined by

$$\begin{aligned} \tau_v^- &= (1 - H(u - \theta_v^-)) \tau_{v_1}^- + H(u - \theta_v^-) \tau_{v_2}^-, \\ \tau_w^- &= \tau_{w_1}^- + (\tau_{w_2}^- - \tau_{w_1}^-) (1 + \tanh(k_w^-(u - u_w^-))) / 2, \\ \tau_{\text{so}} &= \tau_{\text{so}_1} + (\tau_{\text{so}_2} - \tau_{\text{so}_1}) (1 - \tanh(k_{\text{so}}(u - u_{\text{so}}))) / 2, \\ \tau_s &= (1 - H(u - \theta_w)) \tau_{s_1} + H(u - \theta_w) \tau_{s_2}, \\ \tau_o &= (1 - H(u - \theta_o)) \tau_{o_1} + H(u - \theta_o) \tau_{o_2}, \end{aligned} \quad (2.19)$$

and the infinity values are given by

$$\begin{aligned} v_\infty &= \begin{cases} 1, & u < \theta_v^- \\ 0, & u \geq \theta_v^- \end{cases} \\ w_\infty &= (1 - H(u - \theta_o)) (1 - u / \tau_{w_\infty}) + H(u - \theta_o) w_\infty^*. \end{aligned} \quad (2.20)$$

The rest of the parameters are given in Table 2.11.

	EPI	ENDO	M
u_o	0	0	0
u_u	1.55	1.56	1.61
θ_v	0.3	0.3	0.3
θ_w	0.13	0.13	0.13
θ_v^-	0.006	0.2	0.1
θ_o	0.006	0.006	0.005
τ_{v1}^-	60	75	80
τ_{v2}^-	1150	10	1.4506
τ_v^+	1.4506	1.4506	1.4506
τ_{w1}^-	60	6	70
τ_{w2}^-	15	140	8
k_w^-	65	200	200
u_w^-	0.03	0.016	0.016
τ_w^+	200	280	280
τ_{fi}	0.11	0.1	0.078
τ_{o1}	400	470	410
τ_{o2}	6	6	7
τ_{so1}	30.0181	40	91
τ_{so2}	0.9957	1.2	0.8
k_{so}	2.0458	2	2.1
u_{so}	0.65	0.65	0.6
τ_{s1}	2.7342	2.7342	2.7342
τ_{s2}	16	2	4
k_s	2.0994	2.0994	2.0994
u_s	0.9087	0.9087	0.9087
τ_{si}	1.8875	2.9013	3.3849
$\tau_{w\infty}$	0.07	0.0273	0.01
w_∞^*	0.94	0.78	0.5

Table 2.11: Parameters for MV model as reported in [BOCF08]. In the numerical simulations of this Chapter, the parameter τ_{so1} is modified as indicated in Table 2.5.

2.C Courtemanche, Ramirez and Nattel ionic model [CRN98]

The Courtemanche–Ramirez–Nattel (CRN) model [CRN98] is a physiological model described by 12 ionic currents and 20 other variables. The model has been developed in order to describe the human atrial action potentials properties.

The general formulation reads

$$I_{\text{ion}} = I_{\text{Na}} + I_{\text{K}_1} + I_{\text{to}} + I_{\text{Kur}} + I_{\text{Kr}} + I_{\text{Ks}} + I_{\text{Ca,L}} + I_{\text{p,Ca}} + I_{\text{NaK}} + I_{\text{NaCa}} + I_{\text{b,Na}} + I_{\text{b,Ca}}, \quad (2.21)$$

where each term of the I_{ion} describes a ionic or pump current. In particular, I_{Na} represents the fast Na^+ current, I_{K^+} represents the Inward rectifier K^+ current, I_{to} and I_{Kur} respectively are the implementations of the Transient outward and the Ultrarapid rectifier K^+ currents, the terms I_{Kr} and I_{Ks} implement respectively the rapid and the slow delayed rectifier K^+ currents, $I_{\text{Ca,L}}$ is the L-type slow inward Ca^{2+} current, I_{NaK} gives the Na^+ – K^+ pump and I_{NaCa} the Na^+ / Ca^{2+} exchanger current. For the rest of the currents, their definitions and the PDEs governing the model, we invite to refer to the original formulation in [CRN98].

A schematic representation of currents, pumps and exchanges is given in Figure 2.22. Three intracellular compartments are included: myoplasm, sarcoplasmic reticulum (SR) release compartment and SR uptake compartment. The main parameters are given in Table 2.12.

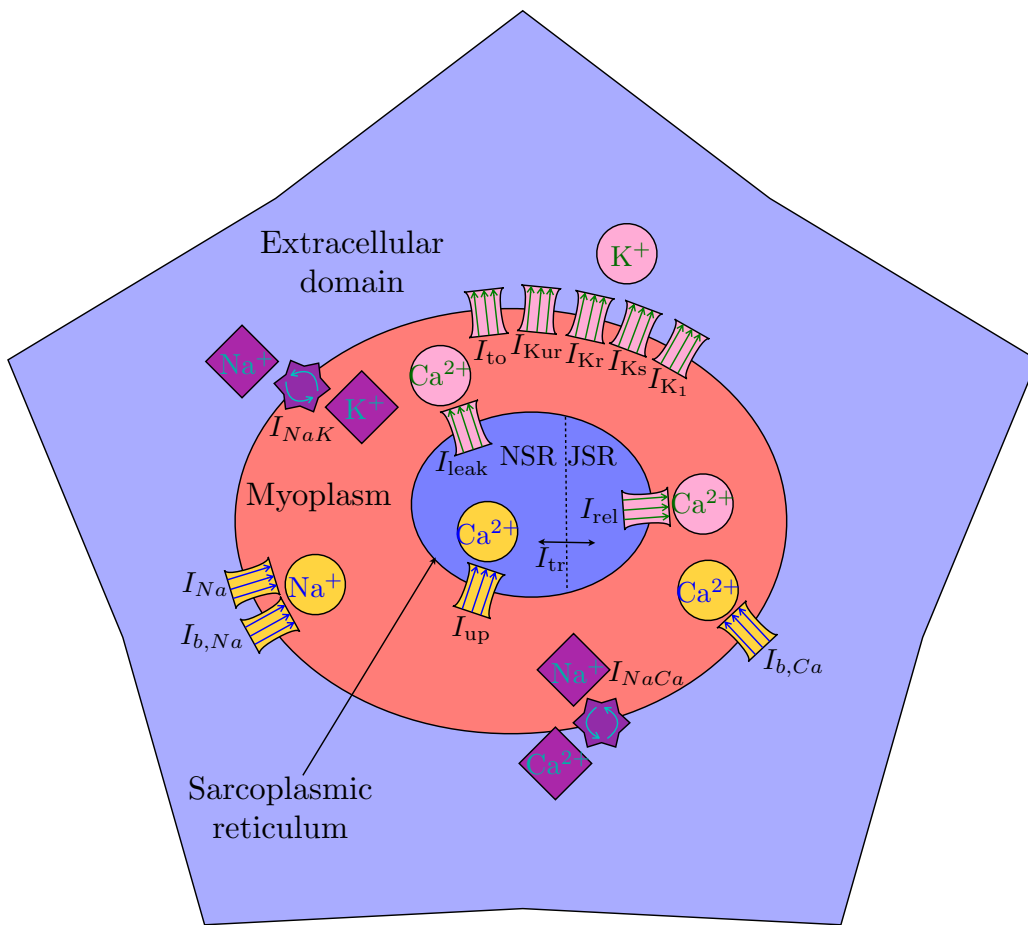


Figure 2.22: Schematic representation of Courtemanche, Ramirez and Nattel ionic model [CRN98]. Inspired from [Col14].

	Definition	Value
V_{cell}	Cell volume	20,100 μm^3
V_i	Intracellular volume	13,668 μm^3
V_{up}	SR uptake compartment volume	1,109.52 μm^3
V_{rel}	SR release compartment volume	96.48 μm^3
$[\text{K}^+]_o$	Extracellular K^+ concentration	5.4 mM
$[\text{Na}^+]_o$	Extracellular Na^+ concentration	140 mM
$[\text{Ca}^{2+}]_o$	Extracellular Ca^{2+} concentration	1.8 mM
g_{Na}	Maximal I_{Na} conductance	7.8 nS/pF
g_{K_1}	Maximal I_{K_1} conductance	0.09 nS/pF
g_{to}	Maximal I_{to} conductance	0.1652 nS/pF
g_{Kr}	Maximal I_{Kr} conductance	0.0294 nS/pF
g_{Ks}	Maximal I_{Ks} conductance	0.129 nS/pF
$g_{\text{Ca,L}}$	Maximal $I_{\text{Ca,L}}$ conductance	0.1238 nS/pF
$g_{\text{b,Ca}}$	Maximal $I_{\text{b,Ca}}$ conductance	0.00113 nS/pF
$g_{\text{b,Na}}$	Maximal $I_{\text{b,Na}}$ conductance	0.000674 nS/pF
$I_{\text{NaK(max)}}$	Maximal I_{NaK}	0.60 pA/pF
$I_{\text{NaCa(max)}}$	Maximal I_{NaCa}	1,600 pA/pF
$I_{\text{p,Ca(max)}}$	Maximal $I_{\text{p,Ca}}$	0.275 pA/pF
$I_{\text{up(max)}}$	Maximal I_{up}	0.005 mM/ms
$K_{\text{Q}_{10}}$	Temperature scaling factor for I_{Kur} and I_{to} kinetics	3
γ	Voltage dependence parameter for I_{NaCa}	0.35
$K_{\text{m,Na(i)}}$	$[\text{Na}^+]_i$ half-saturation constant for I_{NaK}	10 mM
$K_{\text{m,K(o)}}$	$[\text{K}^+]_o$ half-saturation constant for I_{NaK}	1.5 mM
$K_{\text{m,Na}}$	$[\text{Na}^+]_o$ half-saturation constant for I_{NaCa}	87.5 mM
$K_{\text{m,Ca}}$	$[\text{Ca}^{2+}]_o$ half-saturation constant for I_{NaCa}	1.38
k_{sat}	Saturation factor for I_{NaCa}	0.1
k_{del}	Maximal release rate for I_{rel}	30 ms^{-1}
K_{up}	$[\text{Ca}^{2+}]_i$ half-saturation constant for I_{up}	0.00092 mM
$[\text{Ca}^{2+}]_{\text{up(max)}}$	Maximal Ca^{2+} concentration in uptake compartment	15 mM
$[\text{Cmdn}]_{\text{max}}$	Total calmodulin concentration in myoplasm	0.05 mM
$[\text{Trpn}]_{\text{max}}$	Total troponin concentration in myoplasm in myoplasm	0.07 mM
$[\text{Csqn}]_{\text{max}}$	Total calsequestrin concentration in SR release compartment	10 mM
$K_{\text{m,Cmdn}}$	$[\text{Ca}^{2+}]_i$ half-saturation constant for calmodulin	0.00238 mM
$K_{\text{m,Trpn}}$	$[\text{Ca}^{2+}]_i$ half-saturation constant for troponin	0.0005 mM
$K_{\text{m,Csqn}}$	$[\text{Ca}^{2+}]_{\text{rel}}$ half-saturation constant for I_{up}	0.8 mM

Table 2.12: Parameters for CRN model as reported in [CRN98]. In the numerical simulations of this Chapter, the maximal conductance g_{Na} is modified as indicated in Table 2.4.

Theoretical study of the estimate of some parameters of the FitzHugh-Nagumo ionic model

In this chapter, we derive some stability estimations linked to the identification of parameters in models of cardiac electrophysiology. In particular, we deal with the monodomain equations coupled with the FitzHugh-Nagumo ionic model. First, we present some results on the regularity of the solution. Second, we study the estimation of some reaction parameter which appears in the definition of the ionic current, and the estimation of some parameter in the second equation.

The results presented in this chapter lead to the manuscript
Muriel Boulakia, Elisa Schenone, **Theoretical study of the estimate of some
FitzHugh-Nagumo model parameters**, To be submitted.

Contents

3.1	Introduction	81
3.2	State of the art and motivation	81
3.3	Regularity of the solution	83
3.4	Estimation of reaction parameter	88
3.5	Estimation of a parameter in the second equation	92
3.6	Chapter conclusions	96

3.1 Introduction

We are concerned with the estimation of some parameters of the Monodomain equations previously described in Section 1.4.1. Let Ω be a bounded and regular domain in dimension 3. We define $Q = (0, T)$ where $T > 0$ is fixed. The monodomain equations read

$$\begin{cases} A_m(C_m u_t + I_{\text{ion}}(u, w)) - \text{div}(\sigma_m \nabla u) = A_m I_{\text{app}}, & Q \\ w_t + f(u, w) = 0, & Q \\ u(t=0) = u_0, & \Omega \\ w(t=0) = w_0, & \Omega \end{cases} \quad (3.1)$$

with homogeneous Dirichlet boundary conditions

$$u = 0, \quad (0, T) \times \partial\Omega$$

coupled with the FitzHugh-Nagumo ionic model [Fit61, NAY62]

$$\begin{cases} I_{\text{ion}}(u, w) = ku(u - a)(u - 1) + w \\ f(u, w) = \beta w - \gamma u \end{cases} \quad (3.2)$$

where u denotes the transmembrane potential and w the ionic variable.

In particular, we first introduce the problem which motivates our study, give some definitions and the state of the art concerning equations system similar to the Monodomain model (3.1). Then some regularity results on the solution of (3.1) are given. At last, we look for an estimation of the reaction parameter k of the first equation of (3.2) and an estimation of the parameter γ of the second one.

3.2 State of the art and motivation

Let us write the Monodomain equations coupled with Fitzhugh-Nagumo ionic model on Q under the form

$$\begin{cases} u_t - \Delta u = kg(u) - w, & Q \\ w_t = \gamma u - \beta w, & Q \\ u = 0, & (0, T) \times \partial\Omega \\ u(t=0) = u_0, & \Omega \\ w(t=0) = w_0, & \Omega \end{cases} \quad (3.3)$$

where

$$g(u) = u(u - a)(1 - u). \quad (3.4)$$

Let us assume that there exists $u_{\min} > 0$ such that

$$u(t, x) \geq u_{\min}, \quad \forall (t, x) \in Q. \quad (3.5)$$

Also, we assume that k, γ, β are parameters which only depend on space and satisfy

$$0 < a(x) < 1, \quad k(x) > 0, \quad \gamma(x) > 0, \quad \beta(x) > 0, \quad \forall x \in \overline{\Omega}, \quad (3.6)$$

$k, \gamma, \beta \in L^\infty(\Omega)$, and that there exists $M > 0$ such that

$$\|k\|_{L^\infty(\Omega)} + \|\gamma\|_{L^\infty(\Omega)} + \|\beta(x)\|_{L^\infty(\Omega)} \leq M. \quad (3.7)$$

In this work we are interested in the estimation of some parameters of the ionic model, in particular k and γ , using the measure of the solution on a small domain or for a fixed time. The inverse problem of parameter identification is then solved with different techniques in the next chapters.

The solution of the second equation can be easily written as

$$w(t, x) = w_0(x)e^{-t\beta(x)} + \int_0^t \gamma(x)u(\tau, x)e^{-\tau\beta(x)}d\tau. \quad (3.8)$$

Thus, the first equation of (3.3) may be viewed as a reaction-diffusion equation with a memory term. Even in the linear case, having a memory term may lead to difficulties in the theory of control and inverse problems.

In [GI13] the *null controllability* of heat equations with memory is studied. In particular, [GI13] deals with a system of type

$$\begin{cases} y_t - \Delta y + \int_0^t y d\tau = 0, & Q \\ y = v, & (0, T) \times \partial\Omega \\ y(t = 0) = y_0, & \Omega \end{cases} \quad (3.9)$$

where $v \in L^2((0, T) \times \Omega)$ is a control function acting on the boundary of the system. The *null controllability* property for system (3.9) reads as follows: given $y_0 \in L^2(\Omega)$, there exists a control $v \in L^2((0, T) \times \partial\Omega)$ such that the corresponding solution of (3.9) satisfies $y(T, \cdot) \equiv 0$ in $L^2(\Omega)$. It is well-known from literature (see for instance [FI96, Ima95]) that the heat equation satisfies the property of *null controllability*, while in [GI13] it is proved that the property is not satisfied for a memory system such as (3.9). This is due to the fact that the observability inequality does not hold for this system. As we will see, the inequality is also a key point to prove stability estimates to identify some parameters of the model.

A related problem is addressed in [CSRZ14] where the null controllability of a model of viscoelasticity consisting of a wave equation with viscous Kelvin-Voigt and frictional damping is studied with a control acting on tie. The solution of this problem can be written as the first component of the solution of the following system of equations

$$\begin{cases} y_t - \Delta y + (b-1)y = z, & Q \\ z_t + z = 1_{\omega(t)}h + (b-1)y, & Q \end{cases} \quad (3.10)$$

where $b \in L^\infty(\Omega)$ is the frictional damping, $h = h(t, x)$ is the control and $\omega(t)$, for any $0 < t < T$, is a subset of Ω where the control is applied. Thus, this system corresponds to the coupling of a linear parabolic equation and an ODE. If the control domain is fixed, then the controllability result does not hold. This is due to the presence of the ODE which induces a lack of propagation in space-like direction. Thus, the authors consider a control with support which covers the whole domain Ω and get an observability inequality for the coupled system (3.10).

Due to these remarks, it would not be possible to derive a global observability inequality for our coupled system (3.3). However we will see that we can get stability estimates for the identification of some parameters of the model.

Getting a global inequality for the monodomain equation coupled with an ODE would have allowed to prove stability estimates for more general ionic systems. In our case, we will use the fact that w can be expressed explicitly with respect to u (see (3.8)) and this will allow to get stability estimates for the identification of some parameters of the model.

3.3 Regularity of the solution

In this section we deal with the regularity of the solution of equations (3.3) which will be useful in the parameters estimations of Sections 3.4 and 3.5.

PROPOSITION 3.1

Let (u, w) be the solution of equations system (3.3), with initial conditions u_0, w_0 and parameters k, a, γ, β which staisfy (3.6)-(3.7).

If $u_0 \in L^2(\Omega), w_0 \in L^2(\Omega)$, then

$$\begin{aligned} u &\in L^\infty(0, T; L^2(\Omega)) \cap L^\infty(0, T; H^1(\Omega)) \cap L^\infty(0, T; L^4(\Omega)) \\ w &\in H^1(0, T; L^2(\Omega)). \end{aligned} \quad (3.11)$$

and

$$\begin{aligned} \|u\|_{L^\infty(0, T; L^2(\Omega))} + \|u\|_{L^2(0, T; H^1(\Omega))} + \|u\|_{L^4(0, T; L^4(\Omega))}^2 + \|w\|_{L^\infty(0, T; L^2(\Omega))} \leq \\ C(\|u_0\|_{L^2(\Omega)}, \|w_0\|_{L^2(\Omega)}). \end{aligned} \quad (3.12)$$

If $u_0 \in H^1(\Omega), u_0 = 0$ on $\partial\Omega$ and $w_0 \in L^2(\Omega)$, then

$$\begin{aligned} u &\in L^\infty(0, T; H^1(\Omega)) \cap H^1(0, T; L^2(\Omega)) \cap L^\infty(0, T; L^4(\Omega)) \\ w &\in H^1(0, T; L^2(\Omega)). \end{aligned} \quad (3.13)$$

and

$$\begin{aligned} \|u\|_{H^1(0, T; L^2(\Omega))} + \|u\|_{L^\infty(0, T; H^1(\Omega))} + \|u\|_{L^\infty(0, T; L^4(\Omega))}^2 + \|w\|_{H^1(0, T; L^2(\Omega))} \leq \\ C(\|u_0\|_{H^1(\Omega)}, \|w_0\|_{L^2(\Omega)}). \end{aligned} \quad (3.14)$$

Proof of Proposition 3.1.

First, we consider equations (3.3), we multiply the first one for u and the second one for w , and integrate over Ω the sum of them. According to hypotheses (3.6), there exist $k_0 > 0$ and $\beta_0 > 0$ such that $k \geq k_0$ and $\beta \geq \beta_0$. Then, using hypotheses (3.5) and (3.6), we obtain

$$\begin{aligned} \frac{1}{2} \frac{d}{dt} \int_{\Omega} |u|^2 dx + \int_{\Omega} |\nabla u|^2 dx + k_0 \int_{\Omega} |u|^4 dx + \frac{1}{2} \frac{d}{dt} \int_{\Omega} |w|^2 dx + \beta_0 \int_{\Omega} |w|^2 dx \leq \\ \int_{\Omega} (k(1+a)|u|^3 - ka|u|^2 + (\gamma-1)uw) dx \leq \\ \int_{\Omega} \left(\frac{k_0}{2} |u|^4 + C_1 |u|^2 + C_2 |w|^4 \right) dx. \end{aligned} \quad (3.15)$$

which leads to

$$\begin{aligned} \frac{1}{2} \frac{d}{dt} \int_{\Omega} |u|^2 dx + \int_{\Omega} |\nabla u|^2 dx + k_0 \int_{\Omega} |u|^4 dx + \frac{1}{2} \frac{d}{dt} \int_{\Omega} |w|^2 dx + \beta_0 \int_{\Omega} |w|^2 dx \leq \\ C \int_{\Omega} (|u|^2 + |w|^2) dx. \end{aligned} \quad (3.16)$$

Applying Gronwall Lemma and integrating in time on $(0, T)$, we conclude

$$\begin{aligned} \|u\|_{L^\infty(0, T; L^2(\Omega))}^2 + \|u\|_{L^2(0, T; H^1(\Omega))}^2 + \|u\|_{L^4(0, T; L^4(\Omega))}^4 + \|w\|_{L^\infty(0, T; L^2(\Omega))}^2 \leq \\ C(\|u_0\|_{L^2(\Omega)}, \|w_0\|_{L^2(\Omega)}). \end{aligned} \quad (3.17)$$

Second, we multiply the first equation of (3.3) by u_t and the second one by w_t and integrate the sum of them over Ω

$$\begin{aligned} \int_{\Omega} |u_t|^2 dx + \frac{1}{2} \frac{d}{dt} \int_{\Omega} |\nabla u|^2 dx + \frac{1}{4} \frac{d}{dt} \int_{\Omega} k |u|^4 dx + \int_{\Omega} |w_t|^2 dx + \frac{1}{2} \frac{d}{dt} \int_{\Omega} \beta |w|^2 dx \leq \\ \int_{\Omega} (k(1+a)|u|^2 u_t - \frac{ka}{2} |u| |u_t| + u_t w + \gamma u w_t) dx \leq \\ C \int_{\Omega} (|u|^4 + |u|^2 + |w|^2) dx + \frac{1}{2} \int_{\Omega} (|u_t|^2 + |w_t|^2) dx. \end{aligned} \quad (3.18)$$

Then, integrating in time over $(0, T)$ and thanks to (3.17), we have

$$\begin{aligned} \|u\|_{H^1(0, T; L^2(\Omega))} + \|u\|_{L^\infty(0, T; H^1(\Omega))} + \|u\|_{L^\infty(0, T; L^4(\Omega))}^2 + \|w\|_{H^1(0, T; L^2(\Omega))} \leq \\ C(\|u_0\|_{H^1(\Omega)}, \|w_0\|_{L^2(\Omega)}). \end{aligned} \quad (3.19)$$

■

PROPOSITION 3.2

Let the initial condition of (3.3) be such that $u_0 \in H^2(\Omega)$, $w_0 \in L^2(\Omega)$. Then the solution of (3.3) satisfies

$$\begin{aligned} u &\in W^{1,\infty}(0,T;L^2(\Omega)) \cap H^1(0,T;H^1(\Omega)) \cap L^\infty(0,T;H^2(\Omega)) \\ w &\in W^{1,\infty}(0,T;L^2(\Omega)) \end{aligned} \quad (3.20)$$

and

$$\begin{aligned} \|u\|_{W^{1,\infty}(0,T;L^2(\Omega))} + \|u\|_{H^1(0,T;H^1(\Omega))} + \|u\|_{L^\infty(0,T;H^2(\Omega))} + \|w\|_{W^{1,\infty}(0,T;L^2(\Omega))} \leq \\ C(\|u_0\|_{H^2(\Omega)}, \|w_0\|_{L^2(\Omega)}). \end{aligned} \quad (3.21)$$

Moreover if

$$(\Delta u + kg(u) - w)(t=0) = 0, \quad \partial\Omega. \quad (3.22)$$

then

$$\begin{aligned} u &\in H^2(0,T;L^2(\Omega)) \cap W^{1,\infty}(0,T;H^1(\Omega)) \cap L^\infty(0,T;H^2(\Omega)) \\ w &\in H^2(0,T;L^2(\Omega)) \end{aligned} \quad (3.23)$$

and

$$\begin{aligned} \|u\|_{H^2(0,T;L^2(\Omega))} + \|u\|_{W^{1,\infty}(0,T;H^1(\Omega))} + \|w\|_{H^2(0,T;L^2(\Omega))} \leq \\ C(\|u_0\|_{H^2(\Omega)}, \|w_0\|_{L^2(\Omega)}). \end{aligned} \quad (3.24)$$

with parameters k, a, γ, β which satisfy (3.6)-(3.7).

Proof of Proposition 3.2.

First, we take the time derivative of equations (3.3)

$$\begin{cases} u_{tt} - \Delta u_t = kg_t(u) - w_t, & Q \\ w_{tt} = \gamma u_t - \beta w_t, & Q \end{cases} \quad (3.25)$$

with initial condition

$$\begin{aligned} u_t(t=0) &= \Delta u_0 + kg(u_0) - w_0 \\ w_t(t=0) &= \gamma u_0 - \beta w_0 \end{aligned} \quad (3.26)$$

and compatibility condition (3.22). Now, we proceed as in the proof of Proposition 3.1. We multiply the first equation of (3.25) by u_t and the second one by w_t , and we sum up them together. There exist $k_0 > 0$ and $\beta_0 > 0$ such that $k \geq k_0$ and $\beta \geq \beta_0$. Then, using hypotheses (3.5) and (3.6), we obtain that the integral over Ω is given

by

$$\begin{aligned} \frac{1}{2} \frac{d}{dt} \int_{\Omega} |u_t|^2 dx + \int_{\Omega} |\nabla u_t|^2 dx + C \int_{\Omega} |u_t|^2 dx + \frac{1}{2} \frac{d}{dt} \int_{\Omega} |w_t|^2 dx + \\ \beta_0 \int_{\Omega} |w_t|^2 dx \leq C \int_{\Omega} (|u_t|^2 + |w_t|^2) dx \end{aligned} \quad (3.27)$$

since

$$\int_{\Omega} g_t(u) u_t dx = \int_{\Omega} (-3|u|^2 |u_t|^2 + 2(1+a)u |u_t|^2 - a|u_t|^2) dx \quad (3.28)$$

that, using Proposition 3.1, leads to

$$C \int_{\Omega} |u_t|^2 dx \leq C \int_{\Omega} |u|^2 |u_t|^2 dx \leq \int_{\Omega} (\varepsilon |u|^2 |u_t|^2 + C |u_t|^2) dx. \quad (3.29)$$

Then, integrating in time over $(0, T)$, we have

$$\begin{aligned} \|u\|_{W^{1,\infty}(0,T;L^2(\Omega))} + \|u\|_{H^1(0,T;H^1(\Omega))} + \|w\|_{W^{1,\infty}(0,T;L^2(\Omega))} \leq \\ C(\|u_0\|_{H^2(\Omega)}, \|w_0\|_{L^2(\Omega)}). \end{aligned} \quad (3.30)$$

Also, we consider the elliptic equation for all $t \in (0, T)$

$$\begin{cases} \Delta u = -kg(u) + u_t + w, & \Omega \\ u = 0, & \partial\Omega \end{cases} \quad (3.31)$$

where the right-hand side belongs to $L^\infty(0, T; L^2(\Omega))$. Then, for this steady problem, we have

$$\|u(t)\|_{H^2(\Omega)} \leq C(\|u_0\|_{H^2(\Omega)}, \|w_0\|_{L^2(\Omega)}) \quad (3.32)$$

for all $t \in (0, T)$, and $u \in L^\infty(0, T; H^2(\Omega)) \hookrightarrow L^\infty(0, T; L^\infty(\Omega))$.

Second, we consider the integral over Ω of the sum of the first equation of (3.25) multiplied by u_{tt} and of the second one multiplied by w_{tt}

$$\begin{aligned} \int_{\Omega} |u_{tt}|^2 dx + \frac{1}{2} \frac{d}{dt} \int_{\Omega} |\nabla u_t|^2 dx + C \frac{d}{dt} \int_{\Omega} |u_t|^2 dx + \int_{\Omega} |w_{tt}|^2 dx + \frac{1}{2} \frac{d}{dt} \int_{\Omega} \beta |w_t|^2 dx \leq \\ \int_{\Omega} (\varepsilon |u_{tt}|^2 + C |u_t|^2 + \varepsilon |w_{tt}|^2 + C |w_t|^2) dx \end{aligned} \quad (3.33)$$

that leads to

$$\begin{aligned} C \int_{\Omega} |u_{tt}|^2 dx + \frac{1}{2} \frac{d}{dt} \int_{\Omega} |\nabla u_t|^2 dx + C \frac{d}{dt} \int_{\Omega} |u_t|^2 dx + C \int_{\Omega} |w_{tt}|^2 dx + \\ \frac{\beta_0}{2} \frac{d}{dt} \int_{\Omega} |w_t|^2 dx \leq C \int_{\Omega} (|u_t|^2 dx + |w_t|^2) dx. \end{aligned} \quad (3.34)$$

So, integrating in time on $(0, T)$ we conclude

$$\begin{aligned} \|u\|_{H^2(0, T; L^2(\Omega))} + \|u\|_{W^{1, \infty}(0, T; H^1(\Omega))} + \|w\|_{H^2(0, T; L^2(\Omega))} \leq \\ C(\|u_0\|_{H^2(\Omega)}, \|w_0\|_{L^2(\Omega)}). \end{aligned} \quad (3.35)$$

■

PROPOSITION 3.3

Let (u, w) be the solution of equations system (3.3) with initial condition $u_0 \in H^4(\Omega)$, $w_0 \in H^2(\Omega)$. Also, let us assume that the parameters k, a, γ, β satisfy (3.6)-(3.7) and that $k \in H^2(\Omega)$ and $a \in H^2(\Omega)$.

Then the solution (u, w) satisfies

$$\begin{aligned} u \in W^{2, \infty}(0, T; L^2(\Omega)) \cap H^2(0, T; H^1(\Omega)) \cap W^{1, \infty}(0, T; H^2(\Omega)) \\ w \in W^{2, \infty}(0, T; L^2(\Omega)). \end{aligned} \quad (3.36)$$

and

$$\begin{aligned} \|u\|_{W^{2, \infty}(0, T; L^2(\Omega))} + \|u\|_{H^2(0, T; H^1(\Omega))} + \|w\|_{W^{2, \infty}(0, T; L^2(\Omega))} \leq \\ C(\|u_0\|_{H^4(\Omega)}, \|w_0\|_{H^2(\Omega)}) \end{aligned} \quad (3.37)$$

Proof of Proposition 3.3.

We consider the second order time derivative of (3.3)

$$\begin{cases} u_{ttt} - \Delta u_{tt} = kg_{tt}(u) - w_{tt}, & Q \\ w_{ttt} = \gamma u_{tt} - \beta w_{tt}, & Q \end{cases} \quad (3.38)$$

We use the same technique of the proofs as in Propositions 3.1 and 3.2: we integrate over Ω the sum of the first equation of (3.38) multiplied by u_{tt} and of the second one multiplied by w_{tt} . First, we consider

$$\int_{\Omega} kg_{tt}(u)u_{tt}dx = \int_{\Omega} k((-3|u|^2 + 2(1+a)u - a)u_{tt} + (-6u + 2(1+a)|u_t|^2)u_{tt})dx. \quad (3.39)$$

Then

$$C \int_{\Omega} |u_{tt}|^2 dx \leq \int_{\Omega} k(3|u|^2 + a)|u_{tt}|^2 dx \leq C \int_{\Omega} (|u_{tt}|^2 + u_{tt}) dx \quad (3.40)$$

since $k \geq k_0$, $a \geq a_0$ and, thanks to Propositions 3.1 and 3.2, $u \in L^\infty(Q)$ and $u_t \in L^\infty(0, T; L^6(\Omega))$. Thus, we obtain

$$\begin{aligned} \frac{1}{2} \frac{d}{dt} \int_{\Omega} |u_{tt}|^2 dx + \int_{\Omega} |\nabla u_{tt}|^2 dx + C \int_{\Omega} |u_{tt}|^2 dx + \frac{1}{2} \frac{d}{dt} \int_{\Omega} |w_{tt}|^2 + \beta_0 \int_{\Omega} |w_{tt}|^2 dx \leq \\ C \int_{\Omega} (|u_{tt}|^2 + |w_{tt}|) dx. \end{aligned} \quad (3.41)$$

To conclude, we integrate in time on $(0, T)$

$$\|u\|_{W^{2,\infty}(0,T;L^2(\Omega))} + \|u\|_{H^2(0,T;H^1(\Omega))} + \|w\|_{W^{2,\infty}(0,T;L^2(\Omega))} \leq C(\|u_0\|_{H^4(\Omega)}, \|w_0\|_{H^2(\Omega)}). \quad (3.42)$$

Last, since $u \in W^{2,\infty}(0,T;L^2(\Omega)) \cup H^2(0,T;H^1(\Omega))$, then

$$\Delta u = u_t - kg(u) + w \in W^{1,\infty}(0,T;L^2(\Omega)). \quad (3.43)$$

So, we obtain $u \in W^{1,\infty}(0,T;H^2(\Omega))$ and conclude the proof. \blacksquare

3.4 Estimation of reaction parameter

We are first interested in giving an estimation on the reaction parameter k which appears in the first equation of (3.3). We consider the perturbed system with respect to k

$$\begin{cases} \bar{u}_t - \Delta \bar{u} = \bar{k}g(\bar{u}) - \bar{w}, & Q \\ \bar{w}_t = \gamma\bar{u} - \beta\bar{w}, & Q \\ \bar{u}(t=0) = \bar{u}_0, & \Omega \\ \bar{w}(t=0) = \bar{w}_0, & \Omega \\ u = 0, & (0,T) \times \partial\Omega \end{cases} \quad (3.44)$$

where $\bar{u}_0 \in H^4(\Omega)$ and $\bar{w}_0 \in H^2(\Omega)$, $\bar{k} \in H^2(\Omega)$ and there exists $M > 0$ such that $\|\bar{k}\|_{L^\infty(\Omega)} \leq M$.

First, we define $\pi = k - \bar{k}$, $p = u - \bar{u}$ and $q = w - \bar{w}$. Then the difference between equations (3.3) and (3.44) leads to

$$\begin{cases} p_t - \Delta p + kp^3 = F - q \\ q_t = \gamma p - \beta q, \end{cases} \quad (3.45)$$

where

$$F = \pi g(\bar{u}) + kh(p, \bar{u}) \quad (3.46)$$

and

$$h(p, \bar{u}) = (-a + 2(1+a)\bar{u} - 3\bar{u}^2)p + (1+a-3\bar{u})p^2. \quad (3.47)$$

Then, if $q(T/2)$ is known, the solution of the second equation is given by

$$q(t,x) = q(T/2,x)e^{-(t-T/2)\beta(x)} + \int_{T/2}^t \gamma(x)p(\tau,x)e^{-(\tau-T/2)\beta(x)} d\tau. \quad (3.48)$$

PROPOSITION 3.4

Let us consider a nonempty open set ω included in Ω . Let (u, w) be the solution of (3.3) with initial conditions

$$u_0 \in H^2(\Omega), \quad w_0 \in L^2(\Omega)$$

and (\bar{u}, \bar{w}) be the solution of (3.44) with initial conditions

$$\bar{u}_0 \in H^4(\Omega), \quad \bar{w}_0 \in H^2(\Omega).$$

We suppose that k, γ, β, a satisfy (3.6)-(3.7), $a, \bar{k} \in H^2(\Omega)$ and that there exists $C_1 > 0$ such that

$$g(\bar{u}; T/2, x) \geq C_1, \quad \forall x \in \Omega, \forall T > 0. \quad (3.49)$$

Then, for all $T > 0$, there exists $C_2 > 0$ depending on \bar{u}, \bar{w} such that

$$\|\pi\|_{L^2(\Omega)} \leq C_2 (\|p(T/2)\|_{H^2(\Omega)} + \|p(T/2)\|_{L^6(\Omega)}^3 + \|q(T/2)\|_{L^2(\Omega)} + \|p\|_{H^1(0, T; L^2(\omega))}) \quad (3.50)$$

where $p = u - \bar{u}$, $q = w - \bar{w}$, and $\pi = k - \bar{k}$.

Proof of Proposition 3.4.

First, we consider the time derivative of the system of equations (3.45)

$$\begin{cases} \rho_t - \Delta \rho &= G - \nu \\ \nu_t &= \gamma \rho - \beta \nu, \end{cases} \quad (3.51)$$

where $\rho = p_t$ and $\nu = q_t$ and

$$G = -3kp^2\rho + \pi g_t(\bar{u}) + kh_t(p, \bar{u}), \quad (3.52)$$

with

$$g_t(\bar{u}) = \bar{u}_t(-3\bar{u}^2 + 2(1+a)\bar{u} - a) \quad (3.53)$$

and

$$h_t(p, \bar{u}) = \bar{u}_t[(2(1+a) - 6\bar{u})p - 3p^2] + \rho[-a + 2(1+a)\bar{u} - 3\bar{u}^2 + 2(1+a - 3\bar{u})p]. \quad (3.54)$$

Let us define a function ψ in Ω such that

- $\psi \in \mathcal{C}^2(\bar{\Omega})$
- $\psi > 0$ in Ω , $\psi = 0$ on $\partial\Omega$
- $|\nabla\psi| > 0$ in $\bar{\Omega} \setminus \omega$.

We define, for all $\lambda > 0$, the following weights for all $(t, x) \in Q$

$$\varphi(t, x) = \frac{e^{2\lambda\|\psi\|_\infty} - e^{\lambda\psi(x)}}{t(T-t)} \quad (3.55)$$

and

$$\eta(t, x) = \frac{e^{\lambda\psi(x)}}{t(T-t)}. \quad (3.56)$$

First, we evaluate the first equation of (3.45) at a fixed time $T/2$

$$\rho(T/2, x) - \Delta p(T/2, x) + kp^3(T/2, x) = \pi g(\bar{u}; T/2, x) + kh(p, \bar{u}; T/2, x) - q(T/2, x). \quad (3.57)$$

Then, we integrate on Ω the square of (3.57) with weight $e^{-2s\varphi(T/2, x)}$ and obtain

$$\begin{aligned} \int_{\Omega} e^{-2s\varphi(T/2, x)} \pi^2 |g(\bar{u}; T/2, x)|^2 dx &\leq \int_{\Omega} e^{-2s\varphi(T/2, x)} |\rho(T/2, x)|^2 dx + \\ &\int_{\Omega} e^{-2s\varphi(T/2, x)} (|\Delta p(T/2, x)|^2 + |p(T/2, x)|^6) dx + \\ &\int_{\Omega} e^{-2s\varphi(T/2, x)} |h(p, \bar{u}; T/2, x)|^2 dx + \int_{\Omega} e^{-2s\varphi(T/2, x)} |q(T/2, x)|^2 dx \end{aligned} \quad (3.58)$$

since $k \in L^\infty(\Omega)$.

First, we notice that the third term of the right-hand side is bounded by (3.49)

$$\int_{\Omega} e^{-2s\varphi(T/2, x)} |h(p, \bar{u}; T/2, x)|^2 dx \leq \int_{\Omega} e^{-2s\varphi(T/2, x)} (|p(T/2, x)|^2 + |p(T/2, x)|^6) dx. \quad (3.59)$$

By this way, all the terms in the right-hand side, except the first one, well correspond to measurement of p and q at time $T/2$. Let us bound the first term in the right-hand side

$$\begin{aligned} J_1 &= \int_{\Omega} e^{-2s\varphi(T/2, x)} |\rho(T/2, x)|^2 dx = \iint_{Q_0} \frac{d}{dt} (e^{-2s\varphi} |\rho|^2) dx dt \leq \\ &\iint_{Q_0} 2e^{-2s\varphi} (|\varphi_t| |\rho|^2 + |\rho| |\rho_t|) dx dt \leq \\ &\iint_{Q_0} C(T, \lambda) e^{-2s\varphi} (s^2 \eta^2 |\rho|^2 + (s^2 \eta)^{-1} |\rho_t|^2) dx dt \end{aligned} \quad (3.60)$$

where $Q_0 = (0, T/2) \times \Omega$, since $|\varphi_t| \leq C(T, \lambda) |\eta|^2$. Then, we apply the classical Carleman inequality introduced in [FI96] for the heat equation (3.51) satisfied by ρ , and obtain that for s and λ large enough

$$J_1 \leq \frac{C}{s} \iint_Q e^{-2s\varphi} (|G|^2 + |\nu|^2) dx dt + C \iint_{Q_\omega} e^{-2s\varphi} s^2 \eta^3 |\rho|^2 dx dt \quad (3.61)$$

where $Q_\omega = (0, T) \times \omega$. Then, using the definition of G given by (3.52) and the

definition of $\nu = q_t$ given by the second equation of (3.45) we obtain

$$J_2 = \iint_Q e^{-2s\varphi} (|G|^2 + |\nu|^2) dxdt \leq C \iint_Q e^{-2s\varphi} (|\rho|^2 + |p|^4 + |p|^2) dxdt + \iint_Q e^{-2s\varphi} |q|^2 dxdt + C \iint_Q e^{-2s\varphi} |\pi|^2 dxdt \quad (3.62)$$

since a, k, γ, β satisfy (3.6)-(3.7) and \bar{u}, \bar{u}_t satisfy Propositions 3.2 and 3.3. Let us consider the second integral of the right-hand side of (3.62). Using the solution given by (3.48) we obtain

$$J_3 = \iint_Q e^{-2s\varphi} |q|^2 dxdt \leq C \iint_Q e^{-2s\varphi(t,x) - 2(t-T/2)\beta(x)} |q(T/2, x)|^2 dxdt + C \iint_Q e^{-2s\varphi} \left(\int_{T/2}^t |p(\tau, x)|^2 d\tau \right) dxdt \leq C \int_{\Omega} e^{-2s\varphi(T/2)} |q(T/2, x)|^2 dx + C \iint_Q e^{-2s\varphi} |p|^2 dxdt \quad (3.63)$$

Then, for s large enough

$$J_1 \leq C \iint_{Q_\omega} e^{-2s\varphi} s^2 \eta^3 |\rho|^2 dxdt + \frac{C}{s} \iint_Q e^{-2s\varphi} (|p|^2 + |p|^4) dxdt + \frac{C}{s} \int_{\Omega} e^{-2s\varphi(T/2)} |q(T/2, x)|^2 dx + \frac{C}{s} \iint_Q e^{-2s\varphi} \pi^2 dxdt. \quad (3.64)$$

The last integral to take into account deals with the terms with p . According to Proposition 3.2, $u, \bar{u} \in L^\infty(Q)$, thus we obtain

$$\iint_Q e^{-2s\varphi} |p|^4 dxdt \leq \|p\|_{L^\infty(0, T; L^\infty(\Omega))}^2 \iint_Q e^{-2s\varphi} |p|^2 dxdt. \quad (3.65)$$

Then, using the definition of $p_t = \rho$, we can write

$$J_5 = \iint_Q e^{-2s\varphi} |p|^2 dxdt \leq C \iint_Q e^{-2s\varphi} \left(|p(T/2, x)|^2 + \int_{T/2}^t |\rho(\tau, x)|^2 d\tau \right) dxdt \leq C \int_{\Omega} e^{-2s\varphi(T/2, x)} |p(T/2, x)|^2 dx + C \iint_Q e^{-2s\varphi} |\rho|^2 dxdt. \quad (3.66)$$

since $\varphi(T/2) \leq \varphi(t)$ for all $t \in (T/2, T)$.

Finally, using (3.59), (3.64) and (3.66), we find

$$\begin{aligned} \int_{\Omega} e^{-2s\varphi(T/2,x)} \pi^2 |g(\bar{u}; T/2, x)|^2 dx &\leq C \iint_{Q_\omega} e^{-2s\varphi} s^2 \eta^3 |\rho|^2 dx dt + \\ \int_{\Omega} e^{-2s\varphi(T/2,x)} (|\Delta p(T/2, x)|^2 + |p(T/2, x)|^2 + |p(T/2, x)|^6) dx &+ \\ \int_{\Omega} e^{-2s\varphi(T/2,x)} |q(T/2, x)|^2 dx + \frac{C}{s} \iint_Q e^{-2s\varphi} \pi^2 dx dt. &\quad (3.67) \end{aligned}$$

Then, for s large enough, using hypotheses (3.49) we conclude the proof. \blacksquare

3.5 Estimation of a parameter in the second equation

We are now interested in giving an estimation of the parameter γ which appears in the second equation of (3.3). Let us call \hat{u}, \hat{w} the solution for the parameter $\hat{\gamma}$ of system

$$\begin{cases} \hat{u}_t - \Delta \hat{u} = kg(\hat{u}) - \hat{w}, & Q \\ \hat{w}_t = \hat{\gamma} \hat{u} - \beta \hat{w}, & Q \\ \hat{u}(t=0) = \hat{u}_0, & \Omega \\ \hat{w}(t=0) = \hat{w}_0, & \Omega \\ \hat{u} = 0, & (0, T) \times \partial\Omega \end{cases} \quad (3.68)$$

which is a perturbed version of (3.3) with respect to γ .

We define $\alpha = \gamma - \hat{\gamma}$, $z = u - \hat{u}$ and $v = w - \hat{w}$. Then, taking the difference between (3.3) and (3.68) we obtain

$$\begin{cases} z_t - \Delta z + kz^3 = kh(z, \hat{u}) - v \\ v_t = \alpha \hat{u} + \gamma z - \beta v \end{cases} \quad (3.69)$$

where $h(z, \bar{u})$ is defined as in (3.47). If we suppose that we know the solution v for a fixed time $T/2$, $T > 0$, for all $x \in \Omega$, the solution of the second equation of (3.69) can be written as

$$v(t, x) = v(T/2, x) e^{-(t-T/2)\beta(x)} + \int_{T/2}^t (\alpha(x) \hat{u}(\tau, x) + \gamma(x) z(\tau, x)) e^{-(\tau-T/2)\beta(x)} d\tau. \quad (3.70)$$

PROPOSITION 3.5

Let ω be a nonempty open set included in Ω . Let (u, w) be the solution of (3.3) with initial conditions

$$u_0 \in H^4(\Omega), \quad w_0 \in H^2(\Omega)$$

and (\hat{u}, \hat{w}) be the solution of (3.68) with initial conditions

$$\hat{u}_0 \in H^4(\Omega), \quad \hat{w}_0 \in H^2(\Omega).$$

We suppose that k, γ, β, a satisfy (3.6)- (3.7), and $k, a \in H^2(\Omega)$.

Then, for all $T > 0, \delta > 0$, there exists $C > 0$ depending on z, v such that

$$\|\alpha\|_{L^2(\Omega)} \leq C(\|z(T/2 + \delta)\|_{H^2(\Omega)} + \|v(T/2)\|_{L^2(\Omega)} + \|z\|_{H^1(0, T; L^2(\omega))}) \quad (3.71)$$

where $z = u - \hat{u}, v = w - \hat{w}$ and $\alpha = \gamma - \hat{\gamma}$.

Proof of Proposition 3.5.

First, we define $\zeta = z_t$ and $\xi = v_t$. Taking the time derivative of equations (3.69) we obtain

$$\begin{cases} \zeta_t - \Delta\zeta &= Y \\ \xi_t &= \alpha\hat{u}_t + \gamma\zeta - \beta\xi \end{cases} \quad (3.72)$$

where

$$Y := -k\zeta^3 + kh_t(z, \hat{u}) - \xi \quad (3.73)$$

and $h_t(z, \hat{u})$ is defined by (3.54).

We define some functions as in the proof of Proposition 3.4. First a function ψ in Ω defined as in the Proof of Proposition 3.4. Second, we pick a function $\theta \in C^\infty(0, T)$ such that

$$\theta(t) = \begin{cases} (t(T-t))^{-1}, & 0 < t \leq T/2 - 2\delta \\ \text{strictly decreasing,} & T/2 - 2\delta < t \leq T/2 \\ \text{constant,} & T/2 < t \leq T/2 + \delta \\ \text{strictly increasing,} & T/2 + \delta < t \leq T/2 + 2\delta \\ \theta(T-t), & T/2 + \delta < t \leq T \end{cases} \quad (3.74)$$

and for all $\lambda > 0$ and $\delta \in (0, T/2)$, we define the following weights

$$\varphi(t, x) = \theta(t)(e^{2\lambda\|\psi\|_\infty} - e^{\lambda\psi(x)}), \quad (t, x) \in Q \quad (3.75)$$

$$\eta(t, x) = \theta(t)e^{\lambda\psi(x)}, \quad (t, x) \in Q \quad (3.76)$$

where $\|\psi\|_\infty = \|\psi\|_{L^\infty(\Omega)}$.

We consider the first equation of (3.69) for a fixed time $T/2 + \delta$, then

$$\zeta(T/2 + \delta, x) = \Delta z(T/2 + \delta, x) + k(x)z^3(T/2 + \delta, x) + kh(z, \hat{u}; T/2 + \delta, x) - v(T/2 + \delta, x) \quad (3.77)$$

where v is defined by (3.70) and α is the parameter we are interested in. Then, if we

take the square and integrate on Ω with the weight $e^{-2s\varphi(T/2+\delta)}$, we obtain

$$\begin{aligned} \int_{\Omega} e^{-2s\varphi(T/2+\delta,x)} \left| \int_{T/2}^{T/2+\delta} (\alpha(x)\widehat{u}(\tau,x) + \gamma(x)z(\tau,x)) e^{-(\tau-T/2)\beta(x)} d\tau \right|^2 dx \leq \\ \int_{\Omega} e^{-2s\varphi(T/2+\delta)} |\zeta(T/2 + \delta, x)|^2 dx + \\ \int_{\Omega} e^{-2s\varphi(T/2+\delta)} (|\Delta z(T/2 + \delta, x)|^2 dx + |z(T/2' + \delta, x)|^6) dx + \\ \int_{\Omega} e^{-2s\varphi(T/2+\delta)} |h(z, \widehat{u}; T/2 + \delta, x)|^2 dx + \int_{\Omega} e^{-2s\varphi(T/2+\delta)-2\delta\beta(x)} |v(T/2, x)|^2 dx. \end{aligned} \quad (3.78)$$

Since $\beta, \gamma \in L^\infty(\Omega)$, $\varphi(t) \geq \varphi(T/2)$ for all $t \in (T/2, T)$, and u, \widehat{u} satisfy (3.5), we can write

$$\begin{aligned} \int_{\Omega} e^{-2s\varphi(T/2+\delta,x)} |\alpha(x)\widehat{u}(\tau,x)|^2 dx \leq C \int_Q e^{-2s\varphi} |z|^2 dx dt \\ \int_{\Omega} e^{-2s\varphi(T/2+\delta)} |\zeta(T/2 + \delta, x)|^2 dx + \\ \int_{\Omega} e^{-2s\varphi(T/2+\delta)} (|\Delta z(T/2 + \delta, x)|^2 dx + |z(T/2' + \delta, x)|^6) dx + \\ \int_{\Omega} e^{-2s\varphi(T/2+\delta)} |h(z, \widehat{u}; T/2 + \delta, x)|^2 dx + \int_{\Omega} e^{-2s\varphi(T/2+\delta)-2\delta\beta(x)} |v(T/2, x)|^2 dx. \end{aligned} \quad (3.79)$$

As in the Proof of Proposition 3.4, the third term of the right-hand side is bounded as in (3.59). Thus, all the terms in the right-hand side, except the first one, correspond to measurements of v at time $T/2$ and z at time $T/2 + \delta$. Let us then consider the first term in the right hand-side of (3.79). Since $e^{-2s\varphi(t)} \rightarrow 0$ when $t \rightarrow 0$, we have

$$\begin{aligned} I_1 = \int_{\Omega} e^{-2s\varphi(T/2+\delta,x)} |\zeta(T/2 + \delta, x)|^2 dx = \int_0^{T/2+\delta} \int_{\Omega} (e^{-2s\varphi} |\zeta|^2)_t dx dt \leq \\ C(T, \lambda) \iint_Q 2e^{-2s\varphi} (s\eta^2 |\zeta|^2 + |\zeta| |\zeta_t|) dx dt \leq \\ \frac{C(T, \lambda)}{s} \iint_Q e^{-2s\varphi} ((s\eta)^{-1} |\zeta_t|^2 + (s\eta)^3 |\zeta|^2) dx dt \end{aligned} \quad (3.80)$$

since $|\varphi_t| \leq C(T, \lambda)\eta^2$ and $\varphi(t) \geq \varphi(T/2 + \delta)$ for all $t \in (T/2 + \delta, T)$.

We apply the Carleman estimate introduced by [FI96] and obtain

$$\begin{aligned} I_1 \leq \frac{C}{s} \iint_Q e^{-2s\varphi} |Y|^2 dx dt + C \iint_{Q_\omega} e^{-2s\varphi} s^2 \eta^2 |\zeta|^2 dx dt \leq \\ \iint_Q e^{-2s\varphi} (|\zeta|^2 + |z|^2 + |\xi|^2) dx dt + C \iint_{Q_\omega} e^{-2s\varphi} s^2 \eta^2 |\zeta|^2 dx dt \end{aligned} \quad (3.81)$$

since $u_t, \widehat{u}_t \in L^\infty(Q)$ thanks to Proposition 3.3, and $a, k \in L^\infty(\Omega)$. Then, for s large

enough

$$I_1 \leq \frac{C}{s} \iint_Q e^{-2s\varphi} (|z|^2 + |\xi|^2) dxdt + C \iint_{Q_\omega} e^{-2s\varphi} s^2 \eta^2 |\zeta|^2 dxdt. \quad (3.82)$$

Second, we consider the first term of the right-hand side of (3.82) and apply again the Carleman estimate introduced by [FI96], then

$$\begin{aligned} I_2 &= \iint_Q e^{-2s\varphi} |z|^2 dxdt \leq \iint_Q e^{-2s\varphi} \eta^3 |z|^2 dxdt \leq \\ &\frac{C}{s^3} \iint_Q e^{-2s\varphi} (|z|^6 + |h(z, \hat{u})|^2 + |v|^2) dxdt + C \iint_{Q_\omega} e^{-2s\varphi} \eta^2 |z|^2 dxdt \leq \\ &\frac{C}{s^3} \iint_Q e^{-2s\varphi} (|z|^2 + |v|^2) dxdt + C \iint_{Q_\omega} e^{-2s\varphi} \eta^2 |z|^2 dxdt \end{aligned} \quad (3.83)$$

since $u, \hat{u} \in L^\infty(Q)$. For s large enough

$$I_2 \leq \frac{C}{s^3} \iint_Q e^{-2s\varphi} |v|^2 dxdt + C \iint_{Q_\omega} e^{-2s\varphi} \eta^2 |z|^2 dxdt. \quad (3.84)$$

Third, we consider the second term of the right-hand side of (3.82) and use the definition of $\xi = v_t$ given by (3.69), then

$$\begin{aligned} I_3 &= \iint_Q e^{-2s\varphi} |\xi|^2 dxdt = \iint_Q e^{-2s\varphi} |\alpha \hat{u} - \gamma z - \beta v|^2 dxdt \leq \\ &C \iint_Q e^{-2s\varphi} |\alpha|^2 dxdt + C \iint_Q e^{-2s\varphi} (|z|^2 + |v|^2) dxdt \end{aligned} \quad (3.85)$$

since $\beta \in L^\infty(\Omega)$.

Finally, we consider the weighted integral of $|v|^2$ in the right-hand side of (3.85). Then, according to (3.70),

$$\begin{aligned} I_4 &= \iint_Q e^{-2s\varphi} |v|^2 dxdt \leq \iint_Q e^{-2s\varphi - 2(t-T/2)\beta(x)} |v(T/2, x)|^2 dxdt + \\ &\iint_Q e^{-2s\varphi} \left| \int_{T/2}^t (\alpha(x) \hat{u}(\tau, x) + \gamma(x) z(\tau, x)) e^{-(\tau-T/2)\beta} d\tau \right|^2 dxdt \leq \\ &C \int_\Omega e^{-2s\varphi(T/2, x)} |v(T/2, x)|^2 dx + C \int_\Omega e^{-2s\varphi(T/2, x)} |\alpha|^2 dx + \\ &C \iint_Q e^{-2s\varphi} \left(\int_{T/2}^t |z(\tau, x)|^2 d\tau \right) dxdt \leq \\ &C \int_\Omega e^{-2s\varphi(T/2, x)} |v(T/2, x)|^2 dx + C \int_\Omega e^{-2s\varphi(T/2, x)} |\alpha|^2 dx + \\ &C \iint_Q e^{-2s\varphi} |z|^2 dxdt \end{aligned} \quad (3.86)$$

since $\varphi(t) \geq \varphi(\tau)$ for all $\tau \in (T/2, t)$, $\beta, \gamma \in L^\infty(\Omega)$, $\hat{u} \in L^\infty(Q)$, and for s large

enough.

From (3.84)-(3.85), for s large enough we have

$$I_2 + I_3 \leq CI_4 + C \int_{\Omega} e^{-2s\varphi(T/2,x)} |\alpha|^2 dx + C \iint_{Q_\omega} e^{-2s\varphi} s^{-1} \eta^2 |z|^2 dx dt. \quad (3.87)$$

Also, from (3.82), using (3.86)-(3.87) we obtain

$$I_1 \leq \frac{C}{s} \|v(T/2,x)\|_{L^2(\Omega)}^2 + \frac{C}{s} \int_Q e^{-2s\varphi(T/2,x)} |\alpha|^2 dx dt + C \iint_{Q_\omega} e^{-2s\varphi} s^{-2} \eta^2 |z|^2 dx dt + C \iint_{Q_\omega} e^{-2s\varphi} s \eta^2 |\zeta|^2 dx dt. \quad (3.88)$$

Finally, from (3.79), (3.88), for s large enough, we conclude the proof. ■

REMARK 3.1

Contrary to the estimation given in Proposition 3.4 of the parameter k which appears in the first equation of (3.3), in this section we deal with a parameter, γ , which is in the second equation of the system. Then, it is strictly necessary to consider two different time instants, $T/2$, $T/2 + \delta$, $\delta > 0$, and to have an observation of the first variable, z , at time $T/2 + \delta$ and an observation of v at time $T/2$. If δ is equal to zero, the integral in time of the left side of (3.79) would be null and no estimation on α could be possible.

3.6 Chapter conclusions

An estimation of two ionic parameter of the FitzHugh-Nagumo ionic model has been presented. First, in Proposition 3.4 we gave an estimation on the reaction parameter k that appears in the first equation of the ionic model. Second, in Proposition 3.5 an estimation on γ , which is one of the parameters that appear in the second equation of the ionic model, is obtained. These preliminary results, are obtained on a restricted number of the parameters of the model. Future works could investigate the stability of the others parameters of the model, and then apply this estimation in the parameters identification problems.

Reduced-order modeling and parameters identification with Proper Orthogonal Decomposition

In this chapter we present a reduced-order model based on proper orthogonal decomposition (POD) applied to bidomain equations of cardiac electrophysiology. In particular, we focus on the simulation of a myocardial infarction. First we discuss about this pathology and on how to reproduce it thanks to the properties of a ionic model. Then we introduce a POD method in order to obtain realistic electrocardiograms. Finally, the reduced-order model is used in an inverse problem solved by an evolutionary algorithm in order to identify the infarction locations from synthetic electrocardiograms.

The results presented in this chapter lead to the manuscript

Muriel Boulakia, Elisa Schenone, Jean-Frédéric Gerbeau. **Reduced-order modeling for cardiac electrophysiology. Application to parameter identification.** *International Journal for Numerical Methods in Biomedical Engineering*, Volume 28, Issue 6-7, Pages 727-744, 2012.

Contents

4.1	Introduction	99
4.2	Presentation of the model	99
4.3	Proper Orthogonal Decomposition method	101
4.4	Application of POD to forward problems	101
4.4.1	POD for changed parameters problems	101
4.4.2	Full and reduced-order simulation of an infarction	103
4.5	Application of POD to the parameters identification	106
4.5.1	Optimization method	106
4.5.2	Identificatio of four parameters	110
4.5.3	Identification of a myocardial infarction	111
4.6	Chapter conclusions	112
4.A	Genetic algorithm	114

4.1 Introduction

The bidomain equations that used to model the cardiac electrophysiology is known to be very demanding from a computation viewpoint [CFP04, SPM08]. To reduce its complexity, reduced-order models based on physical arguments can be considered. For example, assuming that the anisotropy ratios of the electrical conductivity tensors are the same in the intra and extracellular media, the simplified monodomain model can be derived as shown in Section 1.4.1. Another example of physical simplification is given by the Eikonal model that essentially describes the propagation of the activation front [Kee91, PTH02]. Here, we follow another route: keeping the physics of the model fixed, we reduce the complexity of its discretization by using a Galerkin basis adapted to the kind of solutions that are looked for. This basis can be computed by different approaches. In this chapter, we show one of the most popular one, which is known as the Proper Orthogonal Decomposition (POD) or Karhunen-Loève method. This approach has been used in many fields of science and engineering, but to the best of our knowledge, not for the equations of cardiac electrophysiology. A first application is described in [BG11] where various configurations of interest are considered, such as perturbation of some parameters. POD seems promising in some configurations while in other it has to be used with much care. In this chapter we are interested in applying this technique to perturbation of some parameters and myocardial infarction modeling while Chapter 5 deals with the application to long-time simulations. In all these cases, the results are assessed through the corresponding electrocardiogram (ECG). After a recall of the model, in Section 4.3 the POD method is described, while we invite to read Section 1.6.2 for its general formulation. A description of infarction pathology and its numerical modeling are given in Section 4.4.2.1. In Sections 4.4.2.2 and 4.5 we present its application to perturbation of some parameters and myocardial infarction. First, we look at the forward problem. Second, the reduced-order model is used with an evolutionary algorithm to identify some parameters or the location of infarcted regions from the ECGs. The main conclusions of the study are then summarized in Section 4.6.

4.2 Presentation of the model

The electrical activity in the heart is modeled by the bidomain equations (see for instance [Sac04, SLC⁺06]). We briefly recall the main equations used in this chapter. For a detailed description of the models and parameters used in this work we invite the reader to refer to Section 1.4.

Let us consider the heart domain Ω_H . Then the bidomain equations read on

σ_i^l	σ_e^l	σ_i^t	σ_e^t	σ_T^{lung}	σ_T^{rib}	σ_T^{torso}
3.0×10^{-3}	3.0×10^{-3}	3.0×10^{-4}	1.2×10^{-3}	2.4×10^{-4}	4×10^{-5}	6×10^{-4}

Table 4.1: Conductivity parameters in the torso, σ_T and conductivity tensor parameters in the heart according to fibers orientation, $\sigma_{e,i}^l$ longitudinal values, $\sigma_{e,i}^t$ transversal values.

τ_{in}	τ_{out}	τ_{open}	τ_{close}	$\tau_{\text{close}}^{\text{RV}}$	$\tau_{\text{close}}^{\text{endo}}$	$\tau_{\text{close}}^{\text{mcell}}$	$\tau_{\text{close}}^{\text{epi}}$	v_{gate}	v_{min}	v_{max}
16	360	300	100	120	130	140	90	-67	-80	20

Table 4.2: Ionic parameters.

$\Omega_H \times (0, T)$, $T > 0$,

$$\begin{cases} A_m \left(C_m \frac{\partial v_m}{\partial t} + I_{\text{ion}}(v_m, w) \right) - \text{div}(\sigma_i \nabla v_m) - \text{div}(\sigma_i \nabla u_e) & = A_m I_{\text{app}}(x, t) \\ -\text{div}((\sigma_i + \sigma_e) \nabla u_e) - \text{div}(\sigma_i \nabla v_m) & = 0 \end{cases} \quad (4.1)$$

where u_i and u_e are respectively the intra- and the extra-cellular potential and $v_m := u_i - u_e$ is the transmembrane potential. In this chapter we consider the Mitchell and Schaeffer ionic model [MS03] that writes

$$\begin{cases} I_{\text{ion}}(u, w) & = -w \frac{u^2(1-u)}{\tau_{\text{in}}} + \frac{u}{\tau_{\text{out}}} \\ \frac{\partial w}{\partial t} & = \begin{cases} \frac{1-w}{\tau_{\text{open}}}, & u < u_{\text{gate}} \\ -\frac{w}{\tau_{\text{close}}}, & u > u_{\text{gate}} \end{cases} \end{cases} \quad (4.2)$$

where u_{gate} is the changeover voltage, and τ_{in} , τ_{out} , τ_{open} , τ_{close} the ionic parameters. Although this model describes in a very simplified way the ionic exchanges, it allows to recover realistic action potentials at the cell scale.

We made the assumption of uncoupling heart-torso domains as described in detail in Section 1.4.3. Thanks to this assumption, the heart problem can be solved independently of the torso problem. Then, in order to obtain the ECGs, a linear operator, called transfer matrix, is computed and applied to the heart extra-cellular potential solution (see Section 1.4.3). A complete description of non-pathological ECG is given in Chapter 2.

Finally, some appropriate modeling assumptions are made: for instance, we consider cell heterogeneity in heart tissue, anisotropy of the conductivity tensor according to fiber direction, a simplified model of His bundle. We refer to [BCF⁺10] and to Chapter 1 for a description of the modeling choices made in our study.

All the simulations are performed on an idealized geometry of ventricles based on two ellipsoids (see [SMC⁺06]). The spatial discretization is based on the finite element method, and the time discretization is performed using the second order

Backward Differentiation Formula implicit scheme with an explicit treatment of the ionic current. The mesh contains 418,465 tetrahedra, the time-step is fixed to 0.5ms, and the parameters of the model (4.1)-(4.2) are given in Table 4.1 and 4.2.

4.3 Proper Orthogonal Decomposition method

The bidomain equations (4.1) are known to be very demanding from a computation viewpoint, thus we apply a reduced-order method to reduce the computational time. In general, to solve numerically a PDE system with a reduced-order method, the solution is approximated by a Galerkin projection on a finite space whose dimension is much smaller than the dimension of a typical finite element space. In this work we use a method based on the Proper Orthogonal Decomposition (POD). Essentially, POD is a linear procedure that creates an orthogonal basis using a given collection of input data, *e.g.* some finite element method solutions of the problem itself. The principle of the POD method is briefly recalled in Section 1.6.2. We refer for instance to [KV01, RP04] for more details.

4.4 Application of POD to forward problems

In this section, the reduced-order model is used in different configurations and compared with the full-order one. It is important to note that the accuracy is not assessed on the whole solution, but only on the ECG, which is considered as the ‘output of interest’ of these simulations.

4.4.1 POD for changed parameters problems

A POD basis is computed for a given set of parameters. We consider in this section what happens when this basis is used to solve a reduced-order model with different parameters. Our investigation is restricted to τ_{in} , τ_{close} , A_m , C_m since it has been shown in [BCF⁺10] that they are the ones the ECG is the most sensitive to.

Let us first consider a perturbation of τ_{close} , which mainly affects the repolarization phase, that is, the T-wave in the ECG. In our model, the heart is divided in four regions where τ_{close} takes different constant values. We consider the value in the epicardium of the left ventricle τ_{close}^{epi} and in the right ventricle τ_{close}^{RV} . A POD basis of 80 vectors is first constructed with $(\tau_{close}^{epi}, \tau_{close}^{epi}) = (100, 100)$. Then, the corresponding reduced-order model is solved with $(\tau_{close}^{epi}, \tau_{close}^{epi}) = (80, 130)$. Figure 4.1 (left) shows that the full and reduced models are in good agreement. We only refer to the first lead of the ECG for convenience, but the same trend is observed on the other leads. It is interesting to note that the experiment used to generate the POD basis (with $(\tau_{close}^{epi}, \tau_{close}^{epi}) = (100, 100)$) has a negative T-wave (Figure 4.1 right). It is therefore not trivial that the reduced model is able to provide the correct (positive) T-wave. If, instead of considering the ECG only, we compare the extracellular potential u_e of the full and reduced models, the relative difference is 2.3×10^{-2} in

Euclidean norm in $\Omega_H \times [0, T]$, with $T = 500\text{ms}$. The full 3D solutions are therefore in good agreement too.

Consider now perturbations of τ_{in} , A_m , C_m and $\tau_{\text{close}}^{\text{RV}}$. Simulations are run with $\tau_{\text{in}} = 0.8$, $A_m = 200$, $C_m = 10^{-3}$ and $\tau_{\text{close}}^{\text{RV}} = 120$. We compare the ECGs obtained with the full-order model and with the reduced-order model corresponding to a POD basis generated with $\tau_{\text{in}} = 1.5$, $A_m = 200$, $C_m = 2 \times 10^{-3}$ and $\tau_{\text{close}}^{\text{RV}} = 50$. Despite some differences (slight temporal shift or difference of amplitudes, see Figure 4.2 left), the results reasonably match. Again, this matching is not trivial because the ECG corresponding to the values used to generate the POD basis looks totally different (see Figure 4.2 right).

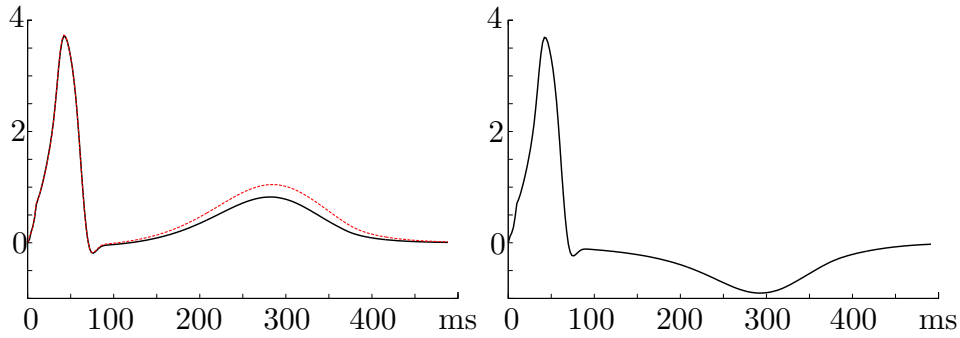


Figure 4.1: Left: First lead of the ECGs with $(\tau_{\text{close}}^{\text{epi}}, \tau_{\text{close}}^{\text{RV}}) = (80, 130)$. Comparison between the full model (dotted red line) and the reduced model (black line) with the POD basis generated with $(\tau_{\text{close}}^{\text{epi}}, \tau_{\text{close}}^{\text{RV}}) = (100, 100)$. Right: First lead of the ECG computed with the full-order model for $(\tau_{\text{close}}^{\text{epi}}, \tau_{\text{close}}^{\text{RV}}) = (100, 100)$.

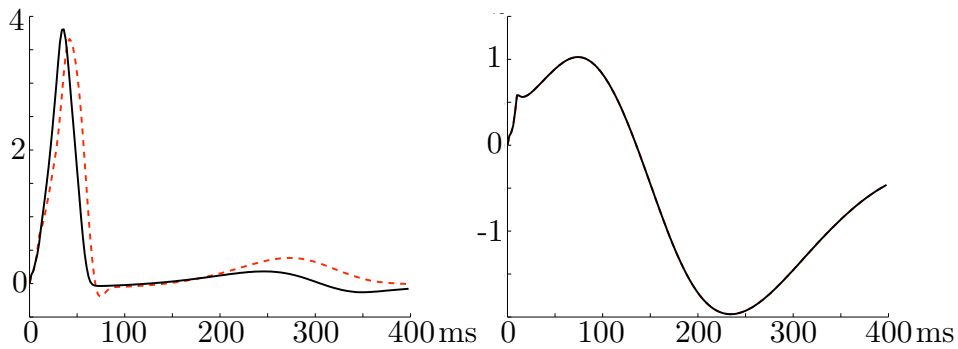


Figure 4.2: Left: First lead of the ECGs with $(\tau_{\text{in}}, C_m, A_m, \tau_{\text{close}}^{\text{RV}}) = (0.8, 10^{-3}, 200, 120)$. Comparison between the full model (dotted red line) and the reduced model (black line) with a POD basis generated with $(\tau_{\text{in}}, C_m, A_m, \tau_{\text{close}}^{\text{RV}}) = (1.5, 2 \times 10^{-3}, 100, 50)$. Right: First lead of the ECG computed with the full-order model for $(\tau_{\text{in}}, C_m, A_m, \tau_{\text{close}}^{\text{RV}}) = (1.5, 2 \times 10^{-3}, 100, 50)$.

4.4.2 Full and reduced-order simulation of an infarction

We are now interested in the simulation of a myocardial infarction both with a full order method and a POD approach. We first describe the procedure used to simulate an infarction with a full order method and then we introduce a POD approximation of the problem.

4.4.2.1 Simulation of myocardial infarction

Heart attacks are one of the leading causes of death for both men and women worldwide. The myocardial infarction (also called *heart attack*) is the consequence of the occlusion of a coronary artery, that causes a deficit of blood in a heart region (ischemia). If the ischemia is left untreated during a long period of time, it can cause an infarction (damage or death of part of the myocardium). One of the tests that can be used to detect heart muscle damage is the ECG.

There are two main kinds of myocardial infarctions: transmural and subendocardial. The last ones involve only a small area in the subendocardial wall of the left ventricle, while the transmural ones are usually the result of a complete occlusion of blood supply and they extend through the whole thickness of the heart muscle. In this work we consider the most common and dangerous ones, left ventricle transmural infarctions. Left ventricle transmural infarctions can be classified according to their position in the heart into posterior, anterior, lateral and inferior.

We simulate this pathology by modifying the ionic model in order to block ionic exchanges. In an infarcted area, the extra-cellular concentration of ions K_+ increases, as explained in details in [PCL07]. The heart tissue is not conductive any more, this leads to a lack of oxygen and consequently to a reduction of Adenosine Tri Phosphate molecules (ATP) production. The deficiency of ATP disturbs the depolarization whose active exchanges occur, *i.e.* with expenditure of energy, and prevents the Na/K pump to be activated, so the flux of ions K_+ and the associated current are negligible.

During the repolarization phase we will act on the associated current. In order to reduce the K_+ current we will decrease the inward current with respect to the outward one by modifying the parameters of the ionic model. In this work our ionic model is the Mitchell and Schaeffer ionic model (4.2) described in section 4.2.

We will model the defect by dividing the parameter τ_{out} by 10 in the infarcted region. With more sophisticated ionic models, we could, for example, modify the behavior of the extracellular potassium [PCL07].

According to electrocardiology books [Dub00, PCF⁺07], the main consequence of an infarction on a real ECG is an elevation or a depression of the ST segment in different leads. The magnitude of this elevation or depression and the leads where these changes are visible depend on the position of infarction. In particular, the main features we should find are as follows:

- in the case of a posterior infarction: a depression in the ST segment in the V_1 and V_2 leads;

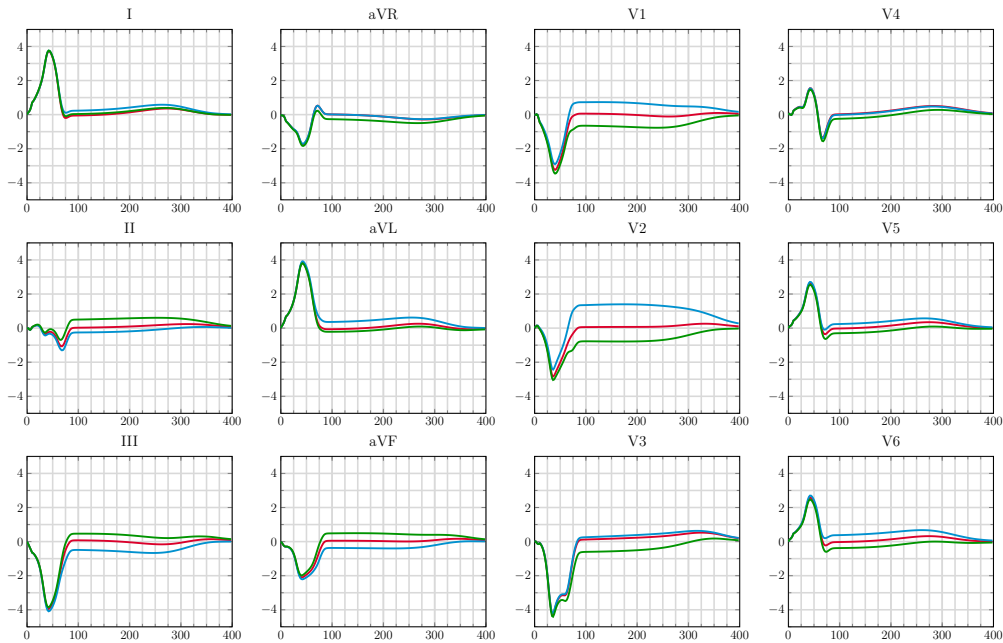


Figure 4.3: Simulated ECG: red line represents the healthy case, blue line the transmural myocardial anterior infarction and green one the posterior infarction.

- in the other cases: an elevation in the ST segment with an inverted T wave;
- in the case of an anterior infarction, we should look at V_1 , V_2 or V_3 , in the case of a lateral infarction at I or aVL and for an inferior infarction at II, III or aVF .

Figures 4.3 and 4.4 show the simulated ECG for the main kinds of infarction: in Figure 4.3, the anterior and the posterior ones, and in Figure 4.4, the lateral and the inferior ones. The result is not very good for the inferior infarction: as expected we see an ST elevation in II, but we also observe an important ST elevation in the last three leads, a depression in III and no sign on aVF , which is not expected. The difficulty of simulating the inferior infarction is probably due to the fact that this zone is very close to the initial activation region. It also seems that the QRS complex are not exactly as they should be. Nevertheless, we find as expected a depression (resp. elevation) of the ST segment in V_1 , V_2 and V_3 leads in presence of a posterior (resp. anterior) infarction. We also find an ST elevation in I and aVL in presence of a lateral infarction. In conclusion, the results obtained with the full-order model for the ST segments are very satisfactory for the anterior, posterior and lateral infarctions.

4.4.2.2 POD application to myocardial infarction

We now propose to investigate the same situations with the reduced-order model. Particularly we would like to build a unique POD basis which can be used to solve a

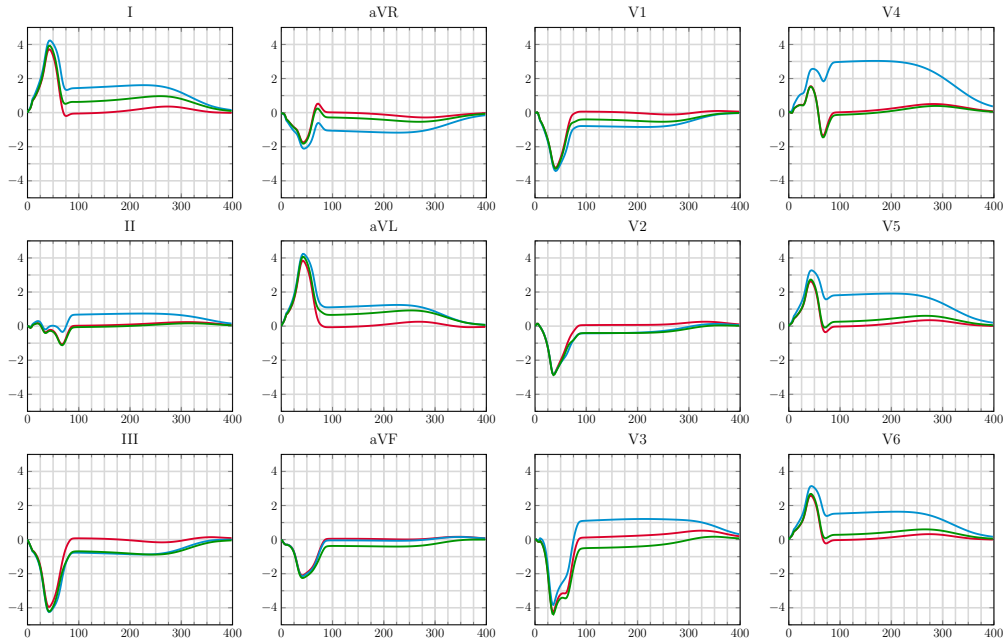


Figure 4.4: Simulated ECG: red line represents the healthy case, blue line the transmural myocardial inferior infarction and green one the lateral infarction.

problem with a generic infarction point.

We first generate the POD basis from the simulation of a heart beat in a healthy case (i.e., without infarction): we run a 400ms simulation for a healthy test case, with a time-step of 0.5ms, keep snapshots every 2ms and obtain a basis of 100 vectors. Then, we use this basis to simulate an infarction centered in the arbitrary red point P indicated by the arrow in Figure 4.5.

A comparison of the green line (reduced-order model) and blue line (full-order model) in Figure 4.6 shows that this basis does not allow to approximate accurately the ECG. A look at the transmembrane potential (Figure 4.7) shows that the POD basis derived from the simulation of a healthy heart beat is indeed unable to capture the sharp variation induced by the infarcted region. This explains the poor results observed on the ECG.

In general, we observe that if we use a POD basis generated for a given infarction area, this POD basis will give very poor results if we use it for a simulation with another infarction area. To improve the approximation property of the POD basis, we propose to enrich the POD basis by collecting the snapshots for different infarction points. More precisely, 100 snapshots are taken from an healthy case and 50 snapshots for each infarction of the 18 points shown in Figure 4.5. Moreover, because most of the solution variation occurs during the first 100ms, half of the snapshots are taken in this period and the other half between 100 and 400ms. Then, a POD basis of 100 vectors is computed as usual.

This new POD basis is used to simulate the infarction on the red point P indicated

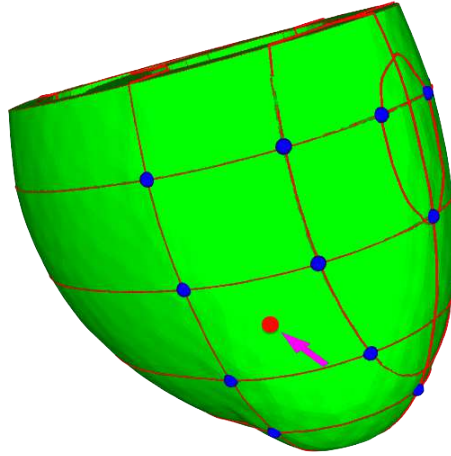


Figure 4.5: The mesh and the 18 points used to build the infarction POD basis. The red point out of the mesh lines, indicated by the pink arrow, is the point P considered in the example.

in Figure 4.5. A comparison of the results obtained with the full and reduced-order models is given in Figure 4.9. Although the results look better than with a basis coming from a pure healthy case, we observe that the solution seems to superimpose the solutions coming from all the nearest infarction points. As a result, the infarcted area seems too large with the reduced-order model during the repolarization phase, which induces a difference of the ST elevations in the corresponding ECG. Indeed, we see in Figure 4.8 that the curves of the ECGs have a similar shape, but different magnitude for the full and reduced-order models. This discrepancy would probably be reduced by refining the grid of the precomputed infarcted regions.

4.5 Application of POD to the identification of some parameter

In this section, we propose an application in parameter identification of the POD method described in the previous section. The first application deals with the identification of the four parameters considered in Section 4.4.1. In the second application, we are interested in recovering the position of an infarction modeled as in Section 4.4.2.1. Note that in this preliminary study, the reference ECGs used for the identification are synthetic, *i.e.* previously computed by the model itself.

4.5.1 Optimization method

Let us present the method which has been used in a general setting. The parameter identification is carried out by minimizing the discrepancy between a

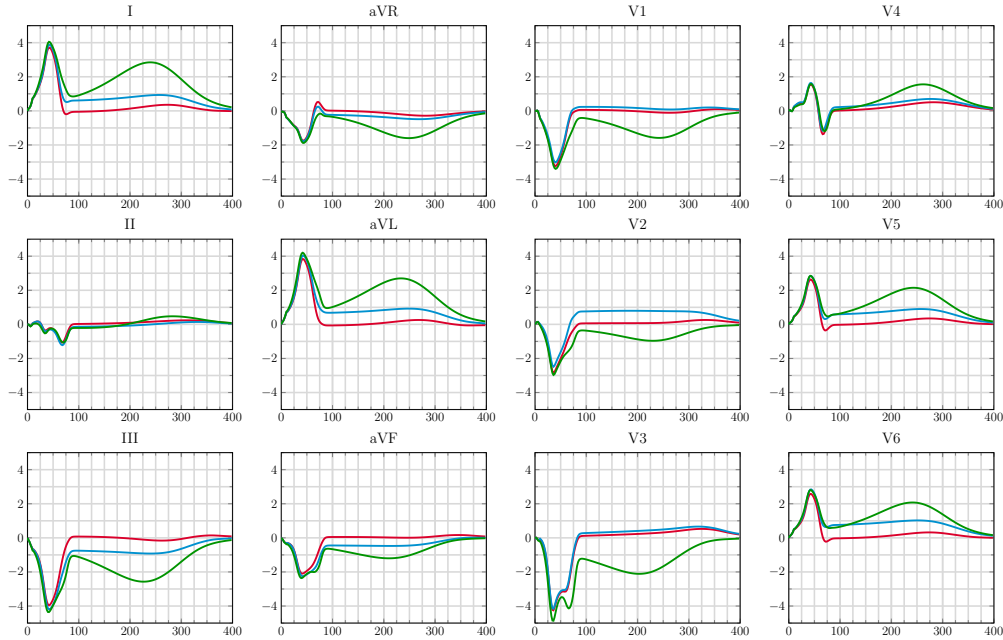
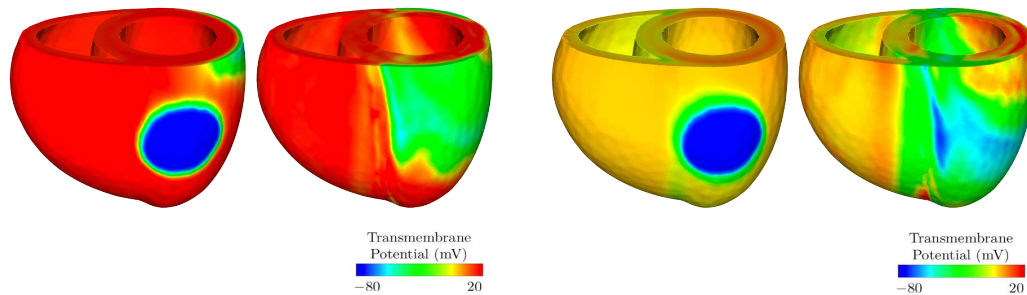


Figure 4.6: Simulated ECGs for an infarction centered in an arbitrary point P with a POD basis generated from the healthy case: ECG with the full model (blue line), ECG with the POD (green line) and healthy full order ECG (red line).



(a) Complete model(left) and reduced-order model (right) at $t = 80$ ms.

(b) Complete model(left) and reduced-order model (right) at $t = 200$ ms.

Figure 4.7: Simulation of an anterior infarction using the complete model (left column) and the reduced model (right column) with a POD basis generated from the healthy case at different time steps.

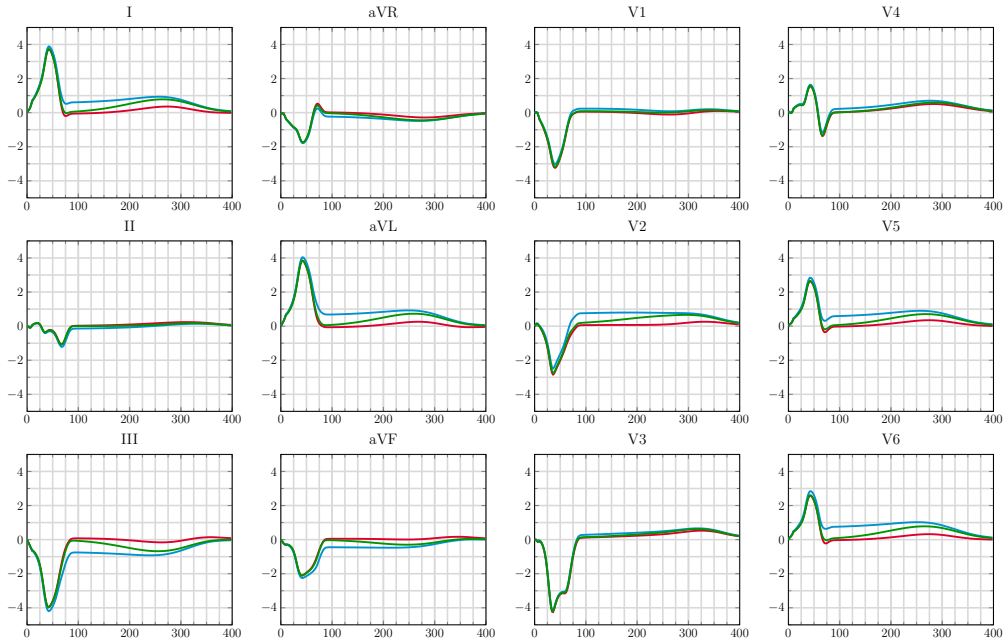
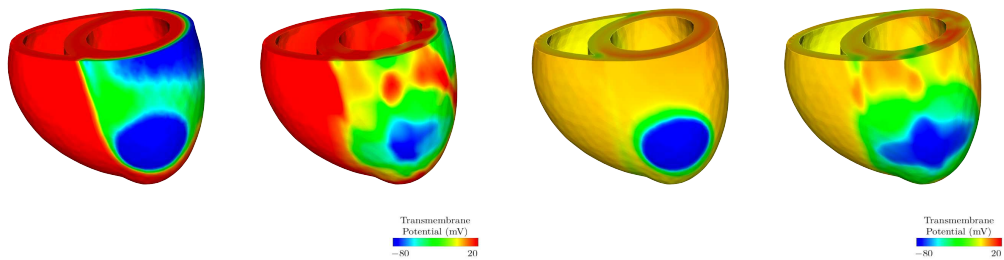


Figure 4.8: Simulated ECGs for an infarction centered in an arbitrary point P with a POD basis generated from the healthy case and the infarction simulations: ECG with the full model (blue line), ECG with the POD (green line) and healthy full order ECG (red line).



(a) Complete model(left) and reduced-order model (right) at $t = 70$ ms. (b) Complete model(left) and reduced-order model (right) at $t = 200$ ms.

Figure 4.9: Simulation of anterior infarction using the complete model (left column) and the reduced model (right column) with a POD basis generated from the healthy case and the infarction simulations at different time steps.

reference ECG and the ECG provided by the model with a given set of parameters. More precisely, let us denote by $n \in \mathbb{N}^*$ the number of parameters and by $\theta \in \mathbb{R}^n$ the vector of parameters we are looking for in a subset \mathcal{I} of \mathbb{R}^n . The subset \mathcal{I} is given by $\mathcal{I}_1 \times \dots \times \mathcal{I}_n$ where $\mathcal{I}_j \subset \mathbb{R}$ is an interval where the value θ_j is assumed to be. The following cost function

$$J(\theta) = \int_0^T |V_I - V_I^{\text{ref}}|^2 + \dots + |V_6 - V_6^{\text{ref}}|^2 dt \quad (4.3)$$

is minimized with respect to $\theta \in \mathcal{I}$, where V_I, \dots, V_6 are the 9 ECG leads given by the simulation for the value θ of the parameters (we consider the three Einthoven leads V_I, V_{II}, V_{III} and the six precordial leads V_1, \dots, V_6) and $V_I^{\text{ref}}, \dots, V_6^{\text{ref}}$ the same leads of the reference ECG. This functional will be approximated by

$$J(\theta) = \delta t \sum_{i=1}^M (|V_{I,i} - V_{I,i}^{\text{ref}}|^2 + \dots + |V_{6,i} - V_{6,i}^{\text{ref}}|^2), \quad (4.4)$$

where W_i is the numerical approximation of $W(t_i)$ for $W = V_I, \dots, V_6, V_I^{\text{ref}}, \dots, V_6^{\text{ref}}$.

This optimization problem is solved by an evolutionary algorithm (see [DEA07, CS10a]). We briefly indicate its main steps, for the sake of completeness. First, an initial population of elements, called individuals, is randomly created. Then, the algorithm modifies the population to promote the best individuals according to the cost function. Considering N_p elements $(\theta_1, \dots, \theta_{N_p}) \in \mathcal{I}^{N_p}$ corresponding to different values of the parameters to identify, the population is regenerated N_g times, where N_g corresponds to the number of generations. At each generation, J is evaluated for each individual, and the population evolves from a generation to another, following three stochastic principles inspired from the Darwinian theory of evolution of species

- Selection: promote the individuals whose value by the cost function is small, the members whose cost function is smaller are preserved in the next generation, whereas those with a high cost function are killed;
- Crossover: create from two individuals a new one by doing a barycentric combination with random and independent coefficients, a linear combination of the two selected vectors is performed to create a new member $\theta \in \mathbb{R}^n$ (for more details see Algorithm 2 in Appendix 4.A);
- Mutation: consist of replacing an individual by a new one randomly chosen in its neighborhood, that is, a member whose values are closer to the referred one in the sense of an Euclidean norm. In our case, the amplitude of the mutation becomes smaller when the number of generations increases (for more details see Algorithm 3 in Appendix 4.A).

At each generation, a one-elitism principle is added to make sure to keep the best individual of the previous population. To summarize the algorithm, a pseudo-code is reported in Algorithm 1 in Appendix 4.A.

Among its advantages, the genetic algorithm can easily be run in parallel. Moreover, unlike deterministic descent methods, which require the computation of the gradient of the cost function, it can be very easily implemented. Its main flaw is to require a large number of evaluations of the direct problem, and because the initial population is chosen randomly, the minimization process has to be run several times. To reduce the number of exact evaluations, we have considered the approximate genetic algorithm on the basis of a surrogate model strategy (see [CS10a]). The idea is to approximate the cost function for a part of the population, taking advantage of the growing database of exact evaluations. The approximation is carried out by interpolation with radial basis functions. The maximum number N_{ex} of total exact evaluations is fixed, and the number of exact evaluations decreases at each generation. For instance, in the case of an initial population of $N_p = 80$ members and a fixed number of $N_g = 15$ generations, we impose the maximum total number of exact evaluations $N_{ex} = 600$; typically, we impose all evaluations to be exact during the first four or five generations, then the number of exact evaluations decreases constantly at each generation (see [CS10a]).

Even with the approximate genetic algorithm, solving the optimization problem is still very time-consuming. Our strategy is thus to speed up the evaluation of the cost function by using the reduced-order model.

4.5.2 Identification of four parameters

In this section, we test our identification strategy for the four parameters τ_{in} , A_m , C_m and τ_{close}^{RV} . The reference ECG used in the cost function is the one computed in Section 4.4.1 obtained with the full-order model for the values $(\tau_{in}, A_m, C_m, \tau_{close}^{RV}) = (0.8, 200, 10^{-3}, 120)$. The values of $(\tau_{in}, A_m, C_m, \tau_{close}^{RV})$ are searched for in the set

$$[0.5, 1.5] \times [100, 300] \times [5 \times 10^{-4}, 2 \times 10^{-3}] \times [50, 150].$$

The key point is to perform the “exact” evaluations required by the optimization algorithm with the reduced-order model. Results presented in Table 4.3 are obtained with 80 POD modes and with the following parameters for the genetic algorithm: $N_p = 120$, $N_g = 12$ and $N_{ex} = 850$. Just to give an idea, the computational time was about 2 days on a PC with 16Go of RAM and using six processors Intel Xeon 3.2 GHz. Each one of the 800 time-steps of the “exact” evaluation requires about 3.5 seconds using the full-order model, while it is reduced to about 0.5 second using the reduced model. If the 850 “exact” evaluations were performed with the full-order model, the computational time will be unacceptable (more than two weeks). The time needed to compute the POD basis is negligible with respect to the time needed by the overall simulation.

The accuracy of the reduced-order model is satisfactory when the four parameters of interest vary within a reasonable range. It is therefore possible to work with a POD basis generated for a single set of parameter θ_0 . This is the approach referred to as **M1** in Tables 4.3 and 4.4. Nevertheless, to improve the accuracy, it is possible

	$(\tau_{in}, A_m, C_m, \tau_{close}^{RV})$	Relative error	Value of J
M1 with $\theta_0 = \theta_0^1$	$(0.95, 185, 9.3 \times 10^{-4}, 126)$	9.6	3.05
M1 with $\theta_0 = \theta_0^2$	$(0.93, 162, 1.05 \times 10^{-3}, 128)$	11.7	7.4
M2	$(0.86, 179, 10^{-3}, 123.5)$	5.2	2.15

Table 4.3: Identification of $(\tau_{in}, A_m, C_m, \tau_{close}^{RV})$ (Reference value $(0.8, 200, 10^{-3}, 120)$).

	$(\tau_{in}, A_m, C_m, \tau_{close}^{RV})$	Relative error	Value of J
M1 with $\theta_0 = \theta_0^1$	$(0.83, 184.2, 1.02 \times 10^{-3}, 123.1)$	4.1	2.2
M1 with $\theta_0 = \theta_0^2$	$(0.91, 153, 1.09 \times 10^{-3}, 126.4)$	12.3	7.55
M2	$(0.83, 189, 1.01 \times 10^{-3}, 123.2)$	3	2.05

Table 4.4: Identification of $(\tau_{in}, A_m, C_m, \tau_{close}^{RV})$ (Reference value $(0.8, 200, 10^{-3}, 120)$) with a larger population.

to use many POD bases computed “off-line” for different values of θ taken in a finite subset \mathcal{A} of I . Next, for a given value $\theta \in I$, the POD basis used for the resolution corresponds to the closest value of $\theta \in \mathcal{A}$. This is the approach **M2** in Tables 4.3 and 4.4.

The relative error is the mean relative error given by the following formula:

$$\frac{1}{4} \left(\frac{|\tau_{in} - 0.8|}{0.8} + \frac{|A_m - 200|}{200} + \frac{|C_m - 10^{-3}|}{10^{-3}} + \frac{|\tau_{close}^{RV} - 120|}{120} \right).$$

Here, $\theta_0^1 = (1, 200, 10^{-3}, 100)$, $\theta_0^2 = (1.3, 170, 1.4 \times 10^{-3}, 90)$ and in the last line of the table, we have considered the POD method **M2** with \mathcal{A} given by

$$\mathcal{A} = \{0.5; 1; 1.5\} \times \{100; 200; 300\} \times \{5 \times 10^{-4}; 10^{-3}; 1.5 \times 10^{-3}; 2 \times 10^{-3}\} \times \{50; 100; 150\}. \quad (4.5)$$

The genetic algorithm is run several times and the results shown corresponds to a mean value. On this example, we see that method **M2** allows approximately to divide the error by 2. The price of this improvement was to compute 108 POD bases. Although this computation was done off-line, this approach therefore requires a significant computational effort. A larger population has also been considered in Table 4.4 with $N_p = 300$, $N_g = 20$ and $N_{ex} = 1700$. Here again, we notice that method **M2** allows to improve the identification results.

4.5.3 Identification of a myocardial infarction

Finally, we are interested in estimating the location of an infarcted area, modeled as explained before. The infarcted area corresponds to a sphere of fixed radius and we want to recover its center denoted by P . Thus we want to identify 3 parameters corresponding to the coordinates $\theta = (x_P, y_P, z_P)$ of P .

We want to minimize the discrepancy between a reference and a simulated ECG,

using the genetic algorithm reported in Section 4.A. The key point is to perform the exact evaluations required by the optimization algorithm with the reduced-order model.

We consider the minimization function (4.4). The reference ECG is obtained by solving the complete model for an infarction area centered at point P as described in Section 4.4.2.2. The genetic algorithm is run with $N_p = 80$, $N_g = 15$ and $N_{ex} = 600$. The point P is only searched for in the left ventricle domain.

The results are reported in Figures 4.10 and 4.11. The reference ECG (blue lines in Figure 4.10) is well approximated by the one obtained from the resolution of the genetic algorithm (green lines). The identified infarcted region is actually very close to the reference one (Figure 4.11). The solution of the genetic algorithm can be improved by including more off-line experiments, as indicated at the end of Section 4.4.2.2.

For a different approach to tackle this problem, we refer to [NLT07]. An interesting possibility to investigate could be to enrich the cost function giving more weight to the ST deviation, as suggested in [GPF⁺04].

4.6 Chapter conclusions

We have presented some results obtained with a reduced-order model of electrophysiology based on the POD method. A well-known difficulty of reduced-order modeling is to identify those situations where the reduced-model can be considered as reliable. We do not claim that we have answered this difficult question in this chapter. Nevertheless, our experiments may suggest some general trends. First, the reduced-order model seems quite robust when the ionic current parameters are perturbed. This may have interesting applications for example to estimate the ionic current parameters in an optimization loop. Second, a reduced-order model based on a single simulation is totally inadequate to approximate a situation with a spatial change in the parameter: this has been shown in the present study for an infarcted region; in [BG11] the same observation was made for the initial activation region. A natural strategy consisting of precomputing several POD bases with different sets of parameters, or a single POD basis from different experiments, proved to be satisfactory in the cases we have considered. Nevertheless, this solution requires an important off-line effort, which makes it difficult to apply with more than a few parameters. Alternative strategies have therefore to be investigated in future works.

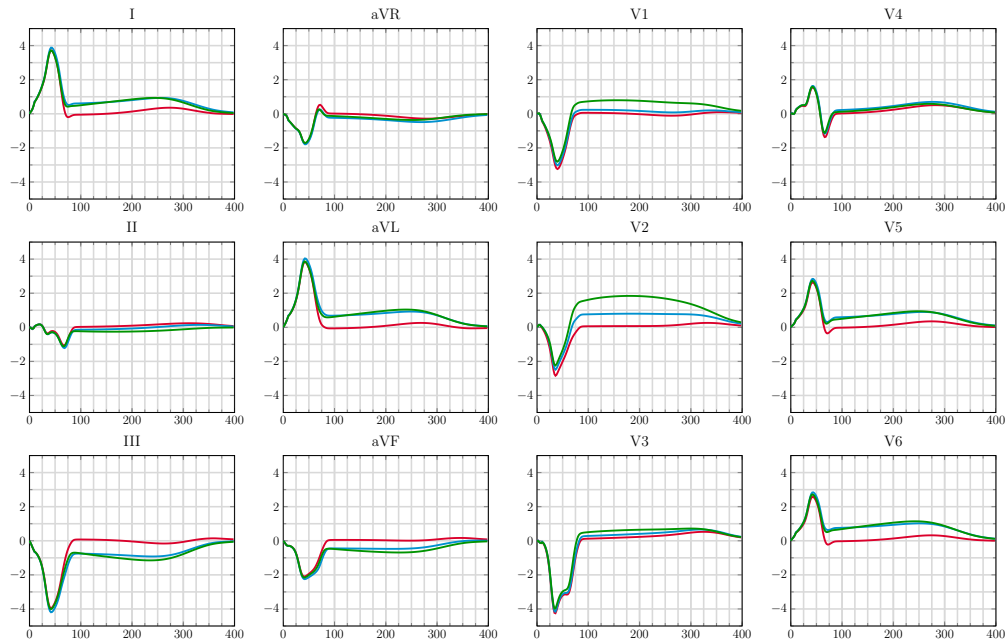
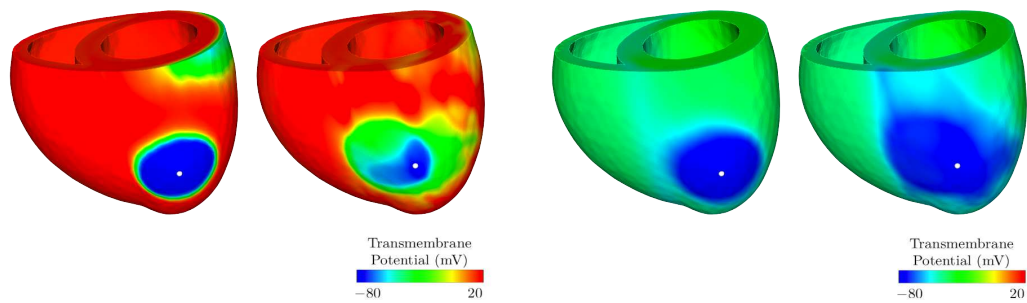


Figure 4.10: Simulated ECG for an infarction located in point P : blue line represents the simulated reference ECG and green line the ECG corresponding to the infarcted center found with the resolution of a genetic algorithm. Red line gives the healthy reference case.



(a) Complete model(left) and reduced-order model (right) at $t = 80$ ms.

(b) Complete model(left) and reduced-order model (right) at $t = 300$ ms.

Figure 4.11: Simulation of an anterior infarction using the complete model (left column) and the reduced model (right column) with a POD basis generated from the healthy case at different time steps.

4.A Genetic algorithm

Algorithm 1 Genetic Algorithm

Choice an initial population $P_1 \subset I$ s.t. $\forall x \in P_0, x_i \in [x_{\min}^i, x_{\max}^i]$
 $n_g = 1$
while $n_g < N_g$ **do**
 evaluate $J(x) \forall x \in P_{n_g}$
 $m = \min_{x \in P_{n_g}} J(x)$
 $X_{n_g} = \arg \min_{x \in P_{n_g}} J(x)$
 elitism :
 if $n_g > 2$ and $J(X_{n_g-1}) < m$ **then**
 $x_{n_g}^i = X_{n_g}$ for a random i
 end if
 for k from 1 to $N_p/2$ **do**
 selection of $(x_{n_g}^\alpha, x_{n_g}^\beta)$
 replace $(x_{n_g}^\alpha, x_{n_g}^\beta)$ with $(y_{n_g}^\alpha, y_{n_g}^\beta)$ by **crossover**
 replace $(y_{n_g}^\alpha, y_{n_g}^\beta)$ with $(z_{n_g}^\alpha, z_{n_g}^\beta)$ by **mutation**
 end for
 $n_g = n_g + 1$
 $P_{n_g} = P_{n_g} \cup X_{\text{new}}$
end while
return $X = \arg \min_{x \in P_{N_g}} J(x)$

Algorithm 2 Crossover

for each couple $X(i), X(i+1)$ **do**
 $u = \text{random coefficient} \in [0,1]$
 $X_{\text{new}}(i) = uX(i) + (1-u)X(i+1)$
end for

Algorithm 3 Mutation

```
for each member of the population  $X(i)$  do  
   $u_1 =$  random coefficient  $\in [0,1]$   
   $u_2 =$  random coefficient  $\in [0,1]$   
  if  $u_1 < 1/2$  then  
     $X_{\text{new}}(i) = X(i) + u_2(X_{\text{max}} - X(i))$   
  else  
     $X_{\text{new}}(i) = X(i) + u_2(X(i) - X_{\text{min}})$   
  end if  
end for
```

Long-time simulations and Restitution Curves with POD

This chapter is dedicated to the study of restitution curves and parameters estimation. Restitution curve (RC) is the relationship between the time of depolarization and the time of previous repolarization of a cell. In this work we consider the Mitchell and Schaeffer ionic model in order to study RC and to investigate some parameters estimation. The Mitchell and Schaeffer model is a phenomenological ionic model which naturally gives rise to an analytical expression of the RC. Previous works used an asymptotic parametrization of this curve, holding under strong model assumptions. As these assumptions do not hold for a complete heart model, we propose a new parametrization which holds for any general parameters choice. First, we use it to estimate the parameters of a zero dimensional model and then we extend the parameters identification method to a three dimensional system. In the last case, the restitution curve is deduced from a synthetic Electrocardiogram (ECG). This definition of ECG-based RC was introduced by Manriquez *et al.* in 2006.

Contents

5.1	Introduction	119
5.2	Presentation of the models	119
5.3	Restitution Curve definition	120
5.3.1	On the minimal value of the gate variable	123
5.3.2	On the asymptotic value of the RC	125
5.4	Parameters identification in 0D case	125
5.5	Parameters identification with an ECG-based RC	126
5.6	Chapter conclusions	129

5.1 Introduction

First, let us give the definition of a Restitution Curve (RC). The restitution curve is the dependence between diastolic interval (DI) and the successive duration of a cardiac action potential (APD). The RC corresponds to the graph of the APD with respect to the previous DI. In the case of a single cell model the DI corresponds to the time during which the transmembrane voltage v_m is smaller than (or equal to) the changeover voltage v_{gate} , while the APD is the time during which the v_m is greater than v_{gate} .

In this work, we focus on the Mitchell and Schaeffer ionic model [MS03] introduced in Section 1.4.2. One of the advantages of this phenomenological model is that it exhibits a new phenomenon that does not occur for other phenomenological models: it naturally give rise to the dependence of the APD as a function of the previous DI. A parametrization of the RC has been introduced in [MS03] under some strong assumption on the parameters. In Section 5.3 we propose a new parametrization of the RC which allows us to relax the assumptions on the parameters. Then, we use this new parametrization in order to identify some parameters in an adimensional case.

The RC is known to be important in the understanding of some arrhythmias [QXGW10, MS03]. The notation of RC can be extended to the whole heart looking at the ECG first lead. DI and APD can be respectively compared to the TQ time, time between the end of T wave and the beginning of the Q wave of the next beat, and the QT time (see Figure 5.5a). This idea has been introduced in [MZM⁺06] and is a way to generalize the notion of restitution curve at the scale of the whole heart. A RC based on ECG is a much more accessible measurement and could allow us to detect pathologies at the scale of the heart.

The simulation of the restitution curve is extremely challenging for 3D models since it requires several dozen of heart beats, whereas the simulation of one heart beat is already very demanding.

In Section 5.5 we reproduce RC based on ECG thanks to 3D numerical simulations. First, we introduce a POD basis in order to run the long time simulations needed to build the RC. Then we use the parametrization introduced in Section 5.3 in order to identify some of the ionic parameters.

5.2 Presentation of the models

The electrical activity in the heart is modeled by the bidomain equations as shown in Section 1.4.1. The extracellular potential u_e and the transmembrane potential v_m

are solutions in the heart domain Ω_H of the following system

$$\begin{cases} A_m(C_m \frac{\partial v_m}{\partial t} + I_{\text{ion}}(v_m, w)) - \text{div}(\sigma_i \nabla v_m) - \text{div}(\sigma_i \nabla u_e) & = A_m I_{\text{app}}(x, t) \\ -\text{div}((\sigma_i + \sigma_e) \nabla u_e) - \text{div}(\sigma_i \nabla v_m) & = 0 \\ \frac{\partial w}{\partial t} + g(v_m, w) & = 0 \end{cases} \quad (5.1)$$

where the functions I_{ion} and g depend on the choice of the ionic model. In this work we consider the Mitchell and Schaeffer ionic model [MS03] described in Section 1.4.2

$$\begin{cases} I_{\text{ion}}(v, h) & = -h \frac{v^2(1-v)}{\tau_{\text{in}}} + \frac{v}{\tau_{\text{out}}} \\ g(v, h) & = \begin{cases} \frac{h-1}{\tau_{\text{open}}}, & v < v_{\text{gate}} \\ \frac{h}{\tau_{\text{close}}}, & v > v_{\text{gate}} \end{cases} \end{cases} \quad (5.2)$$

where v_{gate} is the changeover voltage, and τ_{in} , τ_{out} , τ_{open} , τ_{close} are the ionic parameters. In particular, we are interested in analyzing the behavior of this model in the case of accelerated beats in order to get the related RC, in both 0D and 3D cases.

5.3 Restitution Curve definition

We first deal with a zero dimensional system. Then we consider equations for all $t \geq 0$

$$\begin{cases} \frac{dv}{dt} + I_{\text{ion}}(v, h) & = I_{\text{app}}(t) \\ \frac{dh}{dt} + g(v, h) & = 0 \end{cases} \quad (5.3)$$

coupled with ionic model (5.2). Let us consider the potential v and the gate variable h varying between 0 and 1. We observe that the potential v depends on the inward current $J_{\text{in}} = h \frac{v^2(1-v)}{\tau_{\text{in}}}$ and the outward current $J_{\text{out}} = \frac{v}{\tau_{\text{out}}}$,

$$\frac{dv}{dt} = J_{\text{in}} - J_{\text{out}}, \quad (5.4)$$

where the parameters τ_{in} and τ_{out} are time constants. The gate variable h describes the opening and closing of the ionic channel gate. In particular, it takes value 1 when the gate of the inward current is completely open and takes value 0 when the gate is closed. The behavior of h depends on two parameters, τ_{open} and τ_{close} , that respectively regulate the opening and closing phases.

Mitchell and Schaeffer, in [MS03] parametrize the RC under the assumption

$$\tau_{\text{in}} \ll \tau_{\text{out}} \ll \tau_{\text{open}}, \tau_{\text{close}} \quad (5.5)$$

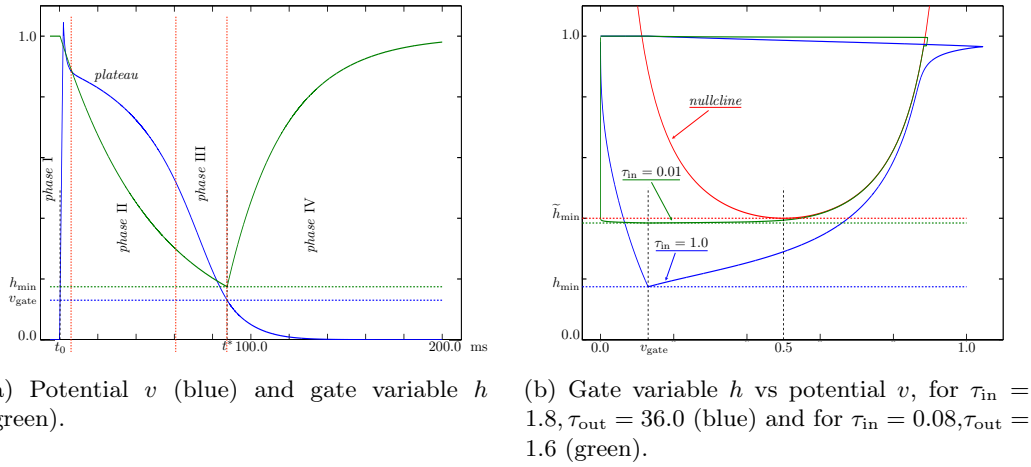


Figure 5.1: Potential v and gate variable h for one electrical cycle of a 0D model. By default, parameters are taken as in Table 5.1.

We want to generalize the results of [MS03], neglecting condition (5.5). In their paper this assumption is the basis of most of the relations they find out, even if they point out that it does not hold for all physiological models. Moreover, in the 3D simulation, see for instance [BCF⁺10] or Chapters 2 and 4, this assumption will not be satisfied.

Let us analyze with precision a cycle of depolarization, see Figure 5.1a. We start from the rest state, it corresponds to point $(v, h) = (0, 1)$ at initial time $t = 0$. The cell electrical cycle is divided into four phases. First, as the gate is open ($h = 1$), the sodium ions Na^+ enter into the cell, this creates an inward ionic current ($I_{\text{ion}} < 0$). So, the potential v increases quickly to 1, *i.e.* the cell depolarizes, with the characteristic time τ_{in} while the gate variable h is almost constant.

Then the gate closes, *i.e.* the gate variable h decreases from 1 to its local minimal value h_{\min} . During the phase of *plateau* the ionic current is negligible, the potential v is almost constant for a time of order τ_{close} .

The repolarization phase follows the *plateau*. The Na/K pump creates an outward ionic current ($I_{\text{ion}} > 0$), so the potential v decreases rapidly during a time of order τ_{out} and the ionic channel is still closed ($h(t) \simeq h_{\min}$).

Finally, during the fourth phase the cell tends to go back to rest and the gate variable increases, $h(t) \simeq 1$. The inward currents are balanced with the outward currents, so $I_{\text{ion}} \simeq 0$ and the potential v is constant.

Let us stimulate a cell at time $t = 0$, as shown in Figure 5.1a. We define $t^0 > 0$

τ_{in}	τ_{out}	τ_{open}	τ_{close}	v_{gate}
1.0	10.0	30.	50.	0.13

Table 5.1: Ionic parameters for 0D model.

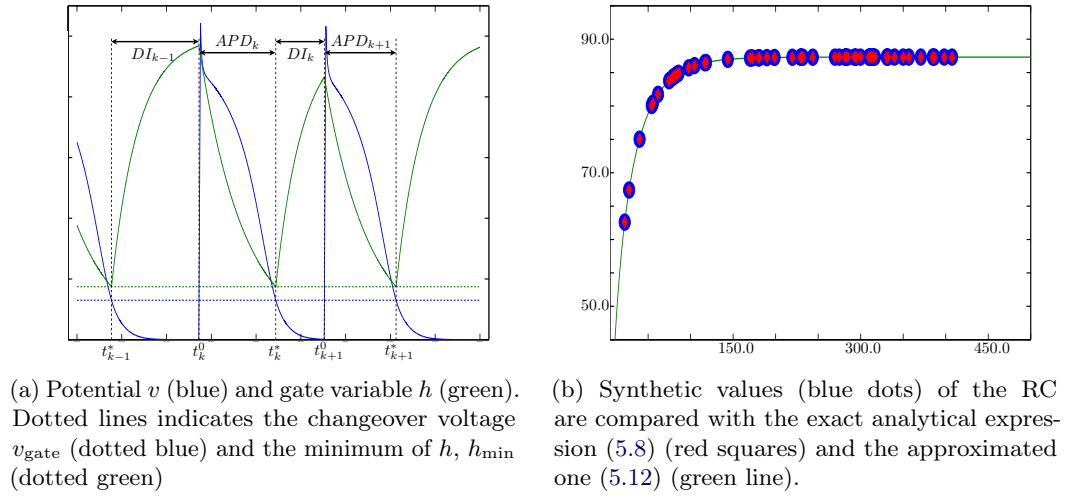


Figure 5.2: On the left hand side, potential v and gate variable h for some electrical cycles of a 0D model. On the right hand side, the associated Restitution Curve. By default, parameters are taken as in Table 5.1.

the time of the beginning of the APD and $t^* > t^0$ the time corresponding to the end of the APD, *i.e.*

- t^0 is the first $t > 0$ such that $v(t^0) = v_{\text{gate}}$, with $v(t) < v_{\text{gate}}$ for any $t < t^0$ and $v(t) > v_{\text{gate}}$ for any $t \in (t^0, t^*)$;
- $t^* > t^0$ is the first time such that $v(t^*) = v_{\text{gate}}$, with $v(t) > v_{\text{gate}}$ for any $t \in (t^0, t^*)$ and $v(t) < v_{\text{gate}}$ for any $t > t^*$.

The local minimal value of the gate variable h is reached at time t^* , $h_{\text{min}} := h(t^*)$. Then, the solution of the second equation of (5.3) can be calculated analytically

$$h(t) = \begin{cases} 1, & 0 < t \leq t_0 \\ e^{-(t-t_0)/\tau_{\text{close}}}, & t^0 < t \leq t^* \\ 1 - (1 - h_{\text{min}})e^{-(t-t^*)/\tau_{\text{open}}}, & t > t^*. \end{cases} \quad (5.6)$$

In order to study the RC, we consider a sequence of different periods beats. We can prove that results do not change in case of accelerated, decelerated or random beats. Let us consider a sequence of $n = 50$ beats of period between 100 and 400ms. We define respectively $|APD_k|$ and $|DI_k|$ the action potential duration and the diastolic interval of the k -th beat, for any $k = 1, \dots, n$ (see Figure 5.2a) and we call respectively t_k^0 and t_k^* the beginning of the k -th APD and DI.

Let us take, as previously, the initial solution $(v, h)(t = 0) = (0, 1)$. If we stimulate the system (5.3) for a sequence of times $\tilde{t}_k > t_k^*$, for any $k = 1, \dots, n$, then the

solution of the second equation of (5.3) is given by

$$h(t) = \begin{cases} 1, & t \leq t_0 \\ h(t_k^0)e^{-(t-t_k^0)/\tau_{\text{close}}}, & t \in APD_k = (t_k^0, t_k^*) \\ 1 - (1 - h(t_k^*))e^{-(t-t_k^*)/\tau_{\text{open}}}, & t \in DI_k = (t_k^*, t_{k+1}^0). \end{cases} \quad (5.7)$$

PROPOSITION 5.1

The Action Potential duration of the $k + 1$ -th beat, $|APD_{k+1}|$, is related to the Diastolic Interval of the previous beat, $|DI_k|$, by equation

$$|APD_{k+1}| = \tau_{\text{close}} \ln \frac{1 - (1 - h(t_k^*))e^{-|DI_k|/\tau_{\text{open}}}}{h(t_{k+1}^*)}. \quad (5.8)$$

Proof. The system of equations (5.3) admits a continuous solution. Then, according to the continuity of the gate variable h at time t_k^* for any $k \geq 1$ we have

$$h(t_k^*) = h(t_k^0)e^{-|APD_k|/\tau_{\text{close}}}. \quad (5.9)$$

Using the expression of $h(t_k^0)$ given by (5.7), we obtain

$$h(t_k^*) = (1 - (1 - h(t_{k-1}^*))e^{-|DI_{k-1}|/\tau_{\text{open}}})e^{-|APD_k|/\tau_{\text{close}}}, \quad (5.10)$$

then

$$h(t_k^*)e^{|APD_k|/\tau_{\text{close}}} = (1 - (1 - h(t_{k-1}^*))e^{-|DI_{k-1}|/\tau_{\text{open}}}), \quad (5.11)$$

which leads to the conclusion of the proposition. ■

REMARK 5.1

If we consider that the local minimum of h , $h(t_k^*)$ is constant, $h_{\min} = h(t_k^*)$, for all $k \geq 1$, then expression (5.8) leads to

$$|APD_{k+1}| = \tau_{\text{close}} \ln \frac{1 - (1 - h_{\min})e^{-|DI_k|/\tau_{\text{open}}}}{h_{\min}}, \quad (5.12)$$

which is the expression given by [MS03]. A discussion on the value of h_{\min} is given in the next paragraph.

5.3.1 On the minimal value of the gate variable

To find out an analytical expression of h_{\min} which depends on the ionic parameters, Mitchell and Schaeffer suppose in [MS03] that the solution (v, h) is on the *nullcline* of the first equation of (5.2) (see Figure 5.1b) thus it satisfies equation

$$0 = h \frac{v^2(1-v)}{\tau_{\text{in}}} - \frac{v}{\tau_{\text{out}}}, \quad (5.13)$$

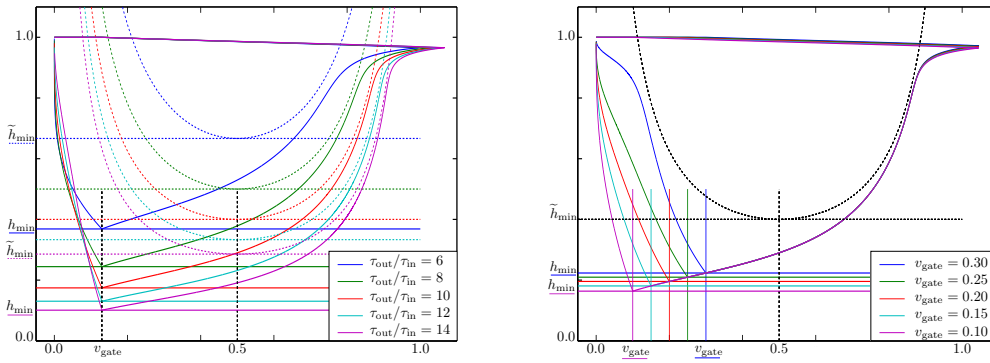
so the relation between h and v is given by

$$h = \frac{\tau_{\text{in}}}{\tau_{\text{out}}} \frac{1}{v(1-v)}. \quad (5.14)$$

Then, the minimal feasible value for h is

$$\tilde{h}_{\text{min}} = 4 \frac{\tau_{\text{in}}}{\tau_{\text{out}}}, \quad (5.15)$$

since $v \in (0,1)$.



(a) Gate variable h vs potential v , varying the value of the parameter τ_{out} from 6.0 to 14.0.

(b) Gate variable h vs potential v , varying the value of the changeover voltage v_{gate} from 0.15 to 0.30.

Figure 5.3: Gate variable h vs potential v for one electrical cycle of a 0D model. By default, parameters are taken as in Table 5.1.

In Figure 5.1b we show the values of h in function of v in two cases. The blue line gives the value for parameters in Table 5.1 while the green line is computed with a smaller value of $\tau_{\text{in}} = 0.01$ and $\tau_{\text{out}} = 0.1$, *i.e.* assumption (5.5) is satisfied only in the second case. We point out that the ratio between τ_{in} and τ_{out} is constant in both cases, $\frac{\tau_{\text{out}}}{\tau_{\text{in}}} = 10$, so that the related *nullcline* (red line) is the same. We remark that the minimum of h corresponding to the green line (assumption (5.5) true) is close to the approximated value \tilde{h}_{min} given by (5.15), while the minimum of the blue one (assumption (5.5) false) is smaller than \tilde{h}_{min} . We can explain this difference if we look at the four different phases. The main condition that has to be respected to correctly evaluate the minimum value of h is that $\tau_{\text{out}} \ll \tau_{\text{open}}$, *i.e.* that the third phase should be negligible compared to the last one. So if we take a smaller τ_{out} this phase is quicker and h stays close to the approximated value.

In order to better investigate the link between the minimal value of h and the ionic parameters, we first compare solutions with different ratio between τ_{in} and τ_{out} . In particular, we change the value of τ_{out} , from 6.0 to 14.0, and take the value of the other parameters as in Table 5.1. In Figure 5.3a we can see that the minimal value of h decreases for higher values of $\tau_{\text{out}}/\tau_{\text{in}}$ as expected, but in any case is always

far from \tilde{h}_{\min} . On the other hand, we investigate the relationship between the h_{\min} and the changeover voltage v_{gate} . In Figure 5.3b we observe a dependence of h_{\min} to v_{gate} . In particular, h_{\min} increases for smaller values of v_{gate} . This confirms that the approximation of h_{\min} by \tilde{h}_{\min} (5.15) may be strongly inaccurate in many cases.

Let us summarize and say that h admits a global minimal value for any parameter set such that $\tau_{\text{out}} > 4\tau_{\text{in}}$. The minimal value of h can be approximated by \tilde{h}_{\min} only if $\tau_{\text{out}} \ll \tau_{\text{open}}$, while in general it depends on the ratio $\tau_{\text{in}}/\tau_{\text{out}}$ and the voltage v_{gate} . Thus, the advantage of the RC expression (5.12) compared to the parametrization given by [MS03] is that it holds for any parameters such that $\tau_{\text{out}} > 4\tau_{\text{in}}$ and any random stimulation sequence.

5.3.2 On the asymptotic value of the RC

Let us better analyze the asymptotic value of the RC given by (5.12). We want to identify the maximal admissible value of the APD. We suppose that the longest APD is related to a stable initial state, *i.e.* $(v, h) = (0, 1)$. In order to reach a stable state the previous DI is supposed to tend to $+\infty$. Then, we define

$$APD_{\infty} := \lim_{|DI_k| \rightarrow \infty} |APD_{k+1}| = -\tau_{\text{close}} \ln(h_{\min}). \quad (5.16)$$

5.4 Parameters identification in 0D case

We observed in the previous section that the RC expression (5.12) perfectly fit some synthetic data, then this equation can be used for the estimation of some parameters. In particular, two ionic parameters can be identified, τ_{open} and τ_{close} , within the longest feasible *APD*.

We simulate a sequence of $n = 50$ beats of random period, varying from 100ms to 500ms, on a single cell model (5.2)-(5.3). Parameters take values given by Table 5.1 and stimulation times $\tilde{t}_k > t_k^*$, for any $k = 1, \dots, n$ as described in Section 5.3. In Figure 5.2a the potential v and the gate variable h are plotted for several beats. We observe that the hypothesis of constant minimal value h_{\min} is numerically verified.

We then build the corresponding RC which will be the reference curve, see Figure 5.2b, and we use their RC to find out the parameters $\theta = (\tau_{\text{open}}, \tau_{\text{close}}, APD_{\infty})$. Referring to [MZM⁺06], we apply a non-linear least square method to minimize the error between the reference curve and the analytical one obtained from equation (5.12). We use the software R¹ to calculate these parameters. The exact solution is $\theta^* = (30, 50, 87.359)$, while the estimated solution is $\theta = (30.01, 49.89, 87.33)$ which is very close to the exact one. The third and fourth columns of Table 5.2 represent respectively the standard deviation of the estimated parameter and the inverse of the relative confidence interval length. We can observe that the standard error is small and that the t-value is more than 10^3 for all the parameters, which means that our solution is estimated with a tiny incertitude.

¹<http://www.r-project.org/>

Parameters	Estimate	Std. Error	t-value
τ_{open}	30.01	$1.157 \cdot 10^{-2}$	$2.594 \cdot 10^3$
τ_{close}	49.89	$4.271 \cdot 10^{-2}$	$1.168 \cdot 10^3$
APD_{∞}	87.33	$7.182 \cdot 10^{-4}$	$1.21585 \cdot 10^5$

Table 5.2: Results obtained with the NLS R algorithm for the curve of Figure 5.2b of a single cell model. Starting point of the algorithm is $\theta_0 = (40,40,100)$. The algorithm converges in 4 iterations and Residual standard error is $4.347 \cdot 10^{-3}$ on 47 degrees of freedom. The exact solution is $\theta^* = (30,50,87.359)$.

τ_{in}	τ_{out}	τ_{open}	$\tau_{\text{close}}^{\text{endo}}$	$\tau_{\text{close}}^{\text{Mcell}}$	$\tau_{\text{close}}^{\text{epi}}$	$\tau_{\text{close}}^{\text{RV}}$	v_{min}	v_{max}	v_{gate}
16	360	100	120	130	140	90	-80	20	-67

Table 5.3: Ionic parameters for heart model.

5.5 Parameters identification with an ECG-based RC

Let us now try to extend the previous study to the 3D problem where the restitution curve is based on the ECG. A long sequence of accelerated beats simulation is run on a simplified heart geometry and the corresponding ECG is obtained with a weak coupling with the thorax as described in Section 1.4.3. The simulation of accelerated heart beat ECG is very challenging from a computational point of view because of the long time simulations and the fact that ECG may be modified when frequency increases. Furthermore, this test presents a medical interest because it can highlight arrhythmia like fibrillation. In order to reduce the computational cost, we propose to apply the POD technique introduced in Section 1.6.2.

Let us first validate the accuracy of the POD method for high frequency simulations. A one-beat finite element simulation is first run. Second, the POD basis is constructed from this simulation (in particular it is sufficient to keep the first 400ms of the solution). Finally, the POD basis is used for a long sequence of accelerated beats. The first beat lasts 1.1 second, which corresponds to an initial heart frequency of about 55 beat per minute. Then the heart rate increases and, after 10 seconds, it reaches a frequency of 110 bpm. We remind that normal heart frequency is between 60 and 100 bpm. When the frequency is higher than 100 bpm, this corresponds to tachycardia and ECG shape becomes unusual.

Figure 5.4 shows the first lead of the ECG obtained with finite element and POD methods. We observe that the two solutions are, as expected, perfectly superposed during the whole simulation.

Once the POD basis is validated, we are interested in using this POD basis to run the parameter identification procedure introduced in the previous section. We run a POD simulation of 60 accelerated beats, frequency varies from 50 beats per minute to 120 bpm. The ionic parameters values are given in Table 5.3. Let us notice that τ_{close} has four values because we have considered different tissues polarization properties. In particular, in the right ventricle its value is given by $\tau_{\text{close}}^{\text{RV}}$, near the

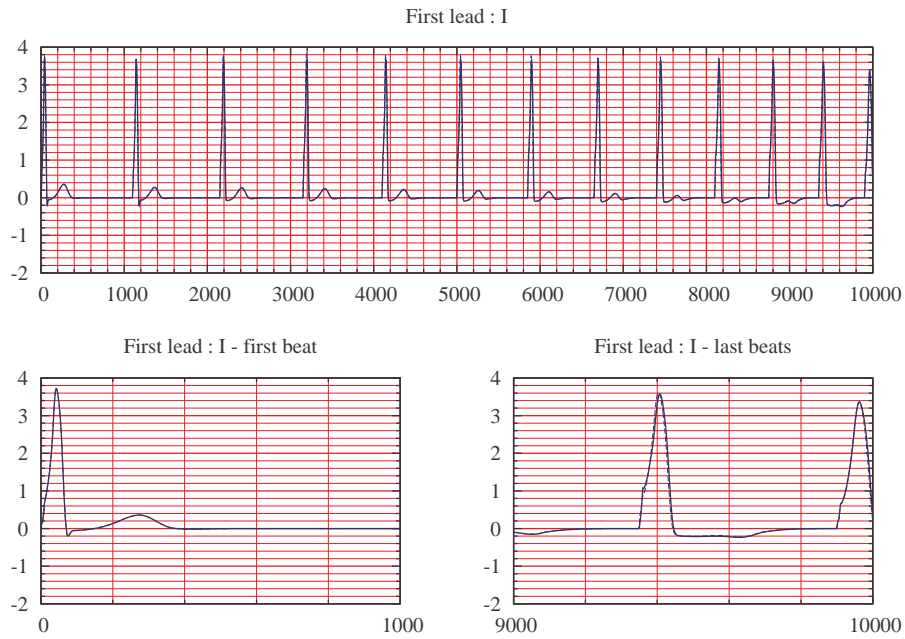
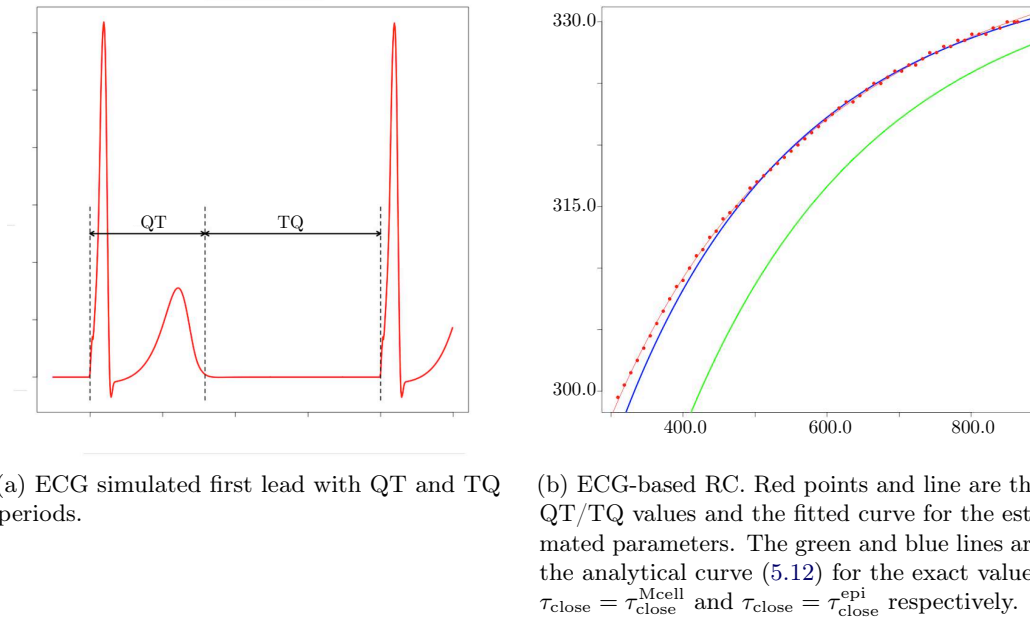


Figure 5.4: Simulated ECG for long period (10 seconds) for accelerated beats (55 beats per minute to 110 bpm) with the finite element method (continuous line) and with the POD (dotted line).



(a) ECG simulated first lead with QT and TQ periods.

(b) ECG-based RC. Red points and line are the QT/TQ values and the fitted curve for the estimated parameters. The green and blue lines are the analytical curve (5.12) for the exact values $\tau_{close} = \tau_{close}^{Mcell}$ and $\tau_{close} = \tau_{close}^{epi}$ respectively.

Figure 5.5: Results from a 75 accelerated beats simulation on the heart domain with parameters of Table 5.3.

Parameters	Estimate	Std. Error	t-value
τ_{open}	369.3480	7.1018	55.81
τ_{close}	63.4092	0.9488	66.83
APD_{∞}	337.7764	0.2443	1382.79

Table 5.4: Results obtained with the NLS R algorithm for the curve of Figure 5.5b: ECG-based RC. Starting point of the algorithm is $\theta_0 = (200, 200, 400)$. The algorithm converges in 6 iterations and Residual standard error is 0.1503 on 57 degrees of freedom. The exact solution is $\theta^* = (300, [90, 140], 335)$. The parameter τ_{close} is heterogeneous and takes four different values depending on its geometry location: 120 in the right ventricle, 130 on left ventricle endocardium, 90 on left ventricle epicardium and 140 in left ventricle medium cells.

left ventricle endocardium it is $\tau_{\text{close}}^{\text{endo}}$, $\tau_{\text{close}}^{\text{dpi}}$ at the left ventricle epicardium and $\tau_{\text{close}}^{\text{Mcell}}$ in the left ventricle myocardium. For more details about the tissue heterogeneity we refer to Section 1.4.4.

As mentioned above, an ECG-based RC is the relationship between the QT time and the previous TQ period (Figure 5.5a). Using the T-wave detection algorithm implemented in [ZIMM⁺05], we obtain the RC in Figure 5.5b (red dots). We observe that the trend of this curve is very close to the blue line which corresponds to equation (5.12) whose ionic parameters are given in Table 5.3, with $\tau_{\text{close}} = \tau_{\text{close}}^{\text{epi}}$, to confirm that the ECG-based RC is related to the standard RC based on APD and DI.

In order to identify the ionic parameters τ_{open} , τ_{close} and the asymptotical value of the RC APD_{∞} we use a nonlinear least square method, within the software R. Results are reported in Table 5.4, exact solution is $\theta^* = (300, [90, 140], 335)$. The APD_{∞} is found with small error and incertitude, while ionic parameters are more difficult to estimate. A 15% relative error is committed on the estimation of τ_{open} and a 30% relative error is committed on the estimation of τ_{close} if the exact solution is assumed to be the $\tau_{\text{close}}^{\text{epi}}$ value. Furthermore, the t-value for ionic parameters reported in Table 5.4 tell us that an incertitude on this estimation is admitted. We remark that the τ_{close} value that we should look for is not the $\tau_{\text{close}}^{\text{epi}}$ value, but a sort of mean value which is not specified. Then, the error committed on the identification of the parameters it is not a good estimator since a more appropriate value of the mean τ_{close} value could be found.

A remark is in order. The error committed on the evaluation of the parameters is only a partial indicator of the estimation. In fact, we have considered $\tau_{\text{close}} = \tau_{\text{close}}^{\text{epi}}$ while four different values are taken into account in the simulation of the reference RC. This, suggest us to consider a “mean” τ_{close} value whose expression could be subject of future works.

5.6 Chapter conclusions

In this chapter, we have proposed a new parametrization of the RC for Mitchell and Schaeffer ionic model (5.2) which is valid in a more general setting. The use of the RC in electrophysiology may represent a new and very fast method for the identification of some parameters. In a one-cell model results with the proposed new parametrization leads to satisfactory solutions and allows to estimate the parameters τ_{open} and τ_{close} . We prospect that the estimation of the parameter h_{min} may lead to the identification of other ionic parameters such as v_{gate} or the rate between τ_{in} and τ_{out} . The study of ECG-based RC is promising too. The estimated values of the ionic parameters are not precise but the approach based on RC represents a costless technique and the result given by this method can be used for instance as an initial guess of iterative methods.

Reduced Order Model with Approximated Lax Pairs

In this chapter a reduced-order method based on Approximated Lax Pairs (ALP) is applied to the integration of electrophysiology models. The main characteristic of ALP method is the time dependence of the basis. In other reduced-order methods, such as the Proper Orthogonal Decomposition used for instance in Chapters 4 and 5, the basis on which the solution is searched evolves in time according to the problem dynamic. Second, contrary to other reduced-order methods, ALP is not based on an off-line/on-line strategy then it is well adapted in case for instance of variable parameters. In this chapter, the method is tested on two and three dimensional electrophysiology test-cases, of increasing complexity. The solutions are compared to the ones obtained by a finite element method. The reduced-order simulation of pseudo-electrocardiograms based on ALP is proposed in the last part.

The results presented in this chapter lead to the manuscript
Damiano Lombardi, Jean-Frédéric Gerbeau, Elisa Schenone. **Reduced Order Model in Cardiac Electrophysiology with Approximated Lax Pairs**. To appear in *Advances in Computational Mathematics*, Special Issue on MoRePas.

Contents

6.1	Introduction	133
6.2	The ALP method	134
6.2.1	Time-dependent basis construction	134
6.2.2	Links with the Lax Pairs	135
6.2.3	Reduced order approximation of the Lax operators	136
6.2.4	Complements on the ALP method	138
6.3	ALP in cardiac electrophysiology	140
6.3.1	ALP for the monodomain equations	141
6.3.2	ALP for the bidomain equations	144
6.4	Numerical experiments	146
6.4.1	Preliminary comments about POD	146
6.4.2	A few comments on the choice of χ	147
6.4.3	Homogeneous parameters 2D case	147
6.4.4	Heterogeneous ionic parameters	152
6.4.5	Source terms	156
6.4.6	Pseudo-electrocardiograms	158
6.5	Chapter conclusions	161

6.1 Introduction

This work is devoted to application of a reduced-order method based on Approximated Lax Pairs (ALP) to cardiac electrophysiology. ALP method has been introduced in [GL14] where the ability of this method to handle propagation phenomena was considered. In the present work, we focus more specifically on its behavior for parametric problems.

From a Reduced-Order Modeling (ROM) standpoint, cardiac electrophysiology is a challenging context. Indeed, the systems describing the electrical activation of tissues are nonlinear, they exhibit front propagations, and they depend on many parameters. For example, the possible presence of infarcted regions requires a modification of the space dependence of some reaction parameters. Similarly, the possible initiation of ectopic stimulations yields source terms which can change in space and in time. Consequently, as shown in Chapter 4 in the case of an infarcted region, a suitable basis can be found but a very large space of parameters has to be visited in order to cover all the possible scenarios.

The ability to deal with parametric systems is one of the main issues in model reduction. We refer for instance to [RHP07] for a discussion on affinely parametrized elliptic partial differential equation systems. The standard methods of model reduction are often based on the construction of a database of pre-computed simulations. Proper Orthogonal Decomposition is a paradigmatic example, as we showed in Chapter 4 and which is widely used in many applications (see e.g. [AF08, HLB96, K VX04, Sir89]). The need of a database can become an issue when dealing with high dimensional parametric spaces, since the construction of the database can be extremely demanding both in time and memory. The method ALP considered in this work does not rely on a database. It therefore avoids the need of an off-line exploration of a large parametric space. Instead, it makes a basis evolve in a way dependent on the dynamics of the solution. In all the examples given in this work, the method will be systematically compared to a full-order model obtained by finite element. For illustration purposes only, it will also be compared to the POD computed from a “simple” set of precomputed solutions.

The structure of the Chapter is as follows. In Section 6.2, the ALP method is detailed. The general principle of the method is recalled in Section 6.2.1, useful complements are presented in Section 6.2.4, then the necessary steps to apply the method to the monodomain and bidomain equations are presented in Sections 6.3.1 and 6.3.2 respectively. In Section 6.4 various numerical experiments are proposed. The first example is a 2D propagation in an isotropic uniform medium. Then, a synthetic infarction is simulated and the problem of ectopic stimuli is investigated. The last case is the 3D simulation of a pseudo-electrocardiogram. Some perspectives of the present study, that are strongly related to the method introduced in Chapter 8, are presented in the conclusion.

6.2 The ALP method

In this section the reduced-order method used in the present work is detailed. It is hereafter derived for a generic PDE of the form:

$$\partial_t u = F(u, \partial_x^{(n)} u), \quad (6.1)$$

where $u(x, t)$, $x \in \Omega \subseteq \mathbb{R}^d$, $t \in (0, 1)$ is the solution of the PDE, with specified initial and boundary conditions. For simplicity, $F(u, \partial_x^{(n)} u)$ will be denoted by $F(u)$.

The basic idea of the method, first proposed in [GL14], is to define a time evolving modal expansion of the form

$$\hat{u}(x, t) = \sum_{i=1}^{N_M} \beta_i(t) \varphi_i(x, t), \quad (6.2)$$

where \hat{u} is the low dimensional approximation of the PDE solution, $\beta_i(t)$ is the representation of \hat{u} in the space defined by the N_M modes $\varphi_i(x, t)$. In order to completely define the basis evolution, an equation and an initial condition for the modes have to be specified. Other works in the literature deal with this type of decomposition. Recent examples are the dynamic low-rank decomposition (see for instance [KL07]), the orthogonal field equations (see [SP09]) and the bi-orthogonal decomposition method presented in [CHZ13a, CHZ13b] to integrate stochastic PDEs.

The hypothesis and the governing equations of the ALP method are detailed in the remainder of this section. It will be assumed that $\langle \varphi_i, \varphi_j \rangle = \delta_{ij}$, $\forall t$, where $\langle \cdot, \cdot \rangle$ is the standard $L^2(\Omega)$ scalar product, δ_{ij} is the Kronecker delta.

Among all the possible formalisms that allow us to define a time-traveling mode expansion, an operator-based approach is chosen. The modes are retrieved in the set of the eigenfunctions of a time varying operator \mathcal{L}_χ which linearly depends upon the solution of the partial differential equation. The operator is represented by its spectrum and its eigenfunctions, which evolve under the action of an evolution operator (the same for all the eigenfunctions), denoted by \mathcal{M} . When applied to integrable systems of equations, these operators are the representation of a Lax pair, as pioneered in [Lax68].

6.2.1 Time-dependent basis construction

In this section, we gather the main results presented in [GL14]. The modes are, at every time instant, a subset of the eigenfunctions of a linear (with inverse compact) selfadjoint operator of Schrödinger-type associated to the potential $-\chi u$

$$\mathcal{L}_\chi(u) \varphi_i = \lambda_i \varphi_i, \quad (6.3)$$

$$(6.4)$$

where u is the solution of (6.1), χ is a real scalar parameter and L is typically $-\Delta$, or any other linear selfadjoint elliptic operator. Then, the modes φ_i are defined as

the eigenfunctions of $\mathcal{L}_\chi(u)$:

$$\mathcal{L}_\chi(u)\varphi := L\varphi - \chi u(x,t)\varphi. \quad (6.5)$$

The choice of the operator is arbitrary (to some extent), and it will be commented in the last part of this work. Let us assume that u has the regularity that justifies the following steps of the derivation.

The operator evolves in time since it depends upon the solution of the PDE. This has important consequences for parametric systems, as it will be investigated by means of numerical experiments. Moreover, it is linear, selfadjoint with a compact inverse for every time, *i.e.* it defines, for every time, an orthonormal basis which is a complete basis of $L^2(\Omega)$.

Let $Q(t)$ be an orthogonal application ($Q^T Q = Q Q^T = I_d$) such that $\varphi_m(t) = Q(t)\varphi_m(0), \forall m$. Taking the time derivative, we have

$$\partial_t \varphi_m(t) = \partial_t Q(t)\varphi_m(0) = \partial_t Q(t)Q^T(t)\varphi_m(t). \quad (6.6)$$

Thus, defining the operator $\mathcal{M}(t) = \partial_t Q(t)Q^T(t)$, the dynamic satisfied by the basis function is defined by

$$\partial_t \varphi_m(t) = \mathcal{M}(t)\varphi_m(t). \quad (6.7)$$

Note that $\mathcal{M}^T = Q\partial_t Q^T = -\partial_t Q Q^T = -\mathcal{M}$, indeed \mathcal{M} is skew-symmetric.

To derive the relations between \mathcal{L}_χ and \mathcal{M} , we take the time derivative of the mode definition (6.3)

$$(\mathcal{L}_\chi - \lambda_i \mathcal{I})\partial_t \varphi_i = \dot{\lambda}_i \varphi_i + \chi F \varphi_i, \quad (6.8)$$

$$(\mathcal{L}_\chi + [\mathcal{L}_\chi, \mathcal{M}])\varphi_i = \dot{\lambda}_i \varphi_i, \quad (6.9)$$

where we define the commutator $[\mathcal{L}, \mathcal{M}] = \mathcal{L}\mathcal{M} - \mathcal{M}\mathcal{L}$. This equation defines the modes evolution. Remark that the PDE expression enters explicitly in the modes evolution. Since the whole modal set is a complete basis, this equation provides a way to compute a smooth change of basis and the representation of this change may be represented on the basis itself, at each time.

6.2.2 Links with the Lax Pairs

Although this is not necessary for what follows, let us briefly show the links between $(\mathcal{L}_\chi, \mathcal{M})$ with the operators introduced by Lax in his seminal work [Lax68]. To integrate a class of nonlinear evolution PDEs, Lax introduced a pair of linear operators $\mathcal{L}(u)$ and $\mathcal{M}(u)$, where u denotes the solution of the PDE. These operators play the same role as in the previous section: the operator $\mathcal{L}(u)$ is defined as in (6.5) and its eigenfunctions are propagated by $\mathcal{M}(u)$ as in (6.7). Lax focused on those particular cases when $\mathcal{L}(t)$ is orthogonally equivalent to $\mathcal{L}(0)$, *ie* when there exists $Q(t)$ orthogonal such that $\mathcal{L}(t) = Q(t)\mathcal{L}(0)Q^T(t)$. Then, defining as before $\mathcal{M} = \partial_t Q Q^T$, we have

$$\partial_t Q^T \mathcal{L} Q + Q^T \partial_t \mathcal{L} Q + Q^T \mathcal{L} \partial_t Q = 0, \quad (6.10)$$

left-multiplying by Q and right-multiplying by Q^T , we obtain the Lax equation:

$$\mathcal{L} + [\mathcal{L}, \mathcal{M}] = 0, \quad (6.11)$$

A comparison of (6.10) and (6.11), shows that in those cases the eigenvalues satisfy $\partial_t \lambda_m = 0$. In other words, when equation (6.11) is satisfied, operators \mathcal{L} and \mathcal{M} are said to be a Lax pair.

6.2.3 Reduced order approximation of the Lax operators

The following proposition shows that it is possible to compute an approximate representation of $\mathcal{M}(u)$ and to derive an evolution equation satisfied by the eigenvalues of $\mathcal{L}_\chi(u)$.

PROPOSITION 6.1 ([GL14])

Let u be a solution of equation (6.1). Let $\mathcal{L}_\chi(u)$ be defined by (6.3). Let $N_M \in \mathbb{N}^*$. For $m \in \{1, \dots, N_M\}$, let $\lambda_m(t)$ be an eigenvalue of $\mathcal{L}_\chi(u(x,t))$, and $\varphi_m(x,t)$ an associated eigenfunction, normalized in $L^2(\Omega)$. Let $\mathcal{M}(u)$ be the operator defined in (6.7). Then the evolution of λ_m is governed by

$$\partial_t \lambda_m = -\chi \langle F(u) \varphi_m, \varphi_m \rangle, \quad (6.12)$$

and the evolution of φ_m satisfies, for $p \in \{1, \dots, N_M\}$,

$$\langle \partial_t \varphi_m, \varphi_p \rangle = M_{mp}(u), \quad (6.13)$$

with

$$\begin{cases} M_{mp}(u) &= \frac{\chi}{\lambda_p - \lambda_m} \langle F(u) \varphi_m, \varphi_p \rangle, & \text{if } p \neq m \text{ and } \lambda_p \neq \lambda_m, \\ M_{mp}(u) &= 0, & \text{if } p = m \text{ or } \lambda_p = \lambda_m. \end{cases} \quad (6.14)$$

We will denote by $M(u) \in \mathbb{R}^{N_M \times N_M}$ the skew-symmetric matrix whose entries are defined by $M_{mp}(u)$.

The proof of this proposition is based on a direct computation and it is shown in detail in [GL14]. The matrix M is a representation of the operator \mathcal{M} on the modes at time t . This representation is convenient from a computational standpoint since it can easily be obtained from the expression $F(u)$ defining the PDE (6.1), without any *a priori* knowledge of $\mathcal{M}(u)$. With this approximation of $\mathcal{M}(u)$, the evolution of the modes can be computed according to the nonlinear dynamics of the system. This is an important difference with standard reduced-order methods, like POD, where the modes are fixed once for all. To set up a reduced order integration method, only a small number N_M of modes will be retained.

Equation (6.3) defines a Hilbert basis, which is used to approximate the solution

$u \in L^2(\Omega)$:

$$\tilde{u}(x) = \sum_{m=1}^{N_M} \beta_m \varphi_m(x). \quad (6.15)$$

Proposition 6.1 gives an approximated way to propagate the eigenmodes and the eigenvalues. Function $F(u)$ is approximated by

$$\tilde{F}(u) = \sum_{m=1}^{N_M} \gamma_m \varphi_m. \quad (6.16)$$

Using these approximations in the PDE (6.1), the following holds

$$\sum_{m=1}^{N_M} \dot{\beta}_m \varphi_m + \beta_m \partial_t \varphi_m = \sum_{m=1}^{N_M} \gamma_m \varphi_m.$$

Projecting this relation on φ_p , and using (6.13), the expression of the PDE on the reduced basis is obtained

$$\dot{\beta} + M\beta = \gamma.$$

Defining $\Theta_{ij} = \langle \tilde{F}(u) \varphi_j, \varphi_i \rangle$, (6.12) and (6.13) are approximated by

$$\dot{\lambda}_i = -\chi \Theta_{ii},$$

and, for $\lambda_i \neq \lambda_j$,

$$M_{ij} = \frac{\chi}{\lambda_j - \lambda_i} \Theta_{ij},$$

respectively. The third order tensor $\langle \varphi_k \varphi_j, \varphi_i \rangle$ is denoted by T_{ijk} . By definition

$$\Theta_{ij} = \langle \tilde{F}(u) \varphi_j, \varphi_i \rangle = \sum_{k=1}^{N_M} \gamma_k T_{ijk}.$$

Computing the time derivative of T_{ijk} gives

$$\dot{T}_{ijk} = \langle \partial_t \varphi_k \varphi_j, \varphi_i \rangle + \langle \varphi_k \partial_t \varphi_j, \varphi_i \rangle + \langle \varphi_k \varphi_j, \partial_t \varphi_i \rangle.$$

Thus

$$\dot{T}_{ijk} = \{M, T\}_{ijk}^{(3)}, \quad (6.17)$$

where

$$\{M, T\}_{ijk}^{(3)} = \sum_{l=1}^{N_M} (M_{li} T_{ljk} + M_{lj} T_{ilk} + M_{lk} T_{ijl}).$$

For the specific problem of interest, a relation linking γ and β will be also derived.

The set of equations which describes the dynamics in the reduced order space is

$$\left\{ \begin{array}{l} \dot{\beta}_i + \sum_{m=1}^{N_M} M_{im} \beta_m - \gamma_i = 0, \\ \dot{\lambda}_i + \chi \sum_{m=1}^{N_M} T_{im} \gamma_m = 0, \\ \dot{T}_{ijk} = \{M, T\}_{ijk}^{(3)}, \\ M_{ij} = \frac{\chi}{\lambda_j - \lambda_i} \sum_{m=1}^{N_M} T_{ijm} \gamma_m, \\ \gamma_i = \gamma_i(\beta), \end{array} \right. \quad (6.18)$$

for $i, j, k = 1 \dots N_M$.

REMARK 6.1

The complexity of the resolution of system (6.18) scales with N_M^3 . As a consequence, the method is only efficient when a small number of basis functions is sufficient to reach the desired accuracy. This actually happens in many cases, as shown in Section 6.4.3. For the cases when a higher number of modes is required, a less expensive variant of the method is currently under investigation, see next chapter.

6.2.4 Complements on the ALP method

6.2.4.1 Evolution of more complex tensors

In the previous section, it was shown how the third order tensor T_{ijk} evolves in time. Depending on the partial differential equation of interest, other tensors may appear in equation (6.18)₅. For the electrophysiology problems considered in this work, it will be useful to study the following type of tensor

$$\mathcal{A}_{i_1, \dots, i_k} := \int_{\Omega} \ell_1(\varphi_1) \dots \ell_k(\varphi_k) d\Omega, \quad (6.19)$$

where the ℓ_i are linear operators which commute with time. The time evolution equation for this tensor reads

$$\partial_t \mathcal{A}_{i_1, \dots, i_k} = \sum_{h=1}^k \int_{\Omega} \ell_i(\partial_t \varphi_h) \dots \ell_k(\varphi_k) d\Omega = \sum_{h=1}^k \sum_{l=1}^{N_M} M_{hl} \mathcal{A}_{i_1, \dots, i_l, \dots, i_k}. \quad (6.20)$$

Let us consider an example with a fourth-order tensor

$$D_{ijkh} = \int_{\Omega} \ell_1(\varphi_i \varphi_j) \ell_2(\varphi_k \varphi_h) d\Omega. \quad (6.21)$$

Then, differentiating in time

$$\partial_t D_{ijkh} = \{M, D\}_{ijkh}^{(4)} = \sum_{l=1}^{N_M} M_{il} D_{ljkh} + \sum_{l=1}^{N_M} M_{jl} D_{ilkh} + \sum_{l=1}^{N_M} M_{kl} D_{ijlh} + \sum_{l=1}^{N_M} M_{hl} D_{ijkl}. \quad (6.22)$$

This will be used in Section 6.3.1.

6.2.4.2 Reconstruction in the high dimensional space

The reconstruction of the solution in the high dimensional space is now detailed. Contrary to standard approaches, this step is not trivial since the basis is time-evolving.

The derivative of the modes can be approximated in the space defined by the modes at the current time instant as follows:

$$\partial_t \varphi_i \approx \sum_{h=1}^{N_M} M_{hi} \varphi_h, \quad (6.23)$$

where the matrices $M \in \mathbb{R}^{N_M \times N_M}$ have been computed during the integration stage.

The practical implementation of the algorithm is the following. The modes are extracted at the very beginning by solving the spectral problem. The initial space is $\Phi^{(0)} := \text{span}\{\varphi_1(x, 0), \dots, \varphi_{N_M}(x, 0)\}$.

Then, at every time instant a two-step scheme is applied. First, the modal space Φ is updated:

$$\Phi^{(n+1)} = \Phi^{(n)} + \Delta t \mathcal{H}(M, \partial_t \Phi), \quad (6.24)$$

where $\Phi \in \mathbb{R}^{\mathcal{N} \times N_M}$ and \mathcal{H} denotes an integration scheme (that can be either explicit or implicit).

For instance, if a second order Crank-Nicolson scheme is used, the update reads:

$$\Phi^{(n+1)} = \Phi^{(n)} + \frac{\Delta t}{2} \left(\Phi^{(n+1)} M^{(n+1)} + \Phi^{(n)} M^{(n)} \right). \quad (6.25)$$

In general the scheme does not guarantee that the eigenfunctions at time $t^{(n+1)}$ are orthonormal. Hence, in a second step, a Modified Gram-Schmidt orthogonalization is applied to the space Φ . The cost of the operation scales as $2\mathcal{N} \times (N_M)^2$ and therefore is linear in the high order dimension \mathcal{N} . In this work this simple reconstruction was adopted and proved to be sufficiently precise.

REMARK 6.2

For a better accuracy, the following alternative procedure could be used. An orthogonal complement can be added to the approximation of the time derivative:

$$\partial_t \varphi_i = \sum_{h=1}^{N_M} M_{hi} \varphi_h + r_i, \quad (6.26)$$

where $\langle r_i, \phi \rangle = 0$. To compute it, the expression of the derivative is injected into the equation governing the modes dynamics and projected on a basis orthogonal to the modes. Let us introduce $\Psi = \text{span}\{\psi_1, \dots, \psi_{N_\perp}\}$ such that $\Psi \perp \Phi$. At initial time the orthogonal basis is chosen as $\Psi = \text{span}\{\varphi_{N_M+1}, \dots, \varphi_{N_M+N_\perp}\}$. Then:

$$\sum_{h=1}^{N_M} M_{hi} (\mathcal{L}_\chi - \lambda_i \mathcal{I}) \varphi_h + (\mathcal{L}_\chi - \lambda_i \mathcal{I}) r_i = \dot{\lambda}_i \varphi_i + F \varphi_i. \quad (6.27)$$

The linear system determining r_i is obtained by projecting the equation onto Ψ :

$$\langle (\mathcal{L}_\chi - \lambda_i \mathcal{I}) r_i, \psi_j \rangle = \langle F \varphi_i, \psi_j \rangle. \quad (6.28)$$

When this correction is taken into account, the cost of the method is higher. Indeed, at each time step, the set of $[\Phi, \Psi]$ have to be orthonormalized with the MGS method, leading to a cost proportional to $2\mathcal{N} \times (N_M + N_\perp)^2$. For the test cases of the present work, this improvement did not improve significantly the results.

6.3 ALP in cardiac electrophysiology

We are now interested in applying the ALP method to the electrophysiology equations. We first derive the ALP algorithm for the monodomain equations [CFPT05] introduced in Section 1.4

$$\begin{aligned} A_m (C_m \frac{\partial v_m}{\partial t} + I_{\text{ion}}(v_m, w)) - \text{div}(\sigma_m \nabla v_m) &= A_m I_{\text{app}} \\ \frac{\partial w}{\partial t} - g(v_m, w) &= 0, \end{aligned} \quad (6.29)$$

coupled with the FitzHugh-Nagumo ionic model [Fit61, NAY62]

$$\begin{aligned} I_{\text{ion}}(u, w) &= su(u - a)(u - 1) + w \\ g(u, w) &= \varepsilon(\gamma u - w) \end{aligned} \quad (6.30)$$

with boundary conditions

$$\sigma_m \nabla v_m \cdot \mathbf{n} = 0 \quad (6.31)$$

Second, we extend the method to Bidomain equations [Tun78]

$$\begin{aligned} A_m (C_m \frac{\partial v_m}{\partial t} + I_{\text{ion}}(v_m, w)) - \text{div}(\sigma_i \nabla v_m) - \text{div}(\sigma_i \nabla u_e) &= A_m I_{\text{app}} \\ -\text{div}((\sigma_i + \sigma_e) \nabla u_e) - \text{div}(\sigma_i \nabla v_m) &= 0 \\ \frac{\partial w}{\partial t} - g(v_m, w) &= 0 \end{aligned} \quad (6.32)$$

with boundary conditions

$$\begin{aligned} \sigma_i \nabla u_e \cdot \mathbf{n} + \sigma_i \nabla v_m \cdot \mathbf{n} &= 0 \\ \sigma_e \nabla u_e \cdot \mathbf{n} &= 0. \end{aligned} \quad (6.33)$$

More details about the models are given in Section 1.4.

6.3.1 ALP for the monodomain equations

In order to apply the technique described above we couple (6.29) to the FitzHugh-Nagumo ionic model and write it as a unique system

$$\begin{aligned} A_m C_m \partial_t v_m &= f(v_m, w), \\ \partial_t w &= g(v_m, w), \end{aligned} \quad (6.34)$$

where

$$f(v_m, w) = A_m s v_m (v_m - a)(1 - v_m) - A_m w + \operatorname{div}(\boldsymbol{\sigma}_m \nabla v_m) + A_m I_{\text{app}}, \quad (6.35)$$

and

$$g(v_m, w) = \varepsilon(\gamma v_m - w). \quad (6.36)$$

The first step to apply the ALP method is to define a linear operator \mathcal{L}_χ . For the present work, the operator \mathcal{L}_χ is defined as

$$\mathcal{L}_\chi(u)\varphi = -\operatorname{div}(\boldsymbol{\sigma}_m \nabla \varphi) - \chi u \varphi, \quad (6.37)$$

and the modes φ_i are solutions of the eigenproblem

$$\mathcal{L}_\chi(u)\varphi_i = \lambda_i \varphi_i. \quad (6.38)$$

Let us remark that the conductivity $\boldsymbol{\sigma}_m$ being a tensor, the modes set can account for some physical anisotropy due to the presence of cardiac fibers.

The eigenproblem is symmetric positive definite. In the examples presented below it is solved using a Krylov-Schur method with a Lanczos decomposition (resp. B-Lanczos for the generalized eigenproblem). Although only N_M modes have to be computed, this step may be expensive. But it is worth noticing that it is solve only once, before the resolution of the reduced order model. In addition, the initial basis does not depend on the PDE parameters (except the conductivity tensor $\boldsymbol{\sigma}_m$). Thus, the same initial basis can be used for different sets of parameters.

Let us now approximate the solution of equations (6.34) in the low dimensional space defined by the N_M modes $\varphi_i(x, t)$ which are the first N_M eigenfunctions defined by (6.38). The transmembrane potential v_m can be approximated by

$$\hat{v}_m = \sum_{i=1}^{N_M} \beta_i(t) \varphi_i(x, t). \quad (6.39)$$

We choose to approximate the ionic variable in the same reduced order space and write

$$\hat{w} = \sum_{i=1}^{N_M} \mu_i(t) \varphi_i(x, t), \quad (6.40)$$

where \widehat{w} is the low dimensional approximation of w , $\mu_i(t)$ is the representation of \widehat{w} in the reduced order space Φ .

Using these Galerkin approximations, we can write

$$\begin{aligned} f(v_m, w) \approx & -A_m s a \sum_{i=1}^{N_M} \beta_i \varphi_i + A_m s (a+1) \sum_{i,j=1}^{N_M} \beta_i \beta_j \varphi_i \varphi_j + \\ & -A_m s \sum_{i,j,k=1}^{N_M} \beta_i \beta_j \beta_k \varphi_i \varphi_j \varphi_k - A_m \sum_{i=1}^{N_M} \mu_i \varphi_i + \\ & + \sum_{i=1}^{N_M} \beta_i \operatorname{div}(\sigma_m \nabla \varphi_i) + A_m I_{\text{app}}(x, t). \end{aligned} \quad (6.41)$$

Using the approximation of v_m in the reduced space Φ , from equations (6.37)-(6.38) we find

$$-\operatorname{div}(\sigma_m \nabla \varphi_i) - \chi \sum_{j=1}^{N_M} \beta_j \varphi_j \varphi_i = \lambda_i \varphi_i, \quad \forall i = 1, \dots, N_M. \quad (6.42)$$

Let us substitute the first term of (6.42) in (6.41). Then the approximation of $f(v_m, w)$ writes

$$\begin{aligned} f \approx & -A_m s a \sum_{i=1}^{N_M} \beta_i \varphi_i - \sum_{i=1}^{N_M} \lambda_i \beta_i \varphi_i + A_m s (a+1) \sum_{i,j=1}^{N_M} \beta_i \beta_j \varphi_i \varphi_j - \chi \sum_{i,j=1}^{N_M} \beta_i \beta_j \varphi_i \varphi_j + \\ & -A_m s \sum_{i,j,k=1}^{N_M} \beta_i \beta_j \beta_k \varphi_i \varphi_j \varphi_k - A_m \sum_{i=1}^{N_M} \mu_i \varphi_i + A_m I_{\text{app}}(x, t). \end{aligned} \quad (6.43)$$

We can now project expression (6.43) onto Φ . Then we define the projection of f , $\gamma_p \forall p = 1, \dots, N_M$, as

$$\begin{aligned} \gamma_p := & -A_m a \sum_{i=1}^{N_M} \beta_i \langle s \varphi_i, \varphi_p \rangle - \sum_{i=1}^{N_M} \lambda_i \beta_i \langle \varphi_i, \varphi_p \rangle - A_m \sum_{i=1}^{N_M} \mu_i \langle \varphi_i, \varphi_p \rangle + \\ & + A_m (a+1) \sum_{i,j=1}^{N_M} \beta_i \beta_j \langle s \varphi_i \varphi_j, \varphi_p \rangle - \chi \sum_{i,j=1}^{N_M} \beta_i \beta_j \langle \varphi_i \varphi_j, \varphi_p \rangle + \\ & - A_m \sum_{i,j,k=1}^{N_M} \beta_i \beta_j \beta_k \langle s \varphi_i \varphi_j, \varphi_k \varphi_p \rangle + A_m \langle I_{\text{app}}, \varphi_p \rangle. \end{aligned} \quad (6.44)$$

Let us assume that the applied stimulus is approximated by

$$I_{\text{app}}(x, t) = \sum_{l=1}^L h_l(t) z_l(x).$$

If we use the orthonormality of Φ , equation (6.44) can be written as

$$\begin{aligned} \gamma_p = & -\lambda_p \beta_p - A_m \mu_p - A_m a \sum_{i=1}^{N_M} B_{ip} \beta_p + A_m (a+1) \sum_{i,j=1}^{N_M} \beta_i \beta_j W_{ijp} + \\ & -\chi \sum_{i,j=1}^{N_M} \beta_i \beta_j T_{ijp} - A_m \sum_{i,j,k=1}^{N_M} \beta_i \beta_j \beta_k Y_{ijkp} + A_m \sum_{l=1}^L h_l(t) \langle z_l, \varphi_p \rangle, \end{aligned} \quad (6.45)$$

where we define the matrix B , and the third and fourth order tensors T , W , Y as

$$\begin{aligned} B_{ij} & := \langle s\varphi_i, \varphi_j \rangle & \forall i, j = 1, \dots, N_M, \\ T_{ijk} & := \langle \varphi_i, \zeta_{jk} \rangle & \forall i, j, k = 1, \dots, N_M, \\ W_{ijk} & := \langle s\varphi_i, \zeta_{jk} \rangle & \forall i, j, k = 1, \dots, N_M, \\ Y_{ijkh} & := \langle s\zeta_{ij}, \zeta_{kh} \rangle & \forall i, j, k, h = 1, \dots, N_M, \end{aligned} \quad (6.46)$$

and the functions ζ by

$$\zeta_{ij} := \varphi_i \varphi_j \quad \forall i, j = 1, \dots, N_M.$$

Note that these tensors are computed once for all at the initialization phase. Then they are simply propagated according to their respective evolution equation.

Dealing with the second equation of (6.34), we write the projection of the approximated function $g(v_m, w)$ as

$$\eta_p := \langle g, \varphi_p \rangle = \varepsilon(\gamma \beta_p - \mu_p), \quad \forall p = 1, \dots, N_M. \quad (6.47)$$

Then, to solve equations (6.34) with the ALP method we have to compute at each time iteration the quantities

$$\begin{aligned} \dot{\beta}_i + \sum_{j=1}^{N_M} \beta_j M_{ji} & = \gamma_i, \\ \dot{\mu}_i + \sum_{j=1}^{N_M} \mu_j M_{ji} & = \eta_i, \end{aligned} \quad (6.48)$$

where γ_i , η_i , for $i = 1, \dots, N_M$ are defined by (6.45) and (6.47). The complete set of equations that describe the dynamics is defined by (6.18)-(6.45)-(6.47), with equations (6.48) replacing the first equation of (6.18).

REMARK 6.3

Note that in the derivation of the ALP equations presented above, the diffusion term was eliminated in equation (6.43) by taking advantage of the modes definition in terms of the Schrödinger operator. Roughly speaking, a third order tensor is introduced, whose computation does not require modes differentiation. This is not the only possibility. Indeed, if the second term of (6.42) is substituted in (6.41), the

approximation of $f(v_m, w)$ writes

$$\begin{aligned}
f \approx & -A_m s a \sum_{i=1}^{N_M} \beta_i \varphi_i - \frac{A_m s (a+1)}{\chi} \sum_{i=1}^{N_M} \lambda_i \beta_i \varphi_i - \frac{A_m s}{\chi^2} \sum_{i=1}^{N_M} \lambda_i^2 \beta_i \varphi_i + \\
& -A_m \sum_{i=1}^{N_M} \mu_i \varphi_i - \frac{A_m s (a+1)}{\chi} \sum_{i=1}^{N_M} \beta_i \operatorname{div}(\boldsymbol{\sigma}_m \nabla \varphi_i) - \frac{A_m s}{\chi^2} \sum_{i=1}^{N_M} \lambda_i \beta_i \operatorname{div}(\boldsymbol{\sigma}_m \nabla \varphi_i) + \\
& + \sum_{i=1}^{N_M} \beta_i \operatorname{div}(\boldsymbol{\sigma}_m \nabla \varphi_i) + \frac{A_m s}{\chi} \sum_{i,j=1}^{N_M} \beta_i \beta_j \operatorname{div}(\boldsymbol{\sigma}_m \nabla \varphi_i) \varphi_j + A_m I_{\text{app}}(x, t). \quad (6.49)
\end{aligned}$$

Equation (6.49) is then projected onto Φ . Let us make the same assumptions as below, i.e. separable form space-time sources. Then, the projection of f , γ_p $\forall p = 1, \dots, N_M$ is therefore defined as:

$$\begin{aligned}
\gamma_p := & -A_m \mu_p - A_m \sum_{i=1}^{N_M} \left(a + \frac{a+1}{\chi} \lambda_i + \frac{1}{\chi^2} \lambda_i^2 \right) B_{ip} \beta_i + \sum_{i=1}^{N_M} A_m \left(\frac{a+1}{\chi} + \frac{1}{\chi^2} \lambda_i \right) \beta_i V_{ip} + \\
& - \sum_{i=1}^{N_M} \beta_i E_{ip} - \frac{A_m}{\chi} \sum_{i,j=1}^{N_M} \beta_i \beta_j U_{ijp} + A_m \sum_{l=1}^L h_l(t) \langle z_l, \varphi_p \rangle, \quad (6.50)
\end{aligned}$$

where we define the matrices B , E , V and the third order tensors U as

$$\begin{aligned}
B_{ij} & := \langle s \varphi_i, \varphi_j \rangle & \forall i, j = 1, \dots, N_M, \\
E_{ij} & := \langle \boldsymbol{\sigma}_m \nabla \varphi_i, \nabla \varphi_j \rangle & \forall i, j = 1, \dots, N_M, \\
V_{ij} & := \langle s \boldsymbol{\sigma}_m \nabla \varphi_i, \nabla \varphi_j \rangle & \forall i, j = 1, \dots, N_M, \\
U_{ijk} & := \langle \boldsymbol{\sigma}_m \nabla \varphi_i, \nabla(\zeta_{jk}) \rangle & \forall i, j, k = 1, \dots, N_M.
\end{aligned} \quad (6.51)$$

This way to proceed is attractive from a reduced-order modeling standpoint, since it allows to get rid of the fourth-order projection tensor appearing when the Galerkin projection of the FitzHugh-Nagumo ionic current is considered. For standard ROM based on Galerkin projection the cost is $\propto N_M^4$, while for ALP, by taking advantage of the definition of the potential in the Schrödinger operator, the cost of the ROM is $\propto N_M^3$. A discussion on the cost and scalability of other ROM approaches is provided in [CBMF11, RVC12]. An effective method to deal with non-polynomial equations and to avoid the computation of high-order projection tensors could be the DEIM approach proposed in [CS10b]. A comparison and an application to these methods to ALP will be the object of further works.

6.3.2 ALP for the bidomain equations

To discretize the bidomain equations in the low dimension space Φ and apply the ALP method, as in Section 6.3.1, we first choose the initial reduced order space.

The operator \mathcal{L}_χ defined for this problem is given by

$$\mathcal{L}_\chi(u)\varphi = -\operatorname{div}(\sigma_i \nabla \varphi) - \chi u \varphi \quad (6.52)$$

where σ_i is the intracellular conductivity tensor, indicated in the following as σ_i .

The second step is the discretization of equations (6.32). We can write the system as

$$\begin{aligned} A_m C_m \partial_t v_m &= f(v_m, u_e, w), \\ \partial_t w &= g(v_m, w), \\ q(v_m, u_e) &= 0, \end{aligned} \quad (6.53)$$

where

$$\begin{aligned} f(v_m, u_e, w) &= A_m s v_m (v_m - a)(1 - v_m) - A_m w + \operatorname{div}(\sigma_i \nabla v_m) + \\ &\quad + \operatorname{div}(\sigma_i \nabla u_e) + A_m I_{\text{app}}, \\ g(v_m, w) &= \varepsilon(\gamma v_m - w), \\ q(v_m, u_e) &= -\operatorname{div}((\sigma_i + \sigma_e) \nabla u_e) - \operatorname{div}(\sigma_i \nabla v_m). \end{aligned} \quad (6.54)$$

The projection onto the space Φ of the first equation of (6.54) gives

$$\begin{aligned} \gamma_p := & -\lambda_p \beta_p - A_m \mu_p - \lambda_p \xi_p - A_m a \sum_{i=1}^{N_M} \beta_j B_{ij} + A_m (a + 1) \sum_{i,j=1}^{N_M} \beta_i \beta_j W_{ijp} + \\ & -\chi \sum_{i,j=1}^{N_M} \beta_i \beta_j T_{ijp} - \chi \sum_{i,j=1}^{N_M} \beta_i \xi_j T_{ijp} - A_m \sum_{i,j,k=1}^{N_M} \beta_i \beta_j \beta_k Y_{ijkp} + \\ & + A_m \sum_{l=1}^L h_l(t) \langle z_l, \varphi_p \rangle, \quad \forall p = 1, \dots, N_M, \end{aligned} \quad (6.55)$$

and the projection of function g gives

$$\eta_p := \varepsilon(\gamma \beta_p - \mu_p), \quad \forall p = 1, \dots, N_M. \quad (6.56)$$

The projection of function q gives a low dimensional linear system defined by

$$\sum_{j=1}^{N_M} Q_{ij} \xi_j = - \sum_{j=1}^{N_M} E_{ij} \beta_j, \quad \forall j = 1, \dots, N_M, \quad (6.57)$$

where matrices Q and E are defined as

$$\begin{aligned} Q_{ij} &:= \langle (\sigma_i + \sigma_e) \nabla \varphi_i, \nabla \varphi_j \rangle & \forall i, j = 1, \dots, N_M \\ E_{ij} &:= \langle \sigma_i \nabla \varphi_i, \nabla \varphi_j \rangle & \forall i, j = 1, \dots, N_M. \end{aligned} \quad (6.58)$$

To summarize, the set of equations which describes the dynamics of system (6.32) in

the reduced order space is

$$\left\{ \begin{array}{l} \dot{\beta} + M\beta - \gamma = 0, \\ \dot{\mu} + M\mu - \eta = 0, \\ \dot{\lambda}_i + \chi \sum_{m=1}^{N_M} T_{iim} \gamma_m = 0, \quad i = 1 \dots N_M \\ \dot{T} = \{M, T\}^{(3)}, \\ \dot{W} = \{M, W\}^{(3)}, \\ \dot{Y} = \{M, Y\}^{(4)}, \\ \dot{B} = [M, B], \\ \dot{Q} = [M, Q], \\ \dot{E} = [M, E], \\ M_{ij} = \frac{\chi}{\lambda_j - \lambda_i} \sum_{m=1}^{N_M} T_{ijm} \gamma_m, \quad i, j = 1 \dots N_M \\ \gamma = \gamma(\beta, \xi, \mu), \\ \eta = \eta(\beta, \mu), \\ Q\xi = -E\beta. \end{array} \right. \quad (6.59)$$

6.4 Numerical experiments

This section is devoted to numerical experiments. First, we consider the propagation of an electrical signal in a homogeneous tissue on a 2D domain. Then, some examples of spatial and temporal heterogeneity in parameters and source terms are proposed. The last application deals with pseudo-electrocardiograms and involve the bidomain equations coupled to a diffusion problem on a 3D domain.

6.4.1 Preliminary comments about POD

In the following numerical simulations, our main objective is to compare ALP with the finite element method (FEM). In some cases, we also compare ALP with the Proper Orthogonal Decomposition (POD), a “classical” technique described in Section 1.6.2 and applied in Chapters 4 and 5.

An important remark is in order. POD is a way to approximate a space spanned by off-line solutions, and the result strongly depends on this space. When the parameters of the problems vary, it is necessary to consider a large number of configurations in order to build an off-line space as rich as possible. In electrophysiology, this strategy was carried out for example in Chapter 4 or in [BSG12]. In the present chapter, we only consider a very simple set of precomputed solutions: the ones obtained with nominal values of parameters. Thus, our POD results correspond to a best case scenario when the nominal values are used to run the reduced-order model, but to a (possibly) very bad scenario when the parameters are modified. In the latter case, it would be clearly possible to improve the POD results by enlarging the off-line dataset as described in Chapters 4, but this would require to explore a huge number

of configurations in the off-line stage. Although possible, this was not done here since POD was not the main topic of this work.

6.4.2 A few comments on the choice of χ

The ALP basis depends upon a real positive scalar parameter χ , that influences the spectrum and the eigenfunctions of the operator \mathcal{L}_χ .

The spectrum of the operator is discrete (the domain is bounded), real, and it can be divided into two parts: one corresponding to negative eigenvalues and one to positive (or null) eigenvalues. The larger the value of χ , the higher is the number of negative eigenvalues. The larger the value of χ , the more peaky the eigenfunctions corresponding to negative eigenvalues. Thus, this parameter can be viewed as a characteristic length for the modes corresponding to negative eigenvalues. Let us illustrate this with a 1D numerical test case.

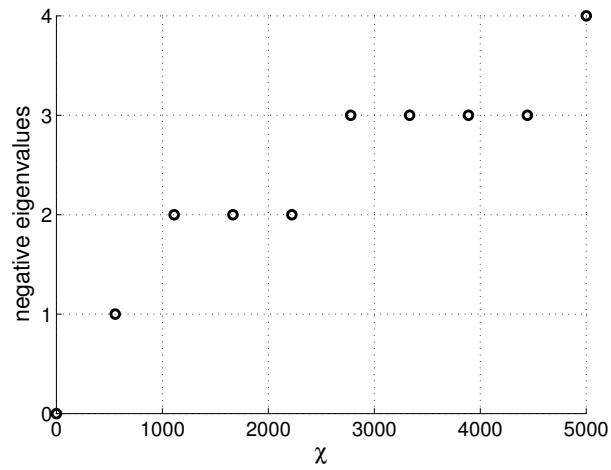
The domain is $\Omega = [0,1]$, the potential is the Gaussian $y = \exp(-250(x - 0.5)^2)$. A piecewise linear finite element discretization is adopted, with $\mathcal{N} = 256$. In Figure 6.1(a) the number of negative eigenvalues is shown for several values of the parameter χ . For $\chi = 0$, there are no negative eigenvalues. The number of negative eigenvalues increases with χ . In Figure 6.1(b) the relative L^2 error in the reconstruction of the potential is shown when only the first mode is used, as a function of χ . There is a minimum for $\chi \approx 2000$. This is related to the fact that, for low values of χ the first mode has a characteristic length much higher than that of the gaussian potential, so that the reconstruction is poor. On the opposite, when χ is too large, the mode tends to a Dirac delta and it cannot represent the potential in a good way. The behavior of the first mode, when χ is varied, is shown in Figure 6.2(a).

Let us comment on the difference between the eigenfunctions corresponding to the negative spectrum and the eigenfunctions corresponding to the positive one. In Figure 6.2(b) the first four modes are shown when $\chi = 2000$. The first two modes correspond to the negative spectrum. Their shape is soliton-like: it is featured by a characteristic length and localized in space. The modes 3 and 4 correspond to the positive spectrum. They are sinus-like global modes, of increasing frequency, perturbed by the potential.

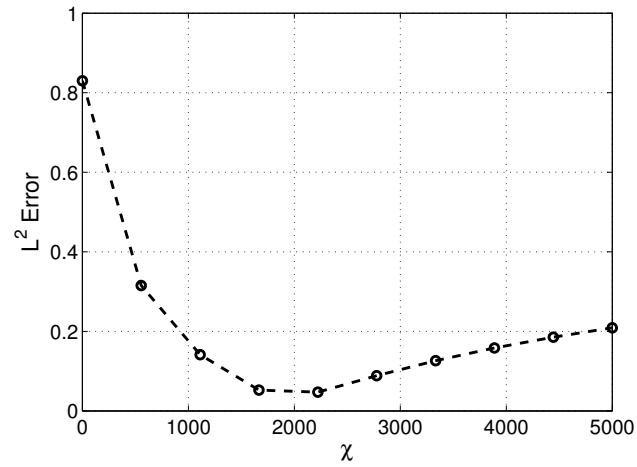
In practice, the value of χ is chosen after a preliminary numerical test, on a given setup, and depends on the domain size as well as on the L^2 norm of the potential. It is chosen in such a way that the initial datum is represented with a low relative error in the space spanned by few modes.

6.4.3 Homogeneous parameters 2D case

We consider a 2D square domain $[0,1]^2$, discretized with a P1 finite element mesh composed of 5,878 vertices, and the monodomain equations (6.29) with the parameters reported in Table 6.1. Concerning the ALP method, we solve the equations presented in Section 6.3.1. ALP results are compared with those obtained with the full order model (FEM) and the POD. The POD basis is generated by



(a) Number of negative eigenvalues.



(b) Error in the reconstruction of the potential when the first mode only is used.

Figure 6.1: Properties when χ is varied.

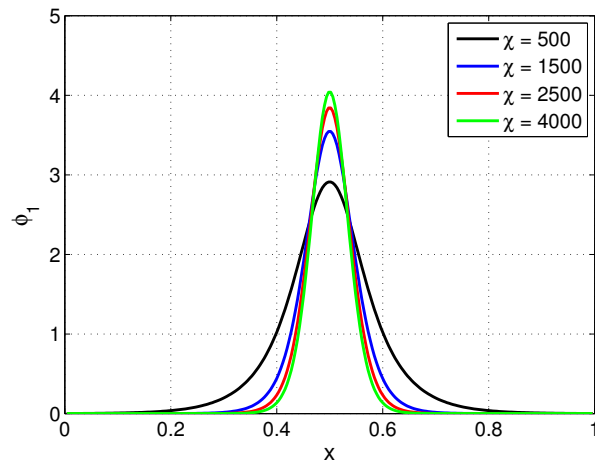
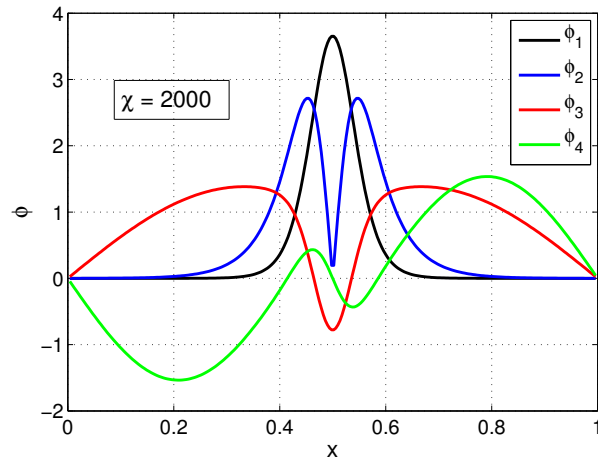
(a) First mode against χ .(b) The first modes when $\chi = 2000$, mode 1 and 2 belong to the negative spectrum, while 3 and 4 to the positive one.

Figure 6.2: Eigenfunctions behavior.

considering snapshots from the homogeneous 2D tissue propagation. For FEM simulations a second order Backward Difference method is used with time step $\delta t = 0.1\text{ms}$, while in the reduced order cases an Explicit Euler method is considered (time step $\delta t = 0.01\text{ms}$).

First we run a FEM simulation with the applied stimulus defined as

$$I_{\text{app}}(\mathbf{x}, t) = h(t)z(\mathbf{x}), \quad (6.60)$$

where h is defined by

$$h(t) = H(t) - H(t - 5), \quad (6.61)$$

H denotes the Heaviside function, and z is defined by

$$z(\mathbf{x}) = 0.04 \cdot \mathbf{1}_{\Omega_c}, \quad \Omega_c = \{(x, y) \text{ s.t. } |(x - 0.25, y)| \leq 0.25\}. \quad (6.62)$$

In order to build the initial time ALP basis $\Phi^{(0)}$ we consider the solution v_m of the FEM simulation after 5ms. The basis is computed solving equation (6.38) with $\chi = 15$. POD basis is generated by considering snapshots from the FEM simulation: 100 snapshots are retained with a sampling time of 0.5ms. The POD model is built by Galerkin projection.

Let us compare FEM and ROM solutions for ROM dimension space $N_M = 25$. We observe good agreement between FEM solution and POD one (see first and last columns of Figure 6.3). ALP solution is in good accordance with FEM one, too (see first and second columns of Figure 6.3).

Then, we compare the relative $L^2(\mathbb{R}^{\mathcal{N}})$ norm errors between FEM solution and ROM ones, computed by

$$\text{error}^2(t^n) = \frac{|u_{\text{FEM}}^{(n)} - u_{\text{ROM}}^{(n)}|^2}{|u_{\text{FEM}}^{(n)}|^2} \quad (6.63)$$

for each time iteration t^n , $n \geq 0$, where $|\cdot|^2$ denotes the discrete norm $|v|^2 = \sum_i v_i^2$, and $u_{\text{FEM}}^{(n)}$, $u_{\text{ROM}}^{(n)}$, represents the FEM, respectively ROM, solution at time t^n in the high dimensional space $\mathbb{R}^{\mathcal{N}}$. We compute the errors varying the dimension of ALP space: $N_M = 15, 20, 25, 30$. In Figure 6.4 we observe the decreasing values of ALP error with respect to the space dimension. In particular, each continuous curve (ALP errors) has a relative minimum after 20ms, *i.e.* when the depolarization front is already gone and the repolarization has not started yet. The relative error increases for any value of N_M after 30 to 35ms, which represents the exit of the repolarization from the domain, this is due to some boundary effects caused by the low dimensional

$A_m^{2D}(\Omega.\text{mV}^{-1})$	$A_m^{3D}(\Omega.\text{mV}^{-1})$	$C_m(\text{mA}.\text{ms}.\text{cm}^{-2})$	σ_m	s	a	ε	γ
2000.0	500.0	0.1	1	0.2	0.075	0.04	0.2

Table 6.1: Physical and ionic parameters.

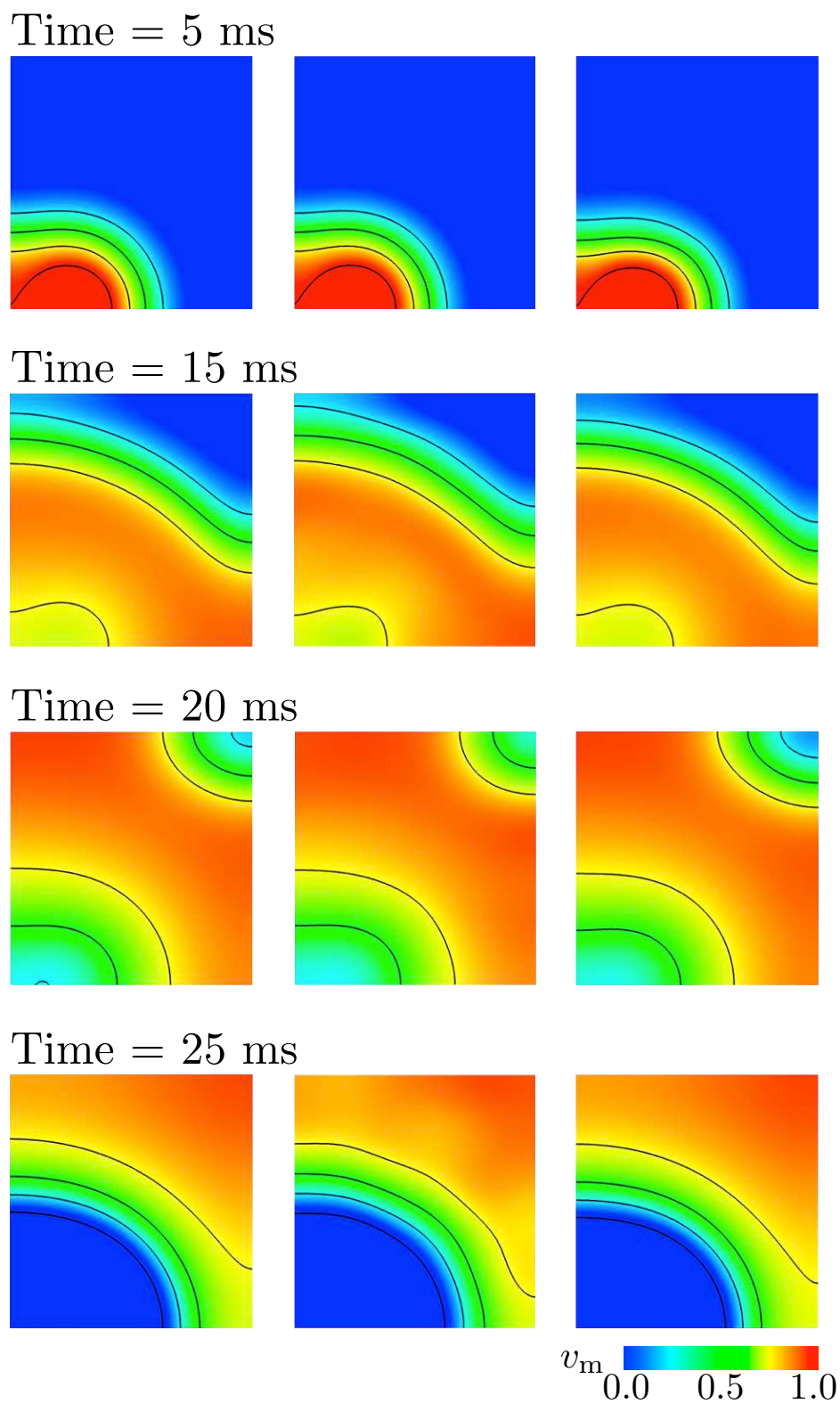


Figure 6.3: Comparison between FEM (left column), ALP ($\chi = 15, N_M = 25$) in the center and POD ($N_M = 25$) on the right for the homogeneous tissue test case (section 6.4.3). Four different times are considered, namely $t = 5, 15, 20, 25$ ms.

Figure 6.4: Relative errors in L^2 norm for the homogeneous tissue test case (section 6.4.3), varying the number of modes used, for ALP method (continuous lines, $\chi = 15$) and POD (dotted line).

approximation. We observe the same behavior for the POD curve, too (dotted line). Finally, we remark that ALP relative error with 25 – 30 modes is less than 10 percent during the whole simulation. We point out that the POD method gives an optimal solution because of the basis is build ad hoc. As we observe in next sections, the POD basis is not as efficient for any perturbation of the signal.

Concerning the computational costs of the algorithm, the gain of the ALP method for the monodomain equations (6.29) with $N_M = 25$ modes was investigated. When a full reconstruction in the physical space is performed, the gain is about 20% compared to the FEM, including all the stages of the method. This speedup is clearly insufficient, and its improvement is the object of an on-going work (see Chapter 8). However, it is worth noticing that, in many applications, the reconstruction in the FE space is not necessary. As will be shown in Section 6.4.6, this is for example the case when only an output of interest depending linearly on the solution is needed. In this case, the update of the basis can be avoided and the ALP method has a computational cost which is one order of magnitude smaller than that of FEM (a speedup of about 8 was observed in our simulations).

6.4.4 Heterogeneous ionic parameters

A test case with heterogeneous ionic parameter s is presented in this section, which is challenging from a ROM point of view. Indeed, $s(x)$ is a function of the space,

Figure 6.5: Relative errors in L^2 norm for the heterogeneous ionic parameter test case (section 6.4.4), varying the number of modes used, for ALP method (continuous lines, $\chi = 15$) and POD (dotted line).

it is a distributed parameter that belongs to a high dimensional (infinite dimensional) space. For the reduced-order techniques that rely on the pre-computation of solutions, this would increase in a significant way the database dimension and the cost of the offline phase. In particular, for the test case considered, the expression of $s(x)$ reads:

$$s(\mathbf{x}) = s_0 \cdot \mathbf{1}_{\Omega \setminus \Omega_s} + s_1(\mathbf{x}) \cdot \mathbf{1}_{\Omega_s}, \quad (6.64)$$

$$\Omega_s = \{(x, y) \mid (0 \leq x \leq 0.5), (0.25 \leq y \leq 0.75)\}, \quad (6.65)$$

$$s_1(\mathbf{x}) = s_0 \frac{36y - 7}{20}. \quad (6.66)$$

The value of the parameter s_0 is reported in Table 6.1. There is a square subdomain in which the ionic parameter s is modified, its value is linear with respect to y : being only 1/10 with respect to the nominal one in the inferior border ($y = 0.25$) and s_0 in the upper boundary ($y = 0.75$). This can be seen as a schematic representation of an obstacle for the depolarization waves.

The ALP method was applied to this scenario. It is worth noting that the initial condition for this simulation is the same as for the homogeneous test case, so that the initial modes set is exactly the same. The ALP ROM was integrated, taking $\chi = 15$ and a time step $\delta t = 0.01$ ms. In Figure 6.5 the L^2 relative error between the FEM solution and the reconstruction of the ALP-ROM one is shown as function of time, varying the number of modes used. The errors are larger with respect to those observed for the homogeneous test case presented in the previous section. This can

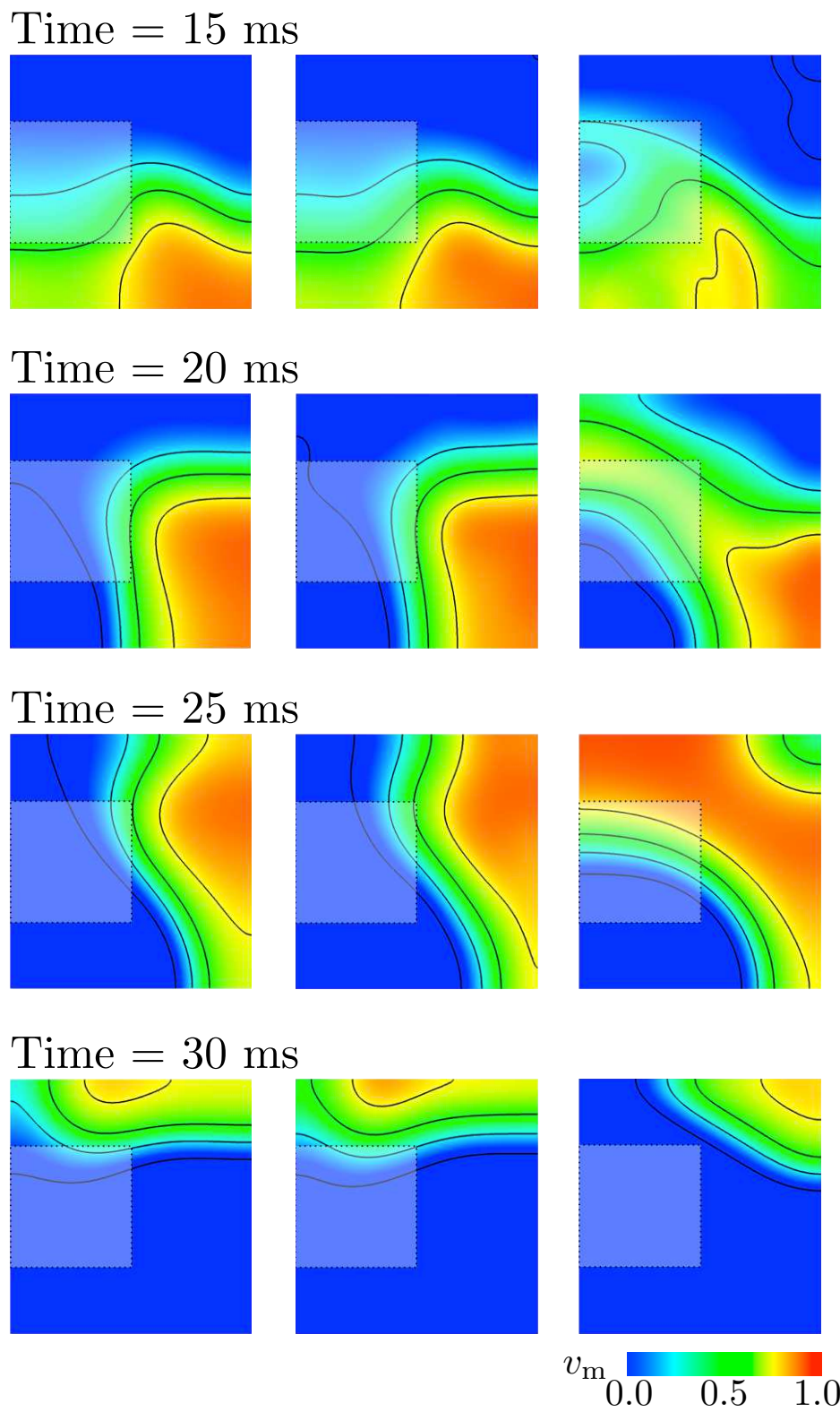


Figure 6.6: Comparison between FEM (left column), ALP ($\chi = 15, N_M = 25$) in the center and POD ($N_M = 25$) on the right for the heterogeneous parameter test case (section 6.4.4). Four different times are considered, namely $t = 15, 20, 25, 30$ ms.

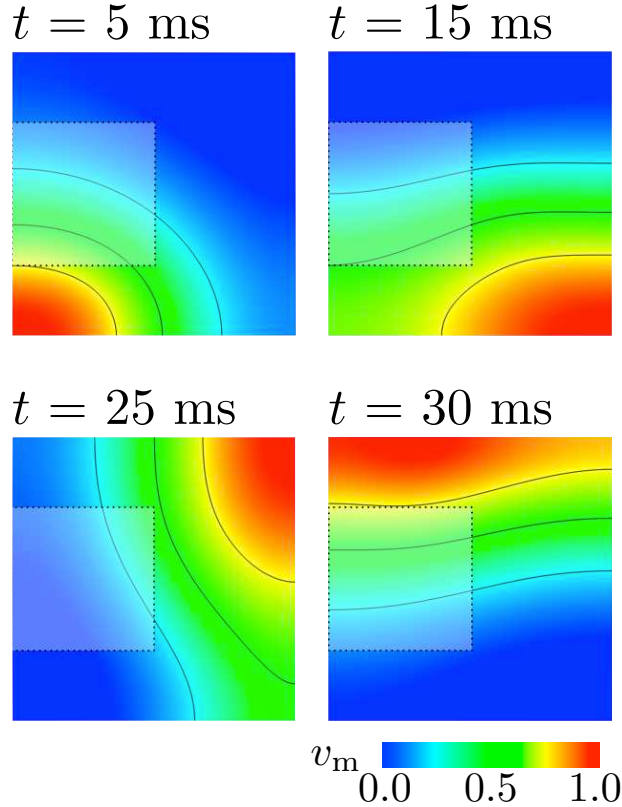


Figure 6.7: Evolution of the first mode for ALP-ROM when heterogeneous parameter test case (section 6.4.4) is integrated, at four different times: $t = 5, 15, 25, 30$ ms.

be explained by considering that in presence of an obstacle the dynamics is complex and a larger number of modes is needed to render it. As expected the error decreases when the number of modes is increased and it is less than 10% when $N_M = 30$ modes are used. The error globally increases in time, but it is not monotonically increasing. The peaks observed corresponds to boundary interactions of the depolarization wave. The dashed lines are the relative errors of the POD reduced-order model when $N_M^{(\text{POD})} = 30$ and $N_M^{(\text{POD})} = 60$. The error has peaks larger than 100% in both cases, and for $N_M^{(\text{POD})} = 60$ it is overall comparable to ALP when $N_M = 15$.

A qualitative comparison between ALP and POD solutions is proposed in Figure 6.6, at four different instants: $t = 15, 20, 25, 30$ ms. The FEM solution is represented on the left column, ALP is in the center and POD on the right. The POD model is not accurate enough out of database and it is not able to account for the dynamics in the presence of an obstacle, if this has not been taken into account in the database. The POD modes number has to be increased up to $N_M^{(\text{POD})} = 60$ in order to start having a realistic behavior. On the contrary, ALP performance is remarkable, all the features of the solution are represented. The errors mainly concern the front shape (which is often less sharp than the FEM one) and the boundary interactions.

In Figure 6.7 the time evolution of the first Schrödinger mode is considered, at

Figure 6.8: Relative error in L^2 norm for ALP ($\chi = 25$) and POD with $N_M = 30$ for the distributed source test case (see section 6.4.5).

four different times, $t = 5, 10, 25, 30$ ms. The mode basically evolves as the solution does. Indeed, the modification in the ionic parameter $s(x)$ makes the modal set evolve in order to match the dynamics of the system.

6.4.5 Source terms

In this section space-time sources are considered. The synthetic test presented hereafter is a schematized example of a realistic ectopic pacemaker. The proposed test case is as follows. The wave starts from the same initial condition as for the previous test cases. At $t = 60$ ms a source term is applied of the form:

$$\begin{aligned} I_{\text{app}}(\mathbf{x}, t) &= [H(t - 60) - H(t - 65)]z(\mathbf{x}), \\ z(\mathbf{x}) &= 0.04 \cdot \mathbf{1}_{\Omega_c}, \end{aligned} \tag{6.67}$$

where H denotes the heaviside function and

$$\Omega_c = \{(x, y) \text{ s.t. } |(x, y - 0.75)| \leq 0.25\}.$$

This is a challenging test case from a model-reduction point of view. Indeed, for a method relying on a database construction, a large number of stimulation locations and times should be pre-computed and the ROM usually performs poorly out-of-database.

The test was performed by varying the number of modes used. The initial

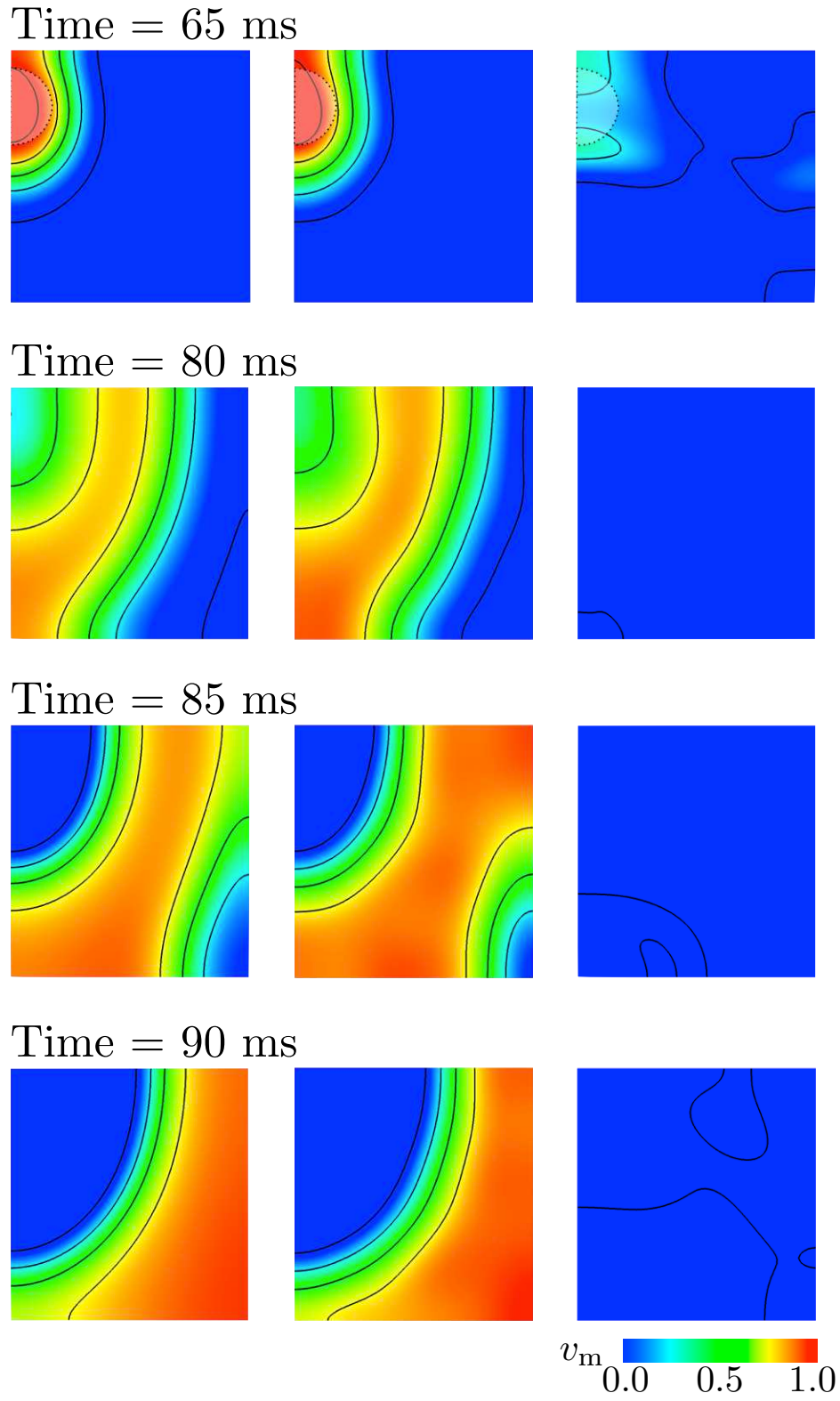


Figure 6.9: Comparison between FEM (left column), ALP ($\chi = 15, N_M = 25$) in the center and POD ($N_M = 25$) on the right for the source test case (section 6.4.5). Four different times are considered, namely $t = 65, 80, 85, 90$ ms. For the first part of the simulation, $t < 60$ ms, see Figure 6.3 (test case of section 6.4.3).

condition for the modal set was extracted by taking $\chi = 25$.

The relative error in L^2 norm was computed (see Figure 6.8). For $t < 60$ ms the curve is the same as for the homogeneous tissue test case presented in section 6.4.3. Let us comment the behavior of the scheme for $t > 60$ ms. The error increases when the current is applied. After a transient phase the modal set adapts and the scheme is able to reproduce the dynamics of the system. As for the previous test cases, the error decreases as the number of modes is increased. The error is in general higher with respect to what observed in the homogeneous test case, with the same number of modes. This is another case for which the POD performances are poor. Indeed, when the sources are not precomputed the POD is not able to reproduce the correct results even with a high number of modes (see Figure 6.9). On the contrary, the ALP method errors are comparable to those obtained in the homogeneous test case (section 6.4.3).

In Figure 6.9, the FEM solution (left column) was compared to the solutions obtained with ALP (center column) and POD (right column) when $N_M = 25$. Four different times are considered, namely $t = 65, 80, 85, 90$ ms. Between $t = 60$ ms and $t = 65$ ms the current source (dash-circle in the first row of the plots) has been applied. Its effect is not represented in the POD modes space since the snapshots were computed without it. Hence, at subsequent times, the polarization cannot propagate and the POD model is not able to provide the solution of the system. In spite of some errors in the position and the shape of the front, ALP is able to account for the wave propagation induced by the source.

6.4.6 Pseudo-electrocardiograms

We are now interested in an application related to electrocardiograms (ECG) computation. ECG represents a convenient and efficient medical test to control the heart behavior, it consists in measuring the electrical potential onto 9 skin points. From a mathematical point of view, the bidomain equations (5.1) are coupled to a diffusion problem in the torso:

$$\operatorname{div}(\sigma_T \nabla u_T) = 0, \quad \text{in } \Omega_T, \quad (6.68)$$

where u_T represents the torso electrical potential and σ_T the torso conductivity, an heterogeneous parameter which takes into account for instance bones and lungs conductivities. Equations (6.68) can be coupled to (5.1) by imposing the continuity of the extracellular potential and current. In this study, we consider a weak coupling between heart and torso potential, *i.e.* only the potential continuity is imposed. Then the boundary conditions for (6.68) are

$$\begin{aligned} u_T &= u_e, & \text{on } \Sigma \\ \sigma_T \nabla u_T \cdot \mathbf{n} &= 0, & \text{on } \partial\Omega_T^{\text{ext}} \end{aligned} \quad (6.69)$$

where $\Sigma = \partial\Omega_H$ represents the external boundary of the heart domain and $\partial\Omega_T^{\text{ext}}$ indicates the external boundary of the torso domain Ω_T .

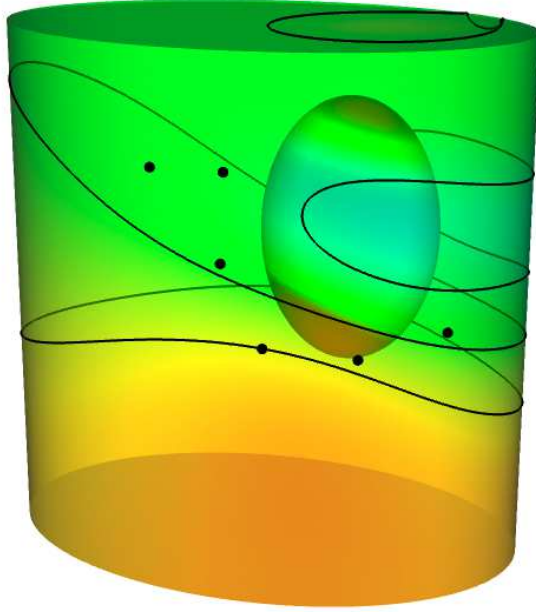


Figure 6.10: FEM heart-torso equations solution at time $t = 25\text{ms}$.

Since we now consider the bidomain equations, we have to treat the extracellular variable. In section 6.3.1 the ionic variable w was approximated in the same reduced order space as the transmembrane potential. We do the same for the extracellular potential u_e and write

$$\hat{u}_e = \sum_{i=1}^{N_M} \xi_i(t) \varphi_i(x, t), \quad (6.70)$$

where \hat{u}_e is the low dimensional approximation of u_e , $\xi_i(t)$ is the representation of \hat{u}_e in the reduced order space Φ .

We denote by $y = (u_T(x_1^{\text{ECG}}), \dots, u_T(x_{N_{\text{ECG}}}^{\text{ECG}}))$ the values of u_T at N_{ECG} locations on the boundary of the torso. The measurement y is the output of interest of this problem. It is related to u_e by the relation

$$y = S\Pi u \quad (6.71)$$

where $\Pi : \mathbb{R}^{\mathcal{N}} \mapsto \mathbb{R}^{N_{\Sigma}}$ denotes the boundary restriction operator, N_{Σ} is the number of vertices on heart/torso interface, $S \in \mathbb{R}^{N_{\text{ECG}} \times N_{\Sigma}}$ denotes the heart-torso transfer matrix, and $u \in \mathbb{R}^{\mathcal{N}}$ denotes the degrees of freedom of the extracellular potential u_e in the finite element space. If we consider the representation of u in the reduced-order space, $u = \Phi\xi$, then the ECG measurements can be written as

$$y = X\xi, \quad (6.72)$$

where

$$X := S\Pi\Phi \in \mathbb{R}^{N_{\text{ECG}} \times N_M} \quad (6.73)$$

Figure 6.11: Comparison between FEM electrodes measures (blue line) and ALP ones (red line) for $\chi = 50$, $N_M = 60$.

is a very small matrix. This linear operator X commutes with time, so we can apply the same technique as in section 6.2.1 in order to compute its time derivative:

$$\dot{X}_{ij} = \sum_{l=1}^{N_M} X_{il} M_{lj}. \quad (6.74)$$

So, the ECG measurement y is computed at each time iteration using the low dimensional vector ξ and the matrix X whose update is easily computed using (6.74), without any reconstruction of the solution in the finite element space.

For the numerical simulations, we consider an ellipsoid, representing the heart, embedded in a cylinder, represented the torso. The mesh of the ellipsoid has 22.140 vertices, while the external one has 338.920 vertices, of which 7.572 are on the interface Σ between the two domains.

We first solve the bidomain equations (5.1) in the ellipsoid using FEM and a second order Backward Difference method to integrate in time. The conductivity tensors σ_i and σ_e are considered isotropic, their values are $\sigma_i = 1$, $\sigma_e = 4$. Then, we solve the torso diffusion problem (6.68) with boundary conditions (6.69) where the extracellular potential is taken from the bidomain solution in the ellipsoid. A snapshot of the solution at time $t = 20\text{ms}$ is shown in Figure 6.10. In particular we are interested in the torso potential measured by 6 electrodes positioned in the black points of Figure 6.10.

Concerning the ALP resolution, we compute the initial basis Φ using the operator \mathcal{L}_χ defined in (6.52) where u is the FEM solution at time $t = 5\text{ms}$ and $\chi = 50$. We solve then equations (6.59) and we compute by equation (6.72) the 6 torso measures

we are interested in. We remark that, as the only output we want to show are the 6 electrodes measures, no reconstruction in the FEM space is needed.

Figure 6.11 compares FEM measures with ALP results run for $N_M = 60$. We observe that ALP curves (red lines) are in good accordance with FEM ones (blue lines), the signal is well reproduced on every leads.

6.5 Chapter conclusions

The ALP method can be seen as a formalism to propagate a basis in a way related to the dynamics of the solution. In this chapter, the ALP reduced-order model was applied to the simulation of high-dimensional parametric systems arising in cardiac electrophysiology. The approach was assessed in a wide range of different situations, including 2D and 3D complex configurations and data assimilation techniques. The main advantage with respect to standard approaches consists in the fact that no database of solutions has to be built to define the reduced-order model.

Several perspectives are in order. The first one consists of the choice in the basis to propagate, that is, the choice of the operator \mathcal{L}_χ . Different options could lead to different results and performances in terms of model reduction. Moreover, the analysis of the stability and accuracy of the method is still missing and is currently under scrutiny.

Also, the method should be extended to non-polynomial problems. In the Chapter 8 we will show some preliminary results on an “hybrid” method between ALP and the Discrete Empirical Interpolation Method (DEIM) [CS10b] that allows to treat non-polynomial terms and to decrease the computational costs of the ALP method. Finally, the case of multiple basis will also be investigated from a theoretical point of view in the Chapter 8.

Inverse problems with ALP reduced-order method

In this Chapter we illustrate some preliminary results of cardiac electrophysiology inverse problems using the reduced-order method based on Approximated Lax Pairs (ALP) presented in the previous chapter. The method is applied within a data assimilation framework in order to estimate the solution (the state) of the system. In particular two cases are investigated. First, the method is used to identify the source term location in the Micro-Electrode Arrays (MEA) technology using some electrodes measurements¹. Second, the reconstruction of the epicardial potential using body surface potential measurements is investigated on a simplified geometry. The work presented in this chapter is still on-going.

¹This work was done in the framework of the ANR LabCom “CardioXComp”, <https://team.inria.fr/reo/cardioxcomp/>

Contents

7.1	Introduction	165
7.2	An overview on data assimilation	165
7.3	Application to Micro-Electrode Arrays measures	167
7.3.1	The Micro-Electrode Array (MEA) technology	167
7.3.2	Formulation of the problem	169
7.3.3	Numerical results	172
7.4	Application to epicardium potential reconstruction	172
7.4.1	Formulation of the problem	173
7.4.2	Numerical results	175
7.5	Chapter conclusions	175

7.1 Introduction

In this chapter we concentrate on some applications of the ALP method described in the previous chapter to inverse problems in cardiac electrophysiology. The “classical” inverse problem of electrocardiology aims at reconstruct the extracellular potential on the epicardium of the heart using some measures on the skin of the torso. In Section 1.5 we give more details about the mathematical formulation of this problem and some standard approaches for its resolution.

We are interested in the reconstruction of the potential on a given domain using some partial or external measures of the potential. In particular, we use a data assimilation technique in order to estimate the solution (state) of the system. The idea is to project the problem defined by the observer operator onto the reduced-order space.

First, we give an overview on data assimilation methods and then apply the technique, using a Luenberger type observer, in a 2D and a 3D cases. Then two applications are detailed.

The first application uses the ALP method to identify the location of one or more source terms using the Micro-Electrode Arrays (MEA) measures, which is a technology used to study the behavior of *in vitro* or *in vivo* cardiac tissue cells. In particular, we consider a 2D squared domain and we assume to know the extracellular potential only on a small subdomain. This information is then used to reconstruct the transmembrane and extracellular potentials on the whole domain.

Finally, we solve the classic electrocardiology inverse problem of reconstructing the extra-cellular potential on the epicardium of the heart using the measures of a synthetic electrodes vest. This study is conducted on a simplified geometry and it represents a preliminary study that could lead to the resolution of the “classical” inverse problem of electrophysiology on real geometries and data.

7.2 An overview on data assimilation

Historically used in weather forecasting and hydrology, data assimilation is the process by which observations are introduced into the model. Usually, the model is a PDEs system and the data arise from real measures, often containing a part of incertitude due for instance to noise. Let us give a brief overview on data assimilation and on the techniques used in this section.

Let us consider a PDEs system described by a dynamical, possibly non-linear, operator A . We define x the solution of the system, also called the *state* of the system. Then, for each time $t > 0$, x satisfies

$$\dot{x}(t) = A(x, \theta, t) \tag{7.1}$$

with an initial condition $x(0)$, where θ indicates a set of parameters of the model. If the initial condition $x(0)$ and the parameters θ are known the problem is well-posed. We suppose that the initial solution $x(0)$ and the parameters set θ can be divided

into two parts: a well-known one (x°, θ°) , and an uncertain one (ζ^x, ζ^θ)

$$x(0) = x^\circ + \zeta^x, \quad \theta = \theta^\circ + \zeta^\theta. \quad (7.2)$$

Then, the problem can be written as

$$\begin{cases} \dot{x}(t) &= A(x, \theta, t), \\ \dot{\theta}(t) &= 0, \\ x(0) &= x^\circ + \zeta^x, \\ \theta(0) &= \theta^\circ + \zeta^\theta. \end{cases} \quad (7.3)$$

In data assimilation technique, we assume that we have some observations of the state, *i.e.* that we are able to measure the exact solution X using an, possibly time dependent, observation operator denoted by H :

$$z(t) = H(X(t), t) + \varepsilon(t), \quad (7.4)$$

where z is the observation and ε the error committed on the measures.

In general, we are interested in retrieving an estimator $(\hat{x}, \hat{\theta})$ of the state and of the parameters. In the applications shown in this work, we will use assimilation data techniques only to reconstruct an estimation of the state \hat{x} . The operator D such that

$$D(z, \hat{x}(t)) = 0 \quad (7.5)$$

is called discrepancy, which in this work is a linear operator

$$D(z, \hat{x}(t)) := z - H(\hat{x}(t), t). \quad (7.6)$$

Then, the system for the observation reads

$$\begin{cases} \dot{\hat{x}}(t) &= A(\hat{x}, \theta, t) + G(z - H(\hat{x}(t), t)), \\ \dot{\theta}(t) &= 0, \\ \hat{x}(0) &= \hat{x}^\circ, \\ \theta(0) &= \theta^\circ, \end{cases} \quad (7.7)$$

where G is the gain operator. In order to define the filter G two families of method are in use. The first one is called *optimal observer* method since in can be shown that it equivalent to an optimization problem in some cases. It leads to a linear or non-linear operator, possibly time dependent, such that

$$\lim_{t \rightarrow +\infty} \hat{x}(t) = x. \quad (7.8)$$

The most known filters are the *Kalman-Bucy filter* [KB61], [Ben71] and its approximated versions such as the *Extended Kalman filter* [Sim06], the *Unscented Kalman filter* [JU97] and the *Ensemble Kalman filter* [Eve09].

Alternatively, a non-optimal filter can be applied. This is the case for the so-called

Luenberger filter introduced by Luenberger [Lue63], [Lue71]. A correction, which is the simplest as possible, is introduced in order to minimize the error between the state and the observer. This type of observer is usually applied only to the state, which is the case we are interested in. Then, the observed system reads

$$\begin{cases} \dot{\hat{x}}(t) &= A(\hat{x},t) + G(z - H(\hat{x}(t),t)), \\ \hat{x}(0) &= \hat{x}^\circ. \end{cases} \quad (7.9)$$

If H and G are linear operators, the filter can be chosen such that $G = aH^*$, where a is a strictly positive value and H^* the adjoint operator of the observation operator.

More details about data assimilation can be found for instance in [Ghi71], [Tal97].

7.3 Application to Micro-Electrode Arrays measures

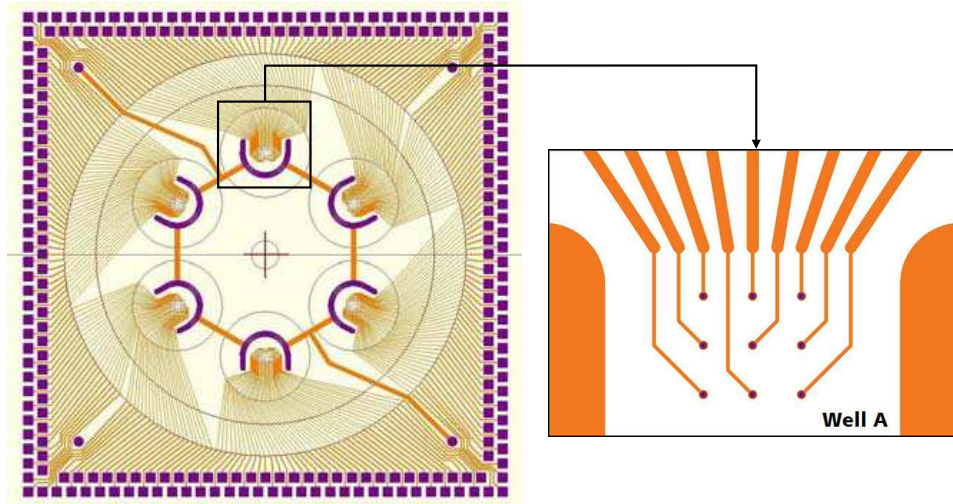
We consider the Micro-Electrode Arrays (MEA) technology. MEA is an arrangement allowing extracellular potential recording and stimulation. In particular, we deal with a 2D squared domain and we suppose to measure the extracellular potential on a small subdomain. Then, the observation problem solved with the ALP method aims at identify the location of the source term using these measures.

7.3.1 The Micro-Electrode Array (MEA) technology

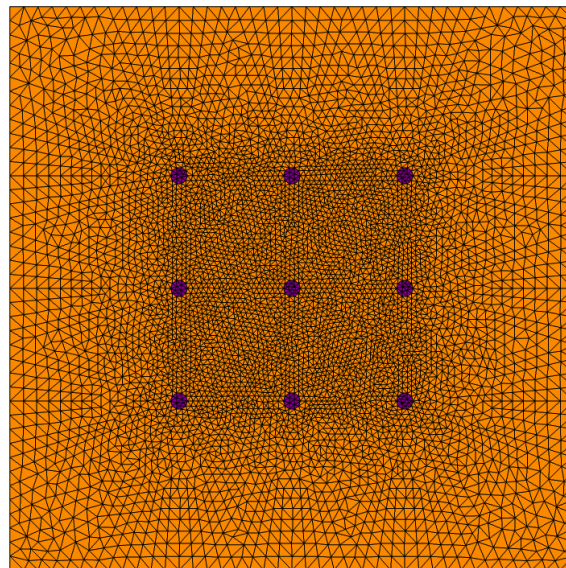
MEAs are designed for use in *in vitro* or *in vivo* studies. Several MEA geometries are provided for various applications, such as extracellular recording in vitro, for example, central or peripheral neurons, cardiac myocytes, whole-heart preparations, or retina. In cardiac electrophysiology many applications to MEAs exist, for instance activation and excitation mapping, monitoring of QT-related prolongation and arrhythmias or longterm characterizations of cell types [MEA].

The MEA device is inserted in a dish where cardiac cells spontaneously generate an action potential. To be able to reproduce the experiments with numerical simulations, it is important to identify the source of the signal recorded by the electrodes.

In our simulations, we consider an MEA with 6 wells, each one containing 9 electrodes, whose real and synthetic geometries are shown in Figure 7.1. The 9 electrodes of each well measure the (mean) extra-cellular potential on the electrode. A well is attached to the ground on its one side (bottom side in Figure 7.1(a) right) and on its two other sides (left and right sides in Figure 7.1(a) right), while it is immersed in the conduction liquid on the fourth side (top side of Figure 7.1(a) right). Thus, the boundary conditions should take into account the non-propagation of the extracellular potential on the three fixed edges (homogeneous Dirichlet condition for u_e) while on the top edge Neumann boundary condition can be used.



(a) Real geometry of a MEA 6 with wells on the left. On the right a single well with 9 electrodes. Source [MEA].



(b) MEA mesh for a single well.

Figure 7.1: Geometry of a well of the MEA device (each well contains 9 electrodes).

7.3.2 Formulation of the problem

We consider the bidomain equations [Tun78]

$$\begin{aligned} A_m \left(C_m \frac{\partial v_m}{\partial t} + I_{\text{ion}}(v_m, w) \right) - \text{div}(\sigma_i \nabla v_m) - \text{div}(\sigma_i \nabla u_e) &= A_m I_{\text{app}} \\ -\text{div}((\sigma_i + \sigma_e) \nabla u_e) - \text{div}(\sigma_i \nabla v_m) &= 0 \\ \frac{\partial w}{\partial t} - g(v_m, w) &= 0 \end{aligned} \quad (7.10)$$

coupled with the FitzHugh-Nagumo ionic model [Fit61, NAY62]

$$\begin{aligned} I_{\text{ion}}(u, w) &= su(u - a)(u - 1) + w \\ g(u, w) &= \varepsilon(\gamma u - w). \end{aligned} \quad (7.11)$$

For simplicity, we make the assumption that the boundary conditions are of Neumann type

$$\begin{aligned} \sigma_i \nabla u_e \cdot \mathbf{n} + \sigma_i \nabla v_m \cdot \mathbf{n} &= 0 \\ \sigma_e \nabla u_e \cdot \mathbf{n} &= 0. \end{aligned} \quad (7.12)$$

In the case of the more realistic boundary conditions described above two basis should be calculated. We will see in Section 8.5 how to deal with them for the ALP-DEIM method presented in the next chapter.

The aim of this work is to use the synthetic MEA measure obtained with a FEM simulation as the observer in order to reconstruct the source term location. Let us define the observation $d = \{d_1, \dots, d_9\} \in \mathbb{R}^9$ as the extra-cellular potential mean measured on each electrode. We consider the linear observation operator \mathcal{H} such that $\mathcal{H}(u_e) = d$, where u_e is the extra-cellular potential on the whole domain. Then the problem reads

$$\begin{cases} A_m C_m \partial_t v_m = f(v_m, u_e, w) + \mathcal{G}(d - \mathcal{H}(u_e)), \\ \partial_t w = g(v_m, w), \\ q(v_m, u_e) = 0, \end{cases} \quad (7.13)$$

where \mathcal{G} is the filter. In this work we use a Luenberger type filter and take $\mathcal{G} = a\mathcal{H}^*$, where $a > 0$. The idea is to apply the filter to the RO model to take advantage of the capability of the ALP method to approximate the solution with only a few degrees of freedom. Then, projecting system (7.13) on the RO space, we obtain

$$\begin{cases} \dot{\beta} + M\beta = \gamma^H, \\ \dot{\mu} + M\mu = \eta, \\ Q\xi + E\beta = 0 \end{cases} \quad (7.14)$$

where the only term which is modified compared to the ALP method is γ^H that takes into account the observer

$$\gamma^H = \gamma(\beta, \xi, \mu) + aH^T(d - H\xi), \quad (7.15)$$

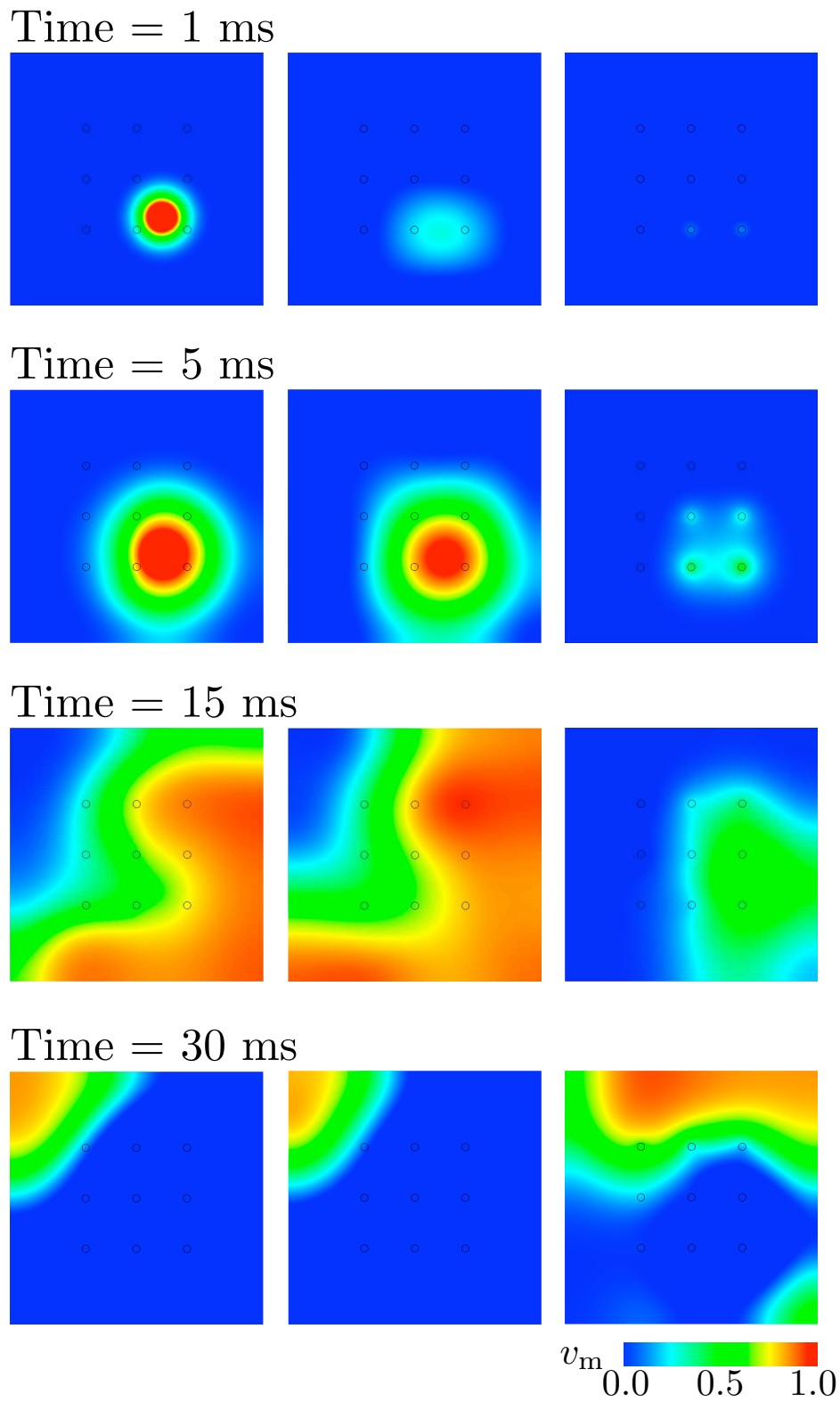
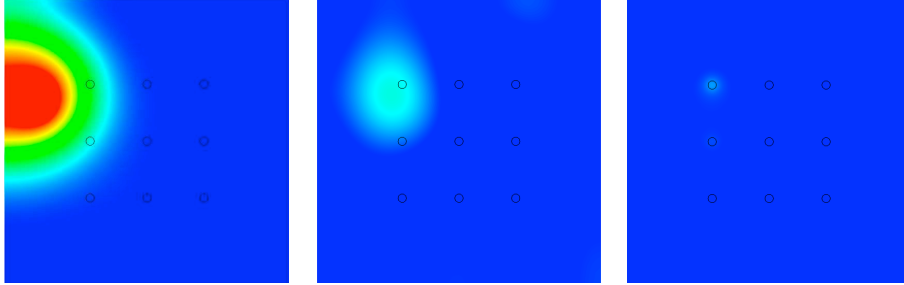
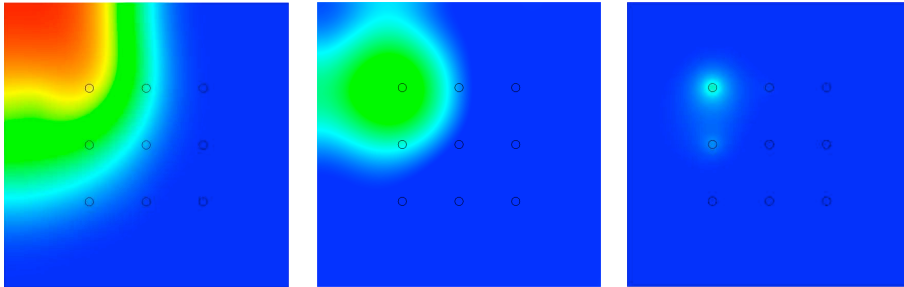


Figure 7.2: Comparison between observation (FEM solution of system (6.32)) on the left, filtering method with ALP approximation (7.14) ($\chi = 25$, $N_M = 25$) in the middle, and with FEM method (7.13) on the right. First source.

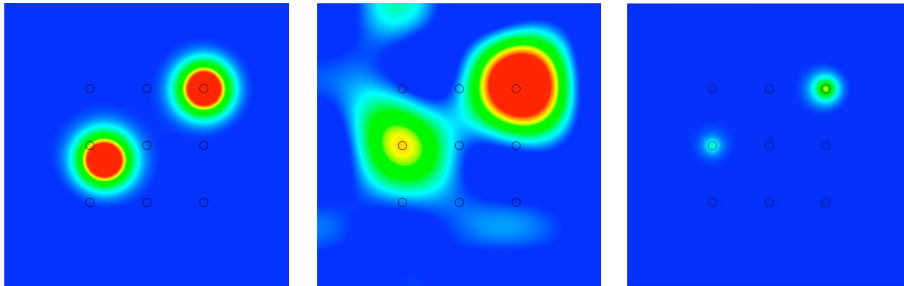
Time = 85 ms



Time = 90 ms



Time = 161 ms



Time = 165 ms

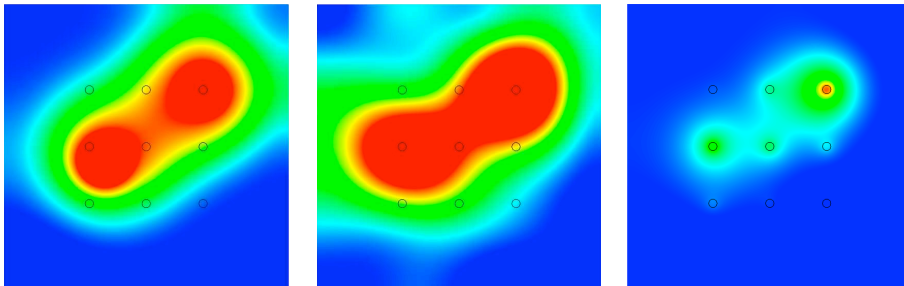

 v_m 
0.0 0.5 1.0

Figure 7.3: Comparison between observation (FEM solution of system (6.32)) on the left, filtering method with ALP approximation (7.14) ($\chi = 25$, $N_M = 25$) in the middle, and with FEM method (7.13) on the right. Second and third sources.

where H is the linear operator \mathcal{H} projected onto the RO space

$$H : \mathbb{R}^{N_M} \rightarrow \mathbb{R}^9, \text{ s.t. } H_i(\xi) = \int_{\Gamma_i} \Phi \xi dx, i = 1, \dots, 9 \quad (7.16)$$

where $\Gamma_i, i = 1, \dots, 9$, are the surfaces of the electrodes.

7.3.3 Numerical results

We apply this method to a square domain $\Omega = [0,1]^2$ representing one well of the MEA technology. The electrodes are represented by the 9 circles in Figures 7.2 and 7.3. The mesh contains about 5k nodes, while we solve the ALP problem with $N_M = 25$ modes and with $\chi = 25$. The time step is $dt = 0.01\text{ms}$ and the filter is applied at each time iteration. The initial basis for the ALP method is given by the eigenfunctions of the Laplacian operator, *i.e.* we assume that we have no information on the initial solution and we take $v_m = u_e = 0$ for all $x \in \Omega$. The observations d are given by a FEM simulation, represented on the left of Figure 7.2 and 7.3. First, a source term I_{app} is placed around $(x,y) = (0.60, 0.35)$. We observe in Figure 7.2 center that after a few iterations the ALP filtering solution behaves as if there was a source term in a point given by the interpolation of the two electrodes that “received” the information. The more the signal propagates, the more precise is the ALP solution that can reproduce the observation for all the depolarization and repolarization fronts. On the opposite, we remark that the filter applied to the FEM problem (Figure 7.2 right) is able to change the solution only locally around the electrodes. After 85ms of simulation, we apply a second source term on the left of the domain (Figure 7.3). Once again, we observe that, when the reference solution reaches the electrodes, this information is immediately transmitted through the filter operator. The ALP method uses the information given by the electrodes and the global character of the basis lets the filter see an interpolation of the observation, while the FEM can apply it only on the electrodes surface. Finally, at 160ms of simulation, we apply two more stimuli simultaneously and observe the same behavior of the ALP and the FE filtering method already observed for the first and second source terms (resp. at 0ms and 80ms).

7.4 Application to epicardium potential reconstruction

The second application of ALP method with filtering is the “classical” inverse problem of electrocardiology. We are interested in reconstructing the extra-cellular potential on the epicardium of the heart using some skin measures. In this section we consider a simplified problem on a synthetic geometry, this work constitutes a preliminary step for the resolution of the problem in real settings.

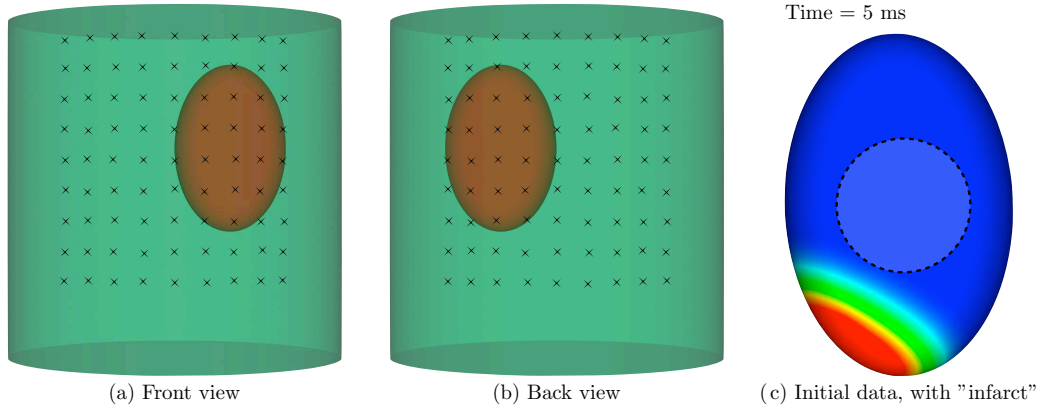


Figure 7.4: Cylinder geometry for the torso with synthetic electrodes (left) and ellipsoid geometry for the heart with the initial condition and the “infarcted” zone.

7.4.1 Formulation of the problem

The inverse problem, introduced in Section 1.5, reads:

$$\text{find } g \in H^{1/2}(\Sigma) \text{ s.t. } \mathcal{S}(g) = d, \quad d \in L^2(\Gamma_{\text{ECG}}), \quad \Gamma_{\text{ECG}} \subset \partial\Omega_{\text{T}}^{\text{ext}}, \quad (7.17)$$

where \mathcal{S} is a linear mapping: $\mathcal{S} : H^{1/2}(\Sigma) \rightarrow L^2(\Gamma_{\text{ECG}})$, $\mathcal{S}(g) = u_{\text{T}}(g)|_{\Gamma_{\text{ECG}}}$ whose discrete approximation $S \in \mathbb{R}^{N_{\text{ECG}} \times N_{\Sigma}}$ is described in Section 6.4.6, and u_{T} is solution of the thorax diffusion problem

$$\begin{aligned} \operatorname{div}(\sigma_{\text{T}} \nabla u_{\text{T}}) &= 0, & \text{in } \Omega_{\text{T}} \\ u_{\text{T}} &= u_{\text{e}}, & \text{on } \Sigma \\ \sigma_{\text{T}} \nabla u_{\text{T}} \cdot \mathbf{n} &= 0, & \text{on } \partial\Omega_{\text{T}}^{\text{ext}} \end{aligned} \quad (7.18)$$

for $u_{\text{e}} = g$.

We apply the same data assimilation technique as in the previous section but we change the filter and the observer operators. In particular, we take advantage of the discrete formulation of the inverse problem (7.17)

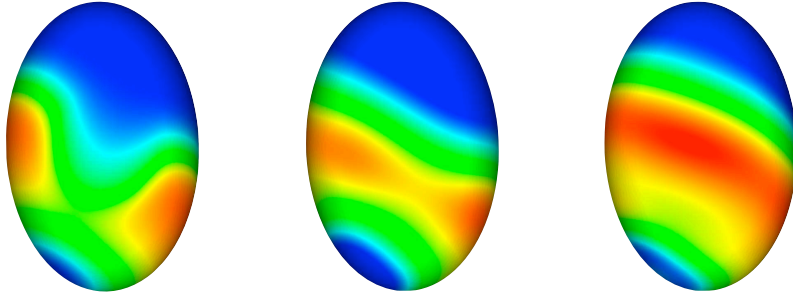
$$\min_{g \in \mathbb{R}^{\mathcal{N}}} \|S\Pi g - d\|_{l^2(\mathbb{R}^{N_{\text{ECG}}})}^2 \quad (7.19)$$

to define the observer and the filter operators. We define the observation operator $H = S\Pi$ and the filter $G = aH^T$. Then, we consider the observation problem projected on the ALP space (7.14) as in the last section, where the right-hand side of the first equation γ^H is

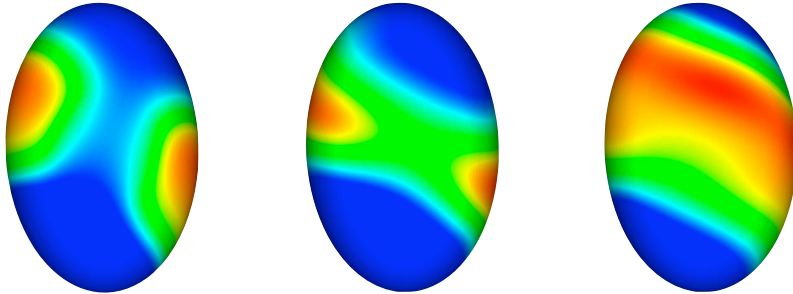
$$\gamma^H = \gamma(\beta, \xi, \mu) + aX^T(d - X\xi) \quad (7.20)$$

where $d \in \mathbb{R}^{N_{\text{ECG}}}$ corresponds to the measures of the torso potential on the skin

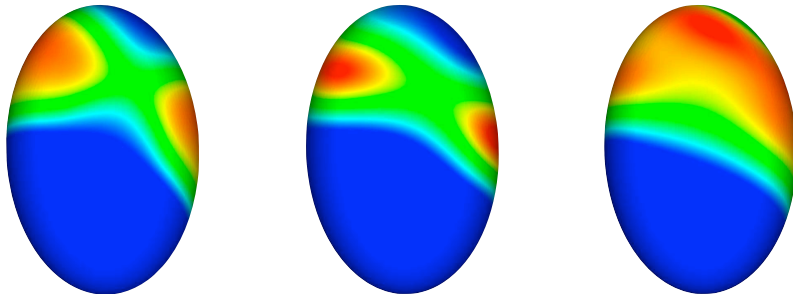
Time = 20 ms



Time = 25 ms



Time = 30 ms



Time = 40 ms

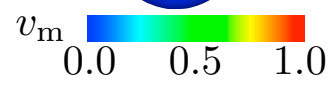
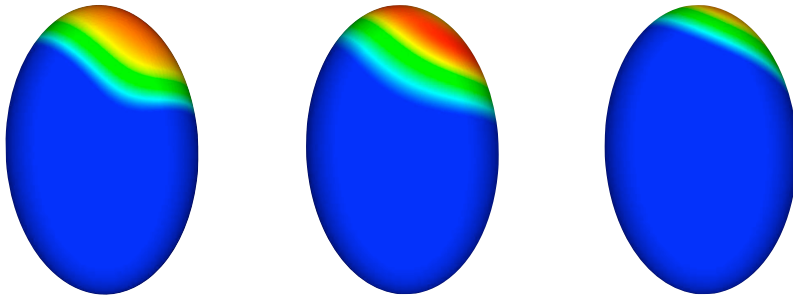


Figure 7.5: Comparison between observation (FEM solution of system (6.32)) on the left, filtering method with ALP approximation (7.14) ($\chi = 50$, $N_M = 60$) in the middle, and with ALP method (6.59) without observer on the right.

electrodes, and $X = S\Pi\Phi$, $X \in \mathbb{R}^{N_{\text{ECG}} \times N_{\text{M}}}$ is the (time evolving) transfer operator in the RO space described in Section 6.4.6.

7.4.2 Numerical results

We apply this method to the synthetic geometries presented in Section 6.4.6, and we take 162 electrodes on the cylinder surface (see Figure 7.4 left). The observations are issued from a FEM simulation in the case of an heterogeneous parameter s that causes an “infarction” in the area indicated in Figure 7.4 right. Both FEM and ALP-filtering problems are solved with the so-called surface-based bidomain equation [CCG12] [CGH⁺13] presented in Chapter 2 for the atrial surface. We observe from Figure 7.5 that the filtered solution (center) well approximates the observed solution (left), on the region of the infarction but also before (after) the depolarization (depolarization) front passes through the infarcted zone, while the non filtered ALP method (right) have also a different depolarization velocity.

7.5 Chapter conclusions

The ALP method has been used in a data assimilation technique, using a Luengerger type observation operator, in order to estimate the state of the system in two different configurations. First, dealing with the MEA technology, we considered a 2D domain and we used some measures on a small subdomain in order to identify the location of one or more source terms. Second, the method has been applied for the resolution of the “classical” inverse problem of electrophysiology. We used some observation of the potential on the external boundary of the torso in order to reconstruct the transmembrane and the extracellular potential on the epicardial surface of the heart. The results presented in this work represents an approximation of the problem in a real configuration. Thus, this application is of particular interest and represents a crucial step for future works. In the perspectives, we have to take into account a reduced-order method that can manage some non-polynomial terms, a different anisotropy for the intra- and the extra-cellular conductivity tensors, and real geometries and data. In the next chapter we will present a new reduced-order method that can deal with non-polynomial terms and we will briefly describe how to treat different anisotropic tensors.

Reduced Order Model with Approximated Lax Pairs and Discrete Empirical Interpolation Method

In this chapter an alternative formulation of the reduced-order method based on Approximated Lax Pairs (ALP) introduced in Chapter 6 is proposed. This new formulation of ALP is conjugated to the recently Discrete Empirical Interpolation Method (DEIM). DEIM is a variant of the Empirical Interpolation Method (EIM) that reduces the complexity of the evaluations of the nonlinear terms. DEIM combines projection with interpolation in order to approximate nonlinear functions. The method which is used here combines the ALP method with the idea of interpolating nonlinear terms. In particular, the functions are interpolated using a collocation operator. The method is tested on a few 2D test cases for cardiac electrophysiology equations including non-polynomial nonlinearities. A particular attention is paid to the perspectives and to the application of the method to real geometries and inverse problems.

The results presented in this chapter lead to the manuscript
Damiano Lombardi, Jean-Frédéric Gerbeau, Elisa Schenone, **Reduced Order Model
in Cardiac Electrophysiology with Approximated Lax Pairs and Discrete
Empirical Interpolation Method**, To be submitted.

Contents

8.1	Introduction	179
8.2	The ALP-DEIM method	180
8.2.1	Motivation and collocation operator	180
8.2.2	Time-dependent basis construction and evolution	181
8.2.3	ALP-DEIM implementation	183
8.2.4	Reconstruction in the physical space	184
8.2.5	Reconstruction in the high dimensional space	184
8.3	ALP-DEIM in cardiac electrophysiology	185
8.3.1	ALP-DEIM for the bidomain equations	186
8.3.2	Computation of the Electrocardiogram	189
8.4	Numerical experiments	190
8.4.1	Homogeneous parameters 2D case	190
8.4.2	Heterogeneous ionic parameters	191
8.4.3	Source terms	193
8.4.4	Anisotropic fiber tensors	197
8.5	Perspectives	197
8.5.1	Two basis computation	197
8.5.2	Inverse problems	199
8.6	Chapter conclusions	200

8.1 Introduction

As illustrated in previous chapters, the use of ROM cardiac electrophysiology equations is very challenging, in particular due to the non-linearities and to the dependence on many parameters. We have shown in the last chapters that the application of a ROM based on Approximated Lax Pairs (ALP) gives good results in the treatments of nonlinearities and changes in parameters. Although the ALP method is very promising, it does not allow the treatment of non-polynomial terms and its computational costs can be non-negligible if the size of the basis increases.

In this chapter we propose a new approach where the ALP method is combined with some ideas arising from the Discrete Empirical Interpolation Method (DEIM) proposed by Chaturantabut and Sorensen [CS10b] which is a discrete variant of the Empirical Interpolation Method (EIM) introduced by Barrault, Maday, Nguyen and Patera [BMNP04]. EIM is a reduced-basis discretization technique that can be used for partial differential equations with non-affine parameter dependence, which is based on an interpolation procedure that leads to an affine offline-online decomposition. The DEIM approach combines projection with interpolation in order to approximate nonlinear functions. In [CS10b] a POD-DEIM method is introduced, which is closely related to Verhoeven work [Ver08]. Both methods propose to compute nonlinear approximations by using some selected spatial points, the difference is the way the basis matrices are obtained: from a least-square solution of the snapshots in [Ver08], and from SVD truncation in the POD-DEIM approach [CS10b]. Many works have risen from [CS10b], see for instance [CS12, WSH14, PBWB14].

The ALP-DEIM method used in this work combines the idea of a time evolving basis, which does not rely on a database, see Chapter 6, and the treatment of nonlinear terms using a selection of spatial points from the DEIM technique. In particular, the definition of the basis functions and of their time evolution does not change compared to the ALP method, but the functions and the operator used to solve the reduced order problem are evaluated on a finite set of points which is typically a subset of the finite elements nodes of small dimension. The ALP-DEIM method allows therefore the treatment of nonlinearities of non-polynomial type and reduces the computational costs compared to the ALP method since no tensors have to be computed.

The structure of the Chapter is the following. First, we present a description of the method, which is strongly related to the previously described ALP approach. Then, in Section 8.3 the method is applied to the cardiac electrophysiology equations, in particular the bidomain equations [Tun78] described in Section 1.4 are coupled with the Mitchell and Schaeffer ionic model [MS03] which is non-polynomial, see Section 1.4. Various 2D numerical examples are proposed in Section 8.4. Many perspectives are in order. In particular, the method is applied under the assumption that the intra- and extra-cellular conductivity tensors have the same anisotropy, see Section 1.4. The steps necessary to apply it to more general problems are described in Section 8.5.

8.2 The ALP-DEIM method

The approach of the ALP-DEIM method is basically the same as the ALP method presented in Chapter 6: a basis, which is defined using the modes of a linear (with inverse compact) operator, evolves in time in a way depending on the problem. The main difference is the fact that the basis and all the objects useful for the resolution of the problem are discretized on a subset P of the nodes of the FE approximation. This will allow us to treat the non-polynomial terms as detailed hereafter.

Let us consider a generic PDE of the form

$$\partial_t u = F(u, \partial_x^{(n)} u) \quad (8.1)$$

where $u(x, t)$, for all $x \in \Omega \subseteq \mathbb{R}^d$, $t > 0$, is the solution of the PDE, with specified initial and boundary conditions, and $F(u) = F(u, \partial_x^{(n)} u)$ is generically nonlinear and non-polynomial.

The first step is then to define an initial basis. Here, as in the ALP method previously presented, we consider the eigenfunctions of a Schrödinger operator associated with the potential $-\chi u$

$$\mathcal{L}(u)\phi = -\operatorname{div}(\nabla\phi) - \chi u\phi, \quad (8.2)$$

where u is the solution of (8.1), and χ is a real positive scalar parameter that represents a characteristic space length associated with the eigenfunction, see Section 6.4.2. Indeed, the initial basis is given by the first N_P eigenfunctions of the eigenproblem

$$\mathcal{L}(u)\phi = \lambda\phi. \quad (8.3)$$

Let us call $V = [\phi_1, \dots, \phi_{N_P}]$ the matrix of the modes discretized on the FE space of dimension \mathcal{N} , $V \in \mathbb{R}^{\mathcal{N} \times N_P}$, $N_P \ll \mathcal{N}$.

8.2.1 Motivation and collocation operator

As in the ALP method, the solution $u = u(x, t)$ is expanded on the eigenfunctions

$$u \simeq \sum_{j=1}^{N_P} \beta_j(t) \phi_j(x, t). \quad (8.4)$$

This expression is injected into the PDE and a projection on the eigenfunctions is performed

$$\partial_t \beta_i + \sum_{j=1}^{N_P} \widetilde{M}_{ij} \beta_j = \langle F(\sum_{j=1}^{N_P} \beta_j \phi_j), \phi_i \rangle, \quad (8.5)$$

where \widetilde{M} is the discrete evolution operator introduced in the Chapter 6 for the ALP method

$$\widetilde{M}_{ij} = \begin{cases} \frac{\chi}{\lambda_j - \lambda_i} \langle F(\sum_{k=1}^{N_P} \beta_k \phi_k) \phi_i, \phi_j \rangle, & \lambda_i \neq \lambda_j \\ 0, & \lambda_i = \lambda_j \end{cases} \quad (8.6)$$

for all $i, j = 1, \dots, N_P$. We denote by \widetilde{M} (instead of M) the discrete evolution operator of the original ALP method because hereafter M will define the evolution operator of the ALP-DEIM method.

The goal of the method is to be able to compute the right-hand side of the equation by staying in the reduced order space. If F is non-polynomial, it cannot be directly represented on the RO space since the integral and F do not commute. The idea is then to find an operator \mathcal{P} such that $\mathcal{P}F(u) = F(\mathcal{P}u)$ and this operator is, for instance, the collocation operator $\mathcal{P} : \mathbb{R}^N \rightarrow \mathbb{R}^{N_P}$, since

$$\widehat{F}_l := F(u(x_l)) = F(\widehat{u}_l), \quad l = 1, \dots, N_P, \quad (8.7)$$

where $\widehat{u} = \mathcal{P}u$. By using this property of the collocation operator, an expression for the right-hand side of (8.1) for each time $t > 0$ is obtained:

$$\widehat{F}_l(t) = F\left(\sum_{j=1}^{N_P} \beta_j(t) \phi_j(x_l, t)\right), \quad l = 1, \dots, N_P. \quad (8.8)$$

As for the definition of the right-hand side \widehat{F} , we need to introduce the collocation matrix for the modes. Let us call $W \in \mathbb{R}^{N_P \times N_P}$ the matrix of the basis functions in the collocation points:

$$W = [w_1, \dots, w_{N_P}], \quad w_j = \mathcal{P}\phi_j, \quad j = 1, \dots, N_P. \quad (8.9)$$

Of course, the number N_P of collocation points could be not small enough to be interesting in the purpose of a model reduction method in order to have computation cost gains. So, let us consider only a restricted number of modes $N_M \leq N_P$. We define the associated matrix $\Phi^{(0)} \in \mathbb{R}^{N_P \times N_M}$, $\Phi^{(0)} = [\varphi_1(t=0), \dots, \varphi_{N_M}(t=0)]$ with $\varphi_i(t=0) = w_i$, for all $i = 1, \dots, N_M$. Then, only the modes defined by the matrix $\Phi^{(0)}$ will evolve in time.

8.2.2 Time-dependent basis construction and evolution

Let us consider the continuous evolution equation obtained from the operator definition (8.2)

$$(\mathcal{L} - \lambda_i) \partial_t \phi_i = \dot{\lambda}_i \phi_i + \chi F(u) \phi_i, \quad i = 1, \dots, N_M, \quad (8.10)$$

see Chapter 6 for more details. Its discretized version on N_P degrees of freedom has the following form:

$$L\partial_t\Phi - G\partial_t\Phi\Lambda = G\Phi\dot{\Lambda} + \chi G\widehat{F} * \Phi, \quad (8.11)$$

where L is the discretization of the \mathcal{L} operator on the space defined by Φ , Λ is the diagonal matrix of the eigenvalues λ , G is the reduced mass matrix defined on the collocation points P , and the $*$ operator is the Hadamard product defined by

$$\widehat{F} * \Phi := \text{diag}(\widehat{F})\Phi, \quad [\widehat{F} * \Phi]_{ij} = \widehat{F}_i\Phi_{ij}, \quad i = 1, \dots, N_P, \quad j = 1, \dots, N_M. \quad (8.12)$$

The computation of the reduced mass matrix G is not trivial. In general, when a restriction of the nodes is taken, it is equivalent to consider a Lagrange interpolant on the N_P collocation points. For the integration purpose, the expression of the collocation basis is useless and it would require the construction of a coarse mesh associated with the collocation points and of the associated FE basis and integration methods. In a pure formal way, the Gram matrix G should be computed as

$$G_{ij} = \langle v_i, v_j \rangle, \quad i, j = 1, \dots, N_P, \quad (8.13)$$

where the v_i , $i = 1, \dots, N_P$, are the FE basis functions on the ‘‘coarse mesh’’ (that we do not want to compute). Since, in most cases, only the Gram matrix G is needed, an alternative technique is possible. Then, in order to compute G , we use that the basis defined on the collocation points associated with the matrix W is orthonormal with respect to the reduced mass matrix G

$$W^T G W = I \quad (8.14)$$

where $I \in \mathbb{R}^{N_P \times N_P}$ is the identity matrix. The matrix W can be QR-decomposed $W = QR$, where Q is an orthonormal matrix and R is a upper triangular matrix, which is obtained without any extra costs when applying a Modified Gram-Schmidt (MGS) orthonormalization as suggested below. Then, the expression of G can be obtained by

$$G = QR^{-T}R^{-1}Q^T. \quad (8.15)$$

Note that

$$L\Phi = G\Phi\Lambda. \quad (8.16)$$

The classical ALP method is thus retrieved by multiplying equation (8.11) by Φ^T :

$$\Lambda\Phi^T G\partial_t\Phi - \Phi^T G\partial_t\Phi\Lambda = \dot{\Lambda} + \chi\Theta, \quad (8.17)$$

where the matrix $\Theta \in \mathbb{R}^{N_M \times N_M}$ reads

$$\Theta = \Phi^T G\widehat{F} * \Phi. \quad (8.18)$$

Also, the discrete evolution operator M (which was previously denoted by \widetilde{M} and defined by equation (8.6)) is defined as the projection onto the space defined by Φ

of the time derivative of the modes Φ :

$$M = \Phi^T G \partial_t \Phi. \quad (8.19)$$

We inject this expression into equation (8.17). Then, equation (8.17) may be written in the compact form

$$\dot{\Lambda} + M\Lambda - \Lambda M + \chi\Theta = 0. \quad (8.20)$$

In the same way as in the ALP method, this equation leads to the definition of the discrete objects $\dot{\Lambda}$ and M . The diagonal elements of equation (8.20) give the following evolution equation for the eigenvalues:

$$\dot{\lambda}_i = -\chi\Theta_{ii}, \quad i = 1, \dots, N_M, \quad (8.21)$$

and the extradiagonal elements to the discrete evolution operator M :

$$M_{ij} = \begin{cases} \frac{\chi}{\lambda_j - \lambda_i} \Theta_{ij}, & \lambda_i \neq \lambda_j \\ 0, & \lambda_i = \lambda_j \end{cases} \quad (8.22)$$

for all $i = 1, \dots, N_M$. Finally, thanks to the matrix M , we define the time evolution of the basis, exactly in the same way as in the ALP method:

$$\partial_t \Phi = \Phi M. \quad (8.23)$$

8.2.3 ALP-DEIM implementation

To sum up, let us describe the general step to apply the ALP-DEIM method. Here is the set of the equations that describes the dynamics in the reduced order space:

$$\left\{ \begin{array}{l} \dot{\beta} + M\beta = \Phi^T G \widehat{F}, \\ \partial_t \Phi = \Phi M, \\ \dot{\lambda}_i = -\chi\Theta_{ii}, \quad i = 1 \dots N_M \\ M_{ij} = \frac{\chi}{\lambda_j - \lambda_i} \Theta_{ij}, \quad i, j = 1 \dots N_M \\ \widehat{u} = \Phi\beta \\ \widehat{F} = F(\widehat{u}), \\ \Theta = \Phi^T G \widehat{F} * \Phi, \end{array} \right. \quad (8.24)$$

where the discretization β of the solution u in the reduced space Φ is of course truncated to N_M terms. Let us remark that, compared to system (6.18) for the ALP method, no tensors have to be computed. Also, the computation of the right-hand side term \widehat{F} is only the evaluation of the continuous operator F in the collocation points P and its computational cost is linear in the N_P dimension. To conclude, the computational cost of system (8.24) is of order $N_M N_P^2$ and the dependence on the FE dimension \mathcal{N} which was the disadvantage of the “classic” ALP method disappeared.

8.2.4 Reconstruction in the physical space

The reconstruction in the physical space is simplified with respect to the original version of ALP. This is possible because, in the derivation of the ALP-DEIM, in order to construct the reduced mass and stiffness matrices, we make use of an intermediate space whose basis is the initial basis of size N_P . Whatever the evolution of the N_M modes is, it can be described exactly in this extended initial basis, that is in a bijection with the collocation basis on the N_P points.

At each time the matrix $\Phi \in \mathbb{R}^{N_P \times N_M}$ is available. The modes at time t^n can be expressed with respect to $W \in \mathbb{R}^{N_P \times N_P}$. Let $\Pi_W \in \mathbb{R}^{N_M \times N_P}$ be the matrix of the change of basis:

$$\Pi_W^{(n)} = W^T G \Phi^{(n)}. \quad (8.25)$$

Since the basis W is simply the restriction of the initial basis $V \in \mathbb{R}^{\mathcal{N} \times N_P}$ on the collocation points, the solution at each time iteration $n \geq 1$ can be computed by

$$u^{(n)} \simeq V \Pi_W^{(n)} \beta^{(n)}. \quad (8.26)$$

This algorithm can be further simplified. Indeed, the expression of $\Pi_W^{(n)}$ is injected into the expression of the approximated solution that reads

$$u^{(n)} \simeq V W^T G \Phi^{(n)} \beta^{(n)}, \quad (8.27)$$

where $\Phi^{(n)} \beta^{(n)}$ can be substituted by $\widehat{u}^{(n)}$. Finally, let us define the extension operator $\Pi_V := V W^T G$ which is a pseudo-inverse of the restriction operator and that can be computed once for all at the beginning of the algorithm. This allows to interpolate the ROM solution on the fine mesh

$$u^{(n)} \simeq \Pi_V \widehat{u}^{(n)}, \quad (8.28)$$

whose cost is $\mathcal{N} \times N_P$.

8.2.5 Reconstruction in the high dimensional space

Since $N_P > N_M$ the time derivatives of the modes can be computed accounting for some components which are orthogonal to the space spanned by the modes at current time. In particular, let us define R the matrix of the residual in the basis evolution equation:

$$\partial_t \Phi = \Phi M + R, \quad (8.29)$$

where R is such that $\Phi^T G R = 0$. We used in this section the same notation Φ as in equation (8.23) for the definition of the basis evolution. The two definitions coincide only if $F * \Phi$ has a null projection in the space spanned by Ψ , as noticed below, otherwise they differ. Except in this section, the basis evolution is governed by (8.23).

The orthogonal modes are defined by exploiting the fact that the modes are evolving in a space of dimension N_P . This space is in a bijection with the space

spanned by N_P modes at the initial time. The orthogonal basis is defined as

$$\Psi = [w_{N_M+1} \cdots w_{N_P}] - \Phi \Phi^T G [w_{N_M+1} \cdots w_{N_P}], \quad (8.30)$$

where w_i is the i -th column of W . Only few elements of Ψ are retrieved, let us call the dimension of Ψ $N^\perp \leq N_P - N_M$. The partial derivatives of the modes is approximated by

$$\partial_t \Phi \simeq \Phi M + \Psi C, \quad (8.31)$$

and this expression is injected into equation (8.11), leading to

$$G\Phi\Lambda M + L\Psi C - G\Phi M\Lambda - G\Psi C\Lambda = G\Phi\dot{\Lambda} + \chi GF * \Phi. \quad (8.32)$$

The projection of this equation onto Φ has already been computed and leads to (8.17), since Ψ is by construction orthogonal to Φ , while the projection onto Ψ allows us to determine the expression of the operator C :

$$\Psi^T L\Psi C - \Psi^T G\Psi C\Lambda = \chi \Psi^T GF * \Phi. \quad (8.33)$$

Thus, a matrix equation for C can be written for each mode separately. It can be demonstrated that the system matrix $\Psi^T L\Psi - \lambda_i \Psi^T G\Psi$, $i = 1, \dots, N_M$, for each mode is positive definite. If $F * \Phi$ has a null projection in the space spanned by Ψ , C vanishes identically. Otherwise, the derivatives of the modes have a non-vanishing projection onto the orthogonal space if and only if the image of the operator $F * \Phi$ has.

8.3 ALP-DEIM in cardiac electrophysiology

We are now interested in applying the ALP-DEIM method to the electrophysiology equations. In particular, we are now able to treat non-polynomial terms, so the choice of the bidomain equations coupled with the Mitchell and Schaeffer ionic model is in order. We concentrate here on the case of intra- and extra-cellular conductivity tensors with the same anisotropy $\sigma_e = \alpha\sigma_i$, for a fixed $\alpha \in \mathbb{R}_+$. If this does not hold, then the extra-cellular potential u_e could not be approximated in the same space as the transmembrane potential v_m and two basis should be defined. This problem is investigated in the perspectives of the present chapter.

REMARK 8.1

Since $\sigma_e = \alpha\sigma_i$ the bidomain equations could be simplified into the monodomain equations. We prefer to keep the bidomain formalism for the sake of consistency with the reminder of this work.

8.3.1 ALP-DEIM for the bidomain equations

Let us consider the bidomain equations [Tun78] introduced in Section 1.4 on a bounded domain $\Omega \subset \mathbb{R}^d$, for any $t > 0$,

$$\begin{cases} A_m \left(C_m \frac{\partial v_m}{\partial t} + I_{\text{ion}}(v_m, w) \right) - \operatorname{div}(\boldsymbol{\sigma}_i \nabla v_m) - \operatorname{div}(\boldsymbol{\sigma}_i \nabla u_e) & = A_m I_{\text{app}}(x, t) \\ -\operatorname{div}((\boldsymbol{\sigma}_i + \boldsymbol{\sigma}_e) \nabla u_e) - \operatorname{div}(\boldsymbol{\sigma}_i \nabla v_m) & = 0 \\ \frac{\partial w}{\partial t} - g(v_m, w) & = 0, \end{cases} \quad (8.34)$$

with the following boundary conditions on $\partial\Omega$

$$\begin{cases} \boldsymbol{\sigma}_i \nabla v_m \cdot \mathbf{n} + \boldsymbol{\sigma}_i \nabla u_e \cdot \mathbf{n} & = 0, \\ \boldsymbol{\sigma}_e \nabla u_e \cdot \mathbf{n} & = 0. \end{cases} \quad (8.35)$$

The term I_{ion} is defined by the Mitchell and Schaeffer ionic model [MS03], see Section 1.4 or for instance Chapter 5,

$$\begin{aligned} I_{\text{ion}}(v_m, w) &= w \frac{v_m^2(1-v_m)}{\tau_{\text{in}}} + \frac{v_m}{\tau_{\text{out}}} \\ g(v_m, w) &= \begin{cases} \frac{w-1}{\tau_{\text{open}}}, & v_m < v_{\text{gate}} \\ \frac{w}{\tau_{\text{close}}}, & v_m > v_{\text{gate}}, \end{cases} \end{aligned} \quad (8.36)$$

where τ_{in} , τ_{out} , τ_{open} , τ_{close} , v_{gate} are scalar parameters.

As we did for the ‘‘classical’’ ALP method, we write the coupled system in the form

$$\begin{aligned} A_m C_m \partial_t v_m &= f(v_m, u_e, w), \\ \partial_t w &= g(v_m, w), \\ q(v_m, u_e) &= 0, \end{aligned} \quad (8.37)$$

where

$$\begin{aligned} f(v_m, u_e, w) &= A_m w \frac{v_m^2(1-v_m)}{\tau_{\text{in}}} + A_m \frac{v_m}{\tau_{\text{out}}} + \operatorname{div}(\boldsymbol{\sigma}_i \nabla v_m) + \operatorname{div}(\boldsymbol{\sigma}_i \nabla u_e) + A_m I_{\text{app}}, \\ g(v_m, w) &= \begin{cases} \frac{w-1}{\tau_{\text{open}}}, & v_m < v_{\text{gate}} \\ \frac{w}{\tau_{\text{close}}}, & v_m > v_{\text{gate}}, \end{cases} \\ q(v_m, u_e) &= -(1+\alpha) \operatorname{div}(\boldsymbol{\sigma}_i \nabla u_e) - \operatorname{div}(\boldsymbol{\sigma}_i \nabla v_m). \end{aligned} \quad (8.38)$$

As usual, the first step is to define the linear operator \mathcal{L} which is defined here in the same way as in the ALP method:

$$\mathcal{L}(u)\phi = -\operatorname{div}(\boldsymbol{\sigma}_i \nabla \phi) - \chi u \phi, \quad (8.39)$$

where the solution u is the transmembrane potential v_m . Then, the modes are the first N_P eigenfunctions of

$$\mathcal{L}(u)\phi = \lambda\phi. \quad (8.40)$$

Also, we remind that we define $V = [\phi_1, \dots, \phi_{N_P}] \in \mathbb{R}^{\mathcal{N} \times N_P}$ the matrix of the modes discretized in the full order space, $W = [w_1, \dots, w_{N_P}] \in \mathbb{R}^{N_P \times N_P}$ the initial modes in the collocation points, $w_i = \mathcal{P}\phi_i$ for all $i = 1, \dots, N_P$ where \mathcal{P} is the collocation operator, and $\Phi = [\varphi_1, \dots, \varphi_{N_P}] \in \mathbb{R}^{N_M \times N_P}$ is the only one that evolves in time, $\varphi_i = w_i$ for all $i = 1, \dots, N_M$ at the initial time.

Let us then approximate the solution of equations (8.37) in the low dimensional space defined by the N_M modes of Φ . We approximate the transmembrane potential v_m and the extra-cellular potential u_e in the collocation points by

$$\hat{v} = \Phi^T \beta = \left(\sum_{i=1}^{N_M} \beta_i(t) \varphi_i(x_j, t) \right)_{j=1}^{N_P}, \quad (8.41)$$

$$\hat{u} = \Phi^T \xi = \left(\sum_{i=1}^{N_M} \xi_i(t) \varphi_i(x_j, t) \right)_{j=1}^{N_P}, \quad (8.42)$$

$$(8.43)$$

where $\hat{v} = \mathcal{P}v_m$, $\hat{u} = \mathcal{P}u_e$, while the ionic variable w is evaluated in the collocation points, $\hat{w} = \mathcal{P}w$, without any approximation in the RO space.

Using these approximation of the solution on the basis Φ of \mathbb{R}^{N_P} , we define \hat{F} the function f in the collocation points:

$$\hat{F} = \mathcal{P}f(v_m, u_e, w) = f(\hat{v}, \hat{u}, \hat{w}), \quad (8.44)$$

where

$$\hat{F}_l = A_m \hat{w}_l \frac{\hat{v}_l^2 (1 - \hat{v}_l)}{\tau_{in}} + A_m \frac{\hat{v}_l}{\tau_{out}} + \sum_{i=1}^{N_M} (\beta_i + \xi_i) \operatorname{div}(\sigma_i \nabla \varphi_i(x_l)), \quad (8.45)$$

for all $l = 1, \dots, N_P$. Thanks to the definition of the \mathcal{L} operator, \hat{F} can be written as

$$\hat{F}_l = A_m \hat{w}_l \frac{\hat{v}_l^2 (1 - \hat{v}_l)}{\tau_{in}} + A_m \frac{\hat{v}_l}{\tau_{out}} - \sum_{i=1}^{N_M} (\beta_i + \xi_i) (\chi \hat{v}_l + \lambda_i) \varphi_i(x_l). \quad (8.46)$$

We remark that, contrary to the ALP method, the approximation of the solution on the basis Φ (*i.e.* the decomposition $\Phi^T \beta$, $\Phi^T \xi$) is not strictly necessary, but it is used here for convenience only in the diffusion terms.

In an analogous way, we consider the right-hand side of the second equation

of (8.37). Let us define $\widehat{G} = \mathcal{P}g(v_m, w) = g(\widehat{v}, \widehat{w})$, its elements are given by

$$\widehat{G}_l = \begin{cases} \frac{\widehat{w}_l - 1}{\tau_{\text{open}}}, & \widehat{v}_l < v_{\text{gate}} \\ \frac{\widehat{w}_l}{\tau_{\text{close}}}, & \widehat{v}_l > v_{\text{gate}}. \end{cases} \quad (8.47)$$

We remark that the second equation of (8.37) is solved only in the collocation points

$$\partial_t \widehat{w}_l = \widehat{G}_l, \quad l = 1, \dots, N_P. \quad (8.48)$$

Finally, let us consider the third equation. Using the Galerkin approximations of the solution, it reads

$$\sum_{i=1}^{N_M} (\beta_i + (1 + \alpha)\xi_i) (\chi \widehat{v}_l + \lambda_i) \varphi_i(x_l) = 0, \quad l = 1, \dots, N_P. \quad (8.49)$$

Let us project it on the mode φ_p , for all $p = 1, \dots, N_M$,

$$\sum_{h,l=1}^{N_P} \varphi_p(x_h) G_{hl} \left(\sum_{i=1}^{N_M} (\beta_i + (1 + \alpha)\xi_i) (\chi \widehat{v}_l + \lambda_i) \varphi_i(x_l) \right) = 0, \quad l = 1, \dots, N_P. \quad (8.50)$$

This is a linear system of size $N_M \times N_M$ for β, ξ which can be rearranged in

$$(1 + \alpha) \sum_{i=1}^{N_M} \left(\sum_{h,l=1}^{N_P} (\chi \widehat{v}_l + \lambda_i) \Phi_{hp} G_{hl} \Phi_{li} \right) \xi_i + \sum_{i=1}^{N_M} \left(\sum_{h,l=1}^{N_P} ((\chi \widehat{v}_l + \lambda_i) \varphi_{hp} G_{hl} \varphi_{li}) \right) \beta_i = 0, \quad (8.51)$$

for all $l = 1, \dots, N_P$. In a way analogous to the ALP method, we define the matrices $E, Q \in \mathbb{R}^{N_M \times N_M}$

$$Q_{pi} = (1 + \alpha) \sum_{h,l=1}^{N_P} (\chi \widehat{v}_l + \lambda_i) \Phi_{hp} G_{hl} \Phi_{li} \quad (8.52)$$

and

$$E_{pi} = \sum_{h,l=1}^{N_P} (\chi \widehat{v}_l + \lambda_i) \Phi_{hp} G_{hl} \Phi_{li} \quad (8.53)$$

for all $i, p = 1, \dots, N_M$. Then the third equation can be approximated by the linear system

$$Q\xi + E\beta = 0, \quad (8.54)$$

where the matrices Q and E need to be updated at each time-iteration using the same technique as the ALP method:

$$\partial_t E = [M, E], \quad \partial_t Q = [M, Q], \quad (8.55)$$

where $[\cdot, \cdot]$ is the commutator $[A, B] = AB - BA$.

Finally, the resolution with the ALP-DEIM method of the bidomain equations coupled with the Mitchell and Schaeffer ionic model, in the case of the same anisotropy for the intra- and the extra-cellular conductivity tensors, can be schematized as

$$\left\{ \begin{array}{l} \dot{\beta} + M\beta = \Phi^T G \widehat{F} \\ Q\xi + E\beta = 0 \\ \partial_t \Phi + \Phi M = 0 \\ \dot{\lambda}_i = -\chi \Theta_{ii}, \quad i = 1 \dots N_M \\ M_{ij} = \frac{\chi}{\lambda_j - \lambda_i} \Theta_{ij}, \quad i, j = 1 \dots N_M \\ \widehat{v} = \Phi \beta \\ \widehat{u} = \Phi \xi \\ \widehat{F} = F(\widehat{v}, \widehat{u}, \widehat{w}) \\ \widehat{G} = G(\widehat{v}, \widehat{w}) \\ \partial_t \widehat{w}_l = \widehat{G} \\ \Theta = \Phi^T G \widehat{F} * \Phi. \end{array} \right. \quad (8.56)$$

8.3.2 Computation of the Electrocardiogram

A comment on the computation of Electrocardiogram is in order. With the ALP-DEIM method, the operator is computed in a slightly different way compared to the ALP method. In fact, we can take advantage of the reconstruction in physical space operator in order to define the reduced transfer matrix, that in this case will be constant.

Let us briefly recall that the Electrocardiogram consists in measuring the electrical potential on some torso skin points. This is obtained by solving a Poisson problem in the torso domain, where on the interface between the heart and the torso, the torso potential is equal to the extracellular potential, and on the external boundary a homogeneous Neumann is imposed. So, we define a discrete linear operator of restriction on the epicardium

$$\Pi : \mathbb{R}^{\mathcal{N}} \rightarrow \mathbb{R}^{N_\Sigma} \text{ s.t. } \Pi u_e = u_e|_\Sigma \in \mathbb{R}^{N_\Sigma} \quad (8.57)$$

where N_Σ is the number of vertices on the heart-torso interface, and a discrete linear operator in the FE space, which associates to the epicardial extracellular potential $u_e|_\Sigma \in \mathbb{R}^{N_\Sigma}$ the ECG measures $y \in \mathbb{R}^{N_{\text{ECG}}}$:

$$S : \mathbb{R}^{N_\Sigma} \rightarrow \mathbb{R}^{N_{\text{ECG}}}, \quad y = S u_e|_\Sigma = S \Pi u_e. \quad (8.58)$$

In the same way as we did for the ALP method, we would be interested in defining an operator $X : \mathbb{R}^{N_M} \rightarrow \mathbb{R}^{N_{\text{ECG}}}$ such that

$$y = X \xi, \quad (8.59)$$

where ξ is the representation of the extracellular potential in the RO space Φ . Using the definition of the change of basis operator $\Pi_W : \mathbb{R}^{N_P} \rightarrow \mathbb{R}^{N_M}$, $\Pi_W^{(n)} = W^T G \Phi^{(n)}$,

we can write

$$y = SIV\Pi_W^{(n)}\xi^{(n)}, \quad (8.60)$$

where $V \in \mathbb{R}^{\mathcal{N} \times N_P}$ is the matrix of the initial basis in the FE space. This leads to the operator $X = SIV\Pi_W^{(n)}$, $X \in \mathbb{R}^{N_M \times N_{ECG}}$, which is of very low dimension but evolves in time, so that its update has to be taken into account.

A second strategy could be more interesting. Instead of using the representation of the extracellular potential in the RO space, we can take advantage of its representation on the collocation points \hat{u} . Then, we look for an operator $\Xi : \mathbb{R}^{N_P} \rightarrow \mathbb{R}^{N_{ECG}}$ such that

$$y = \Xi\hat{u}. \quad (8.61)$$

To define this operator, we use the prolongation operator $\Pi_V = VW^TG$, $\Pi_V \in \mathbb{R}^{\mathcal{N} \times N_P}$, defined in Section 8.2.4. Substituting its expression in (8.58), we obtain

$$\Xi = SIII_V. \quad (8.62)$$

The operator Ξ is constant in time, it can be calculated once for all at the beginning during the basis computation phase and no update of it is necessary.

8.4 Numerical experiments

In this section we present some preliminary results obtained with the ALP-DEIM method. We apply the method to the resolution of the bidomain equations coupled with the Mitchell and Schaeffer ionic model (8.37), (8.38). First, we consider an homogeneous cardiac tissue on a 2D domain. Then, some spatial and temporal heterogeneities are introduced: the parameter that regulates the depolarization plateau duration is changed as in the cardiac tissue; a source term not included in the initial basis is introduced; the fibers anisotropy is taken into account.

The problems are solved on a 2D squared domain $\Omega = [0,1]^2$ discretized with a P1 finite element mesh composed of 5,878 vertices. The collocation points are chosen on a cartesian grid as shown in Figure 8.1 and the number of collocation points is $N_P = 256$ for all the results presented. For all the FE simulations a second order Backward Difference method is used while for the ALP-DEIM resolution an Explicit Euler method is applied, both with time step $\delta t = 0.01\text{ms}$. Numerical results with ALP-DEIM are compared with the FE ones, and the relative error

$$\text{error}(t^n) = \frac{|v_m^n - \Phi^{(n)}\beta^n|}{\max|v_m^n|} \quad (8.63)$$

is shown. Parameters are taken as in Table 8.1.

8.4.1 Homogeneous parameters 2D case

The first case does not present any sensitive difficulty, We consider the bidomain equations with the Mitchell and Schaeffer model, without fiber tensors anisotropy

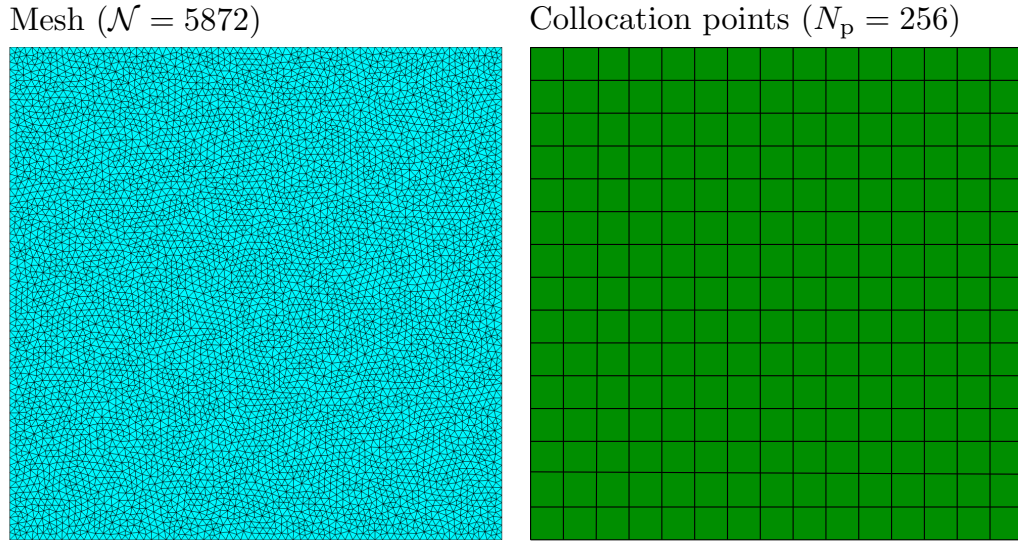


Figure 8.1: 2D test case mesh (left) and interpolation points (right).

and with homogeneous parameters. The challenging point is the treatment of the non-polynomial term in the Mitchell and Schaeffer ionic model.

The initial basis is computed using the FE solution at time $t = 5\text{ms}$, with $\chi = 25$, and the solution is run with $N_M = 25$ basis modes. In Figure 8.2 the results with the ALP-DEIM method (middle) are compared to the FE ones (left). We can see that the ROM solution is very close to the FE element solution. This can also be observed in the relative error plot (Figure 8.2 right) that is less than 10% for most of the time except at about 25ms when the propagation front “exits” the domain, but in all cases it does not exceed 30%.

8.4.2 Heterogeneous ionic parameters

We are now interested in introducing some heterogeneities in the ionic parameters. First, we reproduce the cardiac tissue heterogeneity by considering three different cell types as described in Section 1.4: endocardial, mid-myocardial and epicardial cells. In particular, the parameter τ_{close} of the ionic model varies in the three layers illustrated in Figure 8.3 top-left, and takes values given in Table 8.2. Thanks to this heterogeneity, the solution has a repolarization front in the opposite direction to the depolarization one.

The ROM simulation is run with $N_M = 25$ modes and $\chi = 25$, and the initial

A_m	C_m	σ_i	τ_{in}	τ_{out}	τ_{open}	τ_{close}	v_{gate}
2000.0	0.1	1.0	4.0	50.0	100.0	80.0	0.13

Table 8.1: Bidomain equations and Mitchell and Schaeffer ionic model parameters.

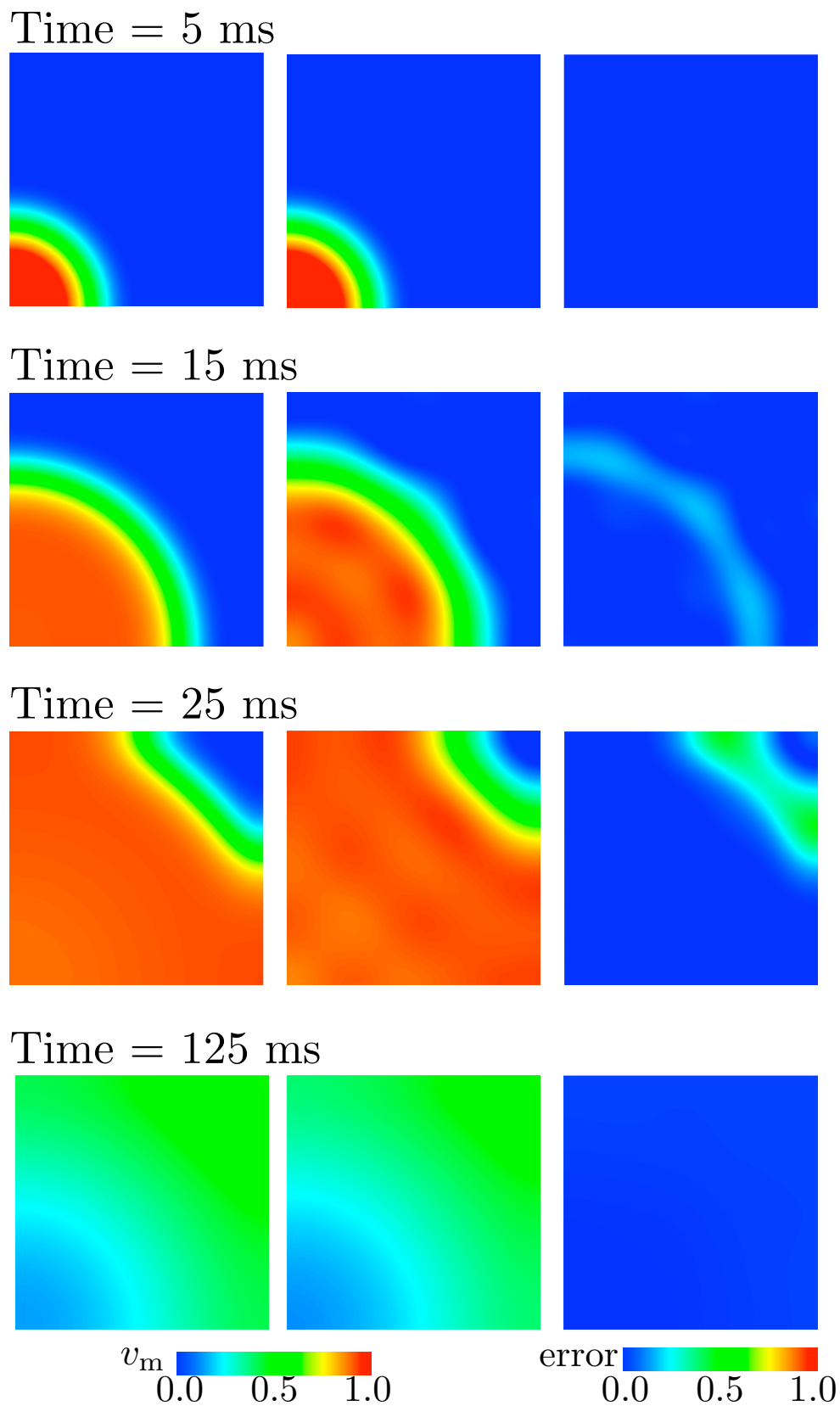


Figure 8.2: 2D test case with homogeneous parameters. FEM solution (left), ALP-DEIM solution (middle) and relative error (right).

basis is computed from the FE solution at time $t = 5\text{ms}$. We can see in Figure 8.3 that the ROM solution (middle) is very close to the FE one (left) both in the depolarization phase (second row) and in the repolarization one (third row), and the error takes locally values of at most 30% and does not exceed 5% elsewhere.

Second, an heterogeneity of “infarction” type is considered. As detailed in Chapter 4, the parameter that has to be decreased in order to obtain a non-depolarized tissue is the τ_{close} . In particular, here we consider a space dependent parameter such that

$$\tau_{\text{close}}(x,y) = \begin{cases} \tau_{\text{close}}(y), & \text{in } \Omega_{\text{inf}} = \{(x,y) \in \Omega : x \leq 0.5, 0.25 \leq y \leq 0.75\} \\ \tau_{\text{close}}, & \text{elsewhere} \end{cases} \quad (8.64)$$

where $\tau_{\text{close}}(y)$ is a linear function in the vertical direction that takes value $\tau_{\text{close}}(y = 0.25) = \tau_{\text{close}}/5$ and $\tau_{\text{close}}(y = 0.75) = \tau_{\text{close}}$.

The basis is build using the FE solution at time $t = 5\text{ms}$ and $\chi = 25$, and the ROM simulation is run with $N_{\text{M}} = 25$ modes. We can observe in Figure 8.4 a good agreement between the FE solution (left) and the ALP-DEIM one (middle). The relative error takes low values, less than 25% but it presents more oscillation on the whole domain, probably this is due to the high challenging character of the problem itself.

8.4.3 Source terms

The next example deals with a source term located in a different position compared to the first one. In particular, the initial solution is given by the FE solution at time $t = 5\text{ms}$ with a source term in the bottom-left corner of the squared domain as shown in Figure 8.2. After the end of the complete cardiac cycle and whole repopazitation of the tissue, a second source term is applied in the top-left corner of the domain as shown in Figure 8.5 (first row). The application of a source term is particularly simple in the context of the ALP-DEIM method since it is sufficient to compute the I_{app} term in the collocation points P .

The results in Figure 8.5 show a good agreement between the FE solution and the ROM one, which is run with $\chi = 25$ and $N_{\text{M}} = 25$ modes. The error presents some oscillations at the moment of the source term application, probably due to the change of direction of the first modes of the basis, but it is in general of very low values, at most less than 10%.

$\tau_{\text{close}}^{\text{endo}}$	$\tau_{\text{close}}^{\text{Mcell}}$	$\tau_{\text{close}}^{\text{epi}}$
90.0	70.0	50.0

Table 8.2: Ionic parameters for heart model.

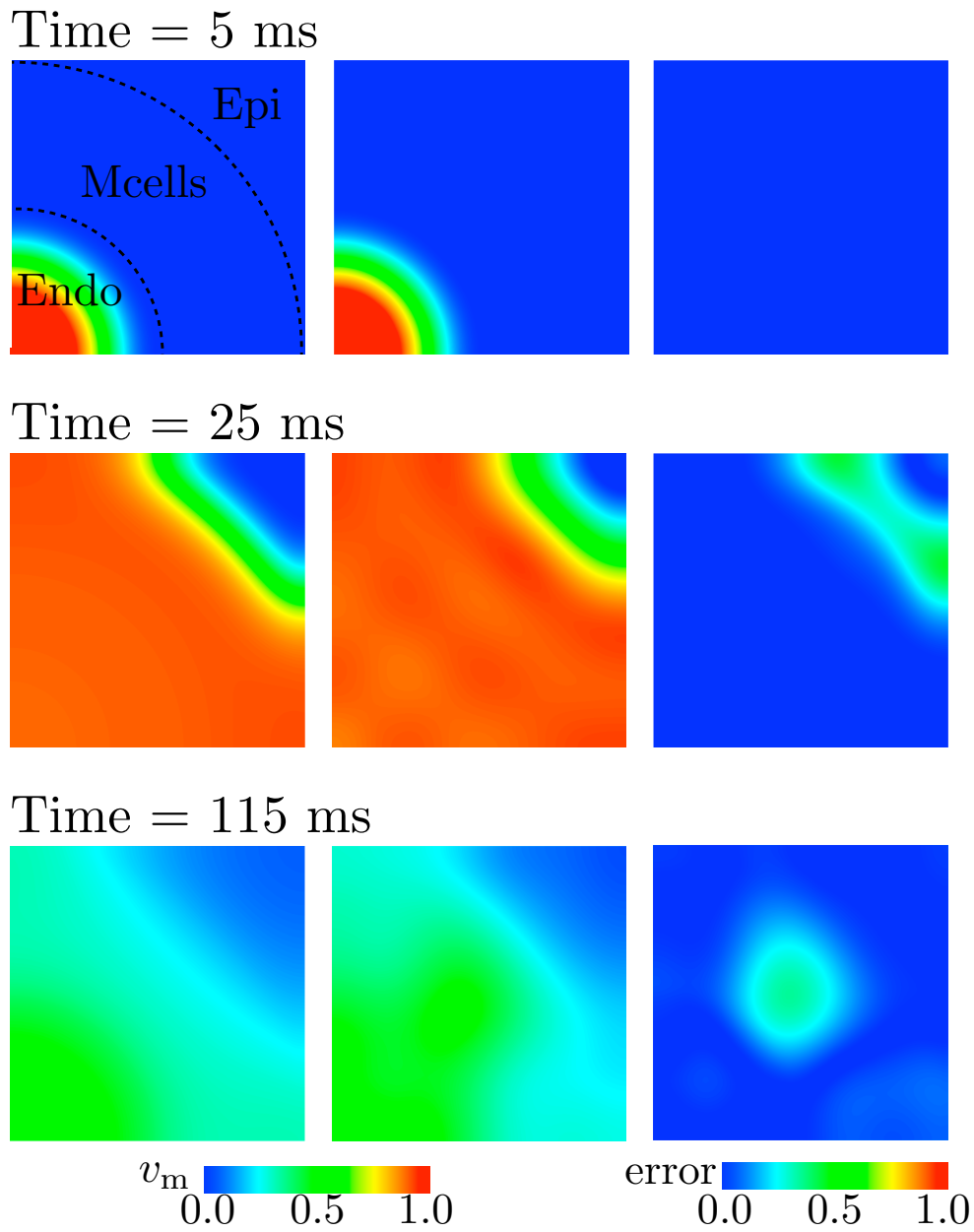


Figure 8.3: 2D test case with heterogeneous parameter τ_{close} . FEM solution (left), ALP-DEIM solution (middle) and relative error (right).

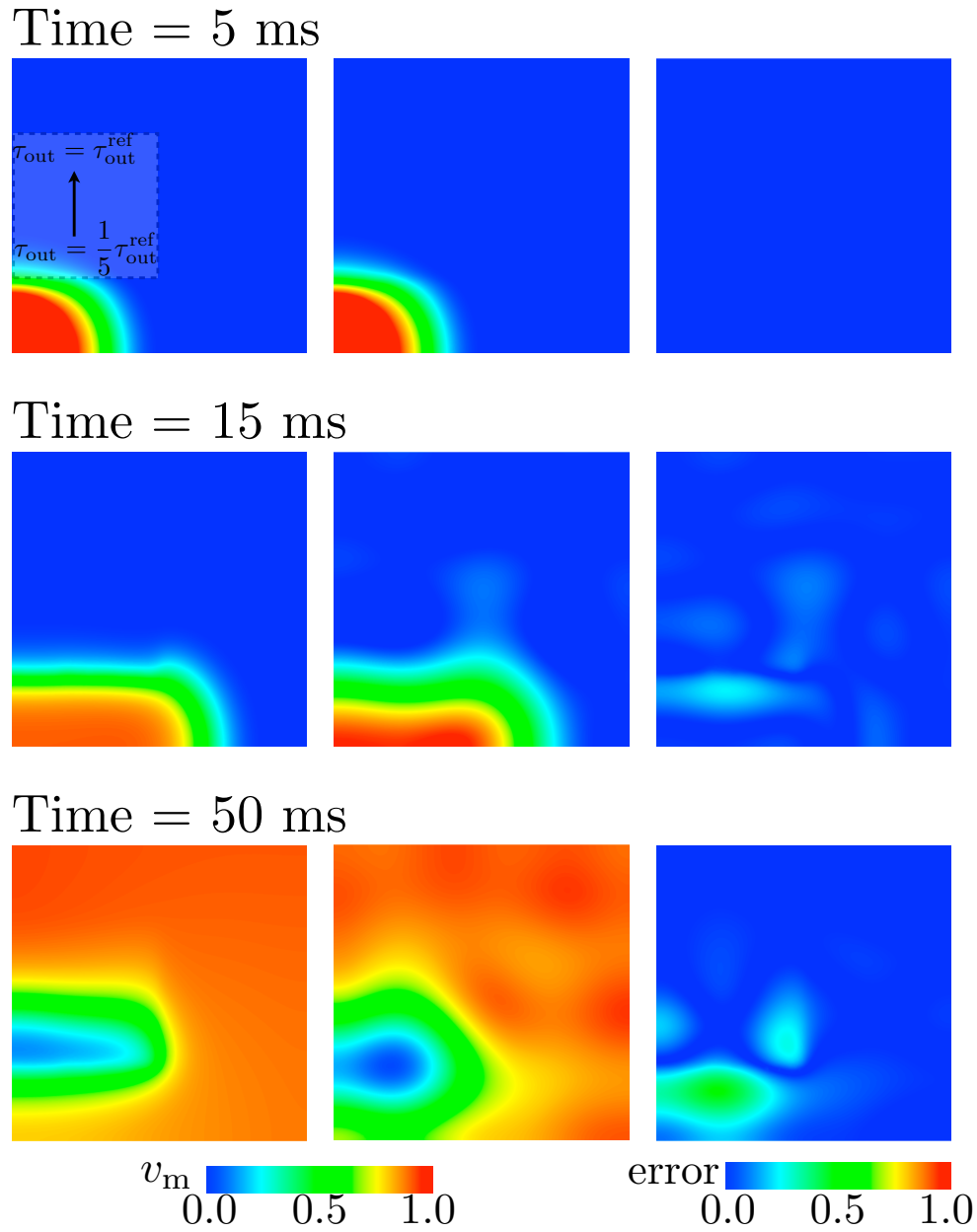


Figure 8.4: 2D test case with homogeneous parameter τ_{out} . FEM solution (left), ALP-DEIM solution (middle) and relative error (right).

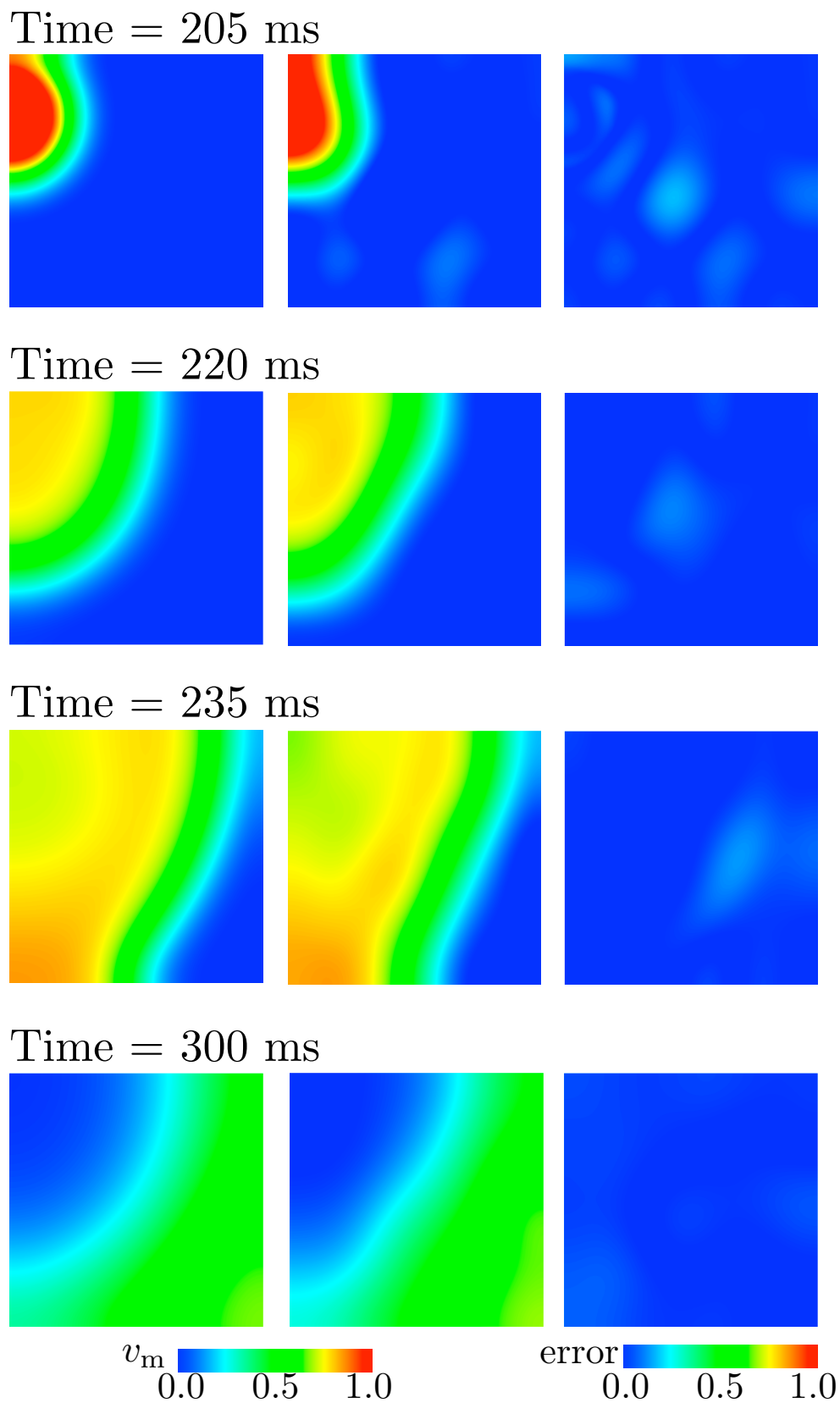


Figure 8.5: 2D test case with source term. FEM solution (left), ALP-DEIM solution (middle) and relative error (right).

8.4.4 Anisotropic fiber tensors

The last numerical example concerns an anisotropic tissue: the intracellular conductivity tensor σ_i reads

$$\sigma_i = \sigma_i^t \mathbf{I} + (\sigma_i^l - \sigma_i^t) \vec{a} \otimes \vec{a}, \quad (8.65)$$

where σ_i^t , σ_i^l are respectively the conductivity coefficients in the transversal and longitudinal directions of the fibers, \mathbf{I} is an identity matrix and \vec{a} is a unit norm vector in the fiber direction. In particular, the fibers are oriented in the diagonal direction as illustrated in Figure 8.6 top-left, and the values of the coefficients are $\sigma_i^t = 1$ and $\sigma_i^l = 4s$. More details about the fibers anisotropy tensors can be found in Section 1.4.

In Figure 8.6 the results are shown. The ALP-DEIM simulation is run with $N_M = 25$ modes and $\chi = 25$ and the initial basis is computed with the FE solution at time $t = 5\text{ms}$, where the fiber direction is taken into account in the \mathcal{L} operator. We observe good results with the ROM (middle): the propagation is higher in the fibers direction than in the transversal one, as for the FE solution (left). The relative error takes its greatest values in the propagation front area, that is also due to the different time scheme used to discretize the FE and the RO problems, but it is very low (less than 20%).

8.5 Perspectives

A few perspectives are in order. Our aim is to apply the method to a model as real as possible, and to use this method in order to solve inverse problems with real a geometry as the one presented in Chapter 2. Let us better analyze two steps that are crucial and particularly challenging from a computational viewpoint:

1. the definition of two basis, the first used for the discretization of the transmembrane potential and the second one for the extracellular potential;
2. the data assimilation applied to ALP method in the two-basis ALP-DEIM context.

8.5.1 Two basis computation

As shown in the numerical examples with ALP and ALP-DEIM, in many cases the transmembrane and the extracellular potentials cannot be approximated in the same reduced space. This is the case in particular when some boundary conditions are imposed, for instance in the Micro-Electrode Arrays (MEA) application (see Section 7.3), or if the intra- and extra-cellular conductivity tensors have different anisotropies, as in real cardiac tissues (see Section 1.4). In this section, we analyze the case of different tensors anisotropies, in the case of different boundary conditions the steps are analogous.

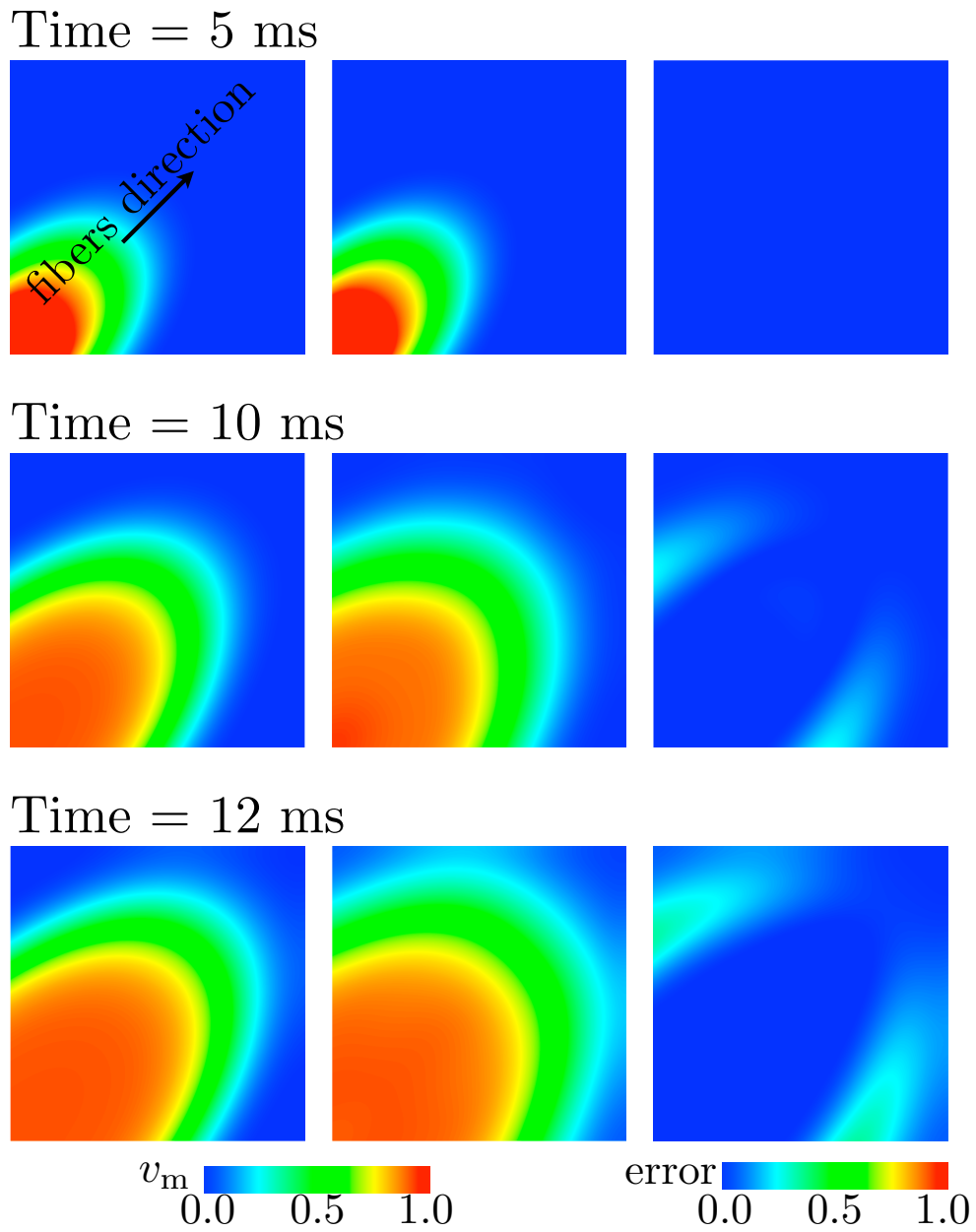


Figure 8.6: 2D test case with fiber tensors. FEM solution (left), ALP-DEIM solution (middle) and relative error (right).

First, two linear operators for the definition of the basis have to be defined. The choice of the operator \mathcal{L}_{v_m} for the definition of the basis used to discretize the transmembrane potential is trivial and it does not differ from the \mathcal{L} operator used above, while the operator \mathcal{L}_{u_e} for the definition of the basis used for the extracellular potential is more tricky. In particular, one can hesitate between taking into account only the extracellular conductivity tensor, which leads to

$$\mathcal{L}_{u_e}(u_e)\phi_{u_e} = -\text{div}(\sigma_e \nabla \phi_{u_e}) - \chi u_e \phi_{u_e}, \quad (8.66)$$

or taking into account both the intra- and extracellular conductivity tensors:

$$\mathcal{L}_{u_e}(u_e)\phi_{u_e} = -\text{div}((\sigma_i + \sigma_e)\nabla \phi_{u_e}) - \chi u_e \phi_{u_e}. \quad (8.67)$$

Second, in the discretization of the right-hand side of the first equation of (8.37) and of the third equation of (8.37), a particular attention should be paid to the fact that the variables v_m , w and u_e are defined on different reduced-order spaces. In particular, the substitution that leads to equation (8.46) for \widehat{F} is valid only for one of the terms (the one with v_m) while it is not possible for the u_e diffusion term. As a consequence, the computation of the matrix Θ will contain both of the basis. In an analogous way, in the third equation, the substitution made thanks to the basis definition would not be possible, and the projection into the subspace in which u_e is defined would lead to spurious multiplications between the matrices of the basis coming from the first and the second \mathcal{L} operators.

Also, the time derivative of the extracellular potential does not appear explicitly in the system (8.37). Then, the computation of the evolution operator cannot be made in a standard way. Probably, it would be sufficient to compute the time derivative of the third equation of (8.37) in order to find a linear relation between $\partial_t u_e$ and $\partial_t v_m$ which will depend on the intra- and extracellular conductivity tensors. This is of course only a preliminary idea, further investigations will be done in the future.

8.5.2 Inverse problems

Once obtained a good “forward” approximation of the bidomain equations including anisotropies and boundary conditions heterogeneities, this modelling results could be used to solve inverse problems as proposed in the previous chapter with the ALP method. The main difference compared to the technique exposed in Chapter 7 is that the observation and filter operators are constant in time.

In Chapter 7 a data assimilation technique was applied in order to recover the state of the system, *i.e.* the electrical potentials. First, when using the Micro-Electrode Arrays (MEA) measures, the electrical potential was reconstructed on the whole well in order to identify the source term location. Second, the electrodes vest type measures on the external boundary of the torso were used to estimate the potential on the epicardial of the heart for a simplified geometry. Let us consider the second application, for the MEA case the steps will be analogous. The right-hand

side of the first equation of (8.37) was modified by adding some control term. In particular, the reduced order system read

$$\begin{cases} \dot{\beta} + M\beta &= \gamma^H, \\ \dot{\mu} + M\mu &= \eta, \\ Q\xi + E\beta &= 0 \end{cases} \quad (8.68)$$

where the term which takes into account the observation is γ^H :

$$\gamma^H = \gamma(\beta, \xi, \mu) + aX^T(d - X\xi), \quad (8.69)$$

where $a > 0$ is a real constant parameter, d represents the torso measures and X is the reduced-order transfer matrix used to compute the torso measures from the reduced order discretization of the extracellular potential.

As we observed in Section 8.3.2, the transfer matrix operator when using the ALP-DEIM method is constant in time and reads

$$\Xi : \mathbb{R}^{N_P} \rightarrow \mathbb{R}^{N_{ECG}}, \quad \Xi = SIII_V. \quad (8.70)$$

Then, in the ALP-DEIM dynamics for the bidomain equations (8.56), the term which will be modified in an observation purpose is \hat{F} . In particular, it will be substituted by

$$\hat{F}^H = \hat{F} + a\Xi^T(d - \Xi\hat{u}). \quad (8.71)$$

The advantage of this choice of operator is that it is constant in time and does not need any update.

8.6 Chapter conclusions

A new approach of the reduced-order ALP method has been proposed. This technique uses the Discrete Empirical Interpolation Method (DEIM) idea of taking only a few spatial nodes to approximate the solution. In the case of ALP method, this allows to treat nonlinearities of non-polynomial types since the evaluation of the nonlinear terms is nodal on a subset of nodes. Also, the ALP-DEIM approach leads to an algorithm which is computationally less expensive than the ALP method, whose complexity was of the order of $(N_M^3 + \mathcal{N} \times N_M^2)$. The fact that the time evolving tensors present in the previous technique disappeared eliminates the N_M^3 factor, while the fact that the basis is discretized only on a small number of points leads to a computational cost proportional to $N_M \times N_P^2$.

The ALP-DEIM method was tested on some 2D cardiac electrophysiology test cases, including non-polynomial terms, parameters heterogeneities and anisotropic tissues. These preliminary results seem very promising for the method. In future works the technique should be applied to 3D simulations, too. Then, as detailed, in Section 8.5, several steps will lead to use this method to solve both forward and inverse electrophysiology problems in realistic geometries and configurations.

Conclusions

The first contribution of this work has been to give some accurate simulations of the cardiac electrical potential. The coupling of the ventricles with the atria, as seen in Chapter 2, allowed us to obtain full cycle electrocardiograms, including the P wave. Moreover, several pathologies have been investigated, including pathologies due to the coupling between atria and ventricles, such as the Wolff-Parkinson-White syndrome.

Then, stability estimations for some of the FitzHugh-Nagumo ionic model have been obtained in Chapter 3.

Several reduced-order methods have been applied to the cardiac electrophysiology models. In Chapter 4, the Proper Orthogonal Decomposition (POD) has been applied in the cases of parameters variations and for the simulation of a myocardial infarction. Owing to the efficiency of the POD methods, a genetic algorithm has been applied in order to estimate some parameters of the model or to identify the location of an infarction. Good results have been obtained in both cases.

The POD has also been used to reproduce the ECG-based restitution curves in Chapter 5. First, we proposed a new parametrization of the curve which is valid in a more general setting compared to the case introduced by the authors of the Mitchell and Schaeffer model. Then, this curve has been used to identify some of the parameters of the model.

The POD method was efficient in the cases investigated in Chapters 4 and 5, but it presented also some limitations. Then, some new techniques have been proposed in Chapters 6, 7 and 8. In particular, satisfying results in the resolution of the bidomain equations, coupled with the FitzHuh-Nagumo ionic model, have been obtained with a method based on the Approximated Lax Pairs (ALP). This method has been used also in a data assimilation technique in Chapter 7 in order to reconstruct the state of the system and gave promising results.

Since, this method can be applied only in the case of problems with polynomial nonlinearities, we proposed a new approach of the ALP method in Chapter 8. This approach merges the ALP method with some ideas arising from the Discrete Empirical Interpolation Method (DEIM). This new method has been applied to the bidomain equations coupled with the Mitchell and Schaeffer ionic model. The preliminary results look very promising and several perspectives are possible.

To conclude, we have proposed in this thesis new results for the forward problem of electrocardiology and we have addressed the inverse problem with an original point of view. Various reduced-order methods have been applied to the electrophysiology

equations, in particular to address the problem of parameters identification or state estimation. For each one of these methods, advantages and limitations have been analyzed. A new reduced order method, called ALP-DEIM, has been proposed in Chapter 8 and gave very promising results. Among the perspectives described in Chapter 8, we have planned to apply in the near future this method to the data assimilation strategy described in Chapter 7. The objective of these future works will be to consider realistic geometries and ionic models, as described in Chapter 2, and real data.

Conclusions (Français)

La première étape de cette thèse a été de fournir des simulations précises du potentiel électrique cardiaque. Grâce au couplage entre les modèles d'oreillettes et ceux de ventricules, nous avons fourni au chapitre 2 des simulations d'électrocardiogrammes complets, onde P incluse. De plus, plusieurs pathologies ont été considérées, entre autres des pathologies spécifiques aux couplages entre les oreillettes et les ventricules comme le syndrome de Wolff-Parkinson-White.

Ensuite, des estimations de stabilité sur certains paramètres du modèle ionique de FitzHigh-Nagumo ont été proposées dans le chapitre 3.

Plusieurs méthodes d'ordre réduit ont été appliquées aux modèles d'électrophysiologie cardiaque. Dans le chapitre 4, la *Proper Orthogonal Decomposition* (POD) a été appliquée dans le cadre où les paramètres varient et pour la simulation de l'infarctus du myocarde. Tirant parti de l'efficacité de cette méthode dans les cas proposés, une méthode d'algorithme génétique a été appliquée pour retrouver certains paramètres du modèle ou encore la zone où se trouve l'infarctus avec des résultats très satisfaisants.

La POD a aussi été utilisée pour reproduire les courbes de restitution basées sur l'électrocardiogramme au chapitre 5. Après avoir proposé une nouvelle paramétrisation de la courbe, valide dans une configuration plus générale que celle proposée par les auteurs du modèle de Mitchell et Schaeffer, cette courbe a été utilisée pour identifier certains paramètres du modèle.

Étant confronté aux limitations de la POD, nous avons appliqué de nouvelles techniques dans les chapitres 6, 7 et 8. En particulier, la méthode ALP basée sur des couples de Lax approchés semble être efficace pour la résolution des équations bidomaines couplées avec des modèles ioniques polynômiaux comme le modèle de FitzHugh-Nagumo. Cette méthode a aussi été utilisée dans une stratégie d'assimilation de données dans le chapitre 7 pour reconstruire l'état du système avec des résultats prometteurs.

Être limité dans de cette méthode aux problèmes polynômiaux nous a conduits à proposer dans le chapitre 8 une nouvelle version de ALP incluant les idées de la méthode d'interpolation empirique discrète (Discrete Empirical Interpolation Method, DEIM). Cette nouvelle méthode a été appliquée aux équations bidomaines couplées avec le modèle de Mitchell et Schaeffer. Les résultats préliminaires semblent très prometteurs et plusieurs perspectives sont possibles.

Pour conclure, nous avons proposé dans cette thèse des résultats nouveaux pour le problème direct de l'électrocardiologie et nous avons abordé le problème inverse

sous un angle original. De plus, plusieurs méthodes d'ordre réduit ont été appliquées aux équations de l'électrophysiologie afin de résoudre des problèmes d'identification de paramètres ou d'estimation d'état. Pour chacune de ces méthodes, les avantages et les limites ont été résumés. La méthode ALP-DEIM, proposée dans le chapitre 8, semble être particulièrement prometteuse. Parmi les perspectives, présentées en détail dans le chapitre 8, nous envisageons d'appliquer prochainement cette méthode aux techniques d'assimilation de données du chapitre 7 pour estimer le potentiel électrique à l'épicarde, avec des géométries et des modèles ioniques réalistes, comme dans le chapitre 2, et avec des données réelles.

APPENDIX A

FELiSCE

We present here the FELiSCE¹ library that has been used for all the simulations presented in the thesis. We summarize the structure and the author main contributions in FELiSCE. FELiSCE stands for Finite Elements for Life SCiences and Engineering. It is a finite elements library developed since 2010 by REO and M \overline{E} DISIM Inria project-teams. The library aims at providing a unique environment which can compute numerical simulations in all the cardiovascular fields the two teams are interested in, for instance fluid and solid mechanics problems, electrophysiology equations and various coupling phenomena. We briefly describe the main classes that manage the resolution of linear and eigenvalue problems and give an idea of how the electrophysiology equations and the reduced-order models are implemented.

¹<http://felisce.gforge.inria.fr/>

Contents

A.1	FELiScE general principles	207
A.2	Structure of the code	207
A.2.1	The Model class	208
A.2.2	The LinearProblem class	209
A.2.3	The EigenProblem class	210
A.3	Electrophysiology equations implementation	211
A.4	Reduced-Order Models implementation	212
A.5	Author's contributions	215

A.1 FELiSCe general principles

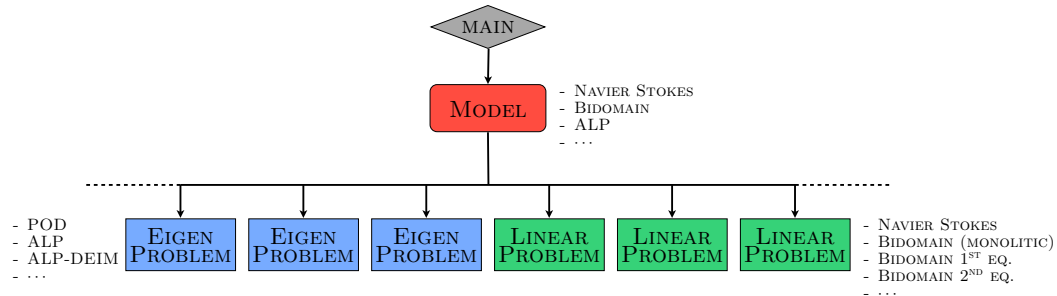
FELiSCe is a parallel finite elements library written in C++ that manages many biophysical partial differential equations systems. It is based on the PETSc² software library, supported by MPI³, that allows to deal with scalable parallel data structure and supply the associated routines. In particular, all the matrices and vectors used in FELiSCe are parallel PETSc objects, and the resolution of linear systems is managed by the KSP component of PETSc which is a scalable linear equations solver based on a Krylov subspace iterative method and a preconditioner, that can be adapted to the problem by the users.

Also, the resolution of eigenvalue problems has been recently integrated to the skills of FELiSCe using the SLEPC⁴ software library, which is an extension of the PETSc library that solves eigenvalue problems. In particular, the resolution is managed by the ESP object of the SLEPC library which provides all the eigenvalues and eigenvectors for standard and generalized eigenproblems using different resolution routines.

FELiSCe is based on a user-friendly interface that allows to solve linear and eigenvalue problems without being concerned with mesh partitioning, degrees of freedom definition, elementary integrals computation, matrices assembling, etc. We briefly describe the structure of the code and the main classes which manage the resolution of different biophysical problems hereafter.

A.2 Structure of the code

From a users viewpoint, there are three main classes which are used for the resolutions of linear and eigenvalue problems: the `Model` class, the `LinearProblem` class and the `EigenProblem` class. Each one of these classes is a pure virtual class, from which many specific classes inherit. For instance, an object of a derived class of `Model` is created in the main file in accordance with the problem of interest. Then, the `Model` object calls one or more linear and/or eigenvalue problems that are concerned with the system resolution.



²Portable, Extensible Toolkit for Scientific Computation, <http://www.mcs.anl.gov/petsc/>

³Message Passing Interface, <http://www.mcs.anl.gov/research/projects/mpi/>

⁴Scalable Library for Eigenvalue Problems Computations, <http://www.grycap.upv.es/slepc/>

A.2.1 The Model class

The Model class scope is to manage the problem. Its main routines, that are shown below, manage the time iterations and updates.

```

MODEL
/*!
 \file model.hpp
 */
#include "linearProblem.hpp"
#include "eigenProblem.hpp"
namespace felisce {
  /*!
   \class Model
   */
  class Model {
  protected:
    /*! Linear Problems.
     std::vector<LinearProblem*> m_linearProblem;
     /*! Eigen Problems.
     std::vector<EigenProblem*> m_eigenProblem;
     ...
  public:
    /*! Constructor.
    Model();
    /*! Destructor.
    virtual ~Model();
    /*! Manage time iteration.
    void updateTime();
    /*! Advance time step.
    virtual void forward()=0;
    /*! Write solution for Ensignt.
    void writeSolution();
    ...
  }
}

```

In particular, the `forward()` function contains all the steps that have to be run at each iteration and it is a pure virtual function since the method depends on the model itself. For instance, in the case of nonlinearities solved with a fixed-point method, this implementation should be integrated in the `forward()` function.

Also, the Model class calls the linear and/or eigenvalue problems useful for the resolution of the system. For instance, in the case of electrophysiology equations, the BidomainModel that inherits from Model is created in the main, while it is the BidomainModel itself that manages the choice of the resolution: the LinearProblemBidomain can be called for a monolithic resolution of the system, or the LinearProblemBidomainTransmPotential and the LinearProblemBidomainExtracellPotential can be both called for a decoupled resolution of the equations. In the second case, sub iterations between the two LinearProblems of a fixed point method will eventually be managed by the BidomainModel in its `forward()` function.

A.2.2 The LinearProblem class

The `LinearProblem` class manages the resolution of linear systems using the PETSC routines. Here is an outline of its main objects and functions.

```

LINEAR PROBLEM
/*!
 \file linearProblem.hpp
 */
#include <vector.h> // Petsc Vector (Vec)
namespace felisce {
  /*!
   \class LinearProblem
   */
  class LinearProblem {
  protected:
    /*! Solution of the problem.
     Vec m_sol
     /*! Useful vectors such as RHS.
     std::vector<Vec> m_vectors;
     /*! Matrices of the system.
     std::vector<Mat> m_matrices;
     /*! KSP object from Petsc class (it solves linear systems).
     KSP m_ksp;
     /*! PC object from Petsc class (it manages the preconditioner).
     PC m_pc;
     ...
  public:
    /*! Constructor.
    LinearProblem();
    /*! Destructor.
    virtual ~LinearProblem();
    /*! Assemble of matrices with a loop on domain element.
    void assembleMatrixRHS(...);
    /*! Build Petsc Ksp object to solve the system.
    virtual void buildSolver();
    /*! Solve a linear problem with Petsc Ksp class.
    void solve();
    ...
  }
}

```

The `LinearProblem` class owns the “solution” object `m_sol`, which is a vector of the PETSC library. The solution is the result of a linear system solved by the KSP routines of PETSC, where the matrix of the system is given by `m_matrices[0]` and the right-hand side is given by `m_vectors[0]`. All the matrices and the vectors are assembled using specific routines implemented in some FELISCE classes that manage the finite elements and the integration and differentiation methods.

A.2.3 The EigenProblem class

The `EigenProblem` class is the analogous of the `LinearProblem` for the resolution of standard or generalized eigenvalue problems. The class uses the SLEPC library in order to solve the problems. Here is an outline of its header file.

```

EIGEN PROBLEM
/*!
 \file eigenProblem.hpp
 */
#include <vector.h> //Petsc Vector (Vec)
#include <slepceps.h>
#include <slepcsvd.h>
namespace felisce {
  /*!
   \class EigenProblem
   */
  class EigenProblem {
  protected:
    /*! Solution of the problem (eigenvectors).
     Vec m_sol
     */
    /*! Solution of the problem (eigenvalues).
     double* m_eigenValue;
     */
    /*! Matrices of the system.
     std::vector<Mat> m_matrices;
     */
    /*! EPS object from Slepc class (it solves Eigen Problems).
     EPS m_eps;
     */
    /*! SVD object from Slepc class (it solves SVD Problems).
     SVD m_svd;
     ...
  public:
    /*! Constructor.
     EigenProblem();
     */
    /*! Destructor.
     virtual ~EigenProblem();
     */
    /*! Assemble of matrices with a loop on domain element.
     void assembleMatrix(...);
     */
    /*! Build Slepc Eps or Svd object to solve the eigen problem.
     virtual void buildSolver();
     */
    /*! Solve an eigen problem with Slepc Eps or Svd class.
     void solve();
     ...
  }
}

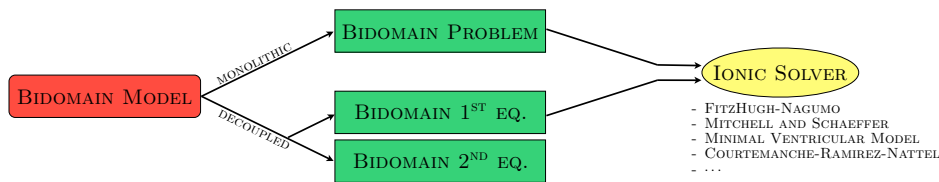
```

Most of the functions are similar to the `LinearProblem` class, for instance all the routines that assemble the matrices and manage the solution. Then, the main change is the problem that has to be solved itself. The SLEPC object `EPS` manages the resolution of eigenvalue problems with different adapted methods. The general routine `solve()` of the class solves with `EPS` the standard eigenvalue problem $Ax = \lambda x$, where A is the PETSC matrix `m_matrices[0]`, for the bigger eigenvalue λ that is saved in `m_eigenvalue[0]` associated to the eigenvector x that is saved in the PETSC vector `m_sol`. The routine `solve()` is adapted to the problem in each of the derived classes. For instance, in the `EigenProblemALP` class the object `m_basis`, which is a standard-library vector of PETSC `Vec`, is created and the `EPS` solves a generalized eigenvalue problem $Ax_i = \lambda_i Bx_i$ for the N_M biggest eigenvalues, where

A is `m_matrices[0]`, B is `m_matrices[1]`, λ_i is `m_eigenvalue[i-1]` and x_i is the PETSc vector `m_basis[i-1]`.

A.3 Electrophysiology equations implementation

All the electrophysiology simulations presented in this work have been computed with FELiSCE. Let us briefly show how the system of equations is solved. As previously explained, the `Model` class, which is in this case the derived class `BidomainModel`, defines the problem that has to be solved and manages the time iterations and eventually the nonlinearities, while the `LinearProblem` classes solve the linear systems. In the case of the “classical” bidomain equations presented in this work, two approaches are possible: a monolithic resolution of the two equations or a decoupled vision of the system. All the simulations showed in this work were run with the monolithic approach with a second order Backward Differentiation Formula for the time discretization (the numerical scheme is detailed in Section 1.4.5).



In both monolithic and decoupled approaches the ionic current term is treated apart by the `IonicSolver` class. This class is a pure virtual class that allows to manage many different ionic models. For instance, the classes `FitzHughNagumoSolver`, `SchaefferSolver`, `MVSolver` and `CourtemancheSolver` inherit from `IonicSolver` and return the I_{ion} term (nodal computation) that is added to the right-hand side of the bidomain (monolithic) problem or to the right-hand side of the first equation problem (decoupled).

Also, the `BidomainCurvModel` and the `LinearProblemBidomainCurv` classes have been implemented for the resolution of the surfaced-based bidomain equations used on thin surfaces as for instance for the atria. Recently, a coupled volume-surface problem has been added to the possible choices in order to solve the complete heart (ventricles and atria) presented in Chapter 2. This case has been treated as an exception of the `BidomainModel-LinearProblemBidomain` classes, and it is possible to use different ionic solvers for the volume and the surface parts of the domain. The main difficulty of this coupled implementation is the assembling of the matrix and the distinction between the boundary of the domains (surfaces for the volume part and edges for the surface one) and the proper domains.

A.4 Reduced-Order Models implementation

In order to solve a problem with one of the reduced-order methods presented in this work, two main steps are in order: the computation of the basis and the resolution itself of the reduced-order model. Concerning the computation of the basis we applied two techniques: the POD and the ALP methods. In order to compute the POD basis, the function `solve()` of the derived class `EigenProblemPOD` uses the SVD routine of the SLEPC library, while for the derived `EigenProblemALP` the `EPS` object of the SLEPC library is used to compute the first N_M larger eigenvalue and the associated eigenvectors. In both cases the solutions are saved in the `std::vector<Vec> m_basis`, then they can be exported in Paraview⁵ format, which is useful for their visualization, or used to solve the reduced-order model.

Second, the reduced-order method is applied by computing a new basis or by reading a previously computed basis from files. These operations are computed by the `Model` and `EigenProblem` derived classes. For instance, for the ALP and ALP-DEIM methods presented in Chapters 6 and 8, the `ALPModel` manages the choice between the two methods: if the standard ALP method is applied, then the `EigenProblemALP` is called; otherwise, the `EigenProblemALPDEIM`, which inherits from `EigenProblemALP`, is used.

Following the same idea as for the `LinearProblem` classes, the `Model` only manages the time iterations while the resolution of the systems is done in the “problem” classes. Since all the reduced-order objects have a small size, most of them are treated as `double*` or `double**`. Also, all the symmetries that can be present in the reduced-order matrices and tensors are taken into account and only a small part of the object is saved. Many of these objects are the representation of their analogous in the reduced-order space that are computed with the `EigenProblem` function `projectOnBasis(...)`, and *viceversa* the function `projectOnFem(...)` computes the opposite operation. The matrices useful for the computation of the basis or the resolution of the reduced-order system are stocked in the `EigenProblem` object `m_matrices` and computed with the same routines as described above.

Let us for instance show the outline of the function `forward()` of the `EigenProblemALP`, with an Explicit Euler time integration method (which is the method used to compute all the simulations presented in this work).

⁵<http://www.paraview.org/>

FORWARD OF ALP MODEL

```

/*!
 \forward function of ALPModel
 */
void ALPModel::forward() {
    // Write the solution for Einsight.
    writeSolution();
    // Update in time.
    updateTime();
    // Switch between time integration methods.
    switch (m_method) {
        case 0: { // Explicit Euler
            //! Update the basis.
            m_eigenProblem[0]->updateBasis();
            //! Update the coefficient \beta (solution in the RO space)
            m_eigenProblem[0]->updateBeta();
            //! Update the eigenvalues \lambda.
            m_eigenProblem[0]->updateEigenvalue();
            //! Update all the RO tensors (e.g. T).
            m_eigenProblem[0]->updateTensors();
            //! Compute the right-hand side in the RO space: \gamma=\gamma(\beta).
            m_eigenProblem[0]->computeGamma();
            //! Compute the discrete evolution operator M.
            m_eigenProblem[0]->computeMatrixM();
            break;
        }
        ...
    }
}

```

Each of the `EigenProblem` functions is then specified for the method ALP or ALP-DEIM that is used. For instance, for the ALP method, the function for the updates of the β coefficients (which are the representation of the solution in the reduced-order space) and the function for the update of the third order tensor T read:

UPDATE OF BETA AND TENSOR T FOR ALP EIGEN PROBLEM

```

/#!/
\updateBeta function of EigenProblemALP (Explicit Euler)
*/
void EigenProblemALP::updateBeta() {
    // Time step.
    double dt = FelisceParam::instance().timeStep;
    // deltaBeta = \beta^{n+1} - \beta^n.
    double deltaBeta[m_dimRomBasis*m_numberOfVariables];
    // Loop on the elements of \beta.
    for (int i=0; i<m_dimRomBasis*m_numberOfVariables; i++) {
        // \beta^{n+1} = \beta^n - dt * \beta^n * M^n + dt * \gamma^n.
        deltaBeta[i] = m_gamma[i];
        for (int j=0; j<m_dimRomBasis*m_numberOfVariables; j++) {
            deltaBeta[i] -= m_beta[j] * m_matrixM[j][i];
        }
    }
    for (int i=0; i<m_dimRomBasis*m_numberOfVariables; i++) {
        m_beta[i] += dt * deltaBeta[i];
    }
}

/#!/
\updateTensor function of EigenProblemALP (Explicit Euler)
*/
void EigenProblemALP::updateTensor() {
    // Time step.
    double dt = FelisceParam::instance().timeStep;
    // 1) Update of (3rd order) tensor T.
    // deltaT = T^{n+1} - T^n.
    double deltaT[m_size3];
    // Loop on the elements of T.
    // Only a part of T is saved since it has 3 symmetries.
    for (int i=0; i<m_dimRomBasis; i++) {
        // T^{n+1} = T^n - dt * [T^n, M^n]^{(3)}.
        for (int j=0; j<i+1; j++) {
            for (int k=0; k<j+1; k++) {
                deltaT[thirdGlobalId(i,j,k)] = 0.;
                for (int l=0; l<m_dimromBasis; l++) {
                    // delta T_ijk = sum_l (M_il * T_ljk + M_jl * T_ilk + M_kl * T_ijl ).
                    deltaT[thirdGlobalId(i,j,k)] += m_matrixM[i][l]*m_tensorT[thirdGlobalId(l,j,k)];
                    deltaT[thirdGlobalId(i,j,k)] += m_matrixM[j][l]*m_tensorT[thirdGlobalId(i,l,k)];
                    deltaT[thirdGlobalId(i,j,k)] += m_matrixM[k][l]*m_tensorT[thirdGlobalId(i,j,l)];
                }
            }
        }
    }
    for (int i=0; i<m_size3; i++) {
        m_tensorT[i] += dt * deltaT[i];
    }
    ... // Update of the other matrices and tensors.
}

```

where $m_dimRomBasis$ represents the number of modes N_M , m_size3 is equal to $\frac{N_M(N_M+1)(N_M+2)}{6}$ and the EigenProblem function `thirdGlobalId(i,j,k)` returns an index in the dimension m_size3 for the position (i,j,k) in the tensor.

A.5 Author's contributions

The author contributed as developer to the implementation of FELiSCE. In particular, the main contributions are included in the cardiac electrophysiology models, in the eigenvalue problems resolution and in the reduced-order models implementation. These implementations represents about 20000 lines of code and are fully incorporated in FELiSCE so that it can be used easily by other users.

Cardiac electrophysiology

The `BidomainModel` and `LinearProblemBidomain` classes, including the volume-surface problem, has been implemented by the author in collaboration with Annabelle Collin, PhD student in the M Ξ DISIM team of Inria-Saclay.

The classes `LinearProblemBidomainTransmPotential` and `LinearProblemBidomainExtracellPotential` have been implemented for the resolution of bidomain equations with a decoupled scheme. The `IonicSolver` class has been added in collaboration with Cesare Corrado, former post-doc of REO team. This class is a pure virtual class from which all the ionic models are derived, for instance the `SchaefferSolver` (in collaboration with Annabelle Collin), the `RevisedSchaefferSolver` which is not used in the work presented in the thesis, the `MVSolver` (in collaboration with Fabien Raphael, engineer in the REO team, and Muriel Boulakia).

Also, a derived `Model` and a derived `LinearProblem` classes have been implemented for the resolution of the “torso” diffusion problem. These models include the possibility of imposing the solution that arises from a precomputed simulation as a Dirichlet or a Robin condition on the heart boundary, the extraction of some ECG or electrodes vest type measures, and the computation of the so-called heart-torso transfer matrix with the resolution of the adjoint problem.

Finally the class `ECG` which computes the ECG in run-time during the bidomain equations resolution, using the heart-torso transfer matrix, is implemented.

Eigenvalue problems and reduced-order models

The `EigenProblem` class, inspired from the `LinearProblem` one, has been fully implemented by the author. All the ALP classes (`ALPModel`, `EigenProblemALP`, `EigenProblemALPDEIM`, `EigenProblemALPCurv`) have been mainly implemented by the author, in collaboration with Damiano Lombardi, researcher in the REO team. Also, the data assimilation technique on the ALP models used in Chapter 6 was implemented in the `EigenProblemALP` and `EigenProblemALPCurv` classes.

Other contributions

The author contributed also to some general improvements. For instance, the classes useful for the backup of the simulation have been implemented in collaboration with Jean-Frédéric Gerbeau: the backup includes the solutions and all the objects

useful for the complete restart of the simulation such as the previous time-step approximations and interpolations of the solutions and other variables. Then, the restart has been implemented: the users can restart a simulation from the state of a previous one at a given time step using the information hold by the backup, which is done with a users defined frequency.

Also, the Robin type boundary conditions have been implemented in collaboration with Annabelle Collin.

High performance computing for the reduced basis method. Application to natural convection

We present here the results obtained during the summer school *Centre d'Été de Mathématiques et de Recherche Avancée en Calcul Scientifique*, CEMRACS12, from July, 16th to August, 24th 2012 at CIRM, *Centre International de Rencontres Mathématiques*, of Luminy - Marseille. The main subject of CEMRACS12 has been **Numerical Methods and Algorithms for High Performance Computing** and this work leads to the project RB4FASTSIM: *Bases réduites certifiées et non intrusives massivement parallèles pour la simulation de modèle multi-physiques non-linéaires*.

This project allowed me to learn and work on different aspects and techniques of reduced basis methods. Working on this subject has been particularly important for the implementation of the ALP method described in Chapter 6, for instance for the manipulation of high order tensors. Furthermore, it has been interesting to face with FEEL++, a C++ parallel finite elements library quite different in its structure and implementation from FELISCE, see Appendix A.

The results presented in this chapter lead to the manuscript

E. Schenone, S. Veys, C. Prud'Homme. **High performance computing for the reduced basis method. Application to natural convection.** ESAIM: PROCEEDINGS, December 2013, Vol. 43, p. 255 – 273.

HIGH PERFORMANCE COMPUTING FOR THE REDUCED BASIS METHOD. APPLICATION TO NATURAL CONVECTION

ELISA SCHENONE^{1,2}, STÉPHANE VEYS³ AND CHRISTOPHE PRUD'HOMME⁴

Abstract. In this paper, we are interested in applying the reduced basis methodology (RBM) to steady-state natural convection problems. The latter has applications in many engineering domains and being able to apply the RBM would allow to gain huge computation savings when querying the model for many parameter evaluations. In this work, we focus on the order reduction of the model — in particular the handling of the non-linear terms, — as well as the design of the RBM computational framework and the requirements on high performance computing to treat 3D models using FEEL++, a C++ open source library to solve partial differential equations. Numerical experiments are presented on 2D and 3D models.

INTRODUCTION

Nowadays, in many application fields, engineering problems require accurate, reliable, and efficient evaluation of quantities of interest. Often, these quantities of interest depend on the solution of a parametrized partial differential equation where the — *e.g.* physical or geometrical — parameters are inputs of the model and the evaluation of quantities of interest are outputs — *e.g.* average values. In a real-time or many-query context, the reduced basis method (RBM) offers a rapid and reliable evaluation of the input-output relationship (see [PRV⁺02, VPP03, VPRP03, PP04, QRM11, RHP07] for the methodology) for a large class of problems.

In this paper, we are interested in studying the RBM applied to steady-state natural convection problems parametrized by the Grashof and Prandtl numbers, see also [VP05, Yan12]. Natural convection has applications in many engineering domains and being able to apply the RBM would allow to gain huge computation savings when querying the reduced model for many parameter evaluations. In this work, we focus on the order reduction of the model — in particular the handling of the non-linear terms, — as well as the design of the RBM computational framework and the requirements on high performance computing (HPC) to treat 3D models. Even though the model considered remains simple with respect to industrial applications, we tackle some of the main difficulties namely order reduction and computational costs. In this work, we underly the difficulties linked to the resolution of non-linear problems in a reduced space. We detail a projection technique that can be applied to any second order problem and that allows to solve it in the reduced space, without any projection onto the FE space. To the authors knowledge, previous works on the RB applied to non-linear steady Navier-Stokes equations concentrate on the choice of the basis and on error estimators, see [VP05, Yan12]. We propose

¹ Laboratoire Jacques Louis Lions, UPMC, 4 Place Jussieu, 75005 Paris, France

² Inria Paris-Rocquencourt, Domaine de Voluceau B.P. 105, 78153 Le Chesnay Cedex, France - elisa.schenone@inria.fr

³ Laboratoire Jean Kuntzmann, Université Joseph Fourier Grenoble 1, BP53 38041 Grenoble Cedex 9, France - stephane.veys@imag.fr

⁴ Université de Strasbourg, IRMA UMR 7501, 7 rue René-Descartes, 67084 Strasbourg Cedex, France - prudhomme@unistra.fr

here a reduced order method that can be applied to any non-linear problem and that does not depend on the choice of the basis.

In order to solve Finite Elements (FE) or Reduced Basis (RB) problems, we use an open-source library called FEEL++ for *Finite Element Embedded Library and Language in C++* ([PCD⁺12,Pru06]). FEEL++ is a library to solve problems arising from partial differential equations (PDEs) with standard or generalized, continuous or discontinuous, Galerkin methods from 1D to 3D, for low to high order approximations (including geometry). Among the many other FEEL++ features, it provides a seamless programming environment with respect to parallel computing using MPI, see Section 4.1. FEEL++ enjoys an implementation of the RBM, see [DVTP13], which can deal with a wide range of problems: elliptic or parabolic models, coercive or non-coercive models, linear or non-linear models. It can handle coupled non-linear multiphysic problems such as the thermo-electric problems in [VDPT12, VCD⁺12]. It is important that such an environment hides as many implementation details as possible and let the user worry only about their model and the high level aspects of the FEM and RBM.

The organisation of the paper is as follows: in section 1 we describe the 2D and 3D steady-state natural convection models; in section 2, we present the finite element discretization and the solution strategy; in section 3, we apply the RBM and focus in particular on the non-linear terms handling; in section 4, we present the computational framework for FEM and RBM as well as some implementation aspects; finally in section 5, we display some numerical experiments in 2D and 3D.

1. PROBLEM SETTING

We start with the description of a standard natural convection model. We consider a heated fluid in a squared or cubical cavity, the fluid circulates towards the low temperature under the action of density and gravity differences. We introduce the adimensionalized steady-state incompressible Navier-Stokes equations coupled with the heat equation and we consider the problem in a two and a three dimensional tanks, see *e.g.* Figure 1: find (u, p, T) such that

$$\left\{ \begin{array}{ll} \mathbf{u} \cdot \nabla \mathbf{u} + \nabla p - \frac{1}{\sqrt{Gr}} \Delta \mathbf{u} = T \mathbf{e}_2 & , \text{ in } \Omega \\ \nabla \cdot \mathbf{u} = 0 & , \text{ in } \Omega \\ \mathbf{u} \cdot \nabla T - \frac{1}{\sqrt{GrPr}} \Delta T = 0 & , \text{ in } \Omega \\ \mathbf{u} = \mathbf{0} & , \text{ on } \partial\Omega \\ T = 0 & , \text{ on } \Gamma_1 \\ \frac{\partial T}{\partial \mathbf{n}} = 0 & , \text{ on } \partial\Omega \setminus (\Gamma_1 \cup \Gamma_3) \\ \frac{\partial T}{\partial \mathbf{n}} = 1 & , \text{ on } \Gamma_3. \end{array} \right. \quad (1)$$

where $\Omega \subset \mathbb{R}^d$, $d = 2, 3$, \mathbf{u} , p and T are respectively the adimensionalized velocity, pressure and temperature, Gr and Pr are the Grashof and the Prandtl numbers, and \mathbf{e}_2 is the inward-pointing normal vector of a border $\Gamma_2 \subset \partial\Omega$. The 2D domain consists in a rectangular tank of height 1 and length W , in the 3D case we consider a rectangular cuboid of height 1, length W and depth 1. A heat flux is imposed on the “right” border Γ_3 while the temperature is fixed on the “left” border Γ_1 and the remaining walls are insulated. Similar boundary conditions apply in 3D. No-slip boundary conditions are set for the fluid velocity in the tank.

The parameters are the Grashof and the Prandtl numbers and we consider the average temperature on Γ_3 as the output. As the Grashof and/or Prandtl numbers increase the average temperature decreases, see *e.g.* Figure 5(a) or Figure 6(a).

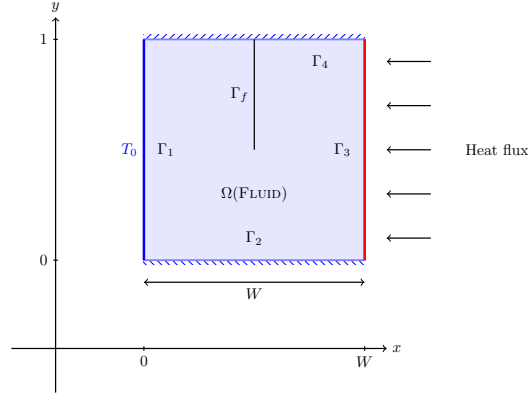


FIGURE 1. Geometry of the 2D model. In 3D case, an extrusion of length 1 in z axis direction is considered.

2. FINITE ELEMENT FORMULATION

In this section, we write the weak Galerkin formulations associated to (1) and we propose an iterative method to solve this problem in case of FE space and a resolution with the RBM.

The weak formulation associated to problem (1) writes

$$\begin{aligned} a(\mathbf{u}, \mathbf{u}, \mathbf{v}) - b(p, \mathbf{v}) + \frac{1}{\sqrt{Gr}} c(\mathbf{u}, \mathbf{v}) - d(T, \mathbf{v}) &= 0, \quad \forall \mathbf{v} \in V \\ b(q, \mathbf{u}) &= 0, \quad \forall q \in Q \\ e(T, \mathbf{u}, \xi) + \frac{1}{\sqrt{GrPr}} g(T, \xi) - \frac{1}{\sqrt{GrPr}} h(\xi) &= 0, \quad \forall \xi \in \Xi \end{aligned} \quad (2)$$

where $V \equiv [H_0^1(\Omega)]^d$, $Q \equiv L^2(\Omega)$, $\Xi \equiv \{\xi \in H^1(\Omega) \text{ s.t. } \xi|_{\Gamma_1} = 0\}$, and we define the tri-linear forms $a : V \times V \times V \rightarrow \mathbb{R}$ and $e : \Xi \times V \times \Xi \rightarrow \mathbb{R}$ as

$$a(\mathbf{u}, \mathbf{w}, \mathbf{v}) = \int_{\Omega} (\mathbf{w} \cdot \nabla \mathbf{u}) \cdot \mathbf{v}, \quad \forall \mathbf{u}, \mathbf{w}, \mathbf{v} \in V \quad (3)$$

$$e(T, \mathbf{v}, \xi) = \int_{\Omega} (\mathbf{v} \cdot \nabla T) \xi, \quad \forall \mathbf{v} \in V, T, \xi \in \Xi \quad (4)$$

the bi-linear forms $b : Q \times V \rightarrow \mathbb{R}$, $c : V \times V \rightarrow \mathbb{R}$, $d : \Xi \times V \rightarrow \mathbb{R}$ and $g : \Xi \times \Xi \rightarrow \mathbb{R}$ as

$$b(q, \mathbf{v}) = \int_{\Omega} q \nabla \cdot \mathbf{v}, \quad \forall \mathbf{v} \in V, q \in Q \quad (5)$$

$$c(\mathbf{w}, \mathbf{v}) = \int_{\Omega} \nabla \mathbf{w} : \nabla \mathbf{v}, \quad \forall \mathbf{w}, \mathbf{v} \in V \quad (6)$$

$$d(\xi, \mathbf{v}) = \int_{\Omega} \xi \mathbf{e}_2 \cdot \mathbf{v}, \quad \forall \mathbf{v} \in V, \xi \in \Xi \quad (7)$$

$$g(T, \xi) = \int_{\Omega} \nabla T \cdot \nabla \xi, \quad \forall T, \xi \in \Xi \quad (8)$$

and the linear operator $h : \Xi \rightarrow \mathbb{R}$ as

$$h(\xi) = \int_{\Gamma_3} \xi, \quad \forall \xi \in \Xi. \quad (9)$$

We introduce now a FE discretization of (2). We define the discrete spaces $V_h \subset V$, $Q_h \subset Q$, $\Xi_h \subset \Xi$ and the associated Galerkin projection of the solution (\mathbf{u}, p, T) of (2) by

$$\begin{aligned} V_h &\equiv \text{span}\{\phi_1, \dots, \phi_{N_u}\}, & \mathbf{u} &\simeq \sum_{j=1}^{N_u} \mathbf{u}_j \phi_j \\ Q_h &\equiv \text{span}\{\psi_1, \dots, \psi_{N_p}\}, & p &\simeq \sum_{j=1}^{N_p} p_j \psi_j \\ \Xi_h &\equiv \text{span}\{\xi_1, \dots, \xi_{N_T}\}, & T &\simeq \sum_{j=1}^{N_T} T_j \xi_j. \end{aligned}$$

The discrete formulation of (2) now reads

$$\begin{aligned} \sum_{i,j=1}^{N_u} \mathbf{u}_i \mathbf{u}_j a(\phi_i, \phi_j, \phi_{k_1}) + \sum_{i=1}^{N_u} \frac{1}{\sqrt{Gr}} \mathbf{u}_i c(\phi_i, \phi_{k_1}) - \sum_{i=1}^{N_p} p_i b(\psi_i, \phi_{k_1}) - \sum_{i=1}^{N_T} T_i d(\xi_i, \phi_{k_1}) = 0, \quad k_1 = 1, \dots, N_u \\ \sum_{i=1}^{N_u} \mathbf{u}_i b(\psi_{k_2}, \phi_i) = 0, \quad k_2 = 1, \dots, N_p \\ \sum_{i=1}^{N_T} \sum_{j=1}^{N_u} T_i \mathbf{u}_j e(\xi_i, \phi_j, \xi_{k_3}) + \frac{1}{\sqrt{GrPr}} \sum_{i=1}^{N_T} T_i g(\xi_i, \xi_{k_3}) - \frac{1}{\sqrt{GrPr}} h(\xi_{k_3}) = 0, \quad k_3 = 1, \dots, N_T \end{aligned} \quad (10)$$

Due to its strong non-linearities, when the Grashof or Prandtl numbers are high, a robust iterative method is required to solve this problem. We apply here a Newton Method. For a given parameter $\boldsymbol{\mu} = (\mu_1, \mu_2) = (Gr^{-1/2}, Pr^{-1})$ and an initial guess (\mathbf{u}^0, p^0, T^0) , at each Newton sub-iteration $n = 1, \dots, n_{max}$ we look for $(\mathbf{u}^{n+1}, p^{n+1}, T^{n+1}) \in \mathbb{R}^{N_u} \times \mathbb{R}^{N_p} \times \mathbb{R}^{N_T}$ such that

$$J(\mathbf{u}^n, p^n, T^n; \boldsymbol{\mu}) [(\mathbf{u}^{n+1}, p^{n+1}, T^{n+1}) - (\mathbf{u}^n, p^n, T^n)] = R(\mathbf{u}^n, p^n, T^n; \boldsymbol{\mu}) \quad (11)$$

where $J = J(\mathbf{u}, p, T; \boldsymbol{\mu})$ is the Jacobian matrix, $R = R(\mathbf{u}, p, T; \boldsymbol{\mu})$ is the residual vector.

In the case of problem (10) the terms of the Jacobian matrix can be easily calculated. For each row $k_1 = 1, \dots, N_u$ they write

$$\begin{aligned} J_{k_1 i}(\mathbf{u}, p, T; \boldsymbol{\mu}) &= \sum_{j=1}^{N_u} \mathbf{u}_j a(\phi_i, \phi_j, \phi_{k_1}) + \sum_{j=1}^{N_u} \mathbf{u}_j a(\phi_j, \phi_i, \phi_{k_1}) + \mu_1 c(\phi_i, \phi_{k_1}), & i = 1, \dots, N_u \\ J_{k_1 N_u + i}(\mathbf{u}, p, T; \boldsymbol{\mu}) &= -b(\psi_i, \phi_{k_1}), & i = 1, \dots, N_p \\ J_{k_1 N_u + N_p + i}(\mathbf{u}, p, T; \boldsymbol{\mu}) &= -d(\xi_i, \phi_{k_1}), & i = 1, \dots, N_T \end{aligned} \quad (12)$$

for all row $k_2 = N_u + k$, $k = 1, \dots, N_p$

$$\begin{aligned} J_{k_2 i}(\mathbf{u}, p, T; \boldsymbol{\mu}) &= b(\psi_k, \phi_i), & i = 1, \dots, N_u \\ J_{k_2 N_u + i}(\mathbf{u}, p, T; \boldsymbol{\mu}) &= 0, & i = 1, \dots, N_p \\ J_{k_2 N_u + N_p + i}(\mathbf{u}, p, T; \boldsymbol{\mu}) &= 0, & i = 1, \dots, N_T \end{aligned} \quad (13)$$

and for all line $k_3 = N_u + N_p + k$, $k = 1, \dots, N_T$

$$\begin{aligned}
 J_{k_3 i}(\mathbf{u}, p, T; \boldsymbol{\mu}) &= \sum_{j=1}^{N_T} T_j e(\xi_j, \phi_i, \xi_k), & i = 1, \dots, N_u \\
 J_{k_3 N_u + i}(\mathbf{u}, p, T; \boldsymbol{\mu}) &= 0, & i = 1, \dots, N_p \\
 J_{k_3 N_u + N_p + i}(\mathbf{u}, p, T; \boldsymbol{\mu}) &= \sum_{j=1}^{N_u} \mathbf{u}_j e(\xi_i, \phi_j, \xi_k) + \mu_1 \mu_2 g(\xi_i, \xi_k), & i = 1, \dots, N_T.
 \end{aligned} \tag{14}$$

In the same way, each term of the residual $R(\mathbf{u}, p, T; \boldsymbol{\mu}) \in \mathbb{R}^{N_u + N_p + N_T}$ can be calculated by

$$\begin{aligned}
 R_k(\mathbf{u}, p, T; \boldsymbol{\mu}) &= -a(\mathbf{u}, \mathbf{u}, \phi_k) + b(p, \phi_k) - \mu_1 c(\mathbf{u}, \phi_k) + d(T, \phi_k), & k = 1, \dots, N_u \\
 R_{N_u + k}(\mathbf{u}, p, T; \boldsymbol{\mu}) &= -b(\psi_k, \mathbf{u}), & k = 1, \dots, N_p \\
 R_{N_u + N_p + k}(\mathbf{u}, p, T; \boldsymbol{\mu}) &= \mu_1 \mu_2 h(\xi_k) - e(T, \mathbf{u}, \xi_k) - \mu_1 \mu_2 g(T, \xi_k), & k = 1, \dots, N_T
 \end{aligned}$$

Remark 2.1. For high Gr and Pr numbers the Newton method might be insufficient. We propose in that case to use the continuation algorithm, Algorithm 1. Note however that we do not apply this continuation method in results presented below.

Algorithm 1 Continuation strategy for high Gr and Pr numbers.

```

Fix parameters  $Gr$  and  $Pr$ 
Fix minimal values of parameters  $Gr_{min} = 1$  and  $Pr_{min} = 10^{-2}$ 
Fix tolerance  $tol$  and max number of iteration  $n_{max}$  for Newton
Calculate number of intermediary parameters:
   $N = \max \{ 1; \max \{ \lceil \log(Gr/Gr_{min}) \rceil, \lceil \log(Pr/Pr_{min}) \rceil \} \}$ 
for i=1:N do
  Logarithmic scale for intermediary parameters:
     $Gr(i) = \exp\{\log(Gr_{min}) + i(\log(Gr/Gr_{min}))/N\}$ 
     $Pr(i) = \exp\{\log(Pr_{min}) + i(\log(Pr/Pr_{min}))/N\}$ 
  Fix Newton initial guess  $u^0 = u_{old}$ 
  while  $\|R\| \geq tol$  or  $n \leq n_{max}$  do
    find  $u^n$  s.t.  $J(u^{n-1})(u^n - u^{n-1}) = R(u^{n-1})$ 
  end while
   $u_{old} = u^n$ 
end for
return Solution  $u = u^n$ 

```

3. REDUCED BASIS FORMULATION

Let us now investigate a reduced basis formulation to solve the heat convection problem introduced above. We first propose a general approach that can be applied to any quadratic problem affine in parameters. The technique is based on the idea to store the more information as possible in the reduced space. So, tensors are introduced and projected as well as matrices and vectors. After an overview on this method we deal with application to the heat convection equations.

3.1. Reduced Basis for a general quadratic problem

We now turn to the generalization of the RBM to a quadratic problem, in abstract form it reads

$$a(u, u, v; \boldsymbol{\mu}) + b(u, v; \boldsymbol{\mu}) = f(v; \boldsymbol{\mu}), \quad \forall v \in V \quad (15)$$

where the solution is $u = u(\boldsymbol{\mu}) \in V$, $\boldsymbol{\mu} \in \mathbb{R}^Q$ indicates Q scalar parameters, V is an Hilbert space defined on a domain $\Omega \subset \mathbb{R}^d$, with $d = 1, 2, 3$, $a : V \times V \times V \rightarrow \mathbb{R}$ is a tri-linear form, $b : V \times V \rightarrow \mathbb{R}$ is a bi-linear form, and $f : V \rightarrow \mathbb{R}$ is a linear operator.

We first introduce the FE approximation of (15) that leads to the RB approximation. The RB formulation of the general problem (15) applies then to (2).

Let us define a FE space $V_{\mathcal{N}} \equiv \text{span}\{v_1, \dots, v_{\mathcal{N}}\} \subset V$, and the approximated solution of (15) as

$$u(\boldsymbol{\mu}) \simeq \sum_{i=1}^{\mathcal{N}} u_i(\boldsymbol{\mu}) v_i$$

then the discrete formulation of (15) writes

$$\sum_{i,j=1}^{\mathcal{N}} u_i u_j a(v_i, v_j, v_k; \boldsymbol{\mu}) + \sum_{i=1}^{\mathcal{N}} u_i b(v_i, v_k; \boldsymbol{\mu}) = f(v_k; \boldsymbol{\mu}), \quad \forall k = 1, \dots, \mathcal{N} \quad (16)$$

where the solution $\mathbf{u} = \mathbf{u}(\boldsymbol{\mu}) = [u_1 \dots u_{\mathcal{N}}]^T \in \mathbb{R}^{\mathcal{N}}$ for each parameter $\boldsymbol{\mu} \in \mathbb{R}^Q$.

In order to describe the RB approximation applied to problems such as (15), we need to define some discrete objects. In particular, we introduce the tensor $A = A(\boldsymbol{\mu}) \in \mathbb{R}^{\mathcal{N} \times \mathcal{N} \times \mathcal{N}}$, the matrix $B = B(\boldsymbol{\mu}) \in \mathbb{R}^{\mathcal{N} \times \mathcal{N}}$, and the vector $\mathbf{f} = \mathbf{f}(\boldsymbol{\mu}) \in \mathbb{R}^{\mathcal{N}}$ defined by

$$(A)_{ijk} = a(v_i, v_j, v_k; \boldsymbol{\mu}), \quad (B)_{ki} = b(v_i, v_k; \boldsymbol{\mu}), \quad (\mathbf{f})_k = f_k = f(v_k; \boldsymbol{\mu})$$

for $i, j, k = 1, \dots, \mathcal{N}$. Note that the tensor A can be considered as a vector of matrices, *i.e.* for each $k = 1, \dots, \mathcal{N}$, we define the matrix $A_k = A_k(\boldsymbol{\mu}) \in \mathbb{R}^{\mathcal{N} \times \mathcal{N}}$ as $(A_k)_{ij} = (A)_{ijk}$, $i, j = 1, \dots, \mathcal{N}$. Using this notation (16) now reads

$$\mathbf{u}^T A_k \mathbf{u} + (B\mathbf{u})_k = f_k, \quad \forall k = 1, \dots, \mathcal{N} \quad (17)$$

where $(B\mathbf{u})_k$ and f_k are respectively the k -th term of vectors $B\mathbf{u}$ and \mathbf{f} .

As described in Section 2 we can treat the non-linearity of the first term in (17) using a Newton Method. For a given parameter $\boldsymbol{\mu} \in \mathbb{R}^Q$, each iteration $n = 1, 2, \dots$ of the Newton algorithm reads

$$J_{\text{row}(k)}(\mathbf{u}^n; \boldsymbol{\mu})(\mathbf{u}^{n+1} - \mathbf{u}^n) = R_k(\mathbf{u}^n; \boldsymbol{\mu}), \quad \forall k = 1, \dots, \mathcal{N} \quad (18)$$

where $J_{\text{row}(k)}(\mathbf{u}^n; \boldsymbol{\mu}) \in \mathbb{R}^{\mathcal{N}}$ and $R_k(\mathbf{u}^n; \boldsymbol{\mu})$ are respectively the k -th row of the Jacobian matrix $J = J(\mathbf{u}; \boldsymbol{\mu}) \in \mathbb{R}^{\mathcal{N} \times \mathcal{N}}$ and the k -th term of the residual $R = R(\mathbf{u}^n; \boldsymbol{\mu}) \in \mathbb{R}^{\mathcal{N}}$ defined by

$$R_k(\mathbf{u}^n; \boldsymbol{\mu}) = f_k - (\mathbf{u}^n)^T A_k \mathbf{u}^n - (B\mathbf{u}^n)_k, \quad k = 1, \dots, \mathcal{N}. \quad (19)$$

For the sake of notation, the dependency of a , b , f , and all associated operators on the parameters $\boldsymbol{\mu}$ is removed.

Now, we just need to calculate the Jacobian matrix $J = J(\mathbf{u}; \boldsymbol{\mu})$. We can write each of its elements as

$$\begin{aligned}
 J_{ki}(\mathbf{u}) &= \frac{\partial a}{\partial u_i}(\mathbf{u}, \mathbf{u}, v_k) + \frac{\partial b}{\partial u_i}(\mathbf{u}, v_k) - \frac{\partial f}{\partial u_i}(v_k) = \\
 &= \sum_{l=1}^{\mathcal{N}} \sum_{j=1}^{\mathcal{N}} \frac{\partial}{\partial u_i}(u_l u_j a(v_l, v_j, v_k)) + \sum_{j=1}^{\mathcal{N}} \frac{\partial}{\partial u_i}(b(v_j, v_k) u_j) = \\
 &= \sum_{l=1}^{\mathcal{N}} \sum_{j=1}^{\mathcal{N}} \frac{\partial}{\partial u_i}(u_l A_{ljk} u_j) + \sum_{j=1}^{\mathcal{N}} \frac{\partial}{\partial u_i}(B_{kj} u_j) = \\
 &= \sum_{j=1}^{\mathcal{N}} u_j A_{jik} + \sum_{j=1}^{\mathcal{N}} A_{ijk} u_j + B_{ki}.
 \end{aligned} \tag{20}$$

In general A is never assembled as it is of size \mathcal{N}^3 , where \mathcal{N} is the dimension of the underlying discretization space. If this is indeed the case for FE discretization, recall however that here we deal with reduced order approximation which enables the computation of A explicitly. Let us then introduce a reduced space $V_N = \text{span}\{\varphi_1, \dots, \varphi_N\}$, with $N \ll \mathcal{N}$ and define the projection $\tilde{\mathbf{u}} = \tilde{\mathbf{u}}(\boldsymbol{\mu}) \in \mathbb{R}^N$ of the solution \mathbf{u} in V_N as

$$\tilde{\mathbf{u}} = \sum_{i=1}^N \tilde{u}_i \varphi_i = \Phi^T \mathbf{u}, \tag{21}$$

where $\Phi = [\varphi_1 \dots \varphi_N] \in \mathbb{R}^{\mathcal{N} \times N}$, $\Phi_{ji} = \hat{\varphi}_{i,j} = (\varphi_i, v_j)_{V_N}$, the coefficients \tilde{u}_i are

$$\tilde{u}_i = (u, \varphi_i)_{V_N} = (u, \sum_{j=1}^{\mathcal{N}} \hat{\varphi}_{i,j} v_j)_{V_N} = \sum_{j=1}^{\mathcal{N}} u_j \hat{\varphi}_{i,j}$$

and $(\cdot, \cdot)_{V_N}$ is the scalar product associated to V_N .

We observe that the Newton method defined in (18) is in fact generic with respect to the discrete spaces and that we can replace $V_{\mathcal{N}}$ by V_N which corresponds to projections of the terms in (18) onto V_N . We now prove this statement.

Following the procedure of (21) we start by defining the projection of the source term \mathbf{f} as $\tilde{\mathbf{f}} = \tilde{\mathbf{f}}(\boldsymbol{\mu}) \in \mathbb{R}^N$

$$\tilde{\mathbf{f}} = \Phi^T \mathbf{f}, \tag{22}$$

then the matrix $\tilde{B} = \tilde{B}(\boldsymbol{\mu}) \in \mathbb{R}^{N \times N}$ as well is the projection of B into the reduced space V_N

$$\tilde{B} = \Phi^T B \Phi, \tag{23}$$

and finally we denote the reduced size tensor $\tilde{A} = \tilde{A}(\boldsymbol{\mu}) \in \mathbb{R}^{N \times N \times N}$. We now prove that it is in fact the projection of the tensor $A \in \mathbb{R}^{\mathcal{N} \times \mathcal{N} \times \mathcal{N}}$ in V_N

$$\begin{aligned}
 \tilde{A}_{ijk} &= a(\varphi_i, \varphi_j, \varphi_k) = \sum_{l,m,h=1}^{\mathcal{N}} \hat{\varphi}_{i,l} \hat{\varphi}_{j,m} \hat{\varphi}_{k,h} a(v_l, v_m, v_h) = \\
 &= \sum_{l,m,h=1}^{\mathcal{N}} \hat{\varphi}_{i,l} \hat{\varphi}_{j,m} \hat{\varphi}_{k,h} A_{lmh} = \sum_{h=1}^{\mathcal{N}} \hat{\varphi}_{k,h} (\Phi^T A_h \Phi)_{ij} = \sum_{h=1}^{\mathcal{N}} \hat{\varphi}_{k,h} (\tilde{A}_h)_{ij}
 \end{aligned} \tag{24}$$

$i, j, k = 1, \dots, N$, where $\tilde{A}_k = \Phi^T A_k \Phi$ is the projection of $A_k \in \mathbb{R}^{\mathcal{N} \times \mathcal{N}}$ in V_N for all $k = 1, \dots, \mathcal{N}$. Let us define the tensorial product $\star : \mathbb{R}^N \times \mathbb{R}^N \rightarrow \mathbb{R}$ as

$$\mathbf{a}^T \star (\mathbf{b}^T \mathbf{A} \mathbf{c}) := \sum_{h=1}^{\mathcal{N}} \mathbf{a}_h (\mathbf{b}^T A_h \mathbf{c}), \quad \forall \mathbf{a}, \mathbf{b}, \mathbf{c} \in \mathbb{R}^{\mathcal{N}}, \forall A \in \mathbb{R}^{\mathcal{N} \times \mathcal{N} \times \mathcal{N}}. \quad (25)$$

Then

$$\tilde{A}_{ijk} = \sum_{h=1}^{\mathcal{N}} \hat{\varphi}_{k,h} (\varphi_i^T A_h \varphi_j) = \varphi_k^T \star (\varphi_i^T A \varphi_j), \quad i, j, k = 1, \dots, N. \quad (26)$$

Using equations (23) and (26) we obtain the projection of the Jacobian $\tilde{J} \in \mathbb{R}^{N \times N}$ at each iteration $n = 1, 2, \dots$, and it reads

$$\tilde{J}_{ik}(\tilde{\mathbf{u}}^n; \boldsymbol{\mu}) = (\tilde{A}_k|_{col(i)})^T \tilde{\mathbf{u}}^n + (\tilde{A}_k|_{row(i)}) \tilde{\mathbf{u}}^n + \tilde{B}_{ik} \quad (27)$$

where $\tilde{A}_k|_{col(i)} = [\tilde{A}_{jik}]_{j=1}^N \in \mathbb{R}^N$ is the i -th column of the matrix \tilde{A}_k for each $k = 1, \dots, N$ and $\tilde{A}_k|_{row(i)} = [\tilde{A}_{ijk}]_{j=1}^N \in \mathbb{R}^N$ is the i -th row of the matrix \tilde{A}_k for each $k = 1, \dots, N$. If we use the tensorial product defined by (25) we simply write

$$\begin{aligned} \tilde{A}_k|_{col(i)} &= \left[\varphi_k^T \star (\varphi_1^T A \varphi_i) \quad \cdots \quad \varphi_k^T \star (\varphi_N^T A \varphi_i) \right] \\ \tilde{A}_k|_{row(i)} &= \left[\varphi_k^T \star (\varphi_i^T A \varphi_1) \quad \cdots \quad \varphi_k^T \star (\varphi_i^T A \varphi_N) \right] \end{aligned}$$

$i, k = 1, \dots, N$. Similarly, each term of the reduced residual $\tilde{R} = \tilde{R}(\tilde{\mathbf{u}}; \boldsymbol{\mu}) \in \mathbb{R}^N$ reads

$$\tilde{R}_k(\tilde{\mathbf{u}}^n; \boldsymbol{\mu}) = \tilde{f}_k - (\tilde{\mathbf{u}}^n)^T \tilde{A}_k \tilde{\mathbf{u}}^n - (\tilde{B} \tilde{\mathbf{u}}^n)_k, \quad k = 1, \dots, N. \quad (28)$$

3.2. Application to heat convection problem

Let us now apply this reduction technique to the natural convection problem introduced in Section 2. The FE formulation of each sub-iteration $n = 1, \dots, n_{max}$ of the Newton Method applied to equations (2) writes

$$\mathbf{J}(\mathbf{u}^n, p^n, T^n) [(\mathbf{u}^{n+1}, p^{n+1}, T^{n+1}) - (\mathbf{u}^n, p^n, T^n)] = R(\mathbf{u}^n, p^n, T^n) \quad (29)$$

with Jacobian and residual terms defined as in Section 2. In order to apply the technique described in the previous paragraph, we introduce matrices and tensors associated to (10). We define the tensors $A \in \mathbb{R}^{N_u \times N_u \times N_u}$ and $E \in \mathbb{R}^{N_T \times N_u \times N_T}$ as

$$\begin{aligned} A &= [A_{ijk}, \quad i, j, k = 1, \dots, N_u], \quad (A_k)_{ij} = A_{ijk} = a(\phi_i, \phi_j, \phi_k) \\ E &= [E_{ijk}, \quad i, k = 1, \dots, N_T, j = 1, \dots, N_u], \quad (E_k)_{ij} = E_{ijk} = e(\xi_i, \phi_j, \xi_k) \end{aligned}$$

the matrices $B \in \mathbb{R}^{N_p \times N_u}$, $C \in \mathbb{R}^{N_u \times N_u}$, $D \in \mathbb{R}^{N_u \times N_T}$, $G \in \mathbb{R}^{N_T \times N_T}$ as

$$\begin{aligned} B &= [B_{ij}, \quad i = 1, \dots, N_u, j = 1, \dots, N_p], \quad B_{ij} = b(\psi_j, \phi_i) \\ C &= [C_{ij}, \quad i, j = 1, \dots, N_u], \quad C_{ij} = c(\phi_j, \phi_i) \\ D &= [D_{ij}, \quad i = 1, \dots, N_u, j = 1, \dots, N_T], \quad D_{ij} = d(\xi_j, \phi_i) \\ G &= [G_{ij}, \quad i = 1, \dots, N_T], \quad G_{ij} = g(\xi_j, \xi_i) \end{aligned}$$

and the vector $H \in \mathbb{R}^{N_T}$ as

$$H = [H_i, \quad i = 1, \dots, N_T], \quad H_i = h(\xi_i).$$

Then, using notation introduced in Section 3.1, the Jacobian matrix writes

$$J(\mathbf{u}, p, T; \boldsymbol{\mu}) = \begin{bmatrix} J^{Nl_1}(\mathbf{u}) + \mu_1 C & -B & -D \\ B^T & \mathbf{0} & \mathbf{0} \\ J^{Nl_2}(T) & \mathbf{0} & J^{Nl_3}(\mathbf{u}) + \mu_1 \mu_2 G \end{bmatrix} \quad (30)$$

where each element of the non-linear submatrices $J^{Nl_1}(\mathbf{u})$, $J^{Nl_2}(T)$, $J^{Nl_3}(\mathbf{u})$ are

$$\begin{aligned} J_{ki}^{Nl_1}(\mathbf{u}) &= \sum_{j=1}^{N_u} ((A_k)_{ij} + (A_k)_{ji}) \mathbf{u}_j = ((A_k|_{col(i)})^T + (A_k|_{row(i)})) \mathbf{u}, \quad k, i = 1, \dots, N_u \\ J_{ki}^{Nl_2}(T) &= \sum_{j=1}^{N_T} (E_k)_{ij} T_j = (E_k|_{row(i)}) T, \quad k = 1, \dots, N_T, i = 1, \dots, N_u \\ J_{ki}^{Nl_3}(\mathbf{u}) &= \sum_{j=1}^{N_u} (E_k)_{ji} \mathbf{u}_j = (E_k|_{col(i)})^T \mathbf{u}, \quad k, i = 1, \dots, N_T \end{aligned} \quad (31)$$

whereas each element of the residual vector of the Newton algorithm (29) writes

$$\begin{aligned} R_k(\mathbf{u}, p, T; \boldsymbol{\mu}) &= -\mathbf{u}^T A_k \mathbf{u} + B_{row(k)} p - \mu_1 C_{row(k)} \mathbf{u} + D_{row(k)} T, \quad k = 1, \dots, N_u \\ R_k(\mathbf{u}, p, T; \boldsymbol{\mu}) &= -(B_{col(k)})^T u, \quad k = N_u + 1, \dots, N_u + N_p \\ R_k(\mathbf{u}, p, T; \boldsymbol{\mu}) &= \mu_1 \mu_2 H_k - \mathbf{u}^T E_k T - \mu_1 \mu_2 G_{row(k)} T \end{aligned} \quad (32)$$

To apply efficiently the RB methodology, a key ingredient is the affine decomposition of the terms in the Newton Method which is readily available for our problem. The Jacobian matrix writes as

$$J(\mathbf{u}, p, T; \boldsymbol{\mu}) = \sum_{q=1}^{Q_J} \theta_J^q(\boldsymbol{\mu}) J^q(\mathbf{u}, p, T) \quad (33)$$

where for the considered example $Q_J = 4$ and the coefficients θ_J are

$$\theta_J^1(\boldsymbol{\mu}) = \mu_1 = \frac{1}{\sqrt{Gr}}, \quad \theta_J^2(\boldsymbol{\mu}) = \mu_1 \mu_2 = \frac{1}{\sqrt{GrPr}}, \quad \theta_J^3(\boldsymbol{\mu}) = \theta_J^4(\boldsymbol{\mu}) = 1. \quad (34)$$

Each sub-matrix can be described using the notation introduced above

$$\begin{aligned} J^1(\mathbf{u}, p, T) &= \begin{bmatrix} C & \mathbf{0} & \mathbf{0} \\ \mathbf{0} & \mathbf{0} & \mathbf{0} \\ \mathbf{0} & \mathbf{0} & \mathbf{0} \end{bmatrix}, & J^2(\mathbf{u}, p, T) &= \begin{bmatrix} \mathbf{0} & \mathbf{0} & \mathbf{0} \\ \mathbf{0} & \mathbf{0} & \mathbf{0} \\ \mathbf{0} & \mathbf{0} & G \end{bmatrix}, \\ J^3(\mathbf{u}, p, T) &= \begin{bmatrix} \mathbf{0} & -B & -D \\ B^T & \mathbf{0} & \mathbf{0} \\ \mathbf{0} & \mathbf{0} & \mathbf{0} \end{bmatrix}, & J^4(\mathbf{u}, p, T) &= \begin{bmatrix} J^{Nl_1}(\mathbf{u}) & \mathbf{0} & \mathbf{0} \\ \mathbf{0} & \mathbf{0} & \mathbf{0} \\ J^{Nl_2}(T) & \mathbf{0} & J^{Nl_3}(\mathbf{u}) \end{bmatrix}. \end{aligned} \quad (35)$$

As to the residual, it is readily decomposed as

$$R(\mathbf{u}, p, T; \boldsymbol{\mu}) = \sum_{q=1}^{Q_R} \theta_R^q(\boldsymbol{\mu}) R^q(\mathbf{u}, p, T) \quad (36)$$

with $Q_R = 3$ terms, we have

$$\theta_R^1(\boldsymbol{\mu}) = \mu_1 = \frac{1}{\sqrt{Gr}}, \quad \theta_R^2(\boldsymbol{\mu}) = \mu_1\mu_2 = \frac{1}{\sqrt{GrPr}}, \quad \theta_R^3(\boldsymbol{\mu}) = 1 \quad (37)$$

and

$$R^1(\mathbf{u}, p, T) = \begin{bmatrix} -C\mathbf{u} \\ \mathbf{0} \\ \mathbf{0} \end{bmatrix}, \quad R^2(\mathbf{u}, p, T) = \begin{bmatrix} \mathbf{0} \\ \mathbf{0} \\ H - GT \end{bmatrix}, \quad (38)$$

$$R^3(\mathbf{u}, p, T) = \begin{bmatrix} -(\mathbf{u}^T A_k \mathbf{u})_{k=1}^{N_u} + Bp + DT \\ B^T \mathbf{u} \\ -((\mathbf{u}^T E_k T)^T)_{k=1}^{N_T} \end{bmatrix}.$$

The last step consists in projecting these equations in a reduced space. As shown for the general problem (15), the reduced Newton method at each iteration $n = 1, \dots, n_{max}$ writes

$$\tilde{J}(\tilde{\mathbf{u}}^n, \tilde{p}^n, \tilde{T}^n) \left[(\tilde{\mathbf{u}}^{n+1}, \tilde{p}^{n+1}, \tilde{T}^{n+1}) - (\tilde{\mathbf{u}}^n, \tilde{p}^n, \tilde{T}^n) \right] = \tilde{R}(\tilde{\mathbf{u}}^n, \tilde{p}^n, \tilde{T}^n) \quad (39)$$

where the \sim indicates the projection onto the reduced space V_N . The computation of vectors and matrices is done in a "classical" way, the terms are calculated in the FE space V_N and projected into the reduced one by the matrix Φ defined by the basis functions. Each basis function is the solution of problem (10) for a fixed parameter $\boldsymbol{\mu}$, possibly orthonormalized. For tensors A and E a different approach is needed because of their high dimensions.

Let us consider a general tensor $A \in R^{\mathcal{N}^3}$ defined by a trilinear form $a : V_{\mathcal{N}}^3 \rightarrow \mathbb{R}$, $A_{ijk} = a(v_i, v_j, v_k)$, $i, j, k = 1, \dots, \mathcal{N}$ as in problem (15). Its projection on a reduced space $V_N = \text{span}\{\varphi_1, \dots, \varphi_N\}$, as shown in Section 3.1, is defined by $\tilde{A} \in \mathbb{R}^{N^3}$, $\tilde{A}_{ijk} = \varphi_k^T \star (\varphi_i^T A \varphi_j)$, $i, j, k = 1, \dots, N$. We observe that $\tilde{A}_{ijk} = a(\varphi_i, \varphi_j, \varphi_k)$ where $\varphi_i, \varphi_j, \varphi_k \in V_N$.

Let us then define an hybrid tensor $\Lambda \in \mathbb{R}^{N \times N \times N}$ whose elements are

$$\Lambda_{ijk} = (\Lambda_k)_{ij} = a(v_i, v_j, \varphi_k), \quad (40)$$

$i, j = 1, \dots, \mathcal{N}$, $k = 1, \dots, N$. We can then use this tensor to redefine the reduced tensor \tilde{A}

$$\begin{aligned} \tilde{A}_{ijk} &= a(\varphi_i, \varphi_j, \varphi_k) = \sum_{l,m=1}^{\mathcal{N}} \hat{\varphi}_{i,l} \hat{\varphi}_{j,m} a(v_l, v_m, \varphi_k) = \\ &= \sum_{l,m=1}^{\mathcal{N}} \Phi_{li} \Phi_{mj} (\Lambda_k)_{lm} = (\Phi^T \Lambda_k \Phi)_{ij}. \end{aligned} \quad (41)$$

So, we proved that

$$\tilde{A}_k = \Phi^T \Lambda_k \Phi. \quad (42)$$

That implies that we can calculate only N matrices Λ_k , $k = 1, \dots, N$, and project them into the reduced space to obtain the reduced tensor \tilde{A} .

Remark 3.3. *The pressure has been included in the RB space in our implementation: although it is a Lagrange multiplier for the divergence free constraint in the original FE problem, it could be removed without leading to any RB solution change as the solutions are already divergence free. We decided however to include the pressure in the RB only for the sake of convenience during the implementation phase.*

4. COMPUTATIONAL FRAMEWORK

In this section we give an overview of the computational framework and its implementation to solve the heat convection problem introduced in Section 2. All the routines described are part of the FE or RB frameworks of FEEL++ library and available in FEEL++ source code. We first introduce the main principles of FEEL++, then we illustrate the FE implementation of problem (1) and finally we introduce the associated RB framework.

4.1. Feel++ principles and design

FEEL++ is a C++ library that provides a clear and easy to use interface to solve complex PDE systems. It aims at bringing the scientific community a tool for the implementation of advanced numerical methods and high performance computing.

FEEL++ relies on a so-called *Domain Specific Embedded Language* (DSEL) designed to closely match the Galerkin mathematical framework. In computer science DS(E)Ls are used to partition complexity. In FEEL++ the DSEL splits low level mathematics and computer science on one side, and high level mathematics as well as physical applications to the other side. This difference between disciplines is reflected on users and developers tasks and allows easily improvements on both sides. Furthermore, it enables using FEEL++ for teaching purposes, solving complex problems with multiple physics and scales or rapid prototyping of new methods, schemes or algorithms.

The DSEL on FEEL++ provides access to powerful tools such as interpolation, with a simple and seamless interface, and allows clear translation of a wide range of variational formulations into the variational embedded language. Combined with this robust engine, it lies also arbitrary order finite elements, high order quadrature formulas and robust nodal configuration sets. The tools at the user's disposal grant the flexibility to implement numerical methods that cover a large combination of choices from meshes, function spaces or quadrature points using the same integrated language and control at each stage of the solution process of the numerical approximations.

In this paper, we use recent developments which allow to operate on large-scale parallel infrastructures. The general strategy used is *parallel data* framework using MPI and thanks to DSEL the MPI communications are seamless to the user: (i) we start with automatic mesh partitioning using GMSH [GR09] (Chaco/Metis) — adding information about ghost cells with communication between neighbor partition; — (ii) the FEEL++ parallel data structures such as meshes, (elements of) function spaces — create a parallel degrees of freedom table with local and global views; — (iii) and finally we use the library PETSC [BBB⁺12, BBE⁺12, BGCMS97] which provides access to a Krylov subspace solvers(KSP) coupled with PETSC preconditioners such as Block-Jacobi, ASM, GASM. A complete description of the FEEL++ high performance framework is available in the thesis [Cha13].

Remark 4.2. *The last preconditioner is an additive variant of the Schwarz alternating method for the case of many subregions, see [SBG04]. For each sub-preconditioners (in the subdomains), PETSC allows to choose a wide range of sequential preconditioners such as LU, ILU, JACOBI, ML. Moreover, preconditioner ASM or GASM can be used with or without an algebraic overlap. Other parallel preconditioners are available in PETSC but not used here. In particular we would like to mention the MUMPS direct parallel solver [ADL00]. We use it both as solver and preconditioner for iterative solves. FIELDSPLIT preconditioners are also of notice for the applications we have: they allow to exploit the structure of block matrix.*

4.3. Finite element model for the reduced basis framework

In this section we briefly introduce the organization of the RB framework of FEEL++ (see Figure 2), and then we see how the user deals with the FE model, needed to interface with the RB framework.

4.3.1. Reduced basis framework

The offline/online strategy developed in the RBM is implemented in the class `CRBTrilinear`.

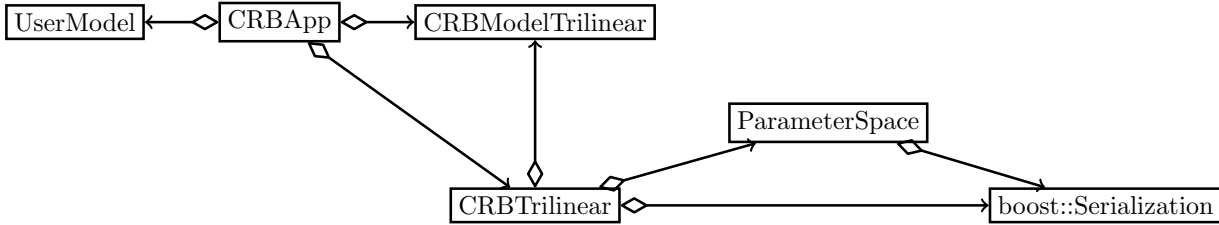


FIGURE 2. Class diagram for the FEEL++ RB framework. Arrows represent instantiations of template classes.

As the offline step of the method can be very expensive, scalar products resulting from the projection of matrices or vectors on the RB are saved in a database. To save objects in the database, we use the concept of "serialization" introduced by the set of libraries for the C++ programming language BOOST.

The class `CRBApp` is the driver for the RB framework. The class `ParameterSpace` manages the construction of the parameter space. First, if no existing database is found the offline step of RBM is run in order to build a basis, while if a database already exists the basis can be enriched or the algorithm passes to the online step.

To solve a linear or nonlinear problem with RB method in FEEL++ the user has to define in his model the variational formulation of the problem. At the state of the art, the variation form must be defined in accord with the affine decomposition, future revisions of the code will introduce an automated affine decomposition. Note that using FEEL++ the user model can be as well a 1D, 2D or 3D model. It is important to keep in mind that to interface with the RB framework the user has to provide only the FE model (*i.e.* parameter space, geometry, variational formulation), it corresponds to `UserModel` in Figure 2 whose interface derives from `CRBModelTrilinear`.

The FEEL++ RB framework support parallel architectures using the MPI technology. As in the FE framework an automatic mesh partitioning using `Gmsh` (Chaco/Metis) is computed, while every data associated to the reduced basis (scalars, vectors and dense matrices, parameter space samplings,...) are duplicated on each processor. However note that since the mesh is partitioned according the number of processors, finite element approximations and thus the reduced basis functions are in fact spread on all processors. Currently the basis functions are saved in the RB database with their associated partitioning. If they are required for visualization purposes or reduced basis space enrichment, the same data partition as in the initial computations must be used. Another particular attention must be paid to parameter space sampling generation: we must ensure that all processors hold the same samplings. To this end, there are generated in a sequential way by only one processor and then broadcasted to other processors.

4.3.2. Finite element model

Let us illustrate the implementation of the FE solution strategy for the problem (1) using FEEL++, we give the main ideas of the solver function, with the continuation algorithm described above, and the computation of Newton method terms.

In Listing 1, we display a snippet of code showing the code describing for a given μ , the solution process to retrieve $(\mathbf{u}(\mu), p(\mu), T(\mu))$: (i) compute the coefficients of the affine decomposition; (ii) assemble the linear terms; (iii) solve the non linear problem where `updateJacobian` and `updateResidual` are computing the jacobian and residual respectively during the Newton iterations. Note that `updateJacobian` need not be called at every iterations. Moreover the code is seamless with respect to geometrical dimension (2D or 3D) and parallel computing.

LISTING 1. Implementation of algorithm 1

```

void solve( parameter_type const& mu, element_ptrtype& T )
  
```

```

{
  this->computeThetaQ( mu ); // Update  $\theta$  coefficients
  this->update( mu ); // Update affine decomposition of the linear terms
  // nonlinear iterative solver, solve for  $U=(u,p,T)$ 
  backend()->nlSolve( _jacobian=updateJacobian,
                    _residual=updateResidual,
                    _solution=U );
}

```

As mentioned earlier, at each Newton iteration, the Jacobian matrix and the residual vector are updated. We start with the linear terms which can be precomputed, see Section 3.2. We show, as an example, the Jacobian sub-matrices assembly. The vector `thetaAq[q]` represents the coefficients θ_J defined in (34), while the matrices `Aq[0]`, `Aq[1]`, `Aq[2]` are respectively the matrices J^1 , J^2 and J^3 defined in (35). The assembly of those matrices is displayed in Listing 2.

LISTING 2. Jacobian Linear terms assembly

```

// Definition of mesh and FE space  $X_h = V_h \times Q_h \times \Xi_h$ 
mesh_ptrtype mesh;
// N polynomial order
Vh = Pch<N+1, Vectorial>( mesh );
Qh = Pch<N>( mesh );
Xih = Pch<N+1>( mesh );
Xh = Vh * Qh * Xih;
// Definition of functions
element_type U( Xh, "u" );
element_type V( Xh, "v" );
// Velocity function and test function
element_0_type u = U. element<0>(); element_0_type v = V. element<0>();
// Pression function and test function
element_1_type p = U. element<1>(); element_1_type q = V. element<1>();
// Temperature function and test function
element_2_type t = U. element<2>(); element_2_type s = V. element<2>();

// 1) Fluid equations
// 1.1) Velocity diffusion:  $Aq[0] = C = \int_{\Omega} \nabla u : \nabla v$ 
form2( _test=Xh, _trial=Xh, _matrix=Aq[0] ) =
  integrate( _range=elements( mesh ), _expr=trace( gradt(u)*trans( grad(v) ) ) );
// 1.2) Heat diffusion:  $Aq[1] = G = \int_{\Omega} \nabla t \cdot \nabla s$ 
form2( _test=Xh, _trial=Xh, _matrix=Aq[1] ) =
  integrate( _range=elements( mesh ), _expr=gradt(t)*trans( grad(s) ) );
// 1.3) Pressure-velocity terms:  $Aq[2] = -B = \int_{\Omega} -p \nabla \cdot v$ 
form2( _test=Xh, _trial=Xh, _matrix=Aq[2] ) =
  integrate( _range=elements( mesh ), _expr= - idt(p) * div(v) );
//  $Aq[2] += B^t = \int_{\Omega} q \nabla \cdot u$ 
form2( _test=Xh, _trial=Xh, _matrix=Aq[2] ) +=
  integrate( _range=elements( mesh ), _expr=divt(u) * id(q) );
// 2) Temperature equation
// 2.1) Buoyancy forces:  $Aq[2] += D = \int_{\Omega} t e_2 \cdot v$ 
form2( _test=Xh, _trial=Xh, _matrix=Aq[2] ) +=
  integrate( elements( mesh ), -idt(t)*( trans( vec( cst(0.), cst(1.0) ) ) * id(v) ) );
// B.C. ...

```

`form2(Xh,Xh,M)` builds a bilinear form $X_h \times X_h \rightarrow \mathbb{R}$ whose algebraic contribution are stored in the matrix `M`. We remark that the finite element space `Xh` used to solve the problem is a composite space: `Vh` is a finite

element space of degree 3 for vectorial functions (velocity), Q_h is a scalar function space of degree 2 (pression) and X_h a scalar space of degree 3 (temperature). Again this is seamless for the user with respect to parallel computing and quite expressive with respect to the mathematical formulation.

Finally we add the contribution of the non-linear terms to the jacobian. The main operations required to this update are showed in Listing 3. We remark that for a given μ the linear part of the jacobian stored in J_{lin} does not need to be updated, its implementation is computed once for all using the code displayed in Listing 2.

LISTING 3. Non-linear terms assembly in jacobian

```
void Convection::updateJacobian( const vector_ptrtype& X, sparse_matrix_ptrtype& J)
{
    //Definition of mesh and FE space Xh, and definition of functions
    //are done in the same way as previously

    Aq[3][0]->zero(); // initialization

    // 1) Fluid equations - fluid convection derivatives:
    //   Aq[3] += u^T*A + A*u = \int_{\Omega}(u \cdot \nabla \cdot v_i v_j + v_i \cdot \nabla \cdot u v_j)
    form2( _test=Xh, _trial=Xh, _matrix=Aq[3] ) +=
        integrate ( _range=elements(mesh), trans( id(v) )*( gradv(u) )*idt(u) );
    form2( _test=Xh, _trial=Xh, _matrix=Aq[3] ) +=
        integrate ( _range=elements(mesh), trans( id(v) )*( gradt(u) )*idv(u) );

    // 2) Temperature equation - heat convection:
    //   Aq[3] += u^T*E + E*T = \int_{\Omega}(u \cdot \nabla(s_i)s_j + u_i \cdot \nabla(T)s_j)
    form2( _test=Xh, _trial=Xh, _matrix=Aq[3] ) +=
        integrate ( elements(mesh), grad(s)*( idv(t)*idt(u) ) );
    form2( _test=Xh, _trial=Xh, _matrix=Aq[3] ) +=
        integrate ( elements(mesh), grad(s)*( idt(t)*idv(u) ) );

    // B.C. ...

    // Jacobian = linear terms of Affine Decomposition + Nonlinear term Aq[3]
    J->zero(); J->addMatrix(1.,Jlin); J->addMatrix(1.,Aq[3]);
}

```

5. NUMERICAL EXPERIMENTS

We present some numerical results: first we compare flow profiles obtained using FEM and RBM, and associated errors, in both 2D and 3D cases. Then, computational times and performances varying model parameters are shown in both FEM and CRB cases. Finally, we compare the average temperature obtained in both cases.

Thanks to the FEEL++ framework, the finite element and reduced basis models are available both in 2D and 3D.

Regarding the 2D case the FEM simulations refer to 6×10^4 degrees of freedom while in the 3D tank we have more than 2×10^4 dof. We consider polynomial basis functions of degree 3 for velocity and temperature variables, and degree 2 for pressure variable. Continuation algorithm (see Algorithm 1) is not used for FEM simulation and RBM as well, a simple Newton Method without parameters continuation is run. The RB used for all results presented here contains 28 elements non orthonormalized. The basis functions are solutions of the FE problem evaluated for Prandtl number fixed to 1 while Grashof number varies randomly from 1 to 10^6 . The parameter varies according to an uniform distribution law, better solutions could be obtained with some a posteriori error estimators. Each 2D simulation is run in parallel on 10 processors, whereas each 3D simulation

is run on 24 processors. In the 2D case we use the solver GMRES and the Additive Schwarz Method (GASM) as preconditioner, whereas the preconditioner LU is used in the 3D case.

5.1. Flow profiles

First we look at the solutions obtained with RBM and compare them with the FEM ones. We investigate the relative error between the two resolutions for increased turbulent flow, *i.e.* high parameters.

Figure 3 shows 2D results for different Grashof values (1, 10^3 , 10^5). On the left there are RBM solutions, we show the velocity magnitude (top) and temperature (bottom) profiles. We observe faster flow for increased Grashof values as expected. On the right, relative errors for velocity (top) and temperature (bottom) are shown. As the flow is more turbulent for increasing parameters, the relative errors increase as well. Furthermore, errors are at least 2×10^{-3} for velocity magnitude and 10^{-2} for temperature profile, which are satisfactory values (we do not consider values for $Gr = 1$ because of it corresponds to a parameter used to build the basis, the error is as expected 10^{-16}).

We analyze the error in 2D and 3D simulations, respectively Figures 5(c) and 6(c), increasing Grashof values. We observe in both cases that the error increases for Grashof between 1 and 10^3 and it stabilizes for values greater than 10^3 . Also, we remark that the solution in a finite 3D tank for high Grashof value represents a flow with a complex pattern (Figure 4).

5.2. Performances

We now compare the RBM computational gain with respect to FEM. Figures 5(b) and 6(b) show the computational times for increased Grashof in both FEM and RBM cases, respectively in the 2D and 3D tanks. In both cases, we show the log-log plot of the computational times (in seconds) vs Gr .

As expected the FEM solution costs is several order more expensive than the RBM one. In particular, we have a factor 6×10^2 for small Grashof and we reach a factor 1.5×10^3 for high Grashof in 2D case, and a factor from 10^3 to 10^4 occurs in 3D case. Furthermore, we observe that the computational time increases in parameters in the case of FEM, while it is almost constant in RBM computations. In both 2D and 3D cases we find few parameters that lead to a higher computational time in RB, this is due to increased number of online Newton iterations, however it still yield good results when inspecting the average temperature, see Figure 5(a) and Figure 6(a).

In Figures 5(b) and 6(b), the computational time comparison between FEM and RBM does not include the offline step of the RBM. The offline step cost is not included in the computational time comparison. If we include the offline cost in the comparison, the RB method becomes competitive for a number of queries slightly greater than the dimension N of the RB space since the cost of the reduction computation are not marginal, in particular it scales as N^3 due to the non-linear terms.

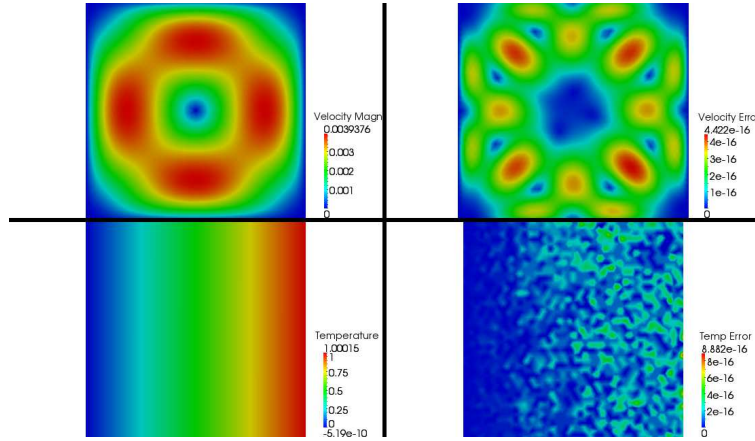
We remark that we do not apply the continuation algorithm neither for FEM nor for RBM. However it may become necessary for FEM resolution in case of non-convergence of the Newton solver, for higher parameter values or more complex geometry. As initial guess of the Newton Algorithm used to solve the online RB problems, the nearest known solution is used, whereas in FEM the initial guess is taken as the zero — although we could also use the nearest basis function as initial guess.

5.3. Outputs

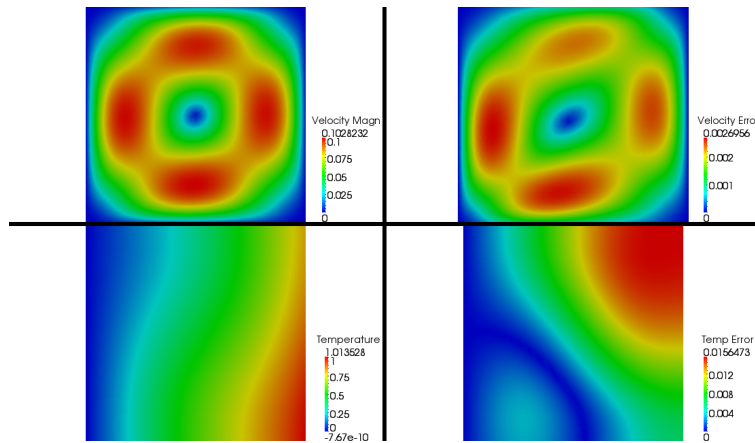
To conclude we look at the average temperature on boundary $\Gamma_3 = \bar{\Omega} \cap \{x = 1\}$ (see Figure 1 for the 2D tank)

$$T_{\text{av}} = \int_{\Gamma_3} T d\sigma. \quad (43)$$

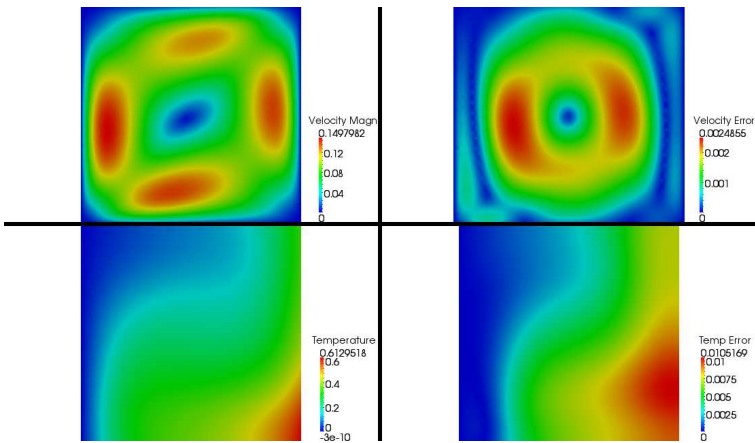
This quantity decreases with increasing Grashof because of faster fluid flows that remove the heat for Γ_3 . In Figures 5(a) and 6(a), respectively 2D and 3D cases, the logarithmic output curves show that the RBM solutions follow the same behavior as in the FEM case. These results confirm the good approximation obtained with RBM in both 2D and 3D simulations.



(a) $Gr=1.e+00$

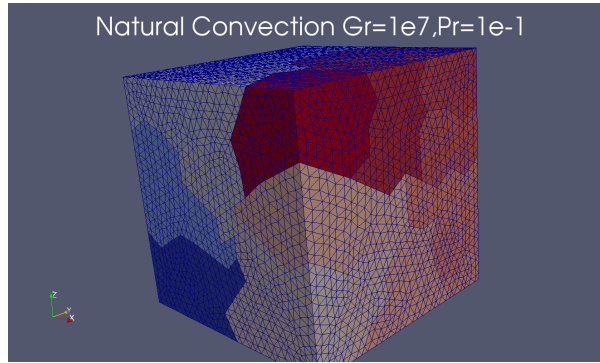


(b) $Gr=1.e+03$

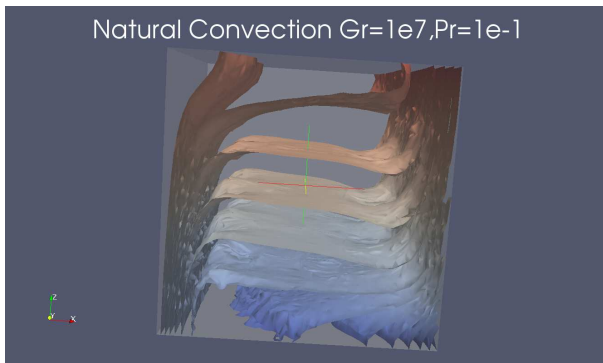


(c) $Gr=1.e+05$

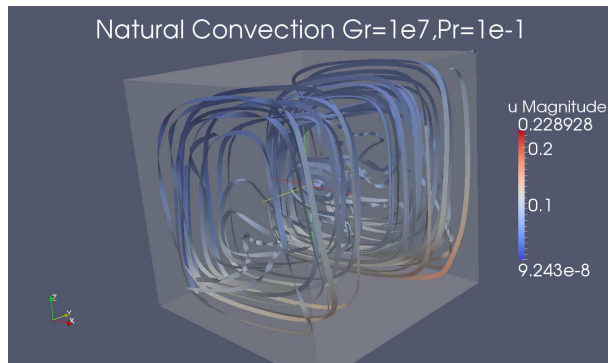
FIGURE 3. Comparisons of FEM and RBM solutions for $Gr = (1, 10^3, 10^5)$ and $Pr = 1$. On the left velocity flow magnitude (top) and temperature profile (bottom) for RBM solutions. On the right velocity error (top) and temperature error (bottom).



(a) mesh partitioning (24 processors)

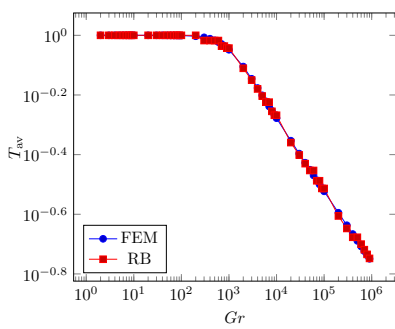


(b) temperature isosurfaces

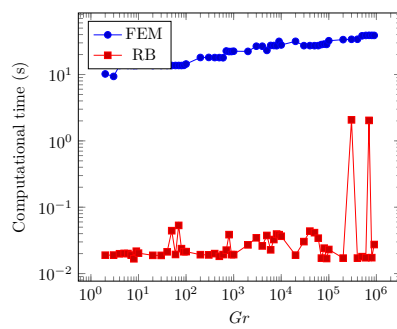


(c) Stream lines

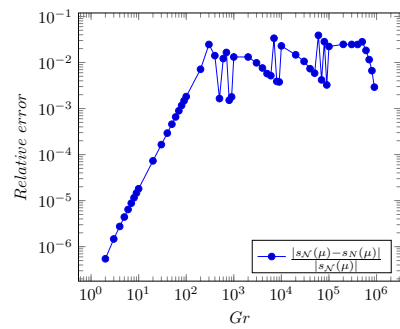
FIGURE 4. 3D computations for $Gr = 1e7, Pr = 0.1$



(a) T_{av} versus Gr

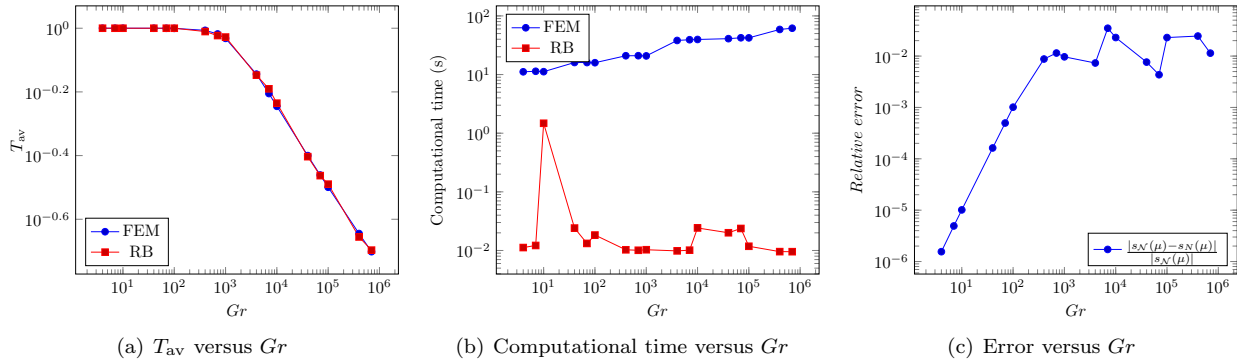


(b) Computational time versus Gr



(c) Error versus Gr

FIGURE 5. 2D computations for $Gr \in [1; 1e6], Pr = 1$.

FIGURE 6. 3D computations for $Gr \in [1; 1e6]$, $Pr = 1$.

6. CONCLUSIONS AND PERSPECTIVES

We have presented a mathematical and computational treatment of the RBM applied to steady-state natural convection. This can be readily applied to other types of problems with quadratic non-linearities. The proposed method gives results that are accurate and efficient. In particular, the efficiency of this technique is remarkable in the case of flows with complex patterns both in 2D and 3D. From a framework point of view, the (offline) database handling raises interesting challenges when dealing with large parallel data.

In terms of perspectives, a posteriori error estimation is a first step not only to assess the quality of the RB approximation but also to guide the RB space construction using greedy strategies [VP05, Yan12, VPRP03]. More complex applications can be considered in particular including geometrical parameters. However it is foreseen that we may require hp-RBM approximations, see *e.g.* [EHKP12]. Finally, we dealt with the steady-state of the natural convection flow, the transient state is also of interest but requires much more involved mathematical and computational framework, see *e.g.* [Yan12].

ACKNOWLEDGEMENTS

The authors wish to thank Vincent Chabannes, Ranine Tarabay and Céline Caldini-Queiros for fruitful discussions during the Cemracs 2012. Stéphane Veys and Christophe Prud'homme acknowledge the financial support of the project ANR HAMM ANR-2010-COSI-009. Finally the authors wish to thank the Cemracs 2012 and its organizers.

REFERENCES

- [ADL00] P.R. Amestoy, I.S. Duff, and J.-Y. L'Excellent. Multifrontal parallel distributed symmetric and unsymmetric solvers. *Computer Methods in Applied Mechanics and Engineering*, 184(2-4):501 – 520, 2000.
- [BBB⁺12] S. Balay, J. Brown, K. Buschelman, W. D. Gropp, D. Kaushik, M. G. Knepley, L. Curfman McInnes, B. F. Smith, and H. Zhang. PETSc Web page. <http://www.mcs.anl.gov/petsc>, 2012.
- [BBE⁺12] S. Balay, K. Buschelman, V. Eijkhout, W. Gropp, D. Kaushik, M. Knepley, L. C. McInnes, B. Smith, and H. Zhang. PETSc Users Manual, 2012.
- [BGCMS97] S. Balay, W. D. Gropp, L. Curfman McInnes, and B. F. Smith. *Efficient Management of Parallelism in Object Oriented Numerical Software Libraries*, 1997.
- [Cha13] Vincent Chabannes. *Vers la simulation des écoulements sanguins*. PhD thesis, Université Joseph Fourier, Grenoble, July 2013.
- [DVTP13] C. Daversin, S. Veys, C. Trophime, and C. Prud'Homme. A reduced basis framework: Application to large scale nonlinear multi-physics problems. *ESAIM: PROCEEDINGS*, 43:225–254, 2013.
- [EHKP12] J.L. Eftang, D.B.P. Huynh, D.J. Knezevic, and A.T. Patera. A two-step certified reduced basis method. *Journal of Scientific Computing*, 51:28–58, 2012.

- [GR09] C. Geuzaine and J.-F. Remacle. Gmsh: a three-dimensional finite element mesh generator with built-in pre-and post-processing facilities. *International Journal for Numerical Methods*, 79(11):1309–1331, 2009.
- [PCD⁺12] C. Prud'homme, V. Chabannes, V. Doyeux, M. Ismail, A. Samake, and G. Pena. Feel++: A computational framework for galerkin methods and advanced numerical methods. In *ESAIM: PROCEEDINGS*, pages 1–10, 2012.
- [PP04] C. Prud'homme and A.T. Patera. Reduced-basis output bounds for approximately parameterized elliptic coercive partial differential equations. *Computing and Visualization in Science*, 6(2-3):147–162, 2004.
- [Pru06] C. Prud'homme. A domain specific embedded language in C++ for automatic differentiation, projection, integration and variational formulations. *Scientific Programming*, 14(2):81-110, 2006.
- [PRV⁺02] C. Prud'homme, D. V. Rovas, K. Veroy, L. Machiels, Y. Maday, A. T. Patera, and G. Turinici. Reliable real-time solution of parametrized partial differential equations: Reduced-basis output bound methods. *Journal of Fluids Engineering*, 124(1):70–80, 2002.
- [QRM11] A. Quarteroni, G. Rozza, and A. Manzoni. Certified reduced basis approximation for parametrized partial differential equations and applications. *Journal of Mathematics in Industry*, 1(1):1–49, 2011.
- [RHP07] G. Rozza, D.B.P. Huynh, and A.T. Patera. Reduced basis approximation and a posteriori error estimation for affinely parametrized elliptic coercive partial differential equations. *Archives of Computational Methods in Engineering*, 15(3):1–47, 2007.
- [SBG04] B. Smith, P. Bjorstad, and W. Gropp. *Domain decomposition: parallel multilevel methods for elliptic partial differential equations*. Cambridge University Press, 2004.
- [VCD⁺12] S. Veys, R. Chakir, C. Daversin, C. Prud'homme, and C. Trophime. A computational framework for certified reduced basis methods: application to a multiphysics problem. In *Conference Record of the 6th European Congress on Computational Methods in Applied Sciences and Engineering*, 2012.
- [VDPT12] S. Veys, C. Daversin, C. Prud'homme, and C. Trophime. Reduced order modeling of high magnetic field magnets. In *Conference Record of the 11th International Workshop on Finite Elements for Microwave Engineering*, 2012.
- [VP05] K. Veroy and A.T. Patera. Certified real-time solution of the parametrized steady incompressible navier-stokes equations: Rigorous reduced-basis a posteriori error bounds. *Int. J. Numer. Meth. Fluids*, 47:773–788, 2005.
- [VPP03] K. Veroy, C. Prud'homme, and A.T. Patera. Reduced-basis approximation of the viscous Burgers equation: Rigorous a posteriori error bounds. *C. R. Acad. Sci. Paris, Série I*, 337(9):619–624, November 2003.
- [VPRP03] K. Veroy, C. Prud'homme, D. V. Rovas, and A.T. Patera. A posteriori error bounds for reduced-basis approximation of parametrized noncoercive and nonlinear elliptic partial differential equations (AIAA Paper 2003-3847). In *Proceedings of the 16th AIAA Computational Fluid Dynamics Conference*, June 2003.
- [Yan12] Masayuki Yano. A space-time Petrov-Galerkin certified reduced basis method : Application to the boussinesq equations. Submitted to *SIAM Journal on Scientific Computing*, December 2012.

Bibliography

- [AANQ11] D. Ambrosi, G. Arioli, F. Nobile, and A. Quarteroni. Electromechanical coupling in cardiac dynamics: the active strain approach. *SIAM Journal on Applied Mathematics*, 71(2):605–621, 2011.
- [AF08] D. Amsallem and C. Farhat. Interpolation method for adapting reduced-order models and application to aeroelasticity. *AIAA journal*, 46(7):1803–1813, 2008.
- [Alp] Mete Alpaslan. doctorecg.com.
- [BCF⁺10] M. Boulakia, S. Cazeau, M.A. Fernández, J.-F. Gerbeau, and N. Zemzemi. Mathematical modeling of electrocardiograms: a numerical study. *Annals of Biomedical Engineering*, 38(3):1071–1097, 2010.
- [BCP09] Y. Bourgault, Y. Coudière, and C. Pierre. Existence and uniqueness of the solution for the bidomain model used in cardiac electrophysiology. *Nonlinear Analysis-Real World Applications*, 10(1):458–482, 2009.
- [BdLGVn⁺99] A. Bayés de Luna, J. Guindo, X Viñolas, A. Martinez-Rubio, R. Oter, and Bayés-Genís A. Third-degree inter-atrial block and supraventricular tachyarrhythmias. *Eurospace*, 1:43–46, 1999.
- [BdLPC⁺12] A. Bayés de Luna, P. Platonov, F. G. Cosio, I. Cygankiewicz, C. Pastore, R Baranowski, A. Bayés-Genis, J. Guindo, X Viñolas, J. Garcia-Niebla, R. Barbosa, S. Stern, and D. Spodick. Interatrial blocks. A separate entity from left atrial enlargement: a consensus report. *Journal of Electrocardiology*, 45(5):445–451, 2012.
- [Ben71] A. Bensoussan. *Filtrage optimal des système linéaires*. Dunod, 1971.
- [BG11] M. Boulakia and J.-F. Gerbeau. Parameter identification in cardiac electrophysiology using Proper Orthogonal Decomposition method. *Lecture Notes in Computer Science*, 6666:315–322, 2011. FIMH 2011, New York, USA.
- [BMNP04] M. Barrault, Y. Maday, N. C. Nguyen, and A. T. Patera. An “empirical interpolation” method: Application to efficient reduced-basis discretization of partial differential equations. *C. R. Math. Acad. Sci. Paris*, 339:667–672, 2004.

- [BOCF08] A. Bueno-Orovio, E. M. Cherry, and F. H. Fenton. Minimal model for human ventricular action potentials in tissue. *Journal of Theoretical Biology*, 253:544–560, 2008.
- [BP84] R. C. Barr and R. Plonsey. Propagation of excitation in idealized anisotropic two-dimensional tissue. *Biophysical Journal*, 45:1191–1202, 1984.
- [BP03] M. L. Buist and A. J. Pullan. The effect of torso impedance on epicardial and body surface potentials: A modeling study. *IEEE Trans. Biomed. Eng.*, 50(7):816 – 824, 2003.
- [BRS77] R.C. Barr, M. Ramsey, and M.S. Spach. Relating epicardial to body surface potential distributions by means of transfer coefficients based on geometry measurements. *Biomedical Engineering, IEEE Transactions on*, 24(1):1–11, 1977.
- [BSG12] M. Boulakia, E. Schenone, and J.-F. Gerbeau. Reduced-order modeling for cardiac electrophysiology. Application to parameter identification. *International Journal for Numerical Methods in Biomedical Engineering*, 28:727–744, 2012.
- [BTR00] J. E. Burnes, B. Taccardi, and Y. Rudy. A noninvasive imaging modality for cardiac arrhythmias. *Circulation*, 102(17):2152–2158, 2000.
- [CBMF11] K. Carlberg, C. Bou-Mosleh, and C. Farhat. Efficient non-linear model reduction via a least-squares Petrov–Galerkin projection and compressive tensor approximations. *International Journal for Numerical Methods in Engineering*, 86(2):155–181, 2011.
- [CCG12] D. Chapelle, A. Collin, and J.-F. Gerbeau. A surface-based electrophysiology model relying on asymptotic analysis and motivated by cardiac atria modeling. *M3AS*, 2012. In press, <http://hal.inria.fr/hal-00723691/en>.
- [CF11] K. Carlberg and C. Farhat. A low-cost, goal-oriented ‘compact proper orthogonal decomposition’ basis for model reduction of static systems. *International Journal for Numerical Methods in Engineering*, 86(3):381–402, 2011.
- [CFCV⁺82] P. Colli-Franzone, L. Cuerci, C. Viganotti, S. Macchi, E. Baruffi, S Spaggiari, and B. Taccardi. Potential fields generated by oblique dipole layers modeling excitation wavefronts in the anisotropic myocardium. *Circulation Research*, 51:330–346, 1982.

- [CFG93] P. Colli Franzone and L. Guerri. Spreading of activation in 3-d models of the anisotropic cardiac tissue: I Validation of the Eikonal model. *Mathematical Bioscience*, 113:145–209, 1993.
- [CFG⁺09] D. Chapelle, M. A. Fernández, J.-F. Gerbeau, P. Moireau, J. Sainte-Marie, and N. Zenzemi. Numerical Simulation of the Electromechanical Activity of the Heart. In *Functional Imaging and Modeling of the Heart*, number 5528 in Lecture Notes in Computer Science, pages 357–365. Springer-Verlag, 2009.
- [CFGR90] P. Colli Franzone, L. Guerri, and S. Rovida. Wavefront propagation in an activation model of the anisotropic cardiac tissue: asymptotic analysis and numerical simulations. *Journal of Mathematical biology*, 28:121–176, 1990.
- [CFP04] P. Colli Franzone and L.F. Pavarino. A parallel solver for reaction-diffusion systems in computational electrocardiology. *Mathematical Models and Methods in Applied Sciences*, 14(6):883–911, 2004.
- [CFPT05] P. Colli Franzone, L.F. Pavarino, and B. Taccardi. Simulating patterns of excitation, repolarization and action potential duration with cardiac Bidomain and Monodomain models. *Mathematical Biosciences*, 197(1):35–66, 2005.
- [CGH⁺13] A. Collin, J.-F. Gerbeau, M. Hocini, M. Haïssaguerre, and D. Chapelle. Surface-based electrophysiology modeling and assessment of physiological simulations in atria. *FIMH*, 7945:352–359, 2013.
- [CHZ13a] M. Cheng, T.Y. Hou, and Z. Zhang. A dynamically bi-orthogonal method for time-dependent stochastic partial differential equations I: Derivation and algorithms. *Journal of Computational Physics*, 242:843–868, 2013.
- [CHZ13b] M. Cheng, T.Y. Hou, and Z. Zhang. A dynamically bi-orthogonal method for time-dependent stochastic partial differential equations II: Adaptivity and generalizations. *Journal of Computational Physics*, 242:753–776, 2013.
- [CM07] K. Chatterjee and B. Massie. Systolic and Diastolic Heart Failure: Differences and Similarities. *Journal of Cardiac Failure*, 13(7):569–576, 2007.
- [Col14] Aannabelle Collin. *Analyse Asymptotique en Électrophysiologie Cardiaque. Applications à la modélisation et à l’assimilation de données*. PhD thesis, Université Pierre et Maire Curie, 2014.
- [CRN98] M. Courtemanche, R.J. Ramirez, and S. Nattel. Ionic mechanisms underlying human atrial action potential properties: insights from

- a mathematical model. *American Journal of Physiology-Heart and Circulatory Physiology*, 44(1):H301–H321, 1998.
- [CS10a] S. Cagnoni and S. Smith. *Medical Applications of Genetic and Evolutionary Computation*. Chapter *How Genetic Algorithms can improve a pacemaker efficiency*. John Wiley and Sons, 2010.
- [CS10b] S. Chaturantabut and D. Sorensen. Nonlinear model reduction via discrete empirical interpolation. *SIAM Journal of Scientific Computing*, 32(5):2737–2764, 2010.
- [CS12] S. Chaturantabut and D. Sorensen. A state space error estimate for POD-DEIM nonlinear model reduction. *SIAM Journal of Numerical Analysis*, 50(1):46–63, 2012.
- [CSRZ14] F. W. Chaves-Silva, L. Rosier, and E. Zuazua. Null controllability of a system of viscoelasticity with a moving control. *Journal de Mathématiques Pures et Appliquées*, 1(2):198–222, 2014.
- [CWS⁺95] G.I. Cohen, M. White, R.A. Sochowski, A.Z. Klein, P.D. Bridge, W.J. Steward, and K.L. Chang. Reference values for normal adult transesophageal echocardiographic measurements. *Journal of the American Society of Echocardiography*, 8(3):221–230, 1995.
- [DEA07] L. Dumas and L. El Alaoui. How genetic algorithms can improve a pacemaker efficiency. *Proceedings of GECCO 2007, London, England UK*, 2007.
- [DGSJ12] D. Deng, Y. Gong, G. Shou, and P. Jiao. Simulation of biatrial conduction via different pathways during sinus rhythm with a detailed human atrial model. *Journal of Zhejiang University-SCIENCE B (Biomedicine and Biotechnology)*, pages 1862–1783, 2012.
- [DR86] J. P. Drouhard and F. A. Roberge. Revised formulation of the Hodgkin–Huxley representation of the sodium current in cardiac cells. *Comput., Biomed. Res.*, 20:333–350, 1986.
- [DR09] S. Deparis and G. Rozza. Reduced basis method for multi-parameter-dependent steady Navier–Stokes equations: applications to natural convection in a cavity. *Journal of Computational Physics*, 228(12):4359–4378, 2009.
- [Dub00] D. Dubin. *Rapid Interpretation of EKGs: An interactive course*. Cover Publishing Company, 2000.
- [ERBL⁺10] D.B. Ennis, G.R. Rudd-Barnard, B. Li, C.G. Fonseca, A.A. Young, Cowan B.R., and R.A. Stewart. Changes in Mitral Annular Geometry and Dynamics with β -Blockade in Patients with Degenerative Mitral Valve Disease. *Circulation cardiovascular imaging*, 3(6):687–693, 2010.

- [Eve09] G. Evensen. *Data Assimilation: The Ensemble Kalman Filter*. Springer, 2009.
- [EY36] G. Eckart and G. Young. The approximation of one matrix by another of lower rank. *Psychometrika*, 1:211–218, 1936.
- [FGHO97] R. D. Fierro, G. H. Golub, P. C. Hansen, and D. P. O’leary. Regularization by truncated total least squares. *SIAM J. Sci. Comput.*, 18(4):1223–1241, 1997.
- [FI96] A.V. Fursikov and O.Yu. Imanuvilov. Controllability of Evolution Equations. Volume 34 of *Lecture Notes Series*. Seoul National University Research Institute of Mathematics Global Analysis Research Center, Seoul, 1996.
- [Fit61] R. Fitzhugh. Impulses and physiological states in theoretical models of nerve membrane. *Biophys. J.*, 1:445–465, 1961.
- [Fre01] P. Frey. Yams: A fully Automatic Adaptive Isotropic Surface Remeshing Procedure. Technical report 0252, Inria, Rocquencourt, France, Nov. 2001.
- [Fye94] W. Bruce Fye. A History of the Origin, Evolution and Impact of Electrocardiology. *The American Journal of Cardiology*, 73(13), 1994.
- [GH98] F. Greensite and G. Huiskamp. An improved method for estimating epicardial potentials from the body surface. *Biomedical Engineering, IEEE Transactions on*, 45(1):98–104, 1998.
- [Ghi71] M. Ghil. Meteorological data assimilation for oceanographers. Part I: description and theoretical framework. *Dyn. Atmos. Oceans*, 13:171–218, 1971.
- [GI13] S. Guerrero and O. Yu. Imanuvilov. Remarks on non controllability of the heat equation with memory. *ESAIM: Control, Optimization and Calculus of Variations*, 19:288–300, 2013.
- [GJ96] S. Gerred and D. Jenkins. ECG library, 1996.
- [GL14] J.-F. Gerbeau and D. Lombardi. Approximated Lax Pairs for the Reduced Order Integration of Nonlinear Evolution Equations. *Journal of Computational Physics*, 265:246–269, 2014.
- [GPF⁺04] Y. Goletsis, C. Papaloukas, D.I. Fotiadis, A. Likas, and L.K. Michalis. Automated ischemic beat classification using genetic algorithms and multicriteria decision analysis. *Trans. Biomed. Eng.*, 51(10):1717–1725, 2004.

- [GR09] C. Geuzaine and J.-F. Remacle. Gmsh: A 3-D finite element mesh generator with built-in pre-and post-processing facilities. *International Journal for Numerical Methods in Engineering*, 79(11):1309–1331, 2009.
- [GRS84] R. M. Gulrajani, F. A. Roberge, and P. Savard. Moving dipole inverse ECG and EEG solutions. *Biomedical Engineering, IEEE Transactions on*, (12):903–910, 1984.
- [Har90] S. B. Harris. The Society for the Recovery of Persons Apparently Dead. *Cryonics*, September 1990.
- [HASQ02] S.Y. Ho, R.H. Anderson, and D. Sánchez-Quintana. Atrial structure and fibres: morphologic bases of atrial conduction. *Cardiovascular Research*, 54(2):325–336, 2002.
- [HC00] D.M. Harrild and S.H. Craig. A computer model of normal conduction in the human atria. *Circulation Research*, 87(7):e25–e36, 2000.
- [HG97] G. Huiskamp and F. Greensite. A New Method for Myocardial Activation Imaging. *IEEE Trans. Biomed. Eng.*, 44(6):433–446, 1997.
- [HH52] A. L. Hodgkin and A. F. Huxley. A quantitative description of membrane current and its application to conduction and excitation in nerve. *Journal of Physiology*, 117(4):500–544, 1952.
- [HK14] D. E. Hurtadoa and E. Kuhl. Computational modelling of electrocardiograms: repolarisation and T-wave polarity in the human heart. *Computer Methods in Biomechanics and Biomedical Engineering*, 17(9):986–996, 2014.
- [HKB13] K. C. Hoang, P. Kerfriden, and S. Bordas. A goal-oriented reduced basis method for the wave equation in inverse analysis. *arXiv preprint arXiv:1305.3519*, 2013.
- [HLB96] P. Holmes, J.L. Lumley, and G. Berkooz. *Turbulence, coherent structures, dynamical systems and symmetry*. Cambridge University Press, 1st edition, 1996.
- [HP10] E. Hand and C. S. Peskin. Homogenization of an electrophysiological model for a strand of cardiac myocytes with gap-junctional and electric-field coupling. *Bulletin of Mathematical Biology*, 72:1408–1424, 2010.
- [HPF⁺05] L.E. Hudsmith, S.E. Petersen, J.M. Francis, M.D. Robson, and S. Neubauer. Normal human left and right ventricular and left atrial dimensions using steady state free precession magnetic resonance imaging. *Journal of cardiovascular magnetic resonance*, 7(5):775–782, 2005.

- [HSQ09] S.Y. Ho and D. Sanchez-Quintana. The Importance of Atrial Structure and Fibers. *Clinical Anatomy*, 22(1):52–63, 2009.
- [Hui98] G. Huiskamp. Simulation of depolarization in a membrane-equations-based model of the anisotropic ventricle. *Biomedical Engineering, IEEE Transactions on*, 45(7):847–855, 1998.
- [HUvO99] R. Hoekema, G. J. Uijen, and A. van Oosterom. On Selecting a Body Surface Mapping Procedure. *Journal of Electrocardiology*, 32(2):93–101, 1999.
- [Ima95] O. Yu. Imanuvilov. Controllability of parabolic equations. *Mat. Sb.*, 186:109–132, 1995.
- [JHR⁺08] P. Jiamsripong, T. Honda, C.S. Reuss, R.T. Hurst, H.P. Chaliki, D.E. Grill, S.L. Schneck, R. Tyler, B.K. Khandheria, and S.J. Lester. Three methods for evaluation of left atrial volume. *European Journal of Echocardiography*, 9(3):351–355, 2008.
- [JU97] S. J. Julier and J. K. Uhlmann. A new extension of the Kalman filter to nonlinear systems. In *Proc. of AeroSense: The 11th Int. Symp. on Aerospace/Defence Sensing, Simulation and Controls*, 1997.
- [JW07] R.A. Johnson and D.W. Wichern. *Applied Multivariate Statistical Analysis*. Pearson Education, sixth edition, 2007.
- [JXS⁺08] M. Jiang, L. Xia, G. Shou, F. Liu, and S. Crozier. Two hybrid regularization frameworks for solving the electrocardiography inverse problem. *Physics in Medicine and Biology*, 53(18):5151, 2008.
- [KB61] R. Kalman and R. Bucy. New results in linear filtering and prediction theory. *Trans. ASME J. Basic. Eng.*, 83:95–108, 1961.
- [Kee91] J.P. Keener. An Eikonal-curvature equation for action potential propagation in myocardium. *Journal of mathematical biology*, 29(7):629–651, 1991.
- [KGAB11] P. Kerfriden, P. Gosselet, S. Adhikari, and S. P.-A. Bordas. Bridging proper orthogonal decomposition methods and augmented Newton–Krylov algorithms: an adaptive model order reduction for highly nonlinear mechanical problems. *Computer Methods in Applied Mechanics and Engineering*, 200(5):850–866, 2011.
- [KL07] O. Koch and C. Lubich. Dynamical low rank approximation. *SIAM Journal of Matrix Analysis and Applications*, 29:435–454, 2007.
- [KST⁺11] M. Krueger, V. Schmidt, C. Tobón, F. Weber, C. Lorenz, D. Keller, H. Barschdorf, M. Burdumy, P. Neher, G. Plank, K. Rhode, G. Seemann, D. Sanchez-Quintana, J. Saiz, R. Razavi, and O. Dössel.

- Modeling atrial fiber orientation in patient-specific geometries: a semi-automatic rule-based approach. *Functional Imaging and Modeling of the Heart*, pages 223–232, 2011.
- [KSW⁺07] D. Keller, G. Seemann, D. Weiss, D. Farina, J. Zehelein, and O. Dössel. Computer based modeling of the congenital long-QT 2 syndrome in the Visible Man torso: From genes to ECG. In *Engineering in Medicine and Biology Society, 2007. EMBS 2007. 29th Annual International Conference of the IEEE*, pages 1410–1413, 2007.
- [KV01] K. Kunisch and S. Volkwein. Galerkin proper orthogonal decomposition methods for parabolic problems. *Numerische Mathematik*, 90(1):117–148, 2001.
- [KVX04] K. Kunisch, S. Volkwein, and L. Xie. HJB-POD-based feedback design for the optimal control of evolution problems. *Journal on Applied Dynamical Systems*, 3(4):701–722, 2004.
- [Lax68] P. D. Lax. Integrals of nonlinear equations of evolution and solitary waves. *Comm. Pure Appl. Math.*, 21:467–490, 1968.
- [LBG⁺03] G. T. Lines, M. L. Buist, P. Grottum, A. J. Pullan, J. Sundnes, and A. Tveito. Mathematical models and numerical methods for the forward problem in cardiac electrophysiology. *Comput. Visual. Sci.*, 5(4):215–239, 2003.
- [LLH06] Z. Liu, C. Liu, and B. He. Noninvasive reconstruction of three-dimensional ventricular activation sequence from the inverse solution of distributed equivalent current density. *Medical Imaging, IEEE Transactions on*, 25(10):1307–1318, 2006.
- [LR94] C.H. Luo and Y. Rudy. A dynamic model of the cardiac ventricular action potential. I. Simulations of ionic currents and concentration changes. *Circulation Research*, 74:1071–1096, 1994.
- [Lue63] D. G. Luenberger. *Determining the State of a Linear with Observers of Low Dynamic Order*. PhD thesis, Stanford University, 1963.
- [Lue71] D. G. Luenberger. An introduction to observers. *IEEE Transaction on Automatic Control*, 16:596–602, 1971.
- [Lum67] J. L. Lumley. The structure of inhomogeneous turbulence. *Atmospheric turbulence and radio wave propagation*, pages 166–178, 1967.
- [MdBV⁺96] M.A. McGuire, J.M. de Bakker, J.T. Vermeulen, Moorman A.F., P. Loh, B. Thibault, J.L. Vermeulen, A.E. Becker, and M.J. Janse. Atrioventricular Junctional Tissue, Discrepancy Between Histological and Electrophysiological Characteristics. *Circulation*, 94(3):571–577, 1996.

- [MDFG12] V. Martin, A. Drochon, O. Fokapu, and J-F. Gerbeau. Magneto-HemoDynamics in the Aorta and Electrocardiograms. *Physics in Medicine and Biology*, 57:3177–3195, 2012.
- [MEA] Microelectrode Array (MEA) Manual.
- [MIG78a] W. T. Miller III and D. B. Geselowitz. Simulation studies of the electrocardiogram. I. The normal heart. *Journal of The American Heart Association*, 43:315–323, 1978.
- [MIG78b] W. T. Miller III and D. B. Geselowitz. Simulation studies of the electrocardiogram. II. Ischemia and Infarction. *Journal of The American Heart Association*, 43:301–315, 1978.
- [MKI⁺77] D. M. Mirvis, F. W. Keller, R. E. Ideker, J.W. Cox, R. F. Dowdie, and D. G. Zettergren. Detection and localization of multiple epicardial electrical generators by a two-dipole ranging technique. *Circulation research*, 41(4):551–557, 1977.
- [MLW⁺09] S. Matsuo, N. Lellouche, M. Wright, M. Bevilacqua, S. Knecht, I. Nault, K.T. Lim, L. Arantes, M.D. O’Neill, P.G. Platonov, =. Carlson, J, F. Sacher, M. Hocini, P. Jaïs, and M. Haïssaguerre. Clinical Predictors of Termination and Clinical Outcome of Catheter Ablation for Persistent Atrial Fibrillation. *Journal of the American College of Cardiology*, 54(9):788–795, 2009.
- [MP95] J. Malmivuo and R. Plonsey. *Bioelectromagnetism - Principles and Applications of Bioelectric and Biomagnetic Fields*. Oxford University Press, 1995.
- [MPR02] Y. Maday, A. T. Patera, and D. V. Rovas. A blackbox reduced-basis output bound method for noncoercive linear problems. *Studies in Mathematics and its Applications*, 31:533–569, 2002.
- [MR02] Y. Maday and E.M. Rønquist. A reduced-basis element method. *Journal of scientific computing*, 17(1):447–459, 2002.
- [MRR88] B.J. Messinger-Rapport and Y. Rudy. Regularization of the inverse problem of electrocardiology: A model study. *Math. Biosci.*, 89:79–118, 1988.
- [MS03] C.C. Mitchell and D.G. Schaeffer. A two-current model for the dynamics of cardiac membrane. *Bulletin Math. Bio.*, 65:767–793, 2003.
- [MSM⁺04] B. Messnarz, M. Seger, R. Modre, G. Fischer, F. Hanser, and B. Tilg. A comparison of noninvasive reconstruction of epicardial versus transmembrane potentials in consideration of the null space. *Biomedical Engineering, IEEE Transactions on*, 51(9):1609–1618, 2004.

- [MTT11] F.H. Martini, M.J. Timmons, and R.B. Tallitsch. *Human anatomy*. Pearson Benjamin Cummings, sixth edition, 2011.
- [MZM⁺06] A. Manriquez, Q. Zhang, C. Medigue, Y. Papelier, and M. Sorine. Electrocardiogram-based restitution curve. *Computers in Cardiology*, pages 493–496, 2006.
- [NAY62] J.S. Nagumo, S. Arimoto, and S. Yoshizawa. An active pulse transmission line simulating nerve axon. *Proc. IRE*, 50(10):2061–2070, 1962.
- [NCL07] B.F. Nielsen, X. Cai, and M. Lysaker. On the possibility for computing the transmembrane potential in the heart with a one shot method: An inverse problem. *Mathematical biosciences*, 210(2):523–553, 2007.
- [Net69] F. H. Netter. *The Heart - The Netter collection of medical illustrations*, volume 5. Saunders Elsevier, 1969.
- [NH00] M.P. Nash and P.J. Hunter. Computational mechanics of the heart, from tissue structure to ventricular function. *Journal of elasticity and the physical science of solids*, 61:113–141, 2000.
- [NLT07] B. F. Nielsen, M. Lysaker, and A. Tveito. On the use of the resting potential and level set methods for identifying ischemic heart disease: An inverse problem. *Journal of Computational Physics*, 220(2):772–790, 2007.
- [Nob62] D. Noble. A modification of the Hodgkin-Huxley equation applicable to Purkinje fiber action and pacemaker potentials. *Journal of Physiology*, 160:317–352, 1962.
- [NP80] A. K. Noor and M. Peters. Reduced basis technique for non-linear analysis of structures. *AIAA Journal*, 18(4):455–462, 1980.
- [OR92] H. S. Oster and Y. Rudy. The use of temporal information in the regularization of the inverse problem of electrocardiography. *Biomedical Engineering, IEEE Transactions on*, 39(1):65–75, 1992.
- [OSTW82] J.A. Ormiston, P.M. Shah, C. Tei, and M. Wong. Size and motion of the mitral valve annulus in man. II. Abnormalities in mitral valve prolapse. *Circulation*, 65:113–120, 1982.
- [PBC05] A. J. Pullan, M. L. Buist, and L. K. Cheng. *Mathematically modelling the electrical activity of the heart*. World Scientific, 2005.
- [PBWB14] B. Peherstorfer, D. Butnaru, K. Willcox, and H.-J. Bungartz. Localized discrete empirical interpolation method. *SIAM Journal of Scientific Computing*, 36(1):A168–A192, 2014.

- [PCF⁺07] M. Potse, R. Coronel, S. Falcao, A.R. LeBlanc, and A. Vinet. The effect of lesion size and tissue remodeling on ST deviation in partial-thickness ischemia. *Heart Rhythm*, 4:200–106, 2007.
- [PCL07] M. Potse, R. Coronel, and A.R. LeBlanc. The role of extracellular potassium transport in computer models of ischemic zone. *Med Bio Eng Comput*, 45:1187–1199, 2007.
- [PDG03] M. Potse, B. Dubé, and R. M. Gulrajani. ECG simulations with realistic human membrane, heart, and torso models. In *Engineering in Medicine and Biology Society, 2003. Proceedings of the 25th Annual International Conference of the IEEE*, volume 1, pages 70–73, 2003.
- [PDV09] M. Potse, B. Dubé, and A. Vinet. Cardiac anisotropy in boundary-element models for the electrocardiogram. *Medical & biological engineering & computing*, 47(7):719–729, 2009.
- [PTH02] A.J. Pullan, K.A. Tomlinson, and P.J. Hunter. A finite element method for an Eikonal equation model of myocardial excitation wavefront propagation. *SIAM Journal on Applied Mathematics*, 63(1):324–350, 2002.
- [QXGW10] Z. Qu, Y. Xie, A. Garnkel, and J.N. Weiss. T-wave alternans and arrhythmogenesis in cardiac diseases. *Frontiers in physiology*, 1(154), 2010. art. 1.
- [RBAP⁺13] R. Ruiz-Baier, D. Ambrosi, S. Pezzuto, S. Rossi, and A. Quarteroni. Activation models for the numerical simulation of cardiac electromechanical interactions. In *Computer Models in Biomechanics*, pages 189–201. Springer, 2013.
- [RBKM99] M. H. Rosner, W. J. Jr. Brady, M. P. Kefer, and M. L. Martin. Electrocardiography in the patient with the Wolff-Parkinson-White syndrome: Diagnostic and initial therapeutic issues. *The American Journal of Emergency Medicine*, 17(7):705–714, 1999.
- [RHP07] G. Rozza, D.B.P. Huynh, and A.T. Patera. Reduced basis approximation and a posteriori error estimation for affinely parametrized elliptic coercive partial differential equations. *Archives of Computational Methods in Engineering*, 15:1–47, 2007.
- [RNPD09] G. Rozza, C.N. Nguyen, A.T. Patera, and S. Deparis. Reduced basis methods and a posteriori error estimators for heat transfer problems. In *ASME 2009 Heat Transfer Summer Conference collocated with the InterPACK09 and 3rd Energy Sustainability Conferences*, pages 753–762. American Society of Mechanical Engineers, 2009.

- [RP04] M. Rathinam and L.R. Petzold. A new look at proper orthogonal decomposition. *Journal on Numerical Analysis*, 41(5):1893–1925, 2004.
- [RVC12] D. Ryckelynck, F. Vincent, and S. Cantournet. Multidimensional a priori hyper-reduction of mechanical models involving internal variables. *Computer Methods in Applied Mechanics and Engineering*, 225:28–43, 2012.
- [Sac04] F.B. Sachse. *Computational Cardiology: Modeling of Anatomy, Electrophysiology and Mechanics*. Springer-Verlag, 2004.
- [Sim06] D. Simon. *Optimal State Estimation: Kalman, H^∞ , and Nonlinear Approaches*. Wiley-Interscience, 2006.
- [Sir89] L. Sirovich. Low dimensional description of complicated phenomena. *Contemporary Mathematics*, 99:277–305, 1989.
- [SLC⁺06] J. Sundnes, G.T. Lines, X. Cai, B.F. Nielsen, K.A. Mardal, and A. Tveito. *Computing the Electrical Activity in the Heart*, volume 1 of *Monographs in Computational Science and Engineering*. Springer-Verlag, 2006.
- [SLN⁺06] J. Sundnes, G. T. Lines, B. F. Nielsen, K.-A. Mardal, and A. Tveito. *Computing the Electrical Activity in the Heart*. Springer, 2006.
- [SMC⁺06] M. Sermesant, Ph. Moireau, O. Camara, J. Sainte-Marie, R. Andriantsimiavona, R. Cimrman, D.L. Hill, D. Chapelle, and R. Razavi. Cardiac function estimation from MRI using a heart model and data assimilation: advances and difficulties. *Med. Image Anal.*, 10(4):642–656, 2006.
- [SMLD13] S. Sovilj, R. Magjarević, N.H. Lovell, and S. Dokos. A Simplified 3D Model of Whole Heart Electrical Activity and 12-Lead ECG Generation. *Computational and Mathematical Methods in Medicine*, 2013.
- [SP09] T.P. Sapsis and Lermusiaux P.F.J. Dynamically orthogonal field equations for continuous stochastic dynamical systems. *Physica D*, 238:2347–2360, 2009.
- [SPM08] S. Scacchi, L.F. Pavarino, and I. Milano. Multilevel Schwarz and Multigrid Preconditioners for the Bidomain System. In *Domain Decomposition Methods in Science and Engineering XVII*, volume 60 of *Lecture Notes in Computational Science and Engineering*, pages 631–638. Springer Berlin Heidelberg, 2008.
- [Str79] D.D. Streeter. Gross morphology and fiber geometry of the heart. *Handbook Physiology, The cardiovascular system*, 1:61–112, 1979.

- [Tal97] O. Talagrand. Assimilation of observation, an Introduction. *Journal of the Met. Soc. of Japan*, 75(1B):191–209, 1997.
- [TD08] G. J. Tortora and B. H. Derrickson. *Principles of anatomy and physiology*. John Wiley & Sons, 2008.
- [TDP⁺04] M.-C. Trudel, B. Dubé, M. Potse, R.M. Gulrajani, and L.J. Leon. Simulation of QRST integral maps with a membrane-based computer heart model employing parallel processing. *IEEE Trans. Biomed. Eng.*, 51(8):1319–1329, 2004.
- [Tun78] L. Tung. *A bi-domain model for describing ischemic myocardial d-c potentials*. PhD thesis, Massachusetts Institute of Technology. Dept. of Electrical Engineering and Computer Science, 1978.
- [Ver08] A. Verhoeven. *Redundancy Reduction of IC Models by Multirate Time-Integration and Model Order Reduction*. PhD thesis, Departement of Mathematics and Computer Science, Eindhoven University of Technology, 2008.
- [VOH89] A. Van Oosterom and G. J. M. Huiskamp. The effect of torso inhomogeneities on body surface potentials quantified by using tailored geometry. *Journal of Electrocardiology*, 22:53–72, 1989.
- [WABI12] Z. Wang, I. Akhtar, J. Borggaard, and T. Iliescu. Proper orthogonal decomposition closure models for turbulent flows: a numerical comparison. *Computer Methods in Applied Mechanics and Engineering*, 237:10–26, 2012.
- [War75] F. Wartak. *Electrocardiogram interpretation*. Medical Education Systems, 1975.
- [Wik14a] Wikipedia. Galvanometer — Wikipedia, the free encyclopedia, 2014. [Online; accessed 10-August-2014].
- [Wik14b] Wikipedia. Passions of the soul — Wikipedia, the free encyclopedia, 2014. [Online; accessed 10-August-2014].
- [Wik14c] Wikipedia. String galvanometer — Wikipedia, the free encyclopedia, 2014. [Online; accessed 10-August-2014].
- [WKJ11] D. Wang, R. M. Kirby, and C. R. Johnson. Finite-element-based discretization and regularization strategies for 3-d inverse electrocardiography. *Biomedical Engineering, IEEE Transactions on*, 58(6):1827–1838, 2011.
- [WKMJ13] D. Wang, R.M. Kirby, R.S. MacLeod, and C.R. Johnson. Inverse electrocardiographic source localization of ischemia: An optimization

- framework and finite element solution. *Journal of computational physics*, 250:403–424, 2013.
- [WOH⁺95] D. Wei, O. Okazaki, K. Harumi, E. Harasawa, and H. Hosaka. Comparative simulation of excitation and body surface electrocardiogram with isotropic and anisotropic computer heart models. *Biomedical Engineering, IEEE Transactions on*, 42(4):343–357, 1995.
- [WSH14] D. Wirtz, D. Sorensen, and B. Haasdonk. A posteriori error estimation for DEIM reduced nonlinear dynamical systems. *SIAM Journal of Scientific Computing*, 36(2):A311–A338, 2014.
- [YA98] G.-X. Yan and C. Antzelevitch. Cellular basis for the normal T wave and the electrocardiographic manifestations of the long-QT syndrome. *Circulation*, 98:1928–1936, 1998.
- [ZBMHO94] T.R. Zwink, I.G. Burwash, C.Y. Miyake-Hull, and C.M. Otto. Changes in Aortic Annulus Diameter During the Cardiac Cycle and its Effect on Predicting Aortic Valve Prosthesis Size. *Journal of diagnostic medical*, 10(5):262–267, 1994.
- [Zem09] Nejib Zemzemi. *Étude théorique et numérique de l’activité électrique du cœur: Applications aux électrocardiogrammes*. PhD thesis, Université Paris-Sud, 2009.
- [ZIMM⁺05] Q. Zhang, A. Illanes Manriquez, C. Medigue, Y. Papelier, and M. Sorine. Robust and efficient location of t-wave ends in electrocardiogram. *Computers in Cardiology*, 32:711–714, 2005.